University of Dundee

# DOCTOR OF PHILOSOPHY

## Swimming patterns of zoospores

Savory, Andrew

*Award date:*
2013

Link to publication

**General rights**
Copyright and moral rights for the publications made accessible in the public portal are retained by the authors and/or other copyright owners and it is a condition of accessing publications that users recognise and abide by the legal requirements associated with these rights.

- Users may download and print one copy of any publication from the public portal for the purpose of private study or research.
- You may not further distribute the material or use it for any profit-making activity or commercial gain
- You may freely distribute the URL identifying the publication in the public portal

**Take down policy**
If you believe that this document breaches copyright please contact us providing details, and we will remove access to the work immediately and investigate your claim.

Download date: 05. May. 2023

DOCTOR OF PHILOSOPHY

# Swimming Patterns of Zoospores

Andrew Savory

2013

University of Dundee

Conditions for Use and Duplication
Copyright of this work belongs to the author unless otherwise identified in the body of the thesis. It is permitted to use and duplicate this work only for personal and non-commercial research, study or criticism/review. You must obtain prior written consent from the author for any other use. Any quotation from this thesis must be acknowledged using the normal academic conventions. It is not permitted to supply the whole or part of this thesis to any other person or to post the same on any website or other online location without the prior written consent of the author. Contact the Discovery team (discovery@dundee.ac.uk) with any queries about the use or acknowledgement of this work.

# Swimming Patterns of Zoospores

By

Andrew Savory

A Thesis submitted for the degree of Doctor of Philosophy

Division of Mathematics

University of Dundee

Dundee

March 2013

# Contents

# List of figures

# List of tables

# Acknowledgements

Firstly, I would like to express sincere gratitude to my supervisor, Dr. Fordyce Davidson. Always on hand for discussions throughout my PhD, his thoughtful insight, knowledge and patient guidance have simply made this thesis possible. I have learned a great deal from him and his enthusiasm for my work has continually encouraged me to persevere and kept me on the right track.

I am very much indebted to all those in the Oomycete group at the University of Aberdeen for educating me in the ways of the lab. Particular thanks to my second supervisor Prof. Pieter van West, Dr. Stephan Wawra and Dr. Laura Grenville-Briggs for all their help with experiment preparation and general good ideas over the years.

I would also like to thank all of the staff in the Division of Mathematics at Dundee for many helpful discussions and for generally making my time here enjoyable. Special mention must be made of the all-knowing Mr. Nick Dawes, who fixed countless technical difficulties.

Last, but not least, a big thank you to all of my friends and family, especially my parents, who have supported me, had faith in me, proofread for me, and helped keep things in perspective during the more difficult times by reminding me that not everything has to be about work. Without all of you, I'm absolutely sure that I would not have been able to finish. It certainly hasn't gone unappreciated.

# Declaration

I declare that the following thesis is my own composition and that it has not been submitted before in application for a higher degree.

Andrew Savory

# Certification

This is to certify that Andrew Savory has complied with all the requirements for the submission of this Doctor of Philosophy thesis to the University of Dundee.

Dr. Fordyce Davidson

# Abstract

*Phytophthora infestans* is a highly destructive plant pathogen and the causal agent of the potato blight disease that devastated Ireland's potato crops in the 19th century. Today, this disease is still a serious problem, with global crop losses and spending on control measures estimated to exceed £3 billion annually.

A key to the success of *P. infestans* is the dispersal of free-swimming zoospore cells from infected plant tissue into aqueous environments. These cells are specialised infection agents that have evolved an array of tactic responses in order to locate and infect new hosts. An interesting and poorly understood aspect of zoospore behaviour is the phenomenon of auto-aggregation. That is, large numbers of zoospores observed *in vitro* are seen to form complex, large-scale patterns in the absence of external signals or stimuli. Current competing hypotheses suggest that patterns are formed by one of two distinct, concentrative phenomena: chemotaxis and bioconvection.

In this thesis we investigate the mechanics and implications of zoospore auto-aggregation behaviour using an interdisciplinary approach that combines continuum mathematical modelling with laboratory experimental work. We investigate the modelling of chemotactic and bioconvective processes and compare results with our experimental observations. Finally, we present a novel bioconvection-chemotaxis model and thus provide strong evidence to support the hypothesis that auto-aggregation in *P. infestans* zoospores results from a necessary combination of these processes.

# Chapter 1

# Introduction

This introductory chapter serves to motivate and outline the work presented in this thesis. An overview of the thesis structure as well as brief descriptions of chapter contents will also be given. We begin by discussing the biological background information for the project.

## 1.1 Biological Background

### 1.1.1 Aggregation in Microorganisms

Microorganisms are everywhere and are estimated to account for close to 60% of the Earth's total biomass. The diversity of these life forms is vast: for example, some bacteria produce vital resources such as oxygen, pathogens cause a variety of diseases in animals and plants and fungi help to break down and recycle decaying matter [78]. The first observations of microbes were made four hundred years ago. However, it is

only recently that communication, cooperation and aggregation amongst these organisms has been revealed and has now become an important field of study in scientific research. Aggregation behaviour can carry many advantages, e.g. in locating nutrients, increasing infection pressure or to provide protection. In fact, the majority of microbial species are able to form what are known as *biofilms* [72]: large communities of cells that adhere to manmade and natural surfaces, held together by a self-produced extracellular polymeric substance (EPS). Most bacteria exist in this form as it provides protection against hostile environments, enhances antibiotic resistance [34], and is a means to share nutrients and genetic material among individuals [3]. For an overview of social behaviour in microbes, see [130] and references therein.

Chemotaxis, the chemically directed motion of cells, is one of the most ubiquitous mechanisms used by microorganisms to coordinate aggregation. The social amoeba and predator of bacteria, *Dictyostelium discoidium*, is commonly found in soil and has become a model organism for studies of cell-cell signalling (reported first in [107]). During the vegetative phase of its life cycle, *D. discoidium* exists as multiple, solitary cells that feed and divide by mitosis. Once the supply of food has depleted, this triggers the release of the chemoattractant, cyclic adenosine 3'5'-monophosphate (cAMP), in starving cells. The amoebae sense and respond to changing concentrations of this signal using receptors on their surface and aggregate to form a so-called "slug". In this multi-cellular form, it travels to the surface of the soil and becomes a fruiting body, which produces new cells. In this way, aggregation plays a crucial role in the survival and reproduction of *D. discoidium*.

The self-organisation of a microbial population certainly does not always require a chemical catalyst to be present, however. Bioconvection [103] is a phenomenon that occurs in some aquatic, free-swimming microbes where individuals are slightly denser than the surrounding fluid and have a tendency to swim towards its surface. The reason for this upswimming varies between organisms. For instance, *Bacillus subtilis* cells are

chemotactically attracted to and consume oxygen. This consumption creates a positive oxygen gradient towards the fluid surface, where the supply is replenished, causing an average flux of cells upwards [63]. Organisms that rely on photosynthesis, such as algae, can exhibit upswimming in response to light gradients [123]. Perhaps the best studied upswimming mechanism is gyrotaxis. Gyrotactic cells, e.g. *Chlamydomonas nivalis*, are bottom-heavy, with a centre of mass offset from the centre of buoyancy, causing the cell to swim upwards on average [68]. Whatever the mechanism, the end result is largely the same: a dense layer forms at the fluid surface and instabilities due to gravity lead to the formation of concentrated "plumes" of cells. A quantitative study of bioconvection patterns in *C. nivalis* was carried out by Bees and Hill [11], which details how the observed patterns relate to suspension density, suspension depth and time.

The advantages of bioconvective pattern formation in the natural habitats of microorganisms are not well understood at this time. One study by Jánosi *et al.* examined whether or not bioconvection patterns enhanced growth in *B. subtilis* and *B. licheniformis* [62]. Their findings indicated no significant differences in growth rates between pattern-forming and non-pattern-forming populations. Moreover, it was concluded that bioconvection was not an efficient means of transporting oxygen (consumed by *B. subtilis*) from the surface to the bulk of the fluid, as had been previously speculated. However, a later study, by Dombrowski *et al.* [32] reported contrasting results. When examining bioconvection of *B. subtilis* cells in a water droplet, plumes formed in the centre at the fluid surface. A "depletion zone" was also observed near the bottom of the drop where cell motility was greatly reduced due to lack of oxygen. Subsequently, plumes were then seen to move down the slanted meniscus of the drop and the resultant fluid motion stirred up and oxygenated cells in the depletion zone. Interestingly, the process as a whole concentrated most cells in the narrow region at the water, air, solid boundary, which was suggested as a possible means to initiate biofilm formation. It

seems then that there could be many ecological advantages to bioconvection that are yet to be uncovered.

In this thesis, we are interested in a particular class of microorganism, the Oomycetes, for which the two types of aggregation outlined above will be of particular relevance.

### 1.1.2 The Oomycetes

The Oomycetes are microorganisms that grow in a similar manner to filamentous fungi and are often referred to as pseudo-fungi. They are a highly destructive group of pathogens responsible for considerable economic losses in both agriculture and aquaculture [126]. Despite the numerous superficial similarities between Oomycetes and filamentous fungi, they in fact belong to the straemenopile kingdom due in part to the unique zoosporic stage in their life cycle (see Figure 1.2). A closer look at Oomycete morphology as well as molecular studies reveal more significant differences. Oomycetes have two copies of each chromosome in one nucleus per cell (diploid) as opposed to the single copy in fungi (haploid). Moreover, their cell wall is made of cellulose and beta glucans instead of the chitin that forms the main component of cell walls of fungi [40]. Further details on this topic can be found in [109].

### 1.1.3 *Phytophthora infestans* and Zoospores

Of the over five hundred known oomycete species, the *Phytophthora* genus comprises around sixty known species but it is estimated there may well be hundreds that are yet to be discovered [18]. Perhaps the most well-known and destructive currently known species is *Phytophthora infestans*. It was discovered in 1876 by Anton de Bary that the *P. infestans* pathogen is the cause of the potato blight disease and, consequently, the cause of the Irish potato famine (*Phytophthora* means "plant destroyer" [30]). It is not

only the potato plant that is susceptible to infection by blight as relatives such as the tomato can be damaged too. Blight can spread extremely rapidly with fields of crops being completely destroyed within one or two weeks of the first signs of infection [40]. Between 1845 and 1851, the blight devastated Ireland's potato crops and led to mass starvation. It is estimated that approximately one million people died and many others emigrated causing a massive fall in Ireland's population.

One hundred and sixty years on, potato blight still causes considerable damage to crops worldwide. An estimated £3 billion is lost every year to the disease (in a combination of crop losses and spending on control measures) and hence *P. infestans* is still considered to be a major global pest [35]. *P. infestans* has even been cited by biological weapons groups as a possible biowarfare threat and was researched for this purpose in the 1940s and 1950s, such is the destructive power of the disease [115]. The organism grows into the stem and leaf tissue causing death. Visible necrosis is usually seen two to four days after the initial infection has taken place. *P. infestans* may also infest the tubers, causing them to become soggy, rotten and inedible (see Figure 1.1). One of the most common control strategies for blight is the application of copper-based fungicides before infection. Acting as a protectant, these can increase yields by 10-40 % compared with non-treated crops [75]. For instance, the copper-based "Bordeaux mixture" has been used for over a century and has been shown to impair germination in sporangia and zoospores [74]. However, the use of fungicides can be very expensive (estimated at around $200 per acre in the USA as of 2001) and the effects of using such large amounts are not known [40]. Furthermore, their use can give rise to resistant strains, as was the case with the popular "metalaxl" fungicide that suffered a severe decline in efficacy [40]. Disease resistant potatoes are also used, a summary of which can be found in the recent review by Nowicki *et al.* [88].

Figure 1.1: Leaves of a potato plant and a tuber showing symptoms of blight.

The wide and fast spread of blight disease can be mainly attributed to the dispersal of free-swimming zoospore cells. Zoospores are single-nucleated, wall-less, non-proliferating cells and are specialised for dispersal in order to infect new host plants. *P. infestans* mainly reproduces asexually: many hundreds of thousands of sporangia sacs are produced on sporangiophores that grow from diseased plant tissue. Provided that the climactic conditions are suitable, namely damp and with a temperature below 12°C, these multi-nucleated sacs begin to divide and form individual zoospore cells. After this "cold shock" has taken place, the newly formed cells are then pushed out of an opening into the surrounding fluid where they can begin to search for new infection sites. The formation of zoospores is considered to be one of the fastest developmental processes in biology, with some species, such as *P. palmivora*, taking only five minutes to complete the sporangial cleaving process [126]. *P. infestans* can also reproduce sexually provided both its mating types, A1 and A2, are present [42]. This is not nearly as common as asexual reproduction in nature, since the two mating types are not often found together. Until the 1980s, the A2 type was only found in Mexico, which is presumed to be the origin of *P. infestans* [46]. However, according to a report from the British Potato Council [112], occurrences of the A2 type in Britain are on the rise: 38.4% of sites surveyed were found to contain the A2 type in 2005, compared with the 10.2% and 5.3% found in 2004 and 2003, respectively. Sexual reproduction is

achieved via formation of diploid oospores [33]. Oospores are released into the soil upon degradation of diseased plant tissue and can withstand the harsh conditions of the winter because of their thick cell walls [129]. The germ tubes produced form sporangia and infection continues as per the asexual cycle. Both the sexual and asexual life cycles of *P. infestans* are illustrated in Figure 1.2.

The anatomy of a zoospore is fairly simple: they are bean shaped and have a groove into which two flagella are inserted (see Figure 1.3). The anterior flagellum is of tinsel-type, adorned with flagellar hairs allowing it to act almost as an oar to propel the zoospore through aqueous environments. The posterior whiplash-type flagellum, on the other hand, is long and smooth and thought to act as a rudder to aid steering [22, 64]. Zoospores can swim for many hours in some cases with the help of internal, most likely lipid, food reserves [22]. Their swimming paths are helical and propel the cell forwards in a fixed direction as zoospores rotate [51]. These runs are punctuated by sharp turns from time to time that are apparently random, but also occur upon physical collisions [73]. As they swim, it is known that zoospores exhibit many different homing responses. For example, both chemotaxis and electrotaxis help guide cells towards infection sites, which will be discussed further in the next section. After a zoospore arrives at such a site, the flagella are shed, the cell becomes immobile and builds a cell wall in a rapid process called encystment [48]. These *cysts* are adhered to the surface of the plant by an, as yet, unknown substance. A germ-tube is then formed that differentiates into an appressorium from which a penetration peg emerges, which is able to infect plant cells directly [47].

Tactic responses, movement and even the morphology of wild type zoospores can be altered through genetic manipulation. For example, silencing of the G-alpha protein, Pigpa1, produced zoospores that turned six to eight times more frequently than the wild-type. Moreover, this mutant displayed an approximate 70% decrease in the efficiency of infection and a suppressed chemotactic response [73]. Normal zoospore

development can be disrupted by silencing Pi-RNH1, which was found to impede cytoplasmic cleavage, producing large zoospores with multiple flagella on their surface that are unable to swim normally [125]. Similar effects were observed in PnPMA1-silenced strains of *P. parasitica*: zoospores were produced that failed to develop flagella, were non-motile and encysted rapidly after being released from sporangia [134]. The transcription factor, bZIP, has also been identified as a key gene in the infection process: zoospores from silenced strains were seen to swim in tight circles (hindering the search for hosts) and also did not produce appressoria [64].

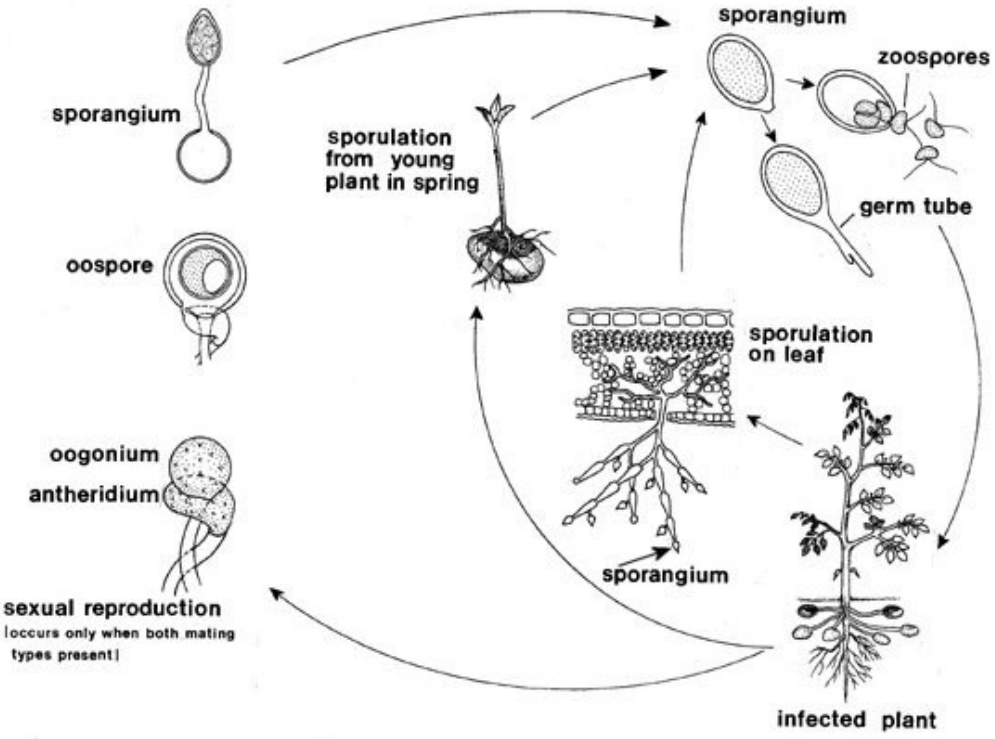


Figure 1.2: The life cycle of *P. infestans*. Image reproduced from [111].

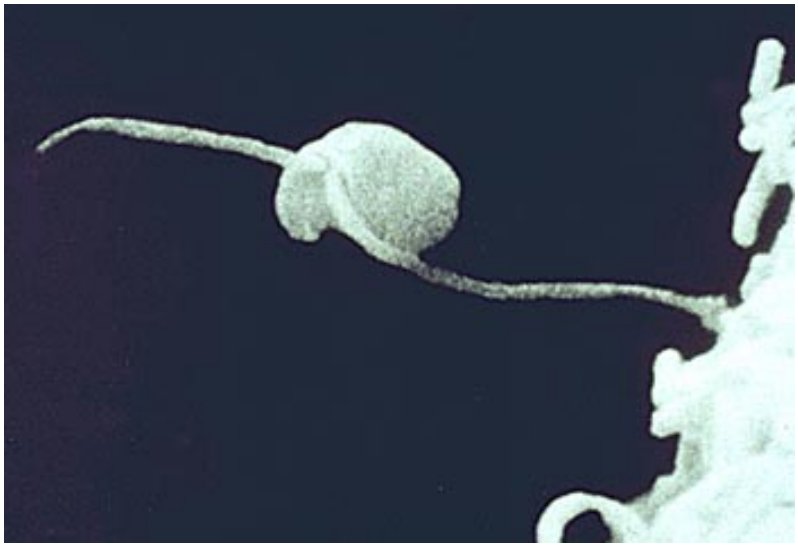

Figure 1.3: Close-up image of a zoospore showing both the tinsel-type and longer, whiplash-type flagella. Image reproduced from [1].

### 1.1.4 Zoospore Aggregation

Zoospores are not too discerning when it comes to selecting potential host plants. That is, the mechanisms for attraction, accumulation and encystment are generally not species-specific [51]. There are exceptions to this, e.g. *Phytophthora cinnamomi* is attracted to roots of avocado plants, but was not found to be attracted to others [133]. Goode first reported the aggregation of zoospores observed on plant roots and subsequently this has also been reported for many other *Phytophthora* species, including *infestans* (see [51] and included references for a summary of these findings). Zoospores tend to gather at the zone of elongation and wound sites of the roots, which is likely to be relevant to infection as this is where the greatest amount of nutrients are exuded [31]. Accumulation is thought to be primarily due to chemotaxis toward amino acids (e.g L-glutamate, L-asparate, L-asparagine and L-glutemine), although a precise correlation is difficult, given that root exudates consist of many possible attractants. Khew and Zentmyer tested the chemotactic responses of five *Phytophthora* species for a wide range of chemicals [69]. Results showed a positive response to many of these, but with a strong directional orientation towards the source of amino acids in particular.

Plant roots also generate exogenous electrical currents in the rhizosphere that can be measured using a vibrating electrode [14]. Morris and Gow [80] conducted *in vitro* experiments that showed the turning frequency of zoospores increased by three to four times in the presence of an electric field, suggesting that it is used by zoospores to detect living roots. In addition, the field also orientated the zoospores' flagella where their directions had been random in its absence. Van West *et al.* [122] showed that the accumulation of *Phytophthora* and *Phythium* zoospores (anodactic and cathodactic species respectively [80]) on plant roots strongly corresponded with the electric field profiles around those roots. In fact, it was also shown that artificial electric fields could be used to override normal chemoattraction.

The effect of pH has also been investigated by Morris *et al.* for zoospores of *P. palmivora* [81]. Zoospores were seen to move in the direction of decreasing pH but also that the artificial modification of naturally occurring gradients around plant roots did not have a significant effect on the pattern of accumulation, i.e. pH is likely not to be a major factor in aggregation.

Zoospores also exhibit chemotaxis towards encysted cells. Thomas and Peterson reported this phenomenon - we will call it *zoospore-cyst attraction* - for *Achlya* zoospores [118]. Circular masses of zoospores between 50-300 $\mu$m in diameter formed and grew at a linear rate as more cells were attracted towards it. An example of one of these cyst masses is shown in Figure 1.4. Germ tubes growing from isolated cysts have also been observed to display clear chemotropism in the direction of a cyst mass. Later, similar experiments were conducted by Reid *et al.* intended to study possible cross-species aggregation and its dependance on calcium [108]. The results showed that zoospores of the *Phytophthora* genus did not interact with those of *Phythium* and *vice versa*, leading to the conclusion that the cyst masses formed as a direct result of a chemically induced taxis. Furthermore, calcium was found to emanate from the centres of aggregates and was deemed to be important to their formation, if not the chemical attractant itself. A more recent experimental study by Galiana *et al.* [41] for *Phytophthora parasitica* zoospores showed that cysts could form biofilms on the surface of a leaf, which again attracted more free-swimming cells through chemotaxis. The attractant involved was suggested to be cAMP in this case, which was detected within microcolonies. This would seem to confirm earlier suggestions [108, 118] that zoospore-cyst attraction serves as a secondary stage of the host location and infection process, amplifying the number of cysts at suitable sites.

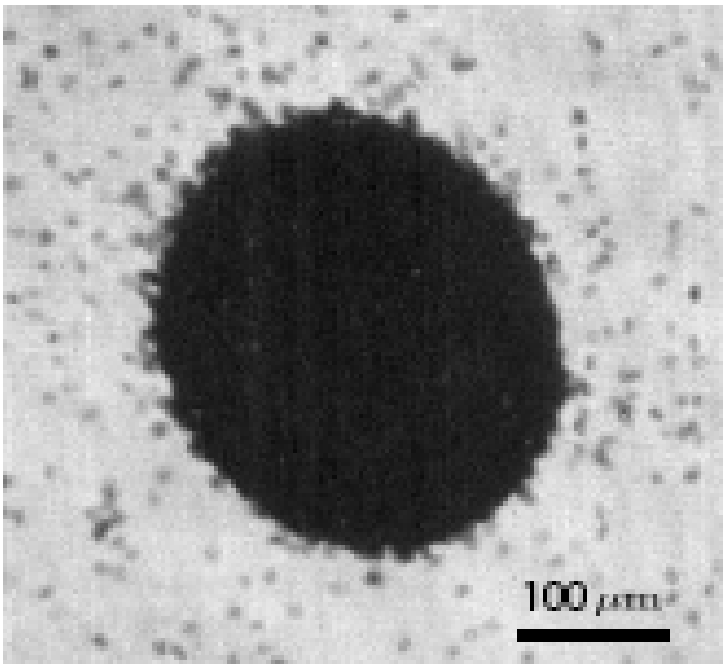


Figure 1.4: A circular aggregate of encysted *Achlya* zoospores. Image reproduced from [118].

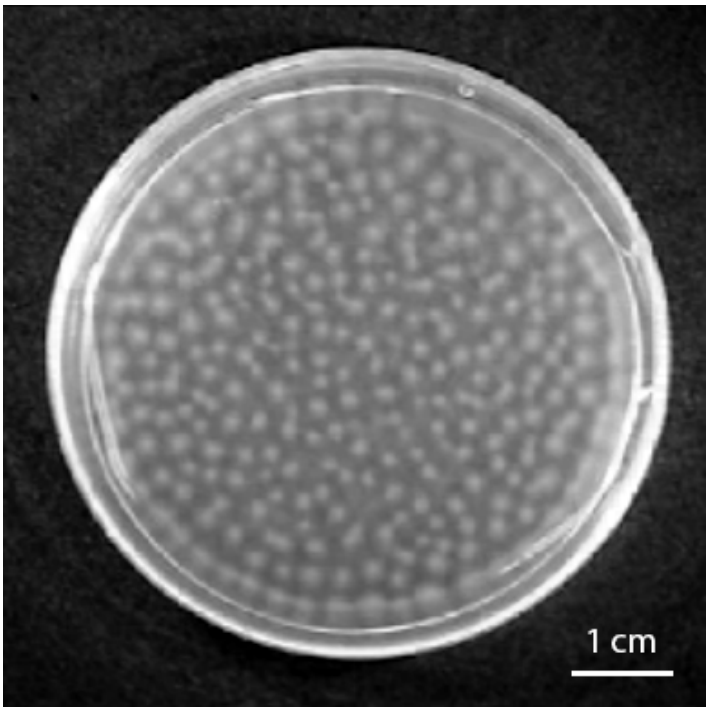


Figure 1.5: Auto-aggregation patterns for a suspension of *P. infestans* zoospores. Distinct spots have formed after approximately two minutes.

The tactic responses described above seem to confer obvious benefits in the context of host location and infection. Zoospores are also known to exhibit aggregation in the absence of external signals: in a suspension of sufficient concentration ($10^5 - 10^6$ cells $\text{ml}^{-1}$), zoospores form large-scale spatial patterns that can be seen with the naked eye. To avoid confusion with the aggregation behaviour described above, we will refer to this process as *auto-aggregation*. This was first reported for zoospores of *Phytophthora palmivora* in 1973 by Ko and Chase [71]. First, high density "bands" of cells were seen to form that subsequently broke up into distinct spots. Each spot had an area of high concentration at its centre and a lower density "cloud" of cells surrounding it. The patterns could be dispersed by gentle shaking of the petri dish but soon reformed, suggesting that they were formed by actively swimming cells [121]. The formation of aggregates was also dependent on suspension depth: suspensions of equal concentration produced patterns for a depth of $\approx$ 4mm but failed to do so for a depth of $\approx$ 0.1mm [70]. It is now believed that these patterns are the result of bioconvection, as first proposed by Carlile [21]. An investigation of bioconvection as a possible cause of zoospore auto-aggregation was carried out later by Ochiai *et al.* for *P. citricola* zoospores [89]. In the majority of their experiments, circular bands of zoospores would form very quickly at the outer part of the petri dish and, over the course of approximately fifteen minutes, contract into a point or line close to the centre. Other potential contributing factors were investigated including phototaxis and the effect of surface tension and were subsequently ruled out. Moreover, chemotactic auto-attraction between zoospores could not be be confirmed and it was concluded that the observed patterns were produced solely through bioconvection. An example of early auto-aggregation patterns for *P. infestans* zoospores is shown in Figure 1.5.

In summary, there are two competing hypotheses for what the mechanism behind

zoospore auto-aggregation could be. Based on observations of chemotaxis to root exudates and zoospore-cyst attraction, it has been speculated that auto-aggregation patterns are also a result of chemotaxis by an unknown attractant released by swimming zoospores [105, 126]. It is thought that this mechanism could help to increase infection potential in the absence of any host stimulus. On the other hand, evidence presented by Ochiai *et al.* suggested that auto-aggregation patterns are the result of zoospore bioconvection alone [89]. These authors were unable to confirm zoospore-zoospore chemotaxis in *P. citricola* zoospores.

## 1.2 Mathematical Background

As molecular biology has advanced to allow for the collection of larger and more detailed data sets on cellular mechanisms and interactions, mathematical modelling of aggregation has become increasingly useful in understanding the collective behaviour of microorganisms. The traditional "bottom-up" approach to modelling aims to use data on the behaviour of individuals to make helpful inferences about emergent, collective behaviour. See [114] for an overview of mathematical modelling in microbial systems biology and how it has developed. Models for collective behaviour fall into two broad classes, continuum and discrete models. We now discuss each approach in turn.

Perhaps the most popular approach to modelling aggregation is to use partial differential equation (PDE) models. In the modelling of chemotaxis, a breakthrough came with the introduction of one such model for chemotactic aggregation in *D. discoidium* cells by Keller and Segel [65, 66]. The model consists of two, coupled equations describing the spatio-temporal evolution of cell density and cAMP concentration. Since its introduction in the early 1970s, this model has precipitated many closely related or

augmented models for a variety of other organisms (see [25, 39, 82, 131] and references for some examples). The classical model is shown below in (1.1).

$$\begin{aligned} \frac{\partial N}{\partial T} &= -\nabla \cdot (-D_N \nabla N + \chi_N \nabla C), \\ \frac{\partial C}{\partial T} &= -\nabla \cdot (-D_C \nabla C) + \alpha N - \beta C, \end{aligned} \qquad \text{in } \Omega \subset \mathbb{R}^k, \tag{1.1}$$

where $N(\mathbf{X}, T)$ represents the density of cells; $C(\mathbf{X}, T)$ represents the concentration of chemoattractant; $D_N$ and $D_C$ are diffusion coefficients; $\chi_N$ is the chemotactic response coefficient and $\alpha$ and $\beta$ are the production and degradation rates of the chemoattractant respectively. These equations hold on a smooth, bounded domain, $\Omega$. In the vast majority of cases, the boundary conditions used are of zero-flux type, but there have been investigations into the effect of alternative boundary conditions on the patterns produced by the model [84]. Keller-Segel type models have invited a great deal of analytical interest, e.g. the study of global existence, structure and stability of solutions. The classical, or minimal, model has global solutions for $\Omega \in \mathbb{R}$, i.e. solutions that exist for all time, but can exhibit finite time blow-up in higher space dimensions [59, 101, 117]. The review paper [53] by Hillen and Painter and included references give an excellent summary of global existence results (among others) for the classical model and a number of other Keller-Segel type systems. The stability of solutions is important to an understanding of the capacity of the model to generate patterns and how these evolve. Linear stability analysis of homogeneous steady states can predict whether patterns are likely to form under certain conditions [83]. The existence of heterogeneous (spatially inhomogeneous) steady-state solutions has also been studied using numerous techniques including bifurcation analysis [49, 110]. A common feature of these solutions is "metastability", where - in the 1-D case for example - all

steady states with more than one point of inflection are marginally unstable with positive eigenvalues that are very close to zero, resulting in a slow evolution towards a stable state with a single peak [106].

The first mathematical investigation into bioconvection was made by Plesset and Winet, who considered a stratified fluid with a dense layer of cells at the top that is gravitationally unstable [104]. Numerical predictions of the wavelengths of initial patterns for *T. pyriformis* could then be made using linear analysis. Models for bioconvection have also made use of PDEs. Such models consist of a conservation equation for the microorganisms coupled with the Navier-Stokes equations for the fluid in which they are suspended. It is normally assumed that this fluid is incompressible and in its general form, a model for bioconvection reads

$$\begin{aligned} \rho_w\left(\frac{\partial \mathbf{U}}{\partial T}+(\mathbf{U}\cdot\nabla)\mathbf{U}\right) &= -\nabla P_e-(\rho_c-\rho_w)vNg\hat{\mathbf{z}}+\mu\nabla^2\mathbf{U}, \\ \nabla\cdot\mathbf{U} &= 0, \qquad \text{in } \Omega\subset\mathbb{R}^k, \\ \frac{\partial N}{\partial T} &= -\nabla\cdot\left[N(\mathbf{U}+\mathbf{V}_N)-\mathbf{D}\cdot\nabla N\right], \end{aligned} \tag{1.2}$$

where $\mathbf{U}(\mathbf{X},T)$ is the fluid velocity; $N(\mathbf{X},T)$ is the cell density; $\rho_w$ and $\rho_c$ are the densities of the fluid and a cell respectively; $P_e(\mathbf{X},T)$ is the excess pressure over hydrostatic; $v$ is the cell volume; $g$ is acceleration due to gravity; $\mu$ is dynamic viscosity; $\mathbf{V}_N$ is the average upswimming velocity of a cell and $\mathbf{D}$ is the diffusivity tensor associated with cells. The equations hold on a bounded domain, $\Omega$. A key assumption in the construction of these models is that the cells are too small to affect the bulk fluid motion other than through gravitational buoyancy (the Boussinesq approximation). For this to make physical sense, the suspension must be dilute, i.e. the volume fraction of the cells in

comparison to the rest of the suspension is small. For a suspension with a concentration of $10^4 - 10^8$ cells ml$^{-1}$, typical of concentrations considered in this thesis, this fraction is within the range $10^{-6} - 10^{-2}$, and so this assumption is justified.

Continuum models for bioconvection have attracted the most attention. Many variations have been proposed and can be distinguished from one another by the form of upswimming velocity used. As discussed above, this largely depends on the organism of interest. The first of these models was proposed by Childress *et al.* for upswimming algae [28, 76] in 1974. Their model is the most generic of its kind as it does not attribute upswimming to any specific mechanism: the upswimming velocity is given by $\mathbf{V_N} = V_N\hat{\mathbf{z}}$, where $V_N$ is a positive constant and $\hat{\mathbf{z}}$ is the upward pointing unit vector. The diffusion tensor was also assumed to be a constant. A more complex model for gyrotactic *C. nivalis* cells was proposed by Pedley *et al.* in 1988 [98]. In the model, gyrotaxis is represented in the cell conservation equation by writing the upswimming velocity as $V_N\mathbf{p}$, where $V_N$ is a positive constant and $\mathbf{p}$ is the unit swimming direction, for which an average can be computed. Diffusion was again assumed to be isotropic. In 1990, Pedley and Kessler re-thought their original approach, proposing that the assumption of isotropic diffusion and the inclusion of a bias in the average swimming direction was inconsistent [99]. Their solution was to use a probabilistic approach, with the swimming direction $\mathbf{p}$ represented by a probability density function, $f(\mathbf{p})$, that is determined as the solution of a Fokker-Planck equation.

As indicated above, bioconvection can be driven by other factors besides a cell's physical shape. A model for bioconvection in *Bacillus subtilis* cells, which exhibit oxytaxis, was proposed by Hillesdon *et al.* [54]. A Keller-Segel type flux term was incorporated into the cell conservation equation, *viz.* $\mathbf{V_N} = \chi\nabla C$, where $\chi$ is a constant chemotactic coefficient and $C$ is the oxygen concentration. Light can also play a role and a model proposed by Vincent and Hill considers this case [123]. It is proposed that the average swimming velocity can be expressed as $V_N T(I)\hat{\mathbf{z}}$, where $V_N$ is as above, $T(I)$ is a taxis

function depending on light intensity, $I$, and $\hat{\mathbf{z}}$ is the upward unit vector as above.

The solutions of bioconvection models have been studied in a variety of ways. Ghorai and Hill studied the original continuum model of Pedley *et al.* and determined conditions for the existence and stability of a 2-D plume in a tall chamber with stress-free sidewalls [43]. It was shown that such a plume is stable in a shallow chamber and becomes unstable in a sufficiently deep chamber. The analytically predicted growth rates of the instabilities agree well with results via numerical integration. The same authors also considered behaviour in a wide chamber and in particular derived results of the horizontal wavelengths of patterns on parameter values and suspension depth [44]. The revised continuum model by Pedley and Kessler has also been analysed: Bees and Hill [12] used linear analysis to predict the growth of patterns from a uniform suspension with finite depth, comparing the results with their experiments in [11]. A numerical scheme for solving the bioconvection equations in three dimensions has also been put forward by Ghorai and Hill [45]. Again, a stable plume is seen to form in a shallow chamber, which becomes unstable in a sufficiently deep chamber. For a more comprehensive overview of the continuum models for bioconvection mentioned above, the review papers [52, 100] and references therein give an excellent summary.

### 1.2.1 Discrete Models

Discrete and hybrid discrete-continuum modelling approaches have also been used to study chemotaxis. One such model was presented by Dallon and Othmer for *D. discoidium* aggregation with adaptive signalling [29]. In this model, cells are considered to be discrete points that move within a continuous concentration field of cAMP, the movements of which are governed by suitable rules that result in an average flux of cells up cAMP gradients. Stochastic models that take into account the noise that is inevitable in any biological system have been proposed. Chavanis presented a stochastic

version of the Keller-Segel model for chemotaxis in [27]. The original model can be recovered in the mean field limit of the stochastic model.

Discrete models of bioconvection have also been developed. For example, the model introduced by Hopkins and Fauci [58] is again a discrete-continuum hybrid, with the fluid velocity represented by the incompressible Navier-Stokes equations and cells as discrete point sources of mass. Each cell is assigned a position, speed and orientation that can be tracked as they are affected by negative geotaxis, gyrotaxis and chemotaxis. The fact that cell geometry, flagellar motion etc. are not considered in this model simplifies computation sufficiently to allow for the simulation of a realistically large number of cells. As with continuum models, this approach shows that the wavelength of bioconvection patterns varies with domain depth and also that the plume stability decreases with depth. The main advantage of using this hybrid approach was that it allowed for the analysis of the path of single cells as they move through a plume. Therefore, this allows the direct analysis of how gyrotaxis orientates a given cell.

## 1.3 Thesis Outline

The rest of this thesis is ordered as follows. In Chapter 2 we review key experimental observations in the literature regarding zoospore pattern formation and outline the materials, methods and results for all our laboratory experiments. Our experiments reveal that the observations reported by Ko and Chase in [71] (among others) on the aggregation of *P. palmivora* zoospores are applicable to *P. infestans* as well. Specifically, our experiments show that *P. infestans* zoospores form spontaneous, macro-scale patterns in the absence of external stimuli that depend on depth and zoospore concentration. We also report novel observations concerning the nature of these patterns such as their dependance on the shape of the containers in which they take place and how patterns

evolve over long times. Our experiments form the main motivation for the mathematical modelling and analysis in subsequent chapters. Also reported in Chapter 2 are our attempts to collect data on individual zoospore movement. This provides a deeper insight into zoospore behaviour at the micro scale and also aids parameterisation of the models we develop.

In Chapter 3 we investigate chemotaxis as a possible contributory mechanism in zoospore auto-aggregation. We give a summary of how the mathematical modelling of chemotaxis has developed historically and present a brief re-derivation of a continuum model of Keller-Segel type with added volume-filling effect. This system comprises two partial differential equations that describe the spatio-temporal evolution of cell density, $N(\mathbf{X},T)$, and concentration of chemoattractant, $C(\mathbf{X},T)$ and is given in dimensional form by

$$\begin{aligned}
&\frac{\partial N}{\partial T} = -\nabla\cdot\left(-D_N\nabla N + N\left(1-\frac{N}{N_M}\right)\chi_N\nabla C\right), \qquad \mathbf{X}\in\Omega\subset\mathbb{R}^k (k=1,2,3),\\
&\frac{\partial C}{\partial T} = -\nabla\cdot(-D_C\nabla C) + \alpha N - \beta C,\\
&\frac{\partial N}{\partial \mathbf{X}} = \frac{\partial C}{\partial \mathbf{X}} = 0 \quad \text{on} \quad \partial\Omega,\\
&N(\mathbf{X},0) = N_0(\mathbf{X}), \quad C(\mathbf{X},0) = C_0(\mathbf{X}),
\end{aligned} \tag{1.3}$$

where $\Omega$ is a bounded domain with smooth boundary, $\partial\Omega$. The values of the parameters in (1.3) are established using our data presented in Chapter 2 and estimates from existing literature. After non-dimensionalising (1.3), we proceed to solve the system in one, two and three space dimensions and examine the sensitivity of patterns to model parameter values. We discuss any qualitative and quantitative agreement with the experimental results reported in Chapter 2 and how zoospore-zoospore chemotaxis may contribute to auto-aggregation patterns.

In Chapter 4, we study the steady states of the volume-filling chemotaxis model in detail. We briefly outline results in the existing literature concerning steady states of chemotaxis models of this type. Such solutions satisfy the following system for non-dimensional cell density, $n$, and chemoattractant density, $c$:

$$\begin{aligned} 0 &= \Gamma\nabla\cdot\left[D\nabla n-\chi n\left(1-\frac{n}{\gamma}\right)\nabla c\right], \quad \mathbf{x}\in\Omega\subset\mathbb{R}^k(k=1,2,3),\\ 0 &= \Gamma\Delta c+n-c,\\ \frac{\partial n}{\partial \nu} &= \frac{\partial c}{\partial \nu}=0 \quad \text{on } \partial\Omega, \end{aligned} \tag{1.4}$$

where $\Gamma$, $\chi$, $D$ and $\gamma$ are positive constants representing domain scaling, chemotactic sensitivity, the relative diffusion of cells to chemoattractant and the maximum cell density, respectively. $\frac{\partial}{\partial \nu}$ represents the outward pointing normal derivative. We investigate bifurcation from uniform steady states and, using phase plane arguments, attempt to derive conditions on model parameters for the existence of all heterogeneous steady state solutions. Important results concerning symmetry in the phase plane will also be given. Next, we consider the stability of steady state solutions. The known conditions for linear instability of the uniform solution, $(n,c)=(1,1)$, of (1.4) are stated and suggest regions in parameter space that could support pattern formation. The connection between these conditions and the existence of non-uniform solutions is studied. Finally, we investigate the stability - or "metastability"- of heterogeneous solutions in 1-D using linear analysis.

Experimental results, including those that we have obtained, point to bioconvection as playing a major role in auto-aggregation patterns. Therefore, in Chapter 5, we discuss the mathematical modelling of zoospore bioconvection using a model first proposed by Pedley *et al.* [98], combined with the chemotaxis model from Chapter 3, *viz.*,

$$\left.\begin{aligned}
\rho_w\left(\frac{\partial \mathbf{U}}{\partial T}+(\mathbf{U}\cdot\nabla)\mathbf{U}\right) &= -\nabla P_e-(\rho_c-\rho_w)vNg\hat{\mathbf{z}}+\mu\nabla^2\mathbf{U},\\
\nabla\cdot\mathbf{U} &= 0,\\
\frac{\partial N}{\partial T} &= -\nabla\cdot\left[N\left(\mathbf{U}+V_N\mathbf{p}+\chi_N\nabla C\right)-D_N\nabla N\right],\\
\frac{\partial C}{\partial T} &= -\nabla\cdot\left[C\mathbf{U}-D_C\nabla C\right]+\alpha N-\beta C.
\end{aligned}\right\}\ \mathbf{X}\in\Omega\subset\mathbb{R}^k(k=2,3),$$

$$\mathbf{U}(\mathbf{X},0)=\mathbf{U}_0(\mathbf{X}),\quad N(\mathbf{X},0)=N_0(\mathbf{X}),\quad C(\mathbf{X},0)=C_0(\mathbf{X}),\quad P_e(\mathbf{X},0)=P_{e0}(\mathbf{X}) \tag{1.5}$$

where $\rho_w$ and $\rho_c$ are the densities of water and cells; $\mathbf{U}(\mathbf{X},T)$ is the fluid velocity; $P_e(\mathbf{X},T)$ is the excess pressure over hydrostatic; $v$ is the volume of a cell; $\mu$ is the dynamic viscosity of the fluid; $g$ is acceleration due to gravity; $V_N$ is the upswimming speed of the cells and; $\mathbf{p}$ is the unit swimming direction vector of cells. All other variables are as defined in (1.3). We consider solutions in a rectangular domain in the $X-Z$ plane with width, $L$, and depth, $H$ that represents a vertical cross section of a petri dish. Boundary conditions are given by

$$\begin{aligned}
\mathbf{U}=\mathbf{0} \quad &\text{at} \quad Z=-H \text{ and } X=0,L,\\
\mathbf{U}\cdot\hat{\mathbf{z}}=0 \text{ and } U_z=0 \quad &\text{at} \quad Z=0,\\
\mathbf{J}_N\cdot\hat{\mathbf{x}}=\mathbf{J}_C\cdot\hat{\mathbf{x}}=0 \quad &\text{at} \quad X=0,L,\\
\mathbf{J}_N\cdot\hat{\mathbf{z}}=\mathbf{J}_C\cdot\hat{\mathbf{z}}=0 \quad &\text{at} \quad Z=0,-H,
\end{aligned}$$

where $\mathbf{J}_N$ and $\mathbf{J}_C$ represent the flux of zoospores and chemoattractant, respectively.

After non-dimensionalising (1.5), we review linear results concerning the gyrotactic

instability of uniform steady states. Next, we study 2-D solutions of the model in the absence of chemotaxis ($\chi = 0$) and compare the results with experimental observations of auto-aggregation. This is done for a variety of chamber widths and depths. Finally, we investigate the effect of chemotaxis on these patterns ($\chi > 0$) and how this effect can be interpreted in the context of auto-aggregation.

In Chapter 6 we present and summarise key results and discuss the possible implications in understanding zoospore behaviour. A discussion of possible future directions for mathematical modelling and experimental work is also given.

# Chapter 2

# Experimental Methods and Results

## 2.1 Introduction

In the following chapter we give details of all experimental work: materials, methods and results. We choose to present all of this work here, rather than give a staggered account that is split over many chapters. We reference this work where appropriate.

First of all, we examine and discuss the phenomenon of zoospore aggregation in a liquid suspension. We discuss the work that has been done previously and experimentally confirm some results for *P. infestans* zoospores that have been reported for other species. We then present what we believe to be novel results about the behaviour of zoospores and emergent pattern formation over longer time scales.

Subsequently we focus on individual zoospore behaviour and, using video analysis and statistical techniques, collect useful data such as average swimming speed and straight run lengths. This data was collected not only for wild-type cells but also for a mutant strain. It will be useful in parameterising mathematical models in later chapters. We were also able to classify the movement of an individual cell by fitting a probability

distribution curve to the data set.

## 2.2 Zoospore Pattern Formation

Certain species of Oomycete, *P. infestans* included, are known to produce zoospores that exhibit aggregation behaviour. That is, in the absence of any external chemical or electrical signals, zoospores can spontaneously form patterns either at the micro scale or at the macro scale, the latter being observable with the naked eye. In the existing literature, there have been observations reported for essentially two different types of pattern formation. Over the years, there have been several names used to describe each of these patterns and they have occasionally contradicted one another. In light of this, it is helpful at this point to clarify any ambiguity and to define consistent terminology that we will use throughout the rest of this thesis.

### 2.2.1 Zoospore-Cyst Attraction

Firstly, we will discuss the chemotactic response of zoospores towards encysted cells, which we will refer to as *zoospore-cyst attraction*. In [118], Thomas and Peterson reported this phenomenon for zoospores of the *Achlya* oomycete species. Given a suspension of zoospores with an approximate concentration of $10^5$ zoospores per ml, after two to three hours circular masses of encysted zoospores formed, which grew at a linear rate of approximately $10^3$ cells per minute. The diameter of individual masses ranged from 50-2000 $\mu$m. After microscopic observation, the mechanism by which these masses were formed was concluded to be chemotaxis. Any zoospore that was sufficiently close to an aggregate would exhibit a period of "excited" swimming behaviour before encysting and joining the mass itself. It was not only cells that showed attraction toward aggregates but also germ tubes, which grew from zoospores that had

encysted on their own, displayed clear chemotropism in the direction of a mass of cysts.

Similar experiments were conducted by Reid *et al.* for various species from the *Phytophthora* and *Phythium* genera in [108]. The type of pattern formation and the time scales involved were very similar. However, their investigations were specifically related to the interactions across species and the role of calcium in the formation of cyst masses. It was concluded again that the pattern formation was a consequence of a chemically-induced, active taxis. Moreover, it also had some dependance on calcium, since calcium gradients were found to emanate from the aggregation centres. The fact that free-swimming zoospores from the *Phytophthora* genus were not attracted to aggregates of *Phythium* and *vice versa* lent further weight to the hypothesis that it was a chemical, not a mechanical, effect being observed.

It has been suggested that aggregation by zoospore-cyst attraction is actually just one part of a two-stage process [108, 118]. The first stage would be the attraction of zoospores to plant roots via chemical or electrical attraction causing cell encystment. Following this, the encysted cells would secrete another, possibly distinct, chemical signal that serves to amplify the first and recruit more zoospores to the infection site. Although the behaviour of the cells in response to signals for each stage were similar, the signal from the encysted cells was found to be stronger than that from the plant roots. A recent experimental study by Galiana *et al.* [41] for *Phytophthora parasitica* zoospores confirmed this to be the case, finding that microcolonies formed on the surface of a host plant would attract free-swimming cells through chemotaxis.

The fact that the aggregation behaviour is only seen after two to three hours indicates that it occurs after the zoospores' endogenous energy reserves have been depleted. This was said to be evidence for zoospore-cyst attraction being a survival mechanism of zoospores.

### 2.2.2 Auto-Aggregation

The second pattern formation process is the one we will study primarily in this thesis. We will refer to it as *auto-aggregation* but it has been known by other names in the past including simply "aggregation" or "pattern swimming" (see [70, 71] and [89] respectively). Ko and Chase first described this process for zoospores of *Phythophthora palmivora* in 1973 [71]. Again, given a suspension of zoospores of sufficient concentration, macro-scale patterns could be seen to form within a few minutes that were quite distinct from those observed in zoospore-cyst attraction. First, high-density bands are seen, which then break up to form spots with the highest concentration of zoospores at the centre. As in zoospore-cyst attraction, the number of aggregates that formed was dependent upon the initial zoospore concentration, the minimum being approximately $10^6$ zoospores per ml. The patterns could be dispersed by gently shaking the plate but soon re-formed, suggesting that these patterns are being formed by actively swimming cells. On examination of a single spot under the microscope, the cells swimming towards the centre were seen to be much faster than those that were swimming in other directions.

It is now thought that the formation of spots and bands in auto-aggregation is the result of bioconvection, first suggested in [21] and later discussed in [89]. Bioconvection is the name given to pattern formation in shallow suspensions of swimming cells, similar to Rayleigh-Benard convection [52]. Earliest recorded observations of this phenomenon date back to 1848, where so-called plumes of cells are set up as a result of an instability as upswimming cells accumulate at the fluid surface. The reasons for this upswimming can be either physical or chemical: cells can be bottom heavy leading to an average vertical swimming direction or they could be attracted to, for instance, an oxygen gradient originating at the fluid surface (see [63] for an example of this with *Bacillus subtilis* cells).

In the case of zoospores, an accumulation of *Phytophthora megasperma* cells at the fluid surface was observed by Ho and Hickman in [55]. In a follow-up paper, [56], the effect of oxytaxis was found to be absent and therefore it was concluded that the effect was physical rather than chemical. Unlike the zoospore-cyst attraction described above, the bioconvective behaviour of zoospores is not species-specific. That is, in experiments with suspensions containing zoospores from more than one species, aggregation was still observed in these suspensions, with the formation of auto-aggregation patterns depending only on the overall zoospore concentration [70]. Subsequent experiments by Cameron and Carlile confirmed this to be the case for other types of *Phytophthora* zoospores [20]. The most likely explanation for this behaviour was found upon closer examination of the cell shape. Ho *et al.* reported that *Phytophthora* zoospores are larger at the rear than at the front, causing the cell to point slightly upwards as it swims [57]. We reasonably assume that upswimming behaviour is present in *P. infestans* zoospores also.

Zoospore-cyst attraction and auto-aggregation have always been considered as separate processes. In [71], Ko and Chase tested the effects of adding encysted cells and plant roots to a zoospore suspension exhibiting auto-attraction. They showed that there was no observable change in aggregation patterns, suggesting that the fluid motion and active swimming of cells were too strong to be disturbed by chemotaxis. Therefore, the role of auto-aggregation in the infection process was unable to be confirmed from these experiments.

Next, we present our own experimental results and observations of auto-aggregation patterns for wild-type *P. infestans* zoospores.

## 2.3 Macro-Scale Experiments - Materials and Methods

*P. infestans* (strain 88069) plates were grown over 12-14 days on rye agar medium with 2% sucrose added at 18°C [23]. New plates were inoculated by transferring three agar plugs from fully grown plates. Sporangial cleavage and zoospore release was initiated by flooding plates with 10ml of cold water. The water was ordinary tap water and not autoclaved or de-mineralised as these practices have been known to inhibit zoospore release in past experiments. The flooded plates were left in a cold room at 4°C to release the zoospores over an average two to three hour period depending on the efficiency of zoospore release.

To harvest the zoospores, a sterile glass spreader was used to gently scrape the liquid off the surface of the plate. Suspensions were filtered through a 40$\mu$m cell strainer to remove any empty sporangia, mycelia or other debris. To determine zoospore concentrations, samples from a suspension were placed into a hemocytometer with depth, 0.1mm. Cells were counted from left to right in five grids with area 0.04mm$^2$ and this number was scaled appropriately in order to determine the concentration per ml. The counting process was repeated three times and an average was used. Photographs of macro-scale patterns were taken with a Nikon Coolpix 8800 digital camera and the microscopic stills from these experiments were taken using a Leitz Labovert microscope and Infinity Capture software. The contrast and colour of the images was adjusted using Photoshop CS6 in order to make the patterns as clear as possible.

### 2.3.1 The Impact of Domain Shape and Suspension Depth

To our knowledge, previously published experiments involving macro-scale pattern formation have been conducted in circular containers only. Ochiai *et al.* made comment on the circularity of auto-aggregation bands produced and suggested that they

were a consequence of the mixing process [89]. Here, we briefly show the contrasting patterns that can be produced by varying the shape of the experimental domain. The still photographs in Figure 2.1 demonstrate this effect. A circular petri dish produces the previously seen circular bands, or rings, whereas a square dish produces square, or straight, bands.

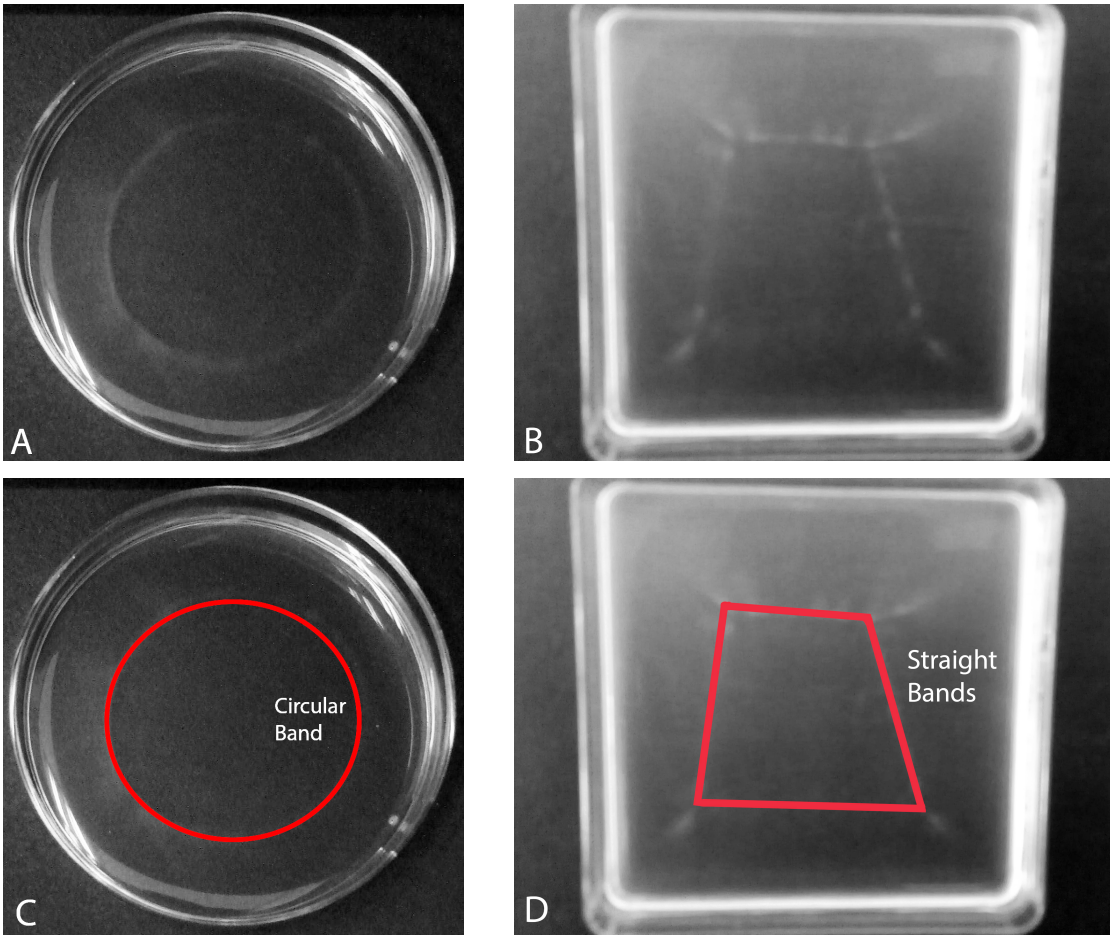


Figure 2.1: Auto-aggregation patterns in a circular (A) and square (B) dish. (A): a circular dish produces a circular, high density band. (B) a square dish produces a square pattern with straight bands. The bands in the square dish have started to break up into spots. (C) and (D) are annotated to clearly show the band shapes. The initial zoospore concentration was approximately $7.1 \times 10^4$ ml$^{-1}$.

There is a clear link here between the domain shape and the shape of auto-aggregation patterns. All of the experiments began with the suspension of zoospores being poured into the plate or other container. This act will inevitably create fluid motion and is, we believe, the explanation for the initial circular or square patterning. Since this initial fluid motion is damped out after short times in comparison with the time scale of the experiment, this does not impact upon the long-term zoospore behaviour, but rather sets up a different initial arrangement of aggregates. The photograph on the right of Figure 2.1 shows break-up of straight bands. This will be discussed further in Chapter 5 where we study a mathematical model for bioconvection. The form of mixing used at the beginning of the experiment can also influence the initial pattern distribution. Figure 2.2 shows an auto-aggregation experiment for which the suspension had been mixed by shaking the dish from left to right for a few seconds before patterns formed. Aggregates distinctly formed at the left and right of the dish, suggesting that the initial shaking concentrated zoospores in these regions.

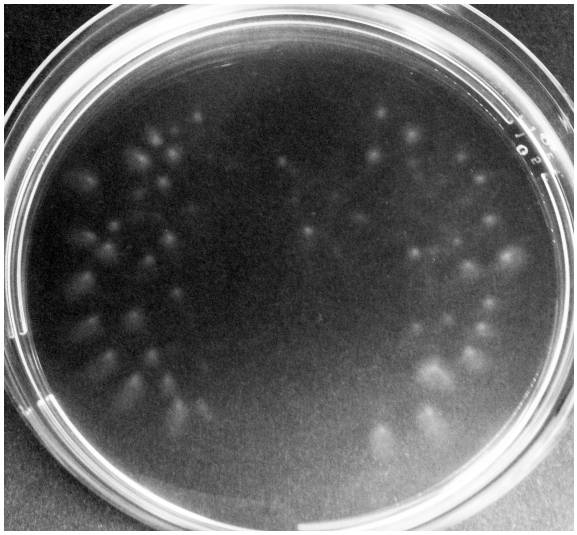

Figure 2.2: Auto-aggregation patterns produced after gentle shaking of a dish from left to right. The initial zoospore concentration was approximately $9.6 \times 10^4$ ml$^{-1}$. Aggregates were primarily located at the left and right of the dish, with one or two closer to the centre. The photograph was taken approximately five minutes after the initial shaking had ceased.

Not only does the domain shape affect pattern formation, but it appears the suspension depth also has considerable influence on the form patterns take. To illustrate this, if we use a single suspension of zoospores, we can test how patterns change in two different sized petri dishes. Figure 2.3 shows images of such an experiment using a 90mm and 60mm petri dish, moving the same suspension between each after a few minutes. Results showed that in a shallow suspension (3mm) an arrangement of spots formed, which had a region of high density at the centre and a roughly circular low density region surrounding it. Increasing the suspension depth (to 7mm) produced different patterns: aggregates were larger in size and had far more irregular shapes. Moreover, a deeper suspension produced high density bands at the fluid surface in addition to spots. The effect of depth variation is also illustrated in Figure 2.3 where a suspension in a tilted dish produced band patterns at the deep end and spot patterns at the shallow end. We acknowledge that the spot patterns in the shallow dish (Figure 2.3A) became distorted at the right-hand edge of the petri dish. This was due to a slightly uneven surface on which the experiment was conducted, leading to the suspension being slightly deeper at this edge. Figure 2.4 shows single spots in a shallow and deep suspension viewed from the side, again showing pattern wavelength to increase with depth.

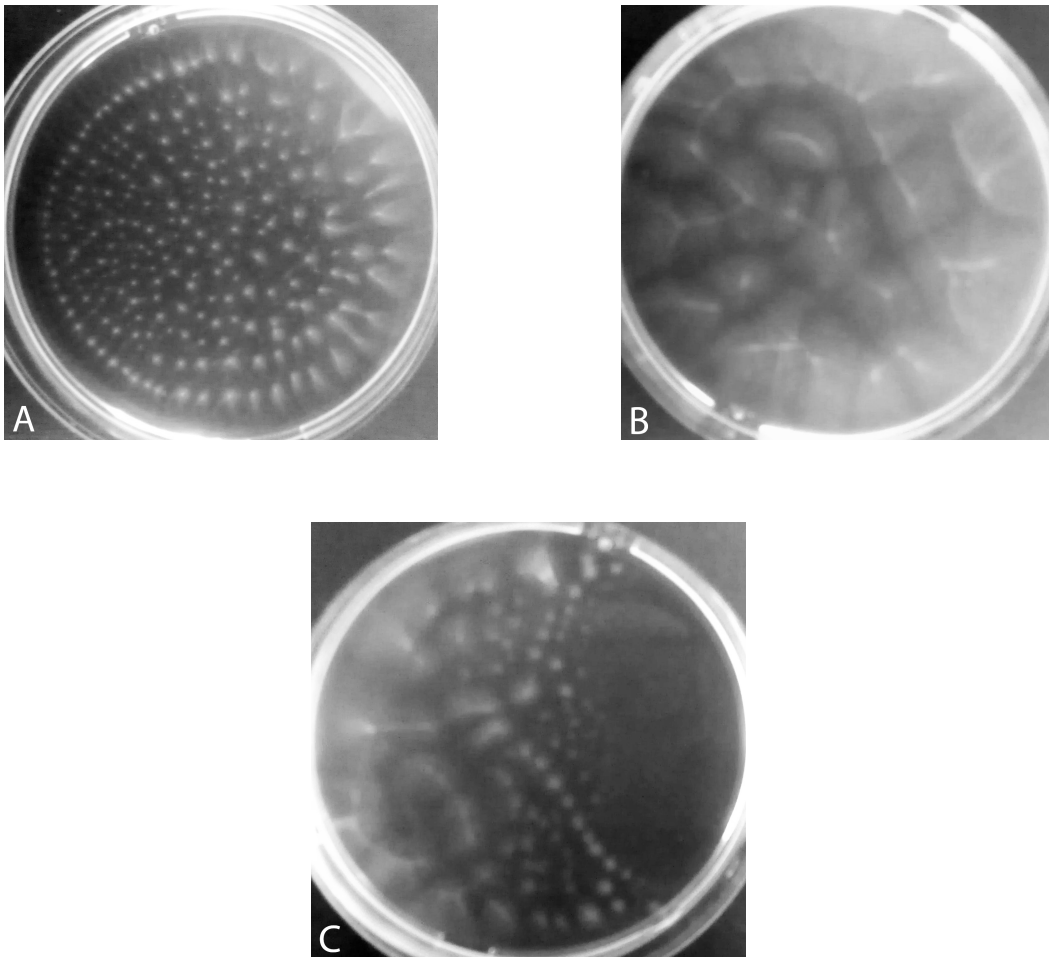


Figure 2.3: Auto-aggregation patterns in a suspension with concentration $2.4 \times 10^6$ zoospores $ml^{-1}$ and varying depths. (A): 3mm deep suspension showing distinct spot formation (dish diameter 90mm) (B): 7mm deep suspension showing the formation of bands. (dish diameter 60mm) (C): 90mm dish that has been tilted. As the depth decreases (from left to right) the patterns change from bands to spots. All photographs were taken five minutes after the suspension was poured into the dish.

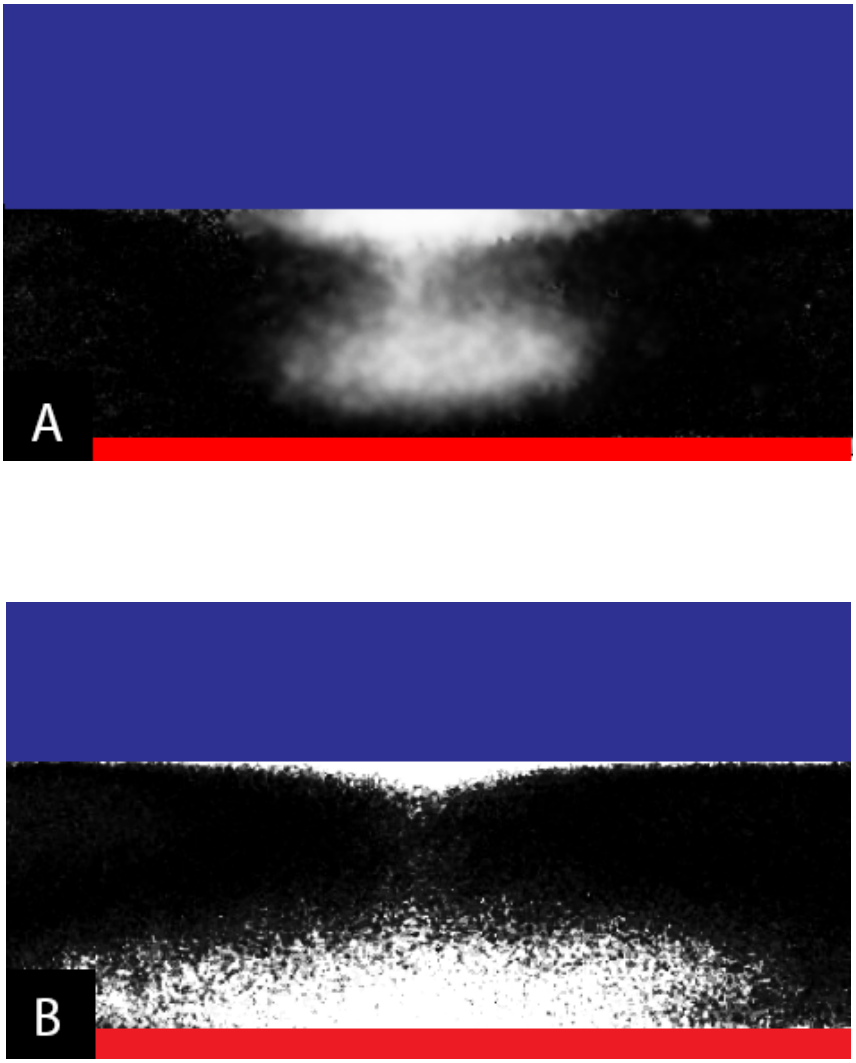


Figure 2.4: Side-on view of aggregates in a shallow and deep chamber. (A): a single plume formed in a suspension with depth $\approx$ 3.5mm. (B): a single plume formed in a suspension with depth $\approx$ 7mm. Images were adjusted so that zoospores appear in white against the rest of the fluid. Blue marks the region above the fluid surface and red marks the solid bottom of the chamber.

### 2.3.2 Auto-Aggregation After Long Times

Previously published observations of auto-aggregation have typically focused on pattern formation in the first few minutes after a suspension has been placed into a petri dish [70, 71, 89, 121]. However, we have discovered that there are patterning dynamics at work over time scales of many hours.

In Figure 2.5 we show snapshots of an experiment taken once every thirty minutes. In the early stages of aggregation, the standard formation of faint dots is again observed. Subsequently, the spots are seen to slowly drift towards one another and combine to form fewer aggregates. These images show the drifting appears not to be random and we therefore discount the possibility that the movement of aggregates is the result of the intrinsic stochasticity in the zoospore swimming. The experiment was repeated in a glass petri dish to measure any possible influence of electrostatic charge present in ordinary plastic dishes. There was no change in the patterns and so we discount the possibility that electrostatic interactions are involved in auto-aggregation. In the final two images ((G) and (H)) in Figure 2.5, faint patterns can be seen around the three plumes with what appear to be streams at the edges. We discuss this further later in this section.

We could also measure the time taken for aggregates to drift and join together. In Figure 2.6, snapshots are shown of an experiment that had run for three hours and only two aggregates remained. Measurements show that it took twenty five minutes for the aggregates to close the initial 7.8mm gap between them.

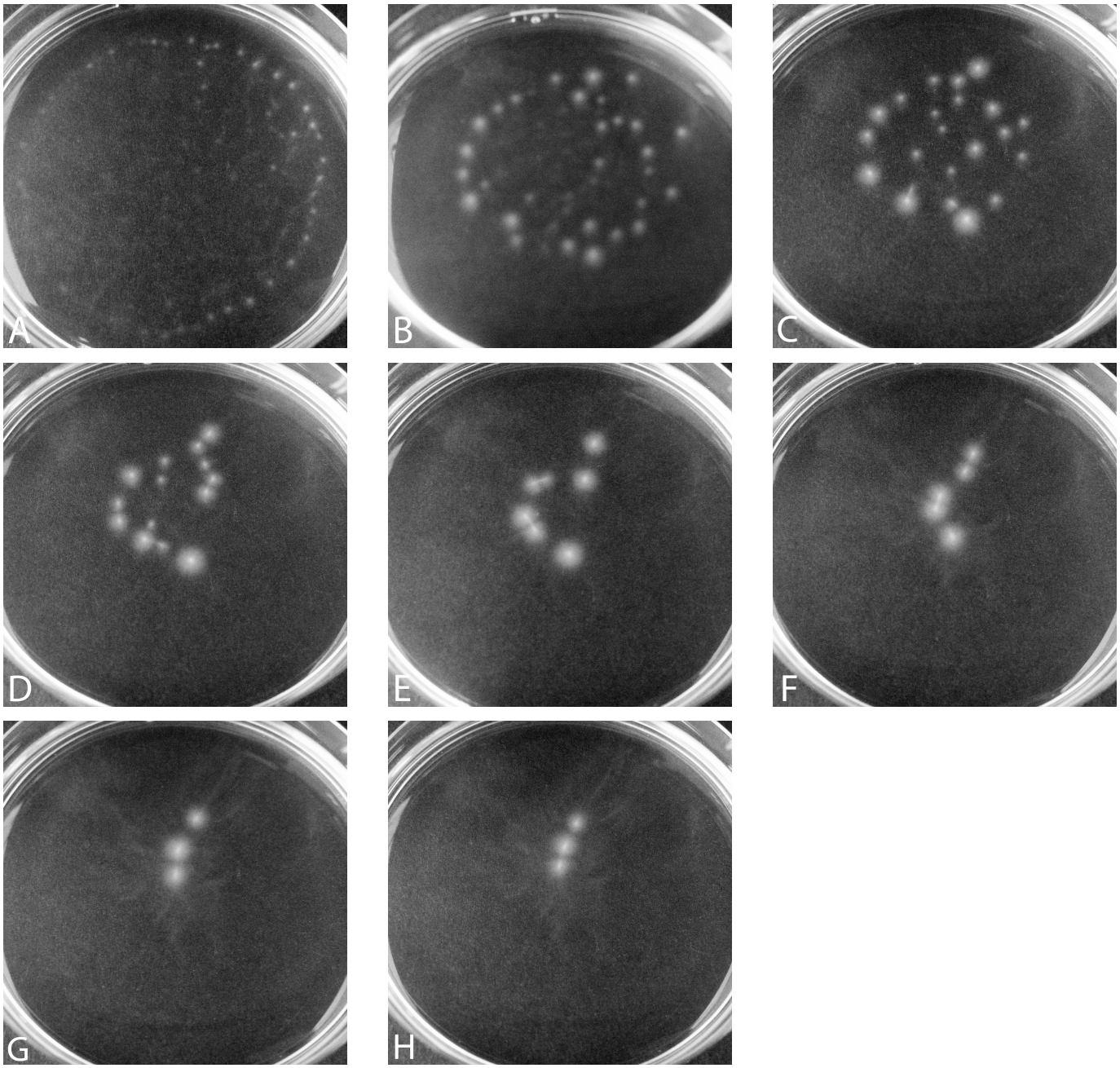


Figure 2.5: Snapshots of zoospore auto-aggregation taken every thirty minutes in order for (A)-(H). Photograph (A) was taken approximately five minutes after the suspension was poured into the dish (diameter 90mm). The suspension depth was approximately 3mm and the initial concentration of zoospores was approximately $7.8 \times 10^5$ ml$^{-1}$.

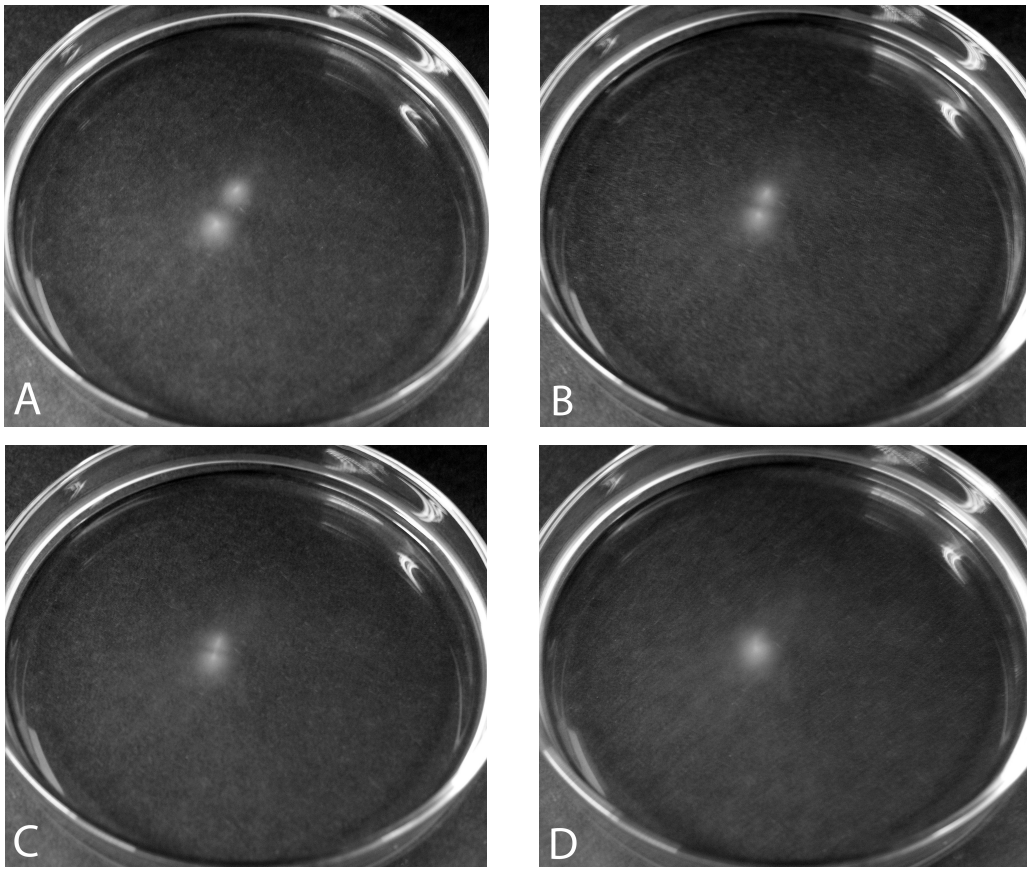


Figure 2.6: Drifting and merging of two plumes in a suspension with initial concentration of $4 \times 10^5$ zoospores ml$^{-1}$. Photographs (A)-(D) were taken 180, 192, 196 and 205 minutes after the experiment was started. The distance between the centre points of the aggregates shown in (A) was approximately 7.8mm.

Once all cells have stopped swimming, either due to encystment or otherwise, there appears to be an order to their final distribution in the suspension. Figure 2.7 shows images of the same experiment as above but after twenty four hours has elapsed and at various magnifications. The final state of the system is what we will call a *sheet* composed of encysted cells and intertwining germ tubes. The shape is roughly circular and this suggests that it was formed by zoospore-cyst attraction. As discussed above, aggregates were previously observed to be circular in shape. Since the zoospores were most concentrated at the centre of the dish in this particular experiment, it is likely

that a high concentration of encysted cells would build up over time and attract free-swimming cells that were not taking part in bioconvection. The streams at the edges of the structure could have resulted from non-uniformity of cyst concentration there. Zoospore-cyst attraction would also explain the faint streams that are visible in Figure 2.5.

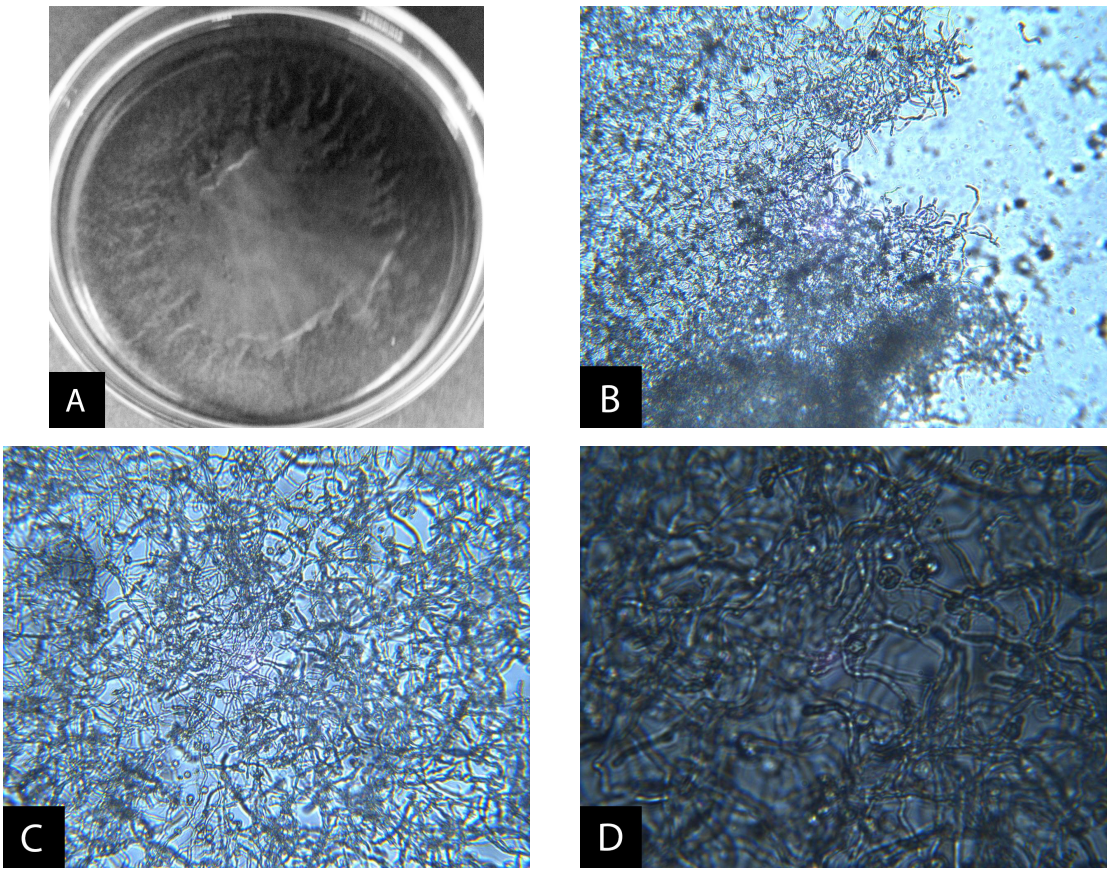


Figure 2.7: Images of an auto-aggregation experiment taken after twenty four hours. (A): circular sheet of germinated cysts with streams at the edges. (B): The edge of the sheet at 5x magnification. (C): The interior of the sheet at 10x magnification. (D): The interior of the sheet at 25x magnification. These are images from the same experiment as shown in Figure 2.6.

## 2.4 The Microscopic Scale

### 2.4.1 Swimming Speeds and Run Lengths

Data on the properties of an individual cell is useful when attempting to parameterise models of the processes under consideration. In this section, we outline the methods and results of our raw data collection, for which we used video analysis. The important measurements for our goals are those related to cell motility: most importantly, the average swimming speed of a cell and also the lengths of straight runs. The latter implicitly defines an average turning frequency. In order to collect this data we examined samples of zoospore suspensions under the microscope, recorded movies and then analysed these using the Kinovea software package [6]. Kinovea is a free, open source video analysis package that is ordinarily used by athletes to study performance but we found it is also very useful for tracking zoospore movement.

### 2.4.2 Materials and Methods

The growth of the 88069 strain of *P. infestans* and the harvesting of the zoospores produced was done using the same procedure as described above. To capture images, nail varnish was painted onto microscope slides in square shapes to create wells that would hold 3 $\mu$L samples. This ensured that zoospores were not restricted too much in their swimming once the cover slip had been applied. Stop motion videos were captured using a Zeiss AxiocamMR3 microscope with an A-plan 5x/0.12 Ph 0 objective. Images are 1388 x 1040 pixels in size with a 1.28 $\mu$m / Pixel scale factor. All videos are 45 seconds long with frame rates varying between 2.53 and 3.02 frames per second. These variations were taken into account in subsequent calculations.

Videos were loaded into the Kinovea package and a randomly chosen sample of cells

was tracked and the paths of individual cells traced. Due to the obvious similarity of individual cells, paths traced in Kinovea were carefully monitored from frame to frame to ensure consistency and were manually corrected when appropriate. We also acknowledge that swimming was not strictly in two dimensions and zoospores drifted slightly out of focus from time to time. However, the movement of zoospores in the vertical direction was negligible in comparison with the run lengths shown here. In Figure 2.8, the zoospore paths are represented by dotted lines with different colours for each cell tracked. Videos were labelled from 1 to 6.

Zoospores appear as grey dots in images shown in Figure 2.8. On first inspection, the swimming path of a given zoospore appears as a number of straight runs and random changes of direction. These new directions also appear to be random, i.e. there is no obvious bias in the zoospore movement. However, run lengths vary considerably between cells. Some have very short runs and hence their net displacement over the observed times is small. Others seem to display longer run lengths on average and hence a larger displacement.

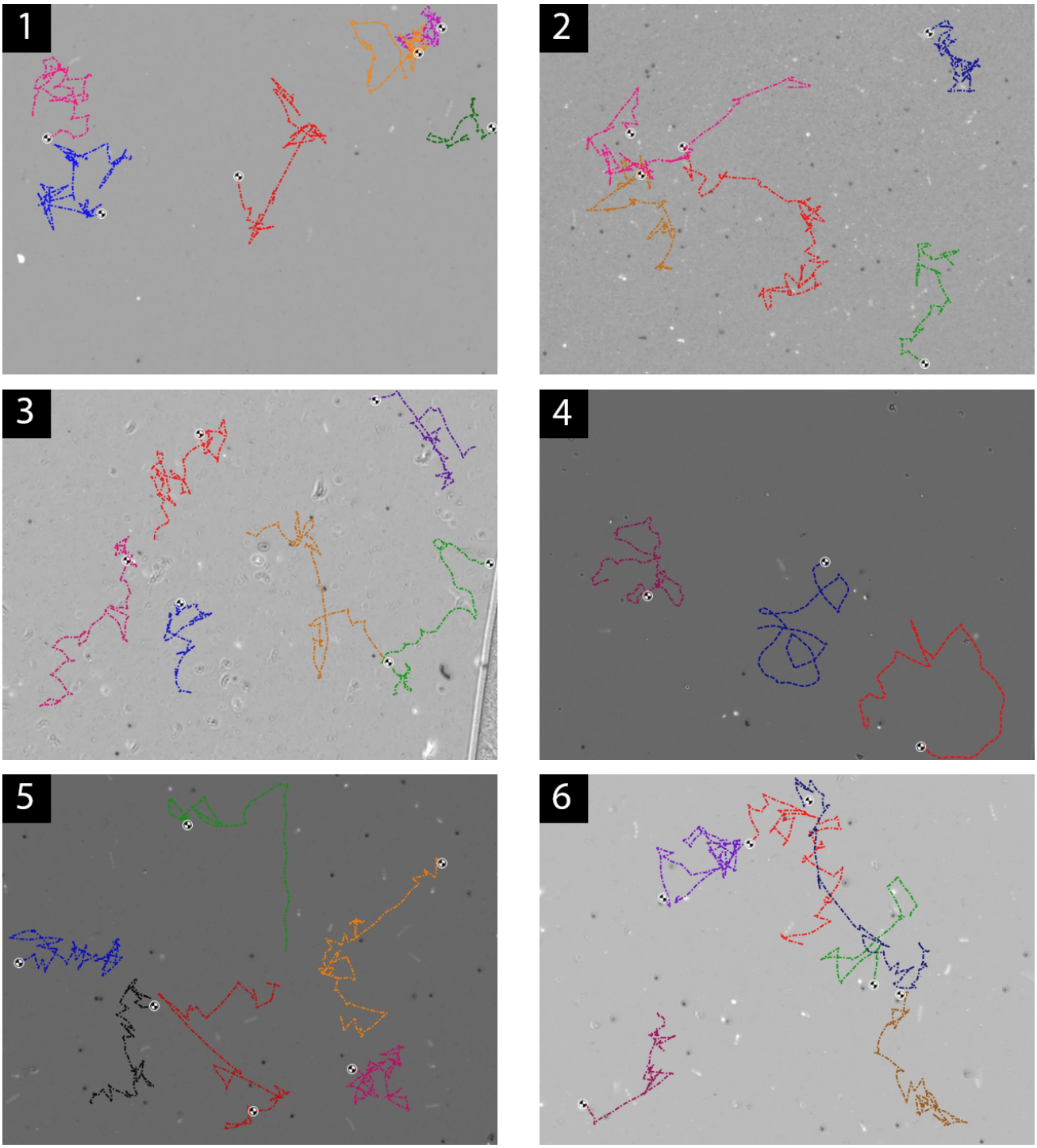


Figure 2.8: Cell paths traced in Kinovea for six sample suspensions of wild-type *P. infestans* zoospores (labelled 1-6). Colours represent the paths of individual cells. Circular markers are placed at the beginning of a zoospore run.

### 2.4.3 Statistical Results

Once the trajectory data has been captured, Kinovea outputs the coordinates of each cell for every frame in a spreadsheet format. From this, the distance travelled per frame can be calculated and hence an instantaneous speed for each frame. The raw output is measured in pixels per frame and so for each video we used the conversion: Speed ($\mu$m/s) = $\frac{1.28D}{\frac{45}{\text{No. of frames}}}$, where $D$ is the distance travelled over the frame. Results from a typical cell path are shown in Figure 2.9.

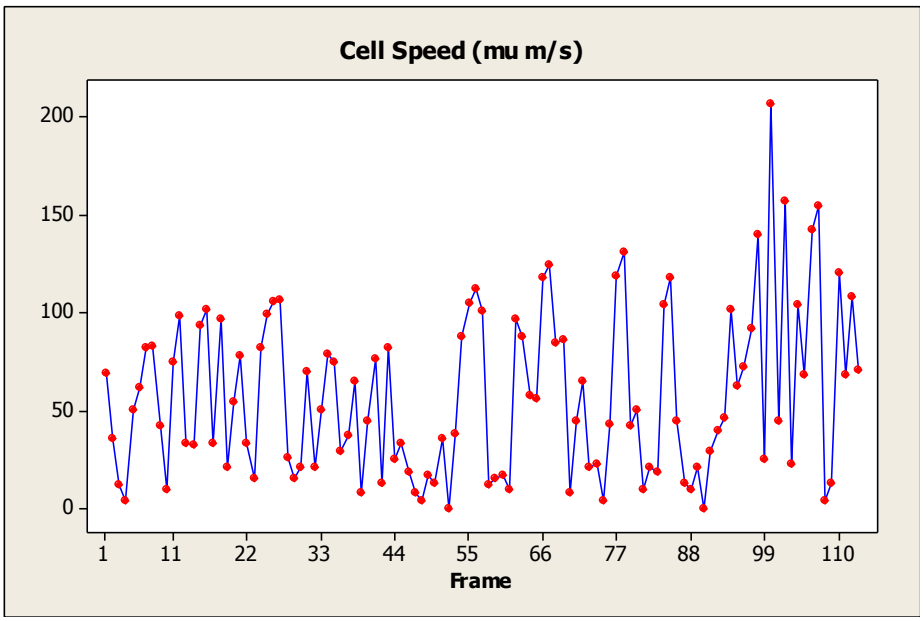


Figure 2.9: Speed of a typical zoospore cell over 114 frames. All values have been scaled to $\mu$m/s using the conversion: Speed ($\mu$m/s) = $\frac{1.28D}{\frac{45}{\text{No. of frames}}}$, where $D$ is the distance travelled over the frame.

For statistical analysis of the raw output we used the Minitab software package [7]. Minitab was used to produce graphical summaries for data from each video shown in Figure 2.8. These summaries are given in Figures 2.10-2.13. The data are shown in a histogram plot with a best-fitting normal curve superimposed. A list of statistics are also given including mean, standard deviation, 95% confidence intervals and a p-value for the Anderson-Darling normality test. All summaries are given below in full.

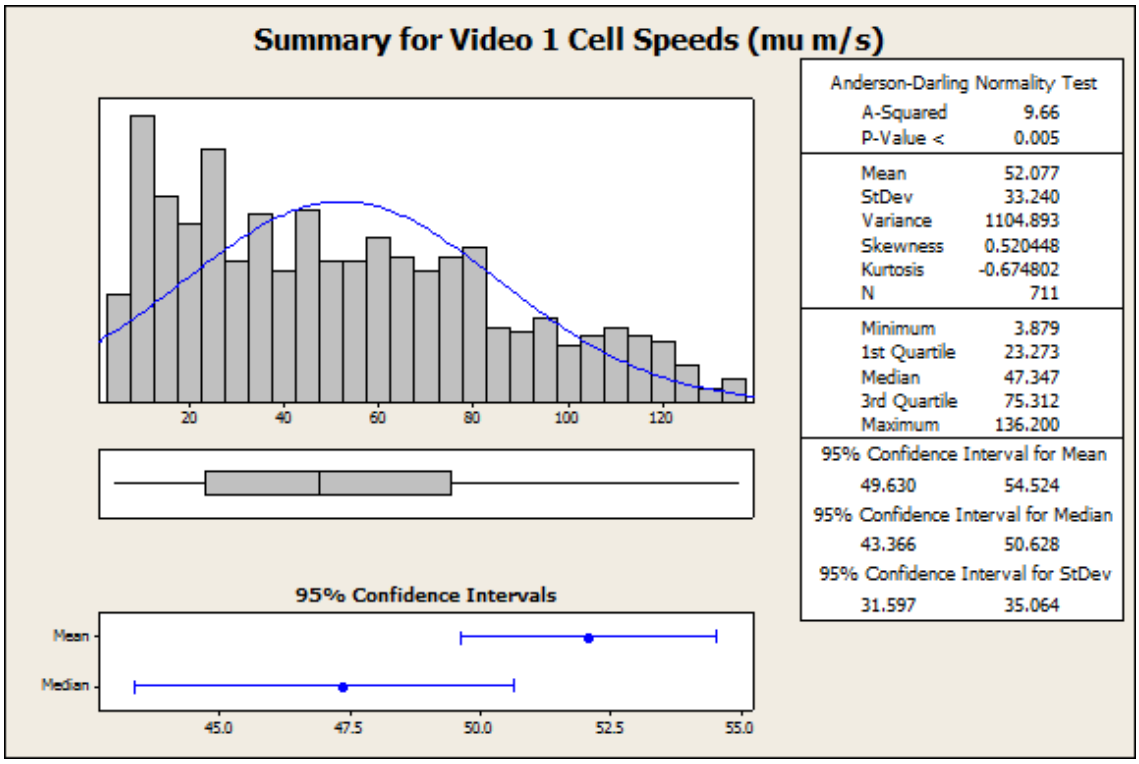


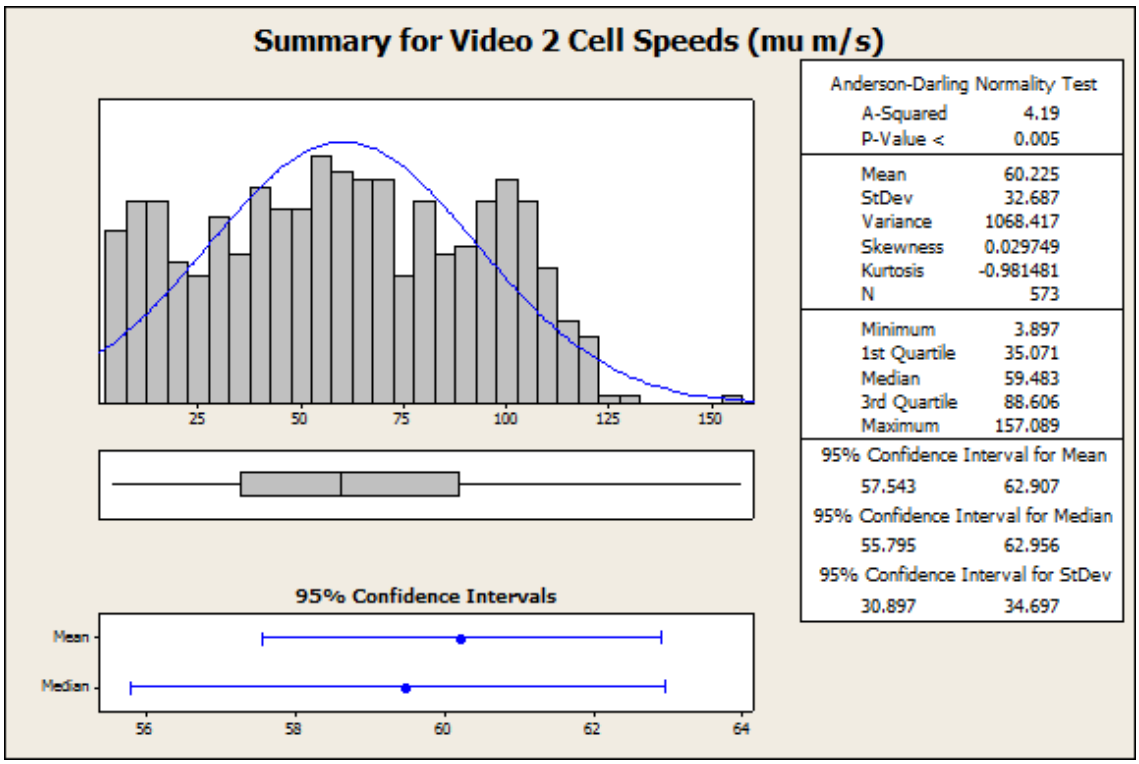


Figure 2.10: Graphical summaries of zoospore swimming speed data from videos 1 (top) and 2 (bottom) produced from Minitab.

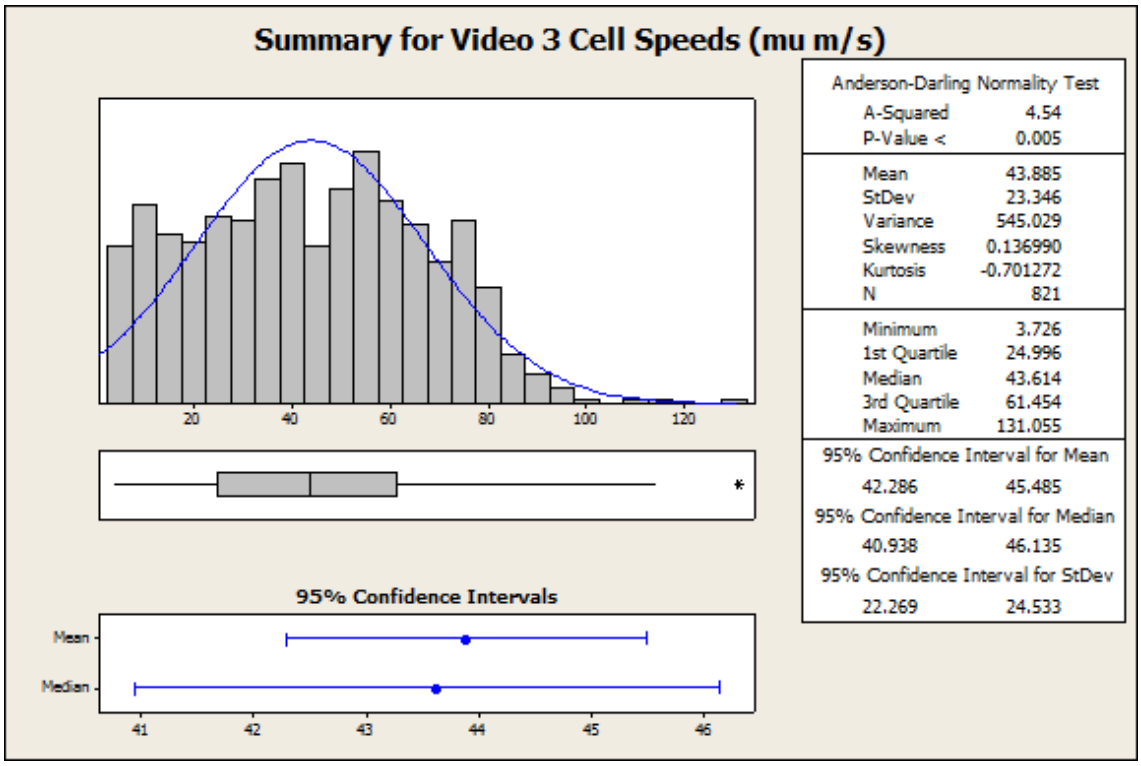


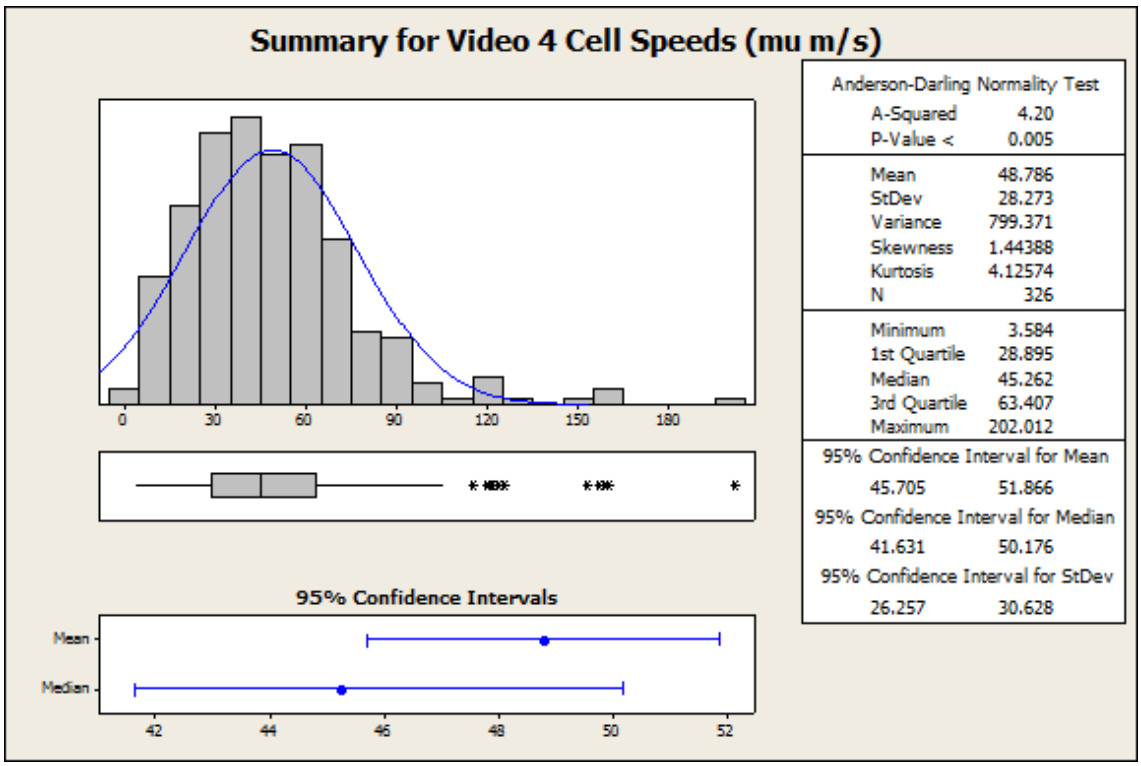


Figure 2.11: Graphical summaries of zoospore swimming speed data from videos 3 (top) and 4 (bottom) produced from Minitab.

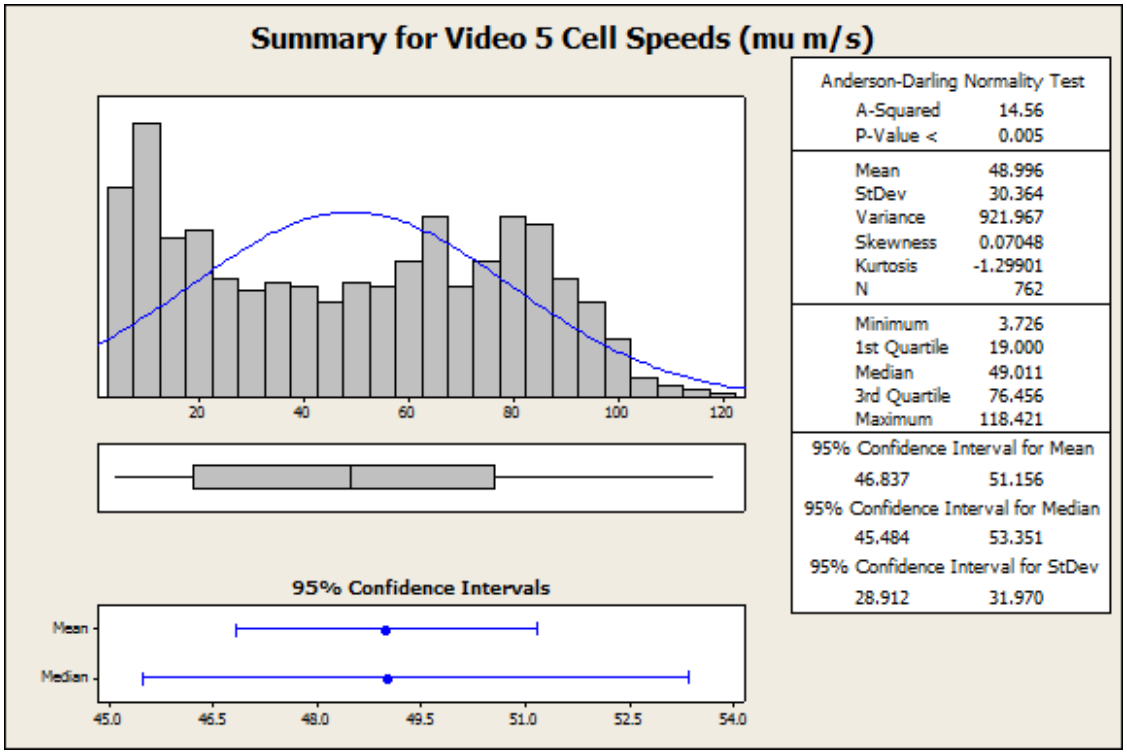


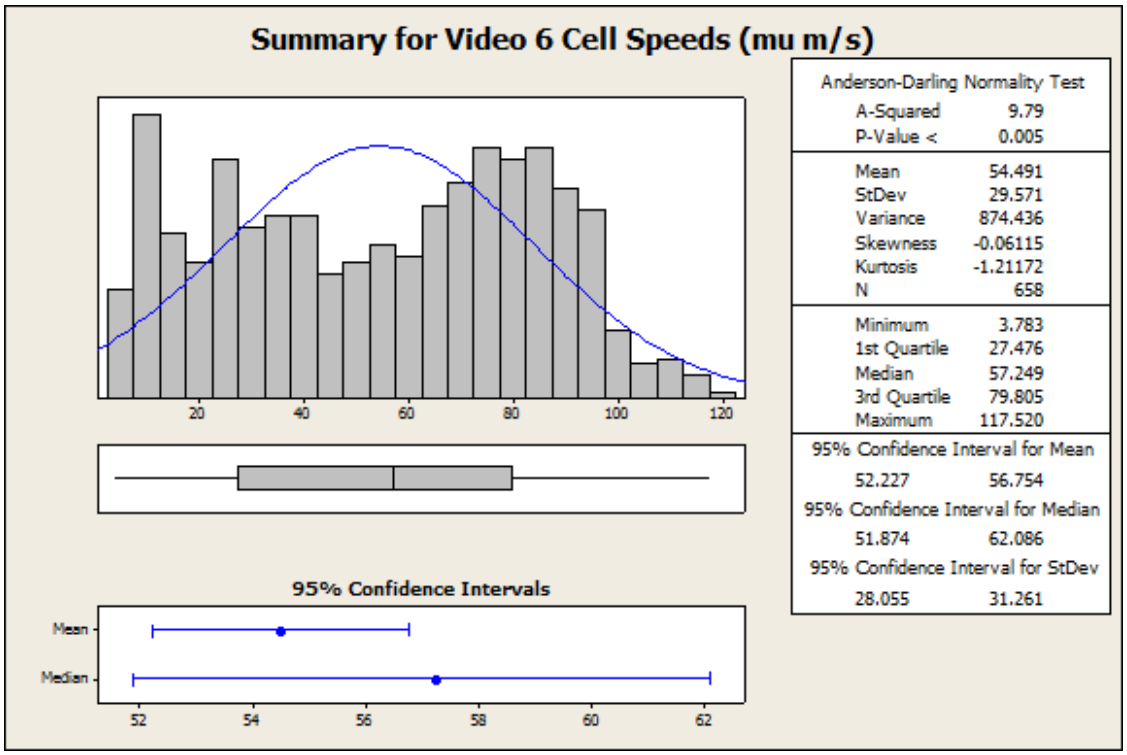


Figure 2.12: Graphical summaries of zoospore swimming speed data from videos 5 (top) and 6 (bottom) produced from Minitab.

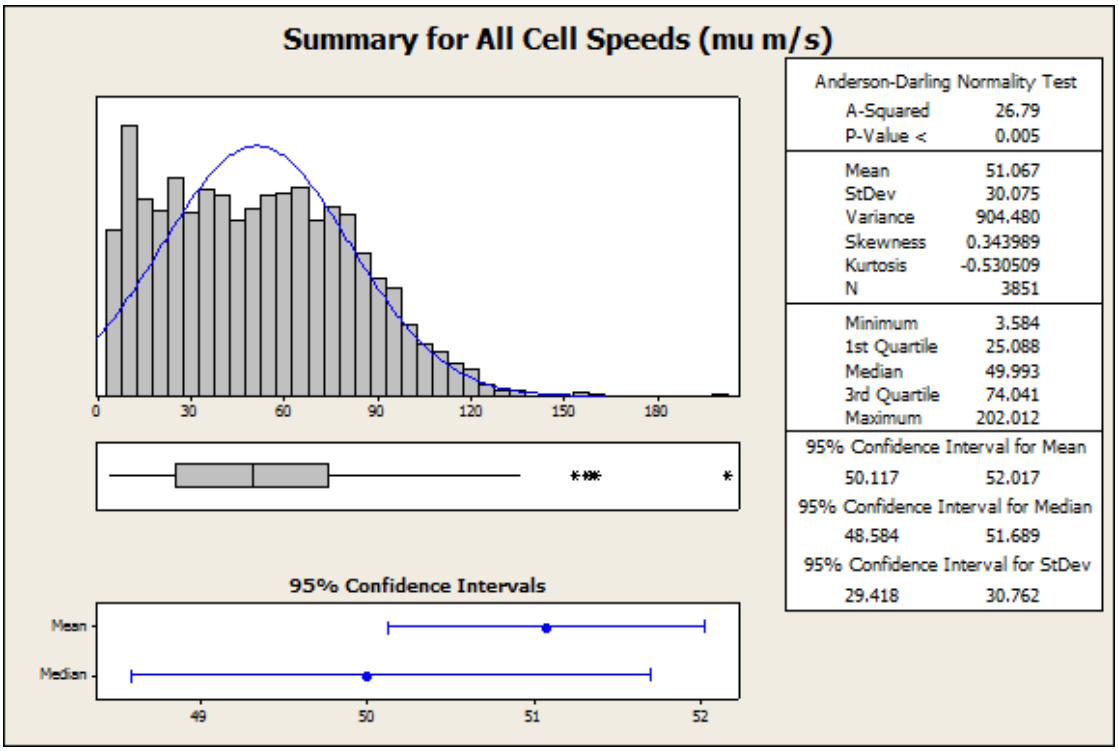


Figure 2.13: Graphical summary for combined zoospore swimming speed data from videos 1-6 produced from Minitab.

There do not appear to be any unifying features of these data sets with respect to their overall shape. Since all $p$-values are below the standard 0.05 $\alpha$-level, no data set was found to be normally distributed by the Anderson-Darling test and so analysis of variance cannot be used. To obtain as close an approximation as possible to the true mean swimming speed, we therefore considered data from all videos. To assess whether or not this was an appropriate course, we used a 2-sample t-test to detect significant statistical differences between sample means. Again, we used a standard $\alpha$-level of 0.05. For any p-value less than 0.05, we rejected the null hypothesis and concluded there was a significant difference between the means. The p-values for each test are summarised in Table 2.1.

| Video No. | 1 | 2 | 3 | 4 | 5 | 6 |
|---|---|---|---|---|---|---|
| 1 | - | $< 0.001$ | $< 0.001$ | 0.1 | 0.064 | 0.155 |
| 2 | $< 0.001$ | - | $< 0.001$ | $<0.001$ | $< 0.001$ | 0.001 |
| 3 | $< 0.001$ | $<0.001$ | - | 0.006 | $< 0.001$ | $< 0.001$ |
| 4 | 0.1 | $<0.001$ | 0.006 | - | 0.912 | 0.003 |
| 5 | 0.064 | $<0.001$ | $< 0.001$ | 0.912 | - | 0.001 |
| 6 | 0.155 | 0.001 | $< 0.001$ | 0.003 | 0.001 | - |

Table 2.1: P-values for 2-sample t-tests conducted for each pair of cell speed data sets as given in Figures 2.10-2.12.

By inspection, we see that videos 1,4 and 5 are statistically similar according to the t-test. From these, we computed the mean swimming speed of *P. infestans* zoospores to be 50.176 $\mu$m s$^{-1}$ with a standard deviation of 31.199 $\mu$m s$^{-1}$. Run lengths can also be calculated in Kinovea using the line tool, after the tracking data has been obtained. After calibration, the distances can be exported and analysed in the same way as cell speeds. The data are given below.

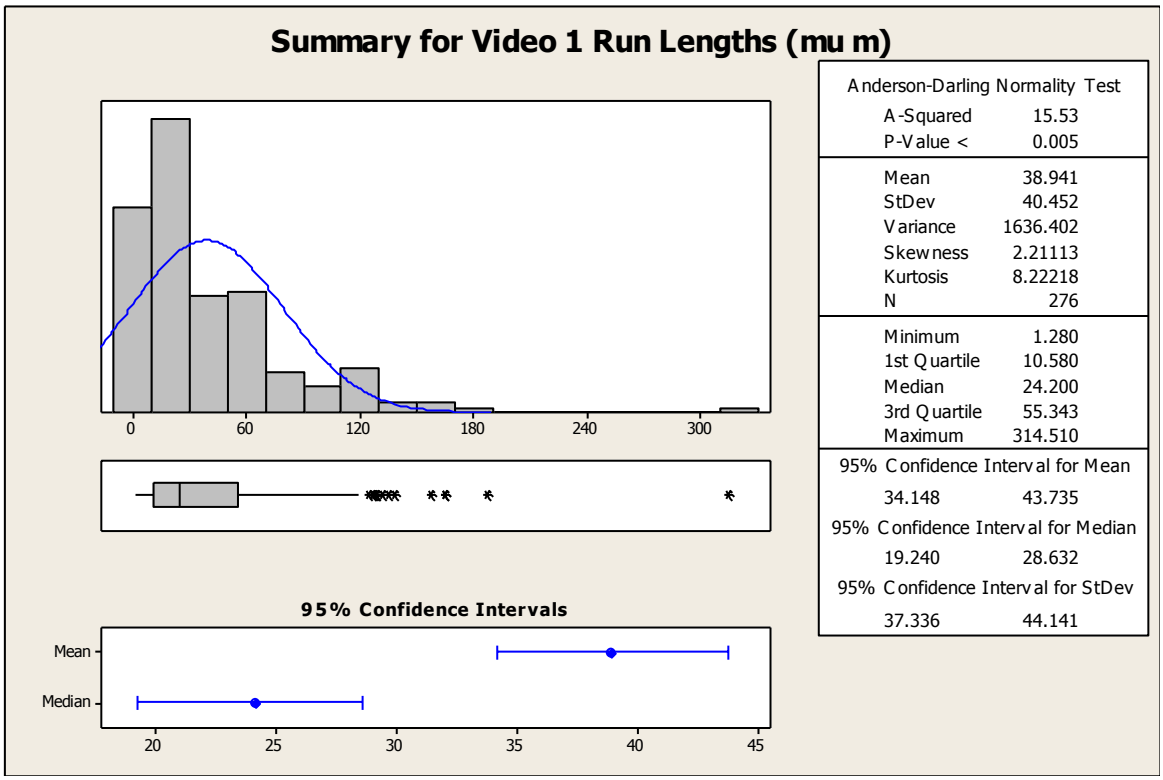


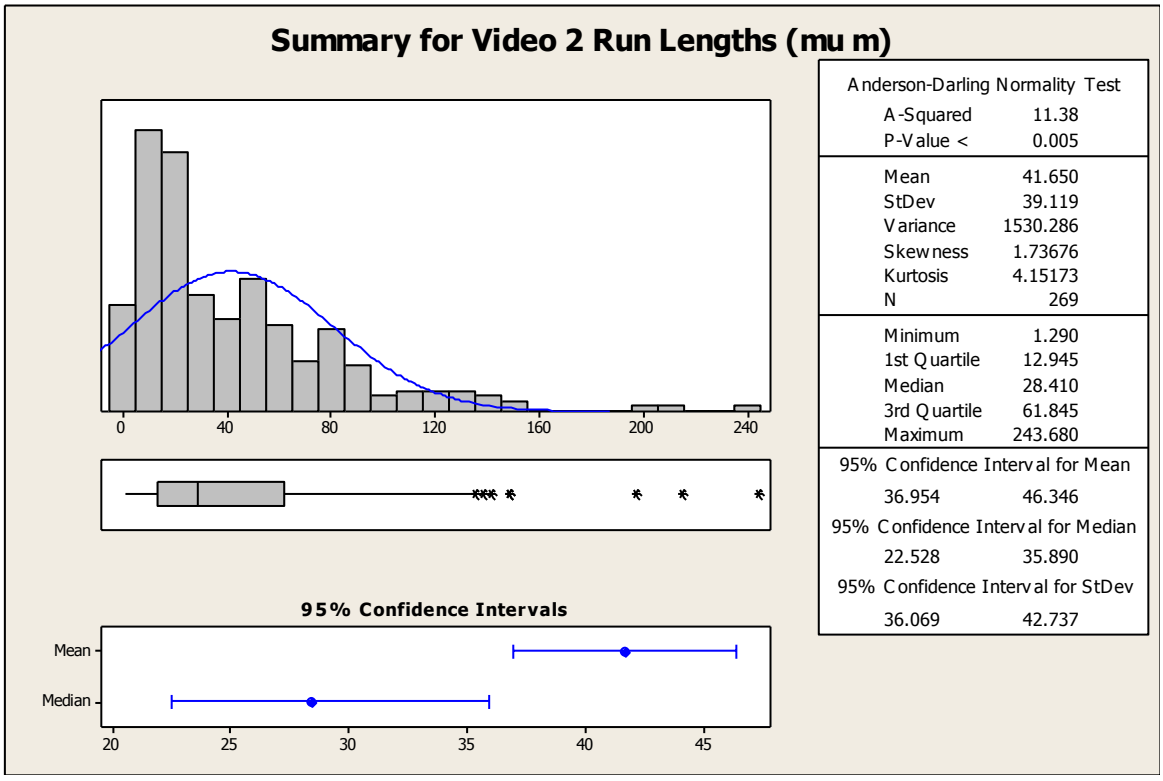


Figure 2.14: Graphical summaries for zoospore run length data from videos 1 (top) and 2 (bottom) produced from Minitab.

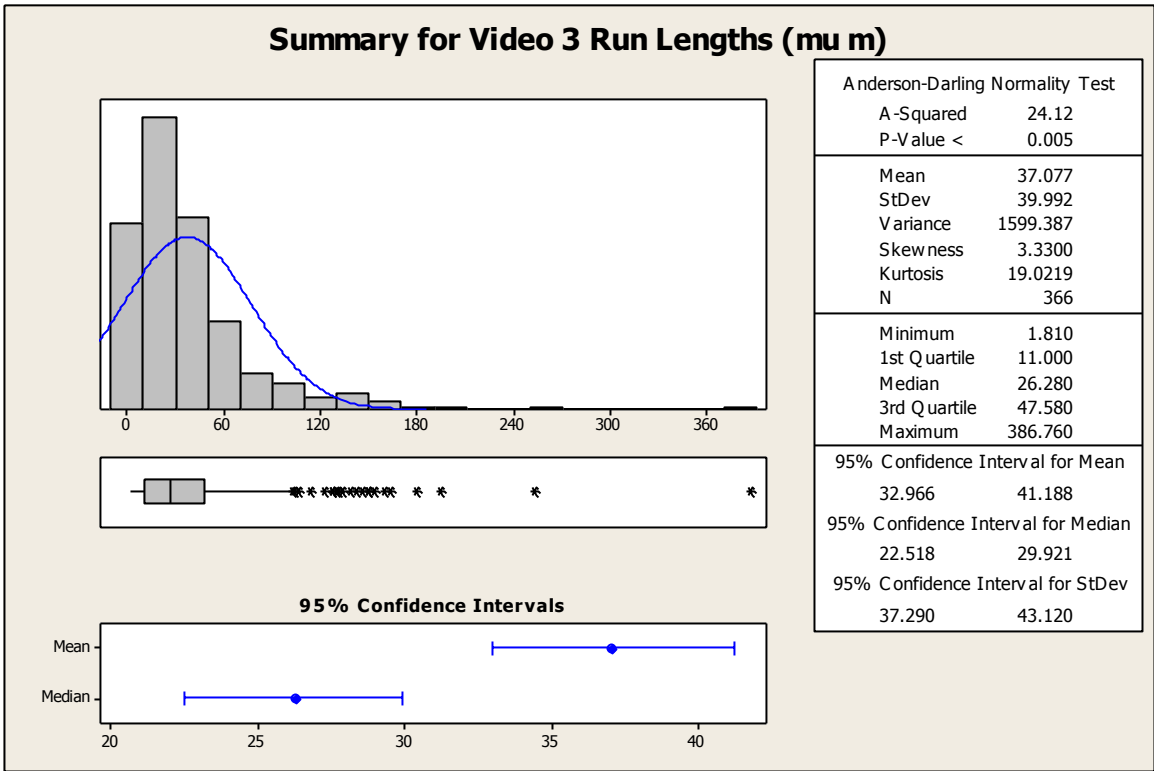


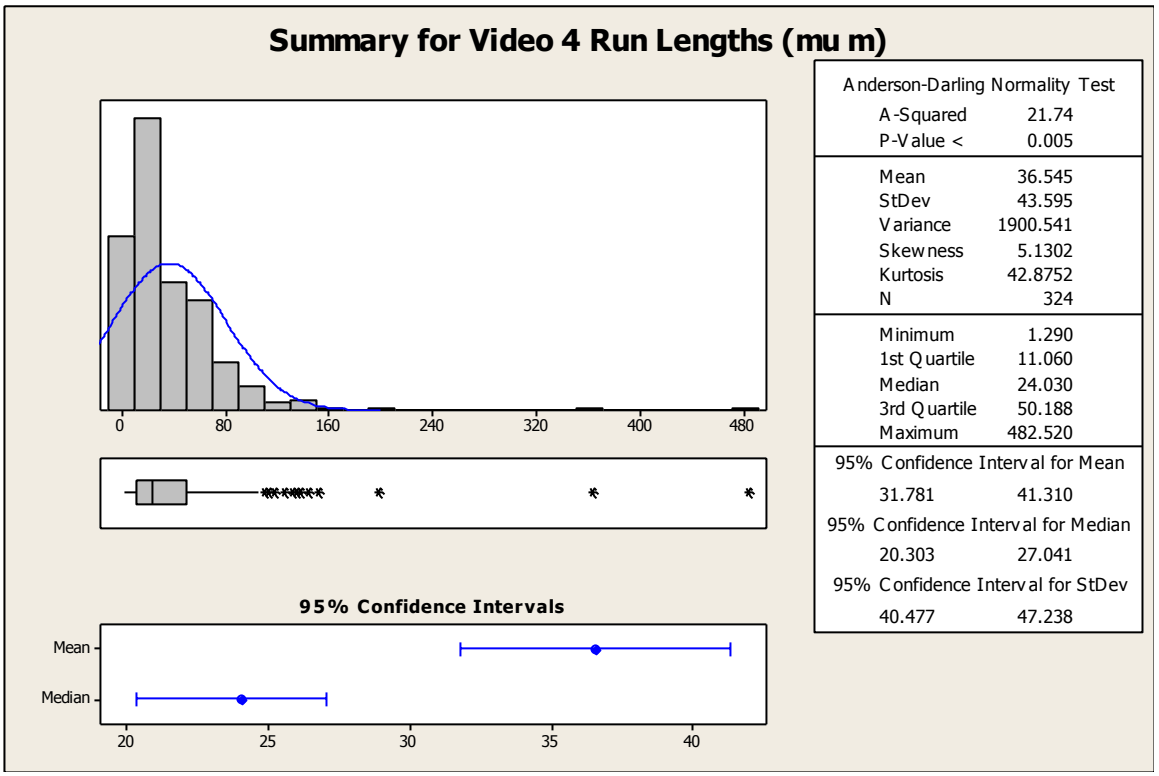


Figure 2.15: Graphical summaries for zoospore run length data from videos 3 (top) and 4 (bottom) produced from Minitab.

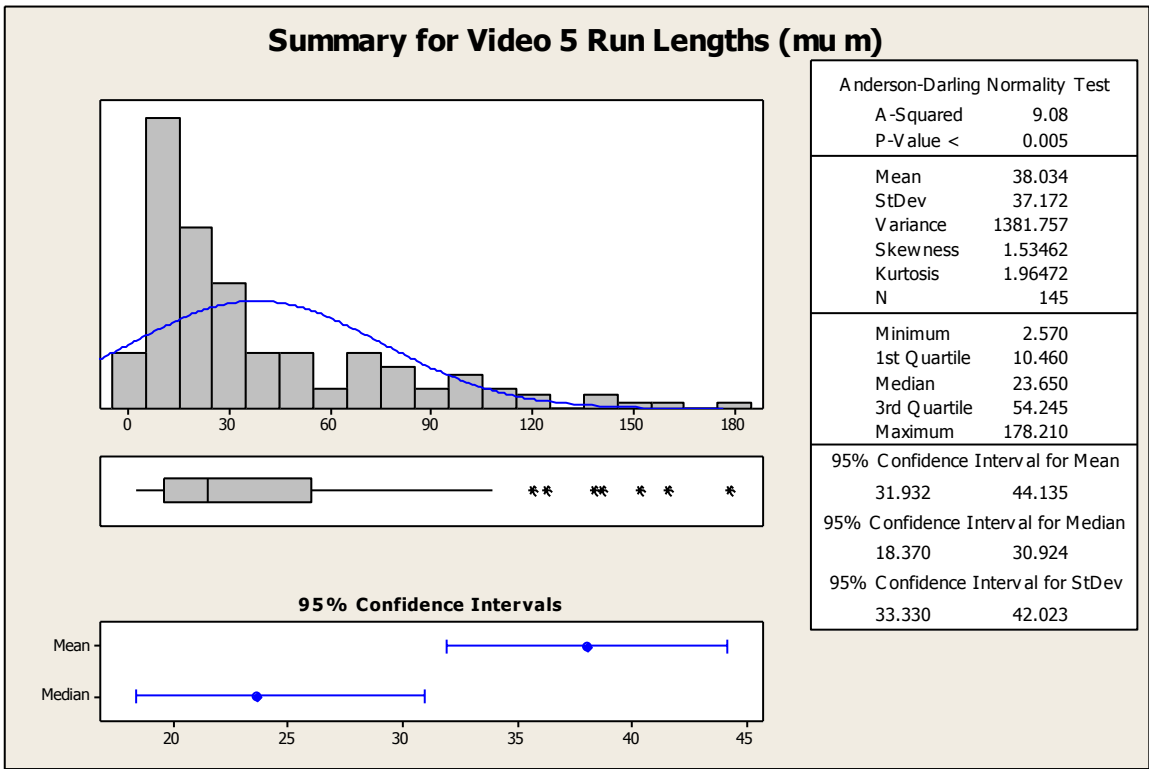


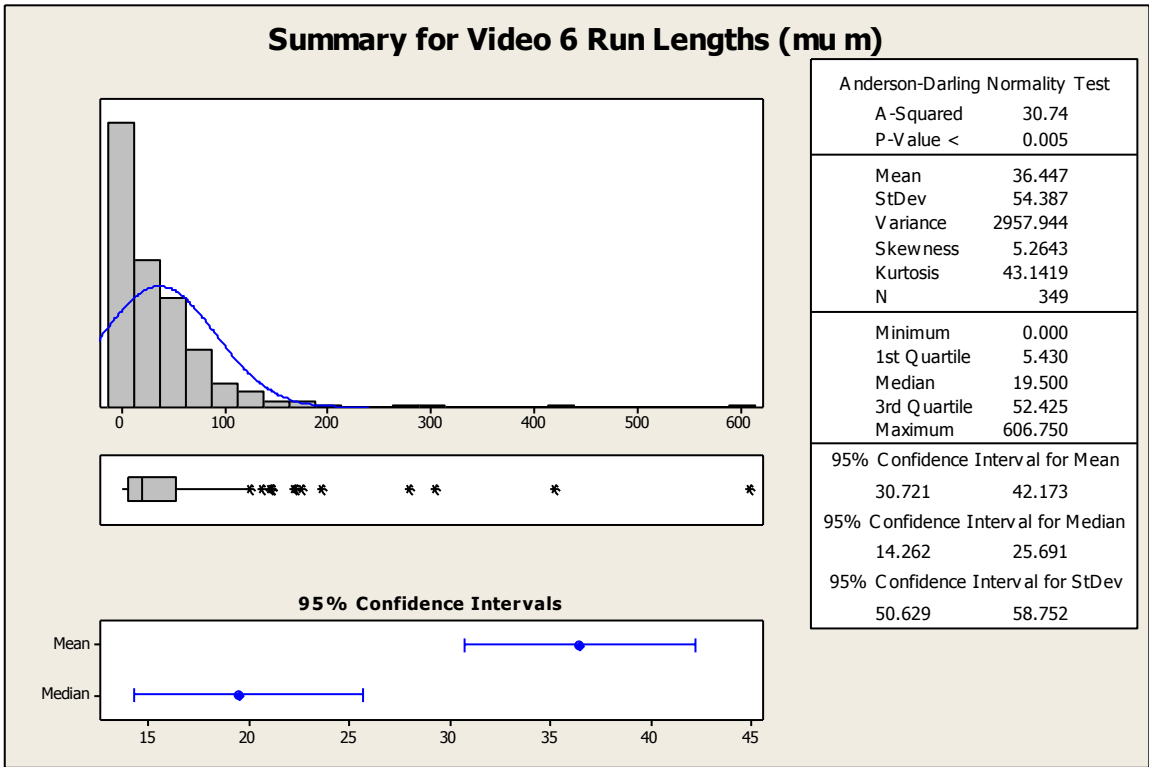


Figure 2.16: Graphical summaries for zoospore run length data from videos 5 (top) and 6 (bottom) produced from Minitab.

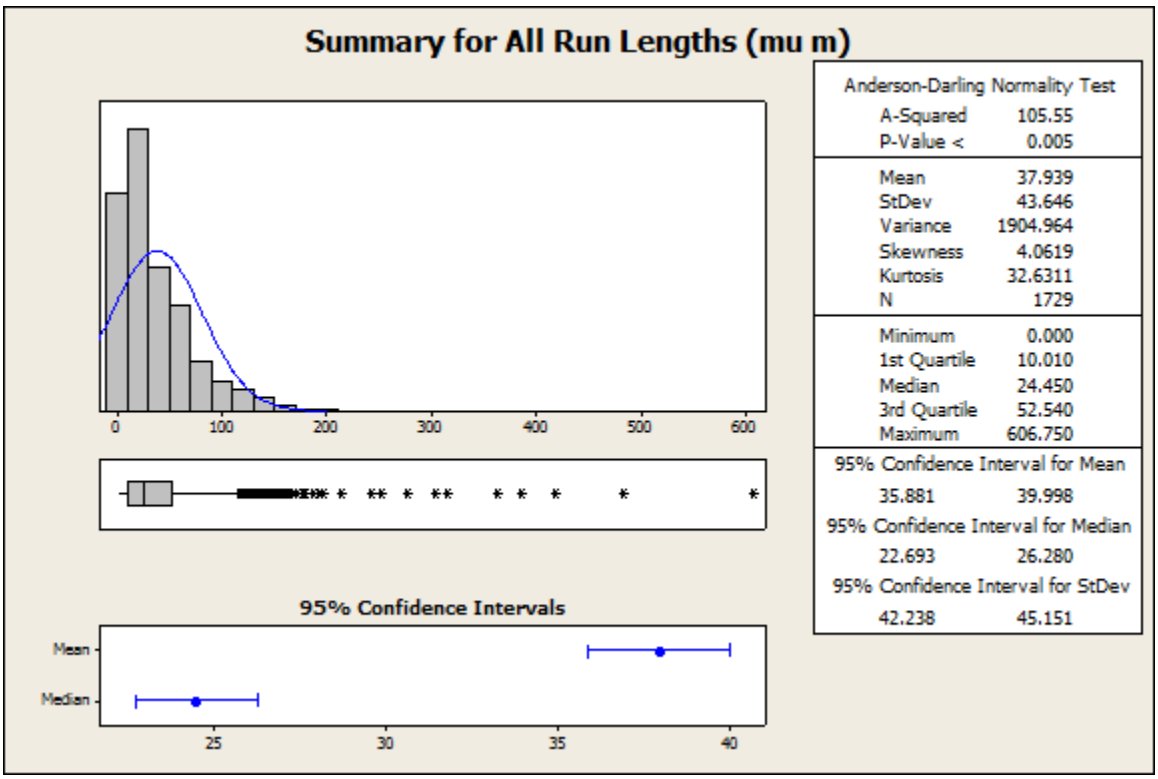


Figure 2.17: Graphical summary for combined zoospore run length data from videos 1-6 produced from Minitab.

Again, no normality was found in these samples, although unlike the cell speed data there is a definite similarity in the data shape. We again performed separate t-tests for each data set to identify any significant statistical differences. Table 2.2 shows that all p-values are sufficiently high to accept the null hypothesis and we concluded that there is no statistical difference between data sets obtained from these samples.

By examining the data as a whole, it is possible to fit a probability distribution curve to the data. The EasyFit software package [5] is designed specifically for this task and is equipped with a much wider selection of distributions than Minitab. At this point it was reasonable to assume that zoospores move according to an ordinary random walk, as is the case for many swimming cells. This assumption implies that the run lengths of zoospores should follow an exponential probability distribution. This distribution has only a single parameter and probability density function (pdf), $f(x) = \lambda e^{-\lambda x}$. EasyFit allowed us to test the hypothesis that zoospore run lengths follow an exponential distribution by applying three different goodness-of-fit tests to the data set. Standard significance levels were used in these tests, i.e. $\alpha = 0.01, 0.02, 0.05, 0.1$ and $0.2$, where $\alpha$ is the probability of falsely rejecting the null hypothesis. So, for $p$-values less than a given $\alpha$, we conclude that the distribution in question does not fit the data. Distribution parameters were obtained using maximum likelihood estimators (MLE) as is standard. The tests used were the Kolmogorov-Smirnov, Anderson-Darling and Chi-squared tests and the results are shown in Table 2.3.

| Video No. | 1 | 2 | 3 | 4 | 5 | 6 |
|---|---|---|---|---|---|---|
| 1 | - | 0.427 | 0.562 | 0.486 | 0.818 | 0.511 |
| 2 | 0.427 | - | 0.150 | 0.134 | 0.355 | 0.167 |
| 3 | 0.562 | 0.150 | - | 0.868 | 0.798 | 0.860 |
| 4 | 0.486 | 0.134 | 0.868 | - | 0.705 | 0.979 |
| 5 | 0.818 | 0.355 | 0.798 | 0.705 | - | 0.709 |
| 6 | 0.511 | 0.167 | 0.860 | 0.979 | 0.709 | - |

Table 2.2: P-values for 2-sample t-tests conducted for each pair of wild-type zoospore run length data sets as given in Figures 2.14-2.16. In all cases, $p$-values are sufficiently high to suggest that data from all videos is statistically similar.

| Video | K-S | A-D | C-S | MLE for $\lambda$ |
|---|---|---|---|---|
| 1 | Fit, $\alpha \leq 0.2$ | Fit, $\alpha \leq 0.1$ | Fit, $\alpha \leq 0.02$ | $\lambda = 0.02568$ |
| 2 | Fit, $\alpha \leq 0.2$ | Fit, $\alpha \leq 0.2$ | Fit, $\alpha \leq 0.1$ | $\lambda = 0.02697$ |
| 3 | Fit, $\alpha \leq 0.02$ | Fit, $\alpha \leq 0.02$ | No Fit | $\lambda = 0.02697$ |
| 4 | Fit, $\alpha \leq 0.1$ | Fit, $\alpha \leq 0.1$ | Fit, $\alpha \leq 0.2$ | $\lambda = 0.02736$ |
| 5 | Fit, $\alpha \leq 0.2$ | Fit, $\alpha \leq 0.1$ | Fit, $\alpha \leq 0.05$ | $\lambda = 0.02629$ |
| 6 | No Fit | No Fit | No Fit | $\lambda = 0.02744$ |

Table 2.3: Results of goodness-of-fit tests for the wild-type zoospore run length data as given in Figures 2.14-2.16. In cases where a statistical fit is obtained, a range of $\alpha$ is given for which the corresponding test was passed (see text). Distribution parameters for each video are given after being determined by maximum likelihood.

There is sufficient agreement to confirm our assumption that the run lengths are exponentially distributed. It is therefore reasonable to assume that zoospores swim in a random manner. We take the average value of $\lambda$ to be to $\bar{\lambda} = 0.02678$. The interpretation of this statistic is that we can expect a zoospore to turn $\bar{\lambda}$ times within every $\mu$m distance it swims. It should be noted that the exponential distribution is not necessarily the best fitting distribution. We used EasyFit to test all available distributions in the same way as above. The results are presented in Table 2.4 for standard $\alpha$-levels.

| Rank | Kolmogorov-Smirnov / Max $\alpha$ | Anderson Darling / Max $\alpha$ | Chi-Squared / Max $\alpha$ |
|---|---|---|---|
| 1 | Fatigue Life (3p) / 0.02 | Fatigue Life (3p) / 0.05 | Fatigue Life / No Fit |
| 2 | Fatigue Life / 0.01 | Fatigue Life / 0.02 | Fatigue Life (3p) / No Fit |
| 3 | Pareto 2 / No Fit | Log-Pearson / No Fit | Lognormal / No Fit |

Table 2.4: Results of goodness of fit tests applied to wild-type zoospore run length data as in Figures 2.14-2.16 for all available distributions in EasyFit. Only the three most suitable distributions are shown for each test. The maximum $\alpha$-level for which a distribution passes a test is also given.

The three parameter Fatigue Life distribution, also called the Birnbaum-Saunders distribution, is statistically the best fit since it passes two out of three goodness of fit tests. The pdf of this distribution is given by

$$\text{Fatigue life pdf} := \left( \frac{\sqrt{\frac{(x-\xi)}{\psi}} + \sqrt{\frac{\psi}{(x-\xi)}}}{2\eta(x-\xi)} \right) \phi \left( \frac{\sqrt{\frac{(x-\xi)}{\psi}} - \sqrt{\frac{\psi}{(x-\xi)}}}{\eta} \right), \qquad (2.1)$$

where $\eta > 0$ is the shape parameter, $\psi > 0$ is the scale parameter and $\xi$ is the location parameter ($\xi = 0$ yields the 2 parameter Fatigue Life distribution). The function, $\phi(\cdot)$ is the standard normal density function with zero mean and unit standard deviation. According to EasyFit's maximum likelihood estimates, these parameters are $\eta = 1.299, \psi = 21.276$ and $\xi = -0.36104$. A comparison of the pdfs of the exponential and Fatigue-Life distributions is shown in Figure 2.18.

The exponential and fatigue life curves are very similar. Hence, there seems little advantage in proceeding with the latter, obscure distribution and, in keeping with existing literature on cell movement, we choose to use the more common exponential curve. We therefore approximate the average run length of zoospores as being the expected value, $\frac{1}{\lambda} = 38\mu$m, which is also the standard deviation.

We also investigated whether the direction of a straight run following a tumble was purely random or if there existed a relationship between the directions of successive runs. To do so, we computed the turning angles along the paths of six cells (one from each video, 205 data points) and looked for possible patterns. This data was seen to be uniformly spread with mean, 180.33°, and a standard deviation of 102.91°. Therefore, evidence suggests that the turning angle is indeed random and we proceed under this assumption from now on.

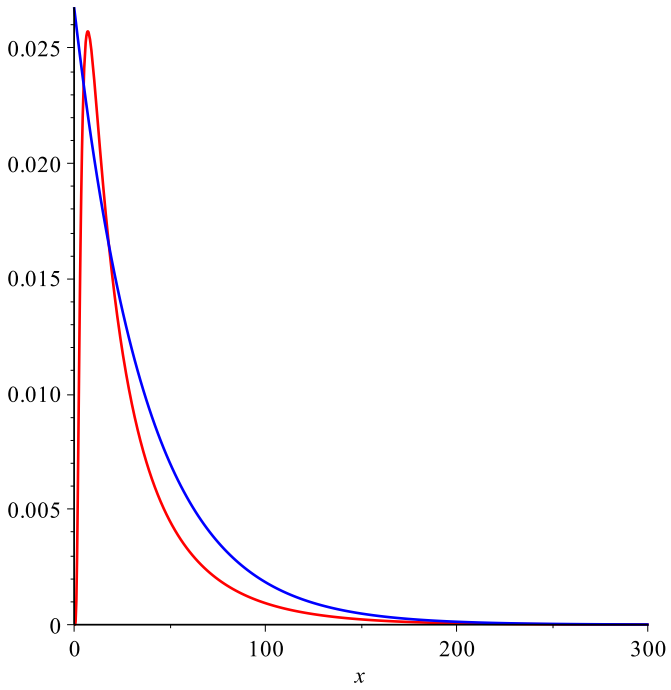


Figure 2.18: Probability density function of the exponential distribution, $\bar{\lambda}\exp(-\bar{\lambda}x)$ (blue), and the Fatigue-Life Distribution, (2.1) (red), showing the probability of a run with length $x\mu$m. Parameters: $\bar{\lambda} = 0.02678$, $\eta = 1.299, \psi = 21.276$ and $\xi = -0.36104$.

### 2.4.4 G$\alpha$-Silenced Strain

In addition to the wild-type, we also studied a modified strain of *P. infestans*, which was obtained using transformation and gene silencing techniques. Specifically, the gene silencing was used for PiGPA1, a gene that encodes G$\alpha$ proteins [73]. Two different methods were used and we call the resultant strains H16 and G24.

Previous experimentation with zoospores produced from PiGPA1-silenced lines have revealed some key differences in behaviour and tactic responses in comparison with the wild-type strain. The turning frequency was found to be 6-8 times greater in the silenced strain and consequently the lengths of straight runs were much shorter. Also, chemotaxis towards glutamic and aspartic acid was shown to be impaired as well as any large-scale aggregation. It may be a reasonable assumption that these effects are

connected, i.e. auto-aggregation requires chemotactic, cell-cell attraction. Virulence in the silenced strain was also found to be suppressed. Again, this could be a consequence of the chemotactic and movement impairments and not a direct result of the genetic modification.

We used the same video analysis techniques as above for this mutant strain in order to draw comparisons with the wild-type in terms of swimming speed and run lengths. The methods used for the growth and handling of the H16 and G24 strains was the same as described above for the 88069 (wild-type) strain. The only exception is the addition of geneticin to the Rye agar mixture before the plates are poured and inoculated. The observed mycelial density was found to be lower in these strains than with 88069 and so it was expected that fewer zoospores would be produced overall. The videos were captured using a different microscope as they were taken at different times. H16 and G24 movies were captured using an Axio Observer. Z1 microscope with an A-Plan 5x/0.12 Ph 0 objective. The size of each image is again 1388 x 1040 pixels but with a 1.25 $\mu$m / pixel scale factor in both the $x$ and $y$ directions. Figures 2.19 and 2.20 show cell paths for the G24 and H16 strains respectively.

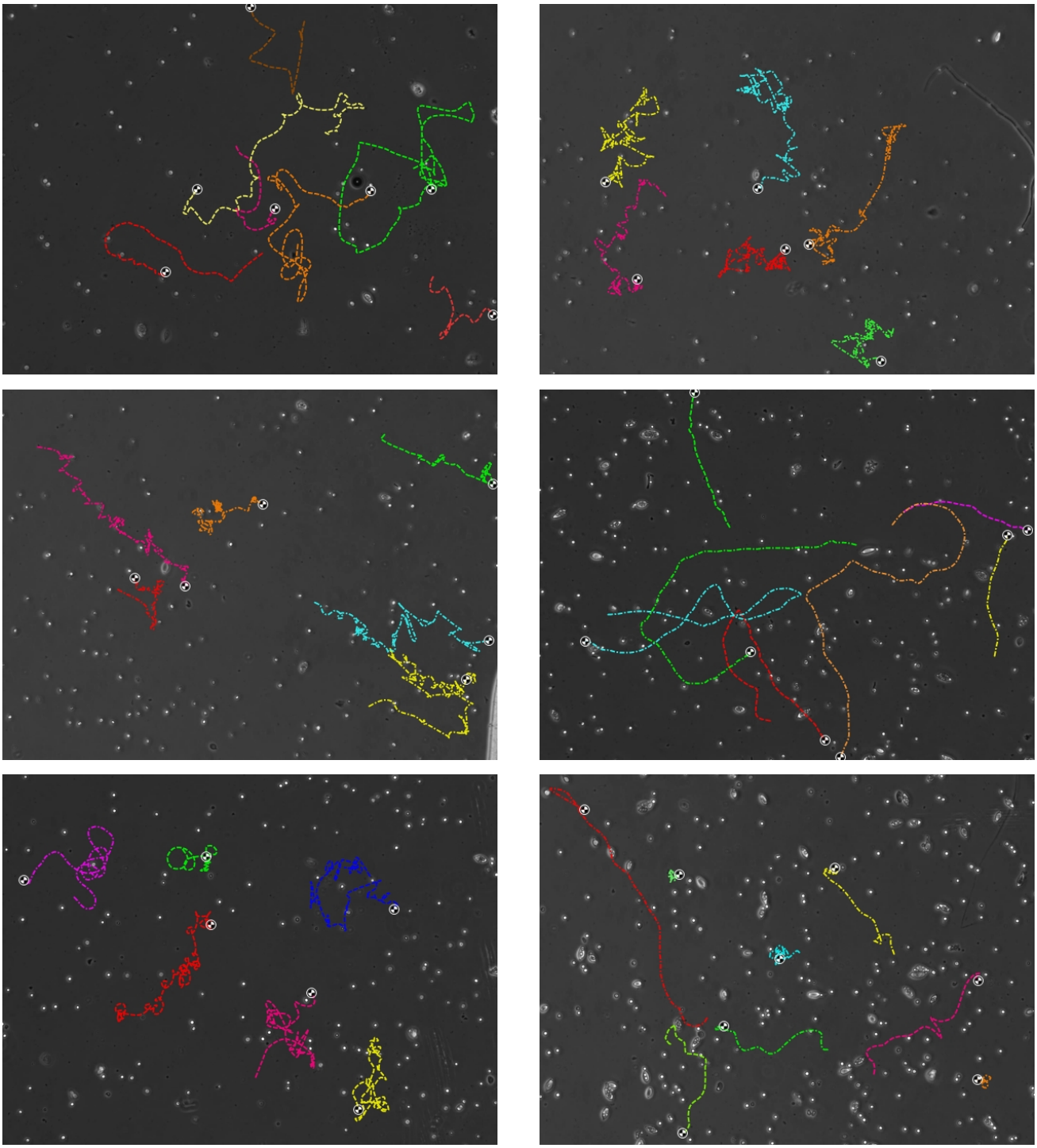

Figure 2.19: Cell paths traced in Kinovea for zoospores from the G24 strain of *P. infestans*. Each image shows a different sample suspension. Colours represent the trajectory of individual zoospores. Circular markers are placed at the beginning of a zoospore run.

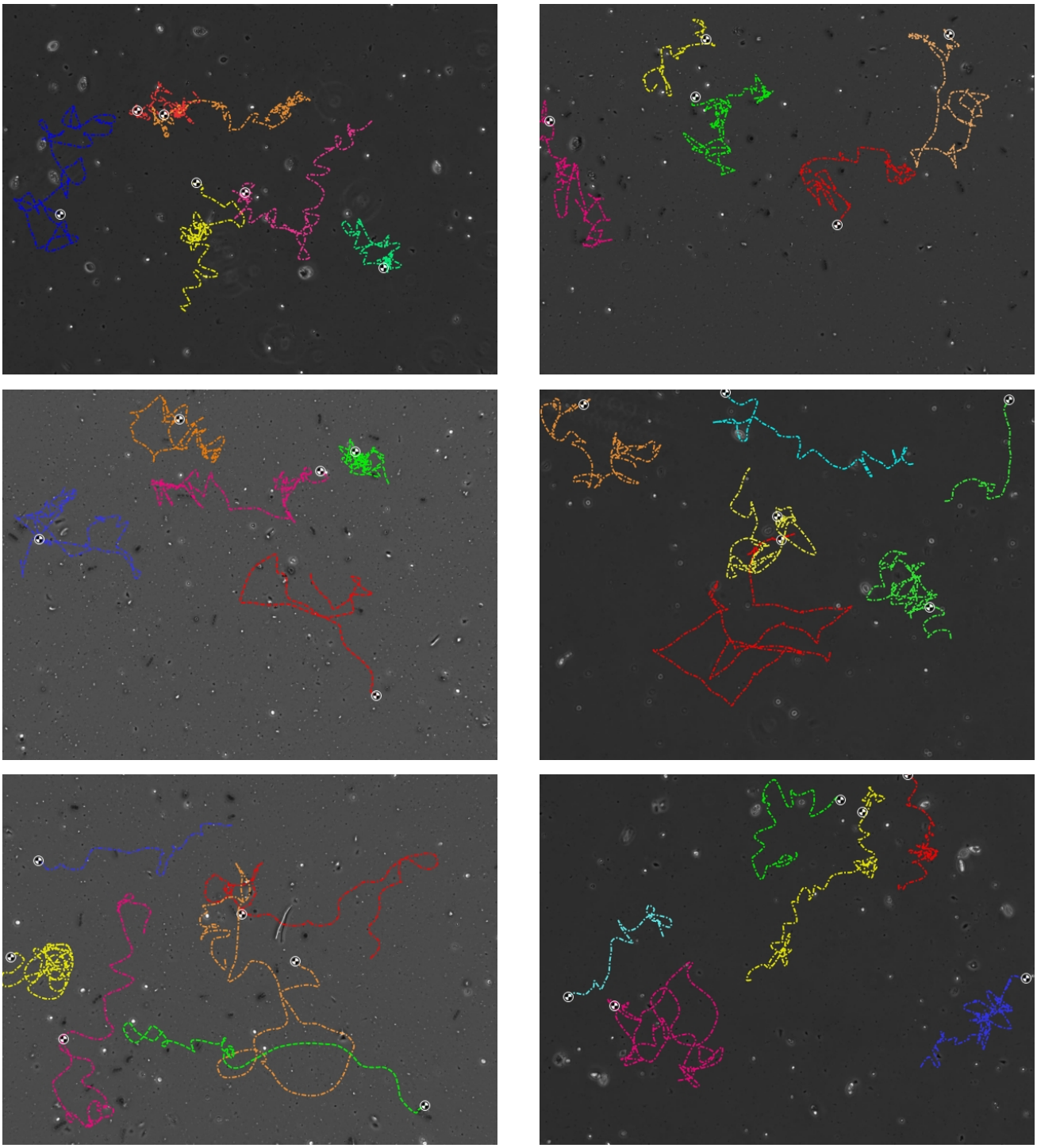

Figure 2.20: Cell paths traced in Kinovea for zoospores from the H16 strain of *P. infestans*. Each image shows a different sample suspension. Colours represent the trajectory of individual zoospores. Circular markers are placed at the beginning of a zoospore run.

| Strain | Mean Cell Speed ($\mu$m s$^{-1}$) , SD ($\mu$m s$^{-1}$) | Mean Run Length ($\mu$m), SD ($\mu$m) |
|---|---|---|
| Wild-Type | 50.176, 31.199 | 37.334, 37.334 |
| G24 | 32.017, 20.818 | 27.729, 26.813 |
| H16 | 42.319, 24.081 | 35.386, 26.503 |
| All Mutants | 37.744, 23.291 | 31.269, 26.937 |

Table 2.5: Comparison of the mean cell speeds and run lengths for zoospores from the mutant and wild-type *P. infestans* strains. Standard deviations for each are also given.

On inspection, there is considerable variation between samples but not any obvious difference between the G24 and H16 paths. This seems to contradict the results of Latijnhouwers *et al.* in [73], which found the zoospore turning frequency to be greatly increased. Here, we can see that long, straight runs are not uncommon. Table 2.5 shows the numerically computed averages of cell speed for each mutant and the wild-type, which confirm the difference in results with [73]. We attribute this difference to a decreased efficiency in the gene silencing and are therefore unable to determine any significant results from any observations of individual cells from these mutant strains.

In addition, the auto-aggregation of each mutant was also tested and no patterns were seen in the vast majority of cases. The reason for this was most likely the suspension density being too low in comparison with the earlier wild-type experiments, in part due to the general low zoospore release in comparison with the wild-type. The few occasions where cells were seen to aggregate can again be attributed to the gene silencing efficiency; some cells behave more like the wild-type than others. The effect was very subtle and so we choose to omit the photographs as they are not helpful.

## 2.5 Conclusions

We used video analysis to collect data on the behaviour of individual zoospores of *P. infestans*. We found that, much like many bacterial cells e.g. *E. coli*, zoospores swim in straight lines that are punctuated by tumbles that occur at random times. By using statistical analysis, we classified zoospore swimming as a simple random walk, i.e. the length of straight runs follows an exponential probability distribution. The orientation angle after a tumble was also found to be random by collecting and analysing sample data. The results for swimming speeds of zoospores are comparable to those published by other researchers and will be useful in parameterising mathematical models in later chapters.

We have considered an aspect of zoospore auto-aggregation that has not been discussed before: the behaviour over long time scales. Our experiments have shown that after the initial bioconvective plumes have formed, plumes that drift slowly toward one-another are consistently observed. This drifting can continue over many hours, the end result being a reduction in the number of plumes by merging. At the same time, given the many hours over which we view these patterns, it is very probable that many zoospores will encyst, also contributing to the reduction in plume numbers. Ho and Hickman reported that a suspension of zoospores containing small, glass beads dramatically decreased the period of normal swimming before encystment when compared with a control group that did not contain these obstacles [56]. Encystment should then occur most often in the areas with the highest concentration of cells as they will collide with one another more often than in the areas of low concentration. Since the encysted cells are immobile, they will sink to the bottom of the dish and any zoospore-cyst attraction will likely not influence the auto-aggregation patterns. It does, however, produce a secondary or sub-pattern that results in a large sheet of encysted, germinated cells that persists long after active swimming has stopped. This pattern seems to be visible only

after several hours have elapsed, presumably when enough cells have encysted and germinated.

The explanation for the drifting of plumes, we believe, is due to chemotactic attraction. For this to be true, chemotaxis must work at a much slower rate than bioconvection, as the structure of the plumes is kept more or less intact. Therefore we predict that zoospore auto-aggregation is likely to be a two stage process. First, the gyrotactic zoospores swim to the surface of the fluid and form bioconvective plumes due to gravity. If indeed the zoospores are releasing a chemical attractant, the second stage is that the plumes will be drawn together over time due to the chemical gradients that will form between aggregates. It is possible that the chemoattractant responsible for zoopsore-cyst attraction is the same as that for auto-aggregation, the latter effect only becoming detectable after plumes of high density have formed.

# Chapter 3

# Modelling Chemotaxis

## 3.1 Introduction

It is well known that zoospores of *P. infestans* utilise chemotaxis in order to locate suitable infection sites [69, 51, 133]. However, in Chapter 2, we hypothesised that chemotaxis could play a major role in the auto-aggregation process as well. In this chapter we study the chemotactic process in isolation to provide insight into how significant this role might be. We first outline the background biological processes involved and then discuss some of the work that has been done on the mathematical modelling of chemotaxis to date. We then construct a model for zoospore chemotaxis via a standard random walk derivation. It is assumed that attraction between one zoospore and another is in response to some chemical that they themselves secrete. Moreover, the movement of cells is restricted by the amount of space available, i.e. a volume-filling effect is present. The values of the parameters involved in this model are discussed as well as how they relate to the experimental results obtained in the previous chapter. We go on to solve these model equations numerically in one, two and three space dimensions and determine reasonable estimates for unknown model parameters. We discuss

the qualitative and quantitative comparison of the solutions of the chemotaxis model with experimental results and possible reasons for any discrepancies. This comparison will help us to better understand the role that chemotaxis might play in zoospore auto-aggregation.

### 3.1.1 Biological Background

Chemotaxis can be broadly defined as chemically directed motion. A large number of biological processes rely on chemotaxis including: the search for nutrients in bacteria; mammalian development; wound healing; the growth of cancerous tumours and; in the zoospore case, the search for new hosts to infect [133]. Chemotaxis was first discovered in the late 19th century by Engelmann and Pfeffer, who each reported that bacterial cells could respond to changes in the extracellular concentration of attractant or repellant chemicals [37, 38, 102]. It was not until the later part of the 20th century, that an understanding of the mechanisms involved began to emerge (see the review papers [10, 96] and references therein).

Much of the work that has been done in the biology of chemotaxis has been related to bacterial cells. The signalling network in prokaryotes involves only small numbers of proteins as opposed to the potential hundreds in eukaryotes, making the former preferable model organisms to study [60]. The identification of the individual components involved in the signalling network required much experimentation. In the 1970s, a connection was established between key chemotaxis genes and proteins using molecular genetics, showing that the products of three key genes (*cheM*, *cheD* and *cheZ*) played an essential role in the chemotactic process [113]. This eventually led to being able to reconstitute the entire chemotaxis signalling network *in vitro* of the common model organism *E. coli*, with complete characterisation of the specific proteins involved [86].

For *E. coli*, the chemotactic process can be described as follows. On the surface of each cell there are an average of four to six flagella, each anchored to flagellar motors that can rotate either clockwise or anti-clockwise using electrochemical energy [16]. Flagella that are rotating counter-clockwise form what is known as a "bundle" and propel the cell forwards at a speed of around $20\mu$m/s in what are called "runs". If one, or several flagella switch the direction of their rotation, the bundle is disrupted causing the cell to tumble and facing it in a new direction for the next run. Also, on the cell surface are receptors, which have been proven to detect changes in concentration of specific chemicals [9]. Now, bacterial cells are too short to be able to detect gradients of these chemicals in a spatial sense, and so instead use temporal measurements along straight runs. It is these measurements that dictate the likelihood of random tumbles. Every cell has some default tumbling propensity with the mean run length being roughly constant in a homogeneous environment. If a cell detects an increase in attractant concentration as it swims forward, the average tumbling propensity is reduced, causing the run lengths to increase. On average, this mechanism leads to a bias in the swimming direction and the net transport of cells up concentration gradients of attractants and down concentration gradients of repellants.

As discussed in Chapter 1, the swimming mechanism of a bi-flagellate *P. infestans* zoospore is quite different to that in bacteria, but given they are of a similar size, it is reasonable to assume that the measurements of chemoattractant concentration by each cell are achieved in a similar way. We proceed under this assumption when the mathematical model is constructed. We note, however, that certain chemical attractants and repellants have been found to work without surface receptor binding [91]. This provides an avenue for further research.

### 3.1.2 Mathematical Modelling Overview

The mathematical modelling of chemotaxis has developed over the years into a large and diverse field. In 1970 and 1971, the seminal papers by Keller and Segel [65, 66] introduced a continuum PDE model for chemotaxis and today it remains widely used and well-studied (see, for example, review papers [53, 59] and references therein for a comprehensive overview). Rather than a detailed description of an individual cell's behaviour, the continuum approach was designed to capture the average behaviour of multiple chemotactic cells. In its original form, the Keller-Segel model consists of two coupled partial differential equations, one describing spatio-temporal distrubtion of cell density and the other for the concentration of chemoattractant. Credit for the advective chemotaxis term in the model is often given to Patlak, who derived a similar, but more general, PDE model by considering biased random walks [97]. Hence, the model is occasionally referred to as the Patlak-Keller-Segel model. Its solutions will be discussed later in the chapter along with numerical experiments. Although the first application was to the aggregation of *D. discoidium*, this type of model has also been successfully used in a diverse range of other biological systems including: embryonic development [94]; other aggregating cells such as *Salmonella typhimurium* and *E. coli* [120, 131] and; the formation of capillary networks in tumour growth [25, 26].

Although continuum models have attracted significant attention, alternatives such as discrete, individual-based models and stochastic models have also proven popular. Dallon and Othmer presented a discrete model of *D. discoidium* aggregation with adaptive signalling [29], in which cells are treated as discrete points that move within a continuous cAMP concentration field. The movement of cells is governed by suitably chosen rules that result in an average flux up concentration gradients of cAMP. Of course, the assumptions made when building deterministic models disregard stochastic noise that would always be present in any biological system. The model derived in [27]

by Chavanis consists of stochastic kinetic equations that take this noise into account. The P-K-S continuum model can be recovered in the mean field limit of the stochastic model and in this way the latter can be thought of as a generalisation. In angiogenesis modelling, a hybrid approach has also been used to combine continuum modelling with discrete, stochastic modelling [25]. This *hybrid* approach was adopted to provide more detailed information than could be obtained with the macroscale approximations of PDEs. In some cases, there are obvious benefits of individual based models in terms of the accuracy of their predictions. However, random noise does not generally become important unless the number of cells in the system is relatively small. Therefore, given the large numbers of cells involved in zoospore auto-aggregation considered here, we view a continuum modelling approach as most appropriate and it is this approach that will be taken in the rest of this thesis.

## 3.2 Constructing the Mathematical Model

### 3.2.1 Derivation From a Random Walk

We begin the derivation of the model by considering the random walk of an individual cell. Here, we follow the approach used by Othmer and Stevens [93] and later by Painter and Hillen [95].

Consider a one-dimensional lattice consisting of equally spaced grid points that are a small distance, $\Delta x$, apart. It is assumed that cells can either move to the left or right after each small time step, $\Delta t$. It is assumed that a cell at a point, $x$, on this lattice can make jumps to either $x \pm \Delta x$ or may remain stationary after each small time step, $\Delta t$. An equation for the change in cell density over the time, $\Delta t$, can then be immediately written down as follows:

$$N(x,t+\Delta t) = N(x,t) + P^{+}_{x-\Delta x}N(x-\Delta x,t) + P^{-}_{x+\Delta x}N(x+\Delta x,t) - (P^{+}_{x} + P^{-}_{x})N(x,t), \tag{3.1}$$

where $N(x,t)$ is the cell number at the point, $x$, and time, $t$, and $P^{\pm}_{x}$ are the probabilities that a cell at point, $x$, will jump to the point, $x \pm \Delta x$, within time, $\Delta t$. How to define these probabilities is now to be decided. In the case of chemotactic cells, it is assumed that the movement direction is biased towards higher concentrations of chemoattractant, which we denote by $C(x,t)$. Following [95], a reasonable choice for $P^{\pm}_{x}$ is

$$P^{\pm}_{x} = a + b(\sigma(C(x \pm \Delta x,t)) - \sigma(C(x,t))), \tag{3.2}$$

where $a$ and $b$ are positive constants and $\sigma$ is a function that describes the chemotactic response. The relative sizes of $a$ and $b\left(\sigma(C(x \pm \Delta x,t)) - \sigma(C(x,t))\right)$ determine the strength of the chemotactic response in comparison with diffusion. If the concentration of chemoattractant is uniformly distributed - or there is no chemical gradient - there is no bias in the movement of cells, $P^{\pm}_{x} = a$, and the motion is purely diffusive (random). Substituting (3.2) into (3.1), expanding terms using Taylor series and dividing by $\Delta t$ gives

$$\begin{aligned}
\frac{\partial N}{\partial t} + \frac{\Delta t}{2}\frac{\partial^2 N}{\partial t^2} + O(\Delta t^2) &= \frac{a\Delta x^2}{\Delta t}\frac{\partial^2 N}{\partial x^2} - \frac{2b\Delta x^2}{\Delta t}N\left(\frac{d\sigma(C)}{dC}\frac{\partial^2 C}{\partial x^2} + \frac{d^2\sigma(C)}{dC^2}\left(\frac{\partial C}{\partial x}\right)^2\right) \\
&\quad - \frac{2b\Delta x^2}{\Delta t}\frac{d\sigma(C)}{dx}\frac{\partial N}{\partial x} + O(\Delta x^4), \\
\frac{\partial N}{\partial t} + \frac{\Delta t}{2}\frac{\partial^2 N}{\partial t^2} + O(\Delta t^2) &= \frac{a\Delta x^2}{\Delta t}\frac{\partial^2 N}{\partial x^2} - \frac{2b\Delta x^2}{\Delta t}\frac{\partial}{\partial x}\left(N\frac{\partial \sigma(C)}{\partial x}\right) + O(\Delta x^4),
\end{aligned} \tag{3.3}$$

where the chain rule has been used for simplification. In order to obtain non-trivial dynamics from these equations, the standard assumption is now made that the limit as $\Delta x, \Delta t \to 0$ of $\frac{\Delta x^2}{\Delta t}$ is a positive constant, known as the parabolic scaling limit. For a discussion of this limit and others, e.g. the hyperbolic limit and the telegraph equation, see [90]. We define

$$\lim_{\Delta x, \Delta t \to 0} \frac{a\Delta x^2}{\Delta t} = D_N \quad \text{and} \quad \lim_{\Delta x, \Delta t \to 0} \frac{2b\Delta x^2}{\Delta t} = \chi_N.$$

Then by taking the limit as $\Delta x \to 0$ and $\Delta t \to 0$ of (3.3), the classical chemotaxis equation,

$$\frac{\partial N}{\partial t} = D_N \frac{\partial^2 N}{\partial x^2} - \frac{\partial}{\partial x}\left(N\chi(C)\frac{\partial C}{\partial x}\right), \tag{3.4}$$

is obtained, with the chemotactic sensitivity function defined by $\chi(C) = \chi_N \frac{d\sigma(C)}{dC}$. This approach can be easily extended to higher space dimensions. The same model can also be derived by considering the total flux of cells to have both a diffusive and a chemotactic component and using Fick's law [36, 82]. An alternative PDE model can also be derived by considering a velocity-jump process, where instantaneous changes in speed and direction of individuals are generated by a Poisson process [92]. This approach may be worthy of further consideration in the future for modelling zoospore movement.

### 3.2.2 Deriving the Diffusion Coefficient

It remains to relate the cell diffusion coefficient, $D_N$, to the experimental results presented in Chapter 2. To do this, we reasonably assume that a zoospore swims at a constant speed, $v = 50\mu$m/s, and an average, straight run lasts for time, $\tau_T = 0.76$s

(values computed in Chapter 2). To determine the diffusion coefficient, $D_N$, we follow [24, 77] and employ results from polymer chemistry and statistics. That is, in three dimensions, we can think of a path of a cell as a polymer chain consisting of $n$ bonds of mean length $\langle l \rangle$ and $\alpha$ representing the mean projection between each bond and the next. It is known that the mean squared end-to-end distance of such a polymer chain,$\langle r^2(t) \rangle$, at time, $t$, (equivalent to the mean squared displacement of a cell in our case) satisfies the following expression given in [77]:

$$\langle r^2(t) \rangle \simeq n \langle l^2 \rangle \frac{1 + (2\langle l \rangle^2 / \langle l^2 \rangle - 1)\alpha}{1 - \alpha}. \tag{3.5}$$

This can be transposed for application to swimming cells by replacing $n$ by $\frac{t}{\tau_T}$, the average number of runs over time, $t$. Experimental evidence suggests that for bacterial cells, the time between tumbles is exponentially distributed. We found the same to be true for zoospores, as reported in Chapter 2 and therefore the probability of a straight run with length, $x$, is given by $Pr(X = x) = \frac{1}{\tau_T v} \exp\left(-\frac{x}{\tau_T v}\right)$. The mean squared run time can then be written as

$$\begin{aligned} \langle l^2 \rangle &= E(X^2) = \int_0^\infty x^2 \frac{1}{v\tau_T} e^{-\frac{x}{v\tau_T}} dx \\ &= 2\tau_T^2 v^2, \end{aligned} \tag{3.6}$$

where $E(\cdot)$ is the standard expected value of a random variable, i.e. the weighted average of all its possible values. A statistical result given in [24] for a particle diffusing in three dimensions relates the mean squared displacement of the particle to the diffusion coefficient, thus

$$D_N \simeq \frac{\langle r^2(t) \rangle}{6t}. \tag{3.7}$$

As discussed in Chapter 2, the zoospore orientation after each tumble appears to be random, with no correlation between the directions of successive runs. Hence we set $\alpha = 0$ without loss of generality. Therefore, combining (3.5)-(3.7) yields an expression for the diffusion coefficient:

$$D_N = \frac{v^2 \tau_T}{3}. \tag{3.8}$$

## 3.3 Formulation of the Model

Using the above results, we can now construct a mathematical model. We consider a population of zoospores, represented by a density field, $N(\mathbf{X}, T)$. It is assumed that each zoospore is attracted to some chemical, represented by the density field, $C(\mathbf{X}, T)$. We have defined the general model for cell movement in (3.4), but at this point we make a final addition. In [95], Painter and Hillen introduced a novel variation on the classical model that included a volume-filling effect. The basic principle underpinning this model is that the movement of cells is restricted by the amount of available space. The full model is given by

$$
\begin{aligned}
&\frac{\partial N}{\partial T} = -\nabla \cdot \left( -D_N \nabla N + N \left( 1 - \frac{N}{N_M} \right) \chi_N \nabla C \right), \qquad \mathbf{X} \in \Omega \subset \mathbb{R}^k \quad (k = 1, 2, 3.), \\
&\frac{\partial C}{\partial T} = -\nabla \cdot (-D_C \nabla C) + \alpha N - \beta C, \\
&\frac{\partial N}{\partial \mathbf{X}} = \frac{\partial C}{\partial \mathbf{X}} = 0 \quad \text{on} \quad \partial\Omega, \\
&N(\mathbf{X}, 0) = N_0(\mathbf{X}), \quad C(\mathbf{X}, 0) = C_0(\mathbf{X}),
\end{aligned}
\tag{3.9}
$$

where diffusion and chemotactic coefficients are as defined above and $\alpha$ and $\beta$ are positive constants that represent chemical production and degradation, respectively. The chemoattractant, $C$, is also assumed to move according to diffusion; the signal kinetics as well as the chemotactic coefficient have been assumed to be linear. The parameter $N_M$ is the maximum cell density. $N_M > 0$ can either be a literal maximum based on the size of a cell or an estimate based on experimental observation. The full derivation of the volume-filling term, $(1 - \frac{N}{N_M})$, can be found in [95]. The decision to include it was made to enhance biological relevance as cells obviously have a finite volume, but it has also been proven to prevent the blow-up of solutions in finite time [128]. It should also be noted that we have neglected to include any terms in the cell equation representing proliferation or death. This is justifiable in our case firstly as zoospores do not proliferate, and secondly the auto-aggregation experiments considered here take place on much shorter time scales than cell death.

The equations in (3.9) are assumed to hold on a bounded spatial domain, $\Omega \subset \mathbb{R}^n$. Given that experiments take place in fixed volumes of fluid, the most biologically relevant boundary conditions to choose are zero-flux at the boundary, $\partial\Omega$, for both $N$ and $C$, since no material enters or leaves the domain. For an investigation of the effects of alternative boundary conditions on solutions see Myerscough *et al.* [84]. It is worth

noting that the total number of cells is conserved, i.e.

$$\int_{\Omega} N(\mathbf{X},T)d\mathbf{X} = \int_{\Omega} N_0(\mathbf{X})d\mathbf{X}. \tag{3.10}$$

This is easily confirmed by integrating (3.9) with $k = 1$ with respect to $\mathbf{X}$. The system possesses a homogeneous steady state when $N = \frac{\alpha}{\beta}C$ =constant. For all steady states of the system,

$$\int_{\Omega} N_0(\mathbf{X})d\mathbf{X} = \int_{\Omega} \frac{\alpha}{\beta}C(\mathbf{X},T)d\mathbf{X}, \tag{3.11}$$

and so $C$ is conserved in the steady state problem. This will be discussed further in Chapter 4 but for now we are interested in the time-dependent problem only. First, system (3.9) can be non-dimensionalised using a scaling similar to that used in [95] to reduce the number of free parameters. Let $N_{ss}$ be the initial zoospore density in an auto-aggregation experiment, then we introduce the scalings and parameter groupings,

$$n = \frac{N}{N_{ss}}, \quad c = \frac{C\beta}{\alpha N_{ss}}, \quad \mathbf{x} = \frac{\mathbf{X}}{L}, \quad t = \beta T, \quad D = \frac{D_N}{D_C}, \quad \chi = \frac{\chi_N \alpha N_{ss}}{\beta D_C},$$

$$\Gamma = \frac{D_C}{\beta L^2}, \quad \gamma = \frac{N_M}{N_{ss}}, \tag{3.12}$$

where $L$ is the diameter of petri dishes used in experiments; $D$ measures the ratio of cell diffusion to chemoattractant diffusion; $\chi$ is the strength of the chemotactic response; $\Gamma$ is a scaling parameter; $n$ is scaled with $N_{ss}$ and $\gamma$ is a non-dimensional volume-filling parameter. The re-scaled system is now

$$
\begin{aligned}
&\frac{\partial n}{\partial t} = \Gamma\nabla\cdot\left(D\nabla n - \chi n\left(1-\frac{n}{\gamma}\right)\nabla c\right), \qquad \mathbf{x}\in\Omega\subset\mathbb{R}^k \quad (k=1,2,3.),\\
&\frac{\partial c}{\partial t} = \Gamma\nabla^2 c + n - c,\\
&\frac{\partial n}{\partial \mathbf{x}} = \frac{\partial c}{\partial \mathbf{x}} = 0 \quad \text{on} \quad \partial\Omega,\\
&n(\mathbf{x},0) = n_0(\mathbf{x}), \quad c(\mathbf{x},0) = c_0(\mathbf{x}).
\end{aligned}
\tag{3.13}
$$

### 3.3.1 Parameter Values

It is important that the units of measurement are defined properly for all variables and parameters in order for comparisons between numerics and experiments to be meaningful. We treat cell density, $N$, as the number of cells per unit volume (ml) and $C$ is the molar concentration of chemoattractant (mol $L^{-1}$). Given the experimental observations that have been made and the scale of the patterns, we choose a length scale of centimetres and a time scale of minutes for all measurements.

Results from Chapter 2 can now be used to determine some of the parameter values for the model. Recall that calculations above showed the diffusion coefficient of the cells to be of the form, $D_N = \frac{\text{(cell speed)}^2\text{(Average run time)}}{3}$. We choose to use the average cell speed (50$\mu$m/s) giving a value of 3.8 x $10^{-4}$ $cm^2$ $min^{-1}$ for $D_N$. Note that this is similar to values obtained for other swimming unicellular organisms such as *E. Coli* [17]. The value of $N_M$ is somewhat more difficult to pin down. Experimental data that could help determine a suitable value can be found in the existing literature. Ko and Chase studied auto-aggregation in zoospores of the *P. palmivora* species and reported measurements of cell densities at the centre and at the periphery of aggregates [71]. Using the values given in this paper, by our calculations the ratio of the average cell

| Dimensional parameter | Description | Value | Reference |
|---|---|---|---|
| $N_{ss}$ | Initial zoospore density | $10^6$ cells ml$^{-1}$ | Set here |
| $D_N$ | Cell diffusion rate | $3.8 \times 10^{-4}$ cm$^2$ min$^{-1}$ | Established here |
| $D_C$ | Chemo diffusion rate | $5.34 \times 10^{-4}$ cm$^2$ min$^{-1}$ | As for cAMP in water [15] |
| $\chi_N$ | Chemotactic sensitivity | $1.7 \times 10^{-3}$ cm$^2$ $\mu$M$^{-1}$ min$^{-1}$ | Set here |
| $\alpha$ | Chemo production rate | $1.25 \times 10^{-9}\mu$mol cell$^{-1}$ min$^{-1}$ | Set here |
| $\beta$ | Chemo degradation rate | 2.5 min$^{-1}$ | Value for cAMP [79] |
| $L$ | Diameter of petri dish | 9 cm | Set here |
| Non-dimensional parameter | | | |
| $D$ | Diffusion ratio | 1 | - |
| $\chi$ | Chemotaxis coefficient | 1.6 | - |
| $\gamma = \frac{N_M}{N_{ss}}$ | Maximum cell density | 3 | Average for *P. palmivora* [70] |
| $\Gamma$ | Scaling coefficient | $2.6 \times 10^{-6}$ | - |

Table 3.1: Estimates for model parameters for the volume-filling chemotaxis model including units of measurement and references where appropriate.

density across an aggregate to the initial cell density ranges from 2.12-4.57. We choose to use an average value of $\frac{N_M}{N_{ss}} = 3$.

For some of the unknown parameters we use estimates based on measurements for the well-studied case of aggregation of *D. discoidium* via cAMP signalling. For the diffusion coefficient of the chemoattractant we choose a typical value used for cAMP in liquid, $D_C = 5.43 \times 10^{-4}$ cm$^2$ min$^{-1}$ [15]. The chemoattractant degradation rate, $\beta$, is taken to be that of cAMP and is taken from the experimental range given in [79]. We assume that the characteristic chemoattractant concentration, $\frac{\alpha N_{ss}}{\beta} = 0.5\mu$M, based on measurements for cAMP by Tomchik and Devreotes in [119] and hence compute

an estimate for $\alpha$ to be 1.25 $\times 10^{-9} \mu$mol cell$^{-1}$ min$^{-1}$. The unknown chemotactic sensitivity, $\chi_N$, has been determined such that numerical simulations best correspond to experimental data, as will be discussed further in the next section. The fact that this value is two orders of magnitude greater than for chemotaxic response to cAMP can be explained by the fact that the swimming speed of zoospores is far greater than the crawling speed of *D. discoidium* cells on agar. $L$ has been set as the diameter of petri dishes most commonly used in experiments. All values for dimensional parameters are given in Table 3.1 along with units of measurement and appropriate references. Also given are the non-dimensional parameters obtained by substituting the dimensional parameters into (3.12). $D$ has been set to 1 for convenience.

## 3.4 Numerical Simulations

### 3.4.1 1-D Solutions and Parameter Variation

Now that the model setup is completed, the system can be solved numerically. The numerical solutions that will be most relevant to study in comparison with experiments will be those in 2-D and 3-D, given the nature of the physical patterns that are observed. However, solving system (3.13) in 1-D has obvious computational benefits compared with solving in higher space dimensions and hence we use this setup to conduct sensitivity analysis of the model parameters established above. We will use `MATLAB`'s well-known pdepe solver to discretise the equations in space and time and obtain approximate solutions at each specified time point (see Appendix 7.1.1). 5000 grid points were used in the spatial discretisation and checks were made to ensure that this was sufficiently high as to rule out numerical errors in solutions. In all simulations, the uniform initial cell density was set as $n_0(x) = 1$ and was perturbed at each grid point using a small ($\ll 1$), uniformly distributed random variable with zero mean.

The initial value for the chemoattractant density, $c_0(x)$ was set to zero, although any uniform initial value produces the same results (data not shown). We begin by studying solutions of (3.13) obtained with the default parameter set given in Table 3.1.

Figure 3.1 shows initial pattern formation over a short time interval and Figure 3.2 shows the behaviour over longer times. Over short times, the chemoattractant density increases uniformly until perturbations to the initial cell density begin to grow and peaks emerge. In general, density peaks (for both $n$ and $c$) have local maxima that are approximately 2-2.5 times greater than the initial, uniform density. Densities fall sharply to around half the initial value in-between these peaks. Although the chemoattractant density follows the same density pattern as the cells, the local maxima are slightly smaller. Once initial peaks have formed, the evolution of the pattern slows down dramatically: the spatial pattern in Figure 3.2 appears to be a stable state of the system. However, as we will discuss in Chapter 4, this is in fact not the case and eventually only one peak will remain. The coarsening observed over long time scales is in line with the conservation property (3.10) described above.

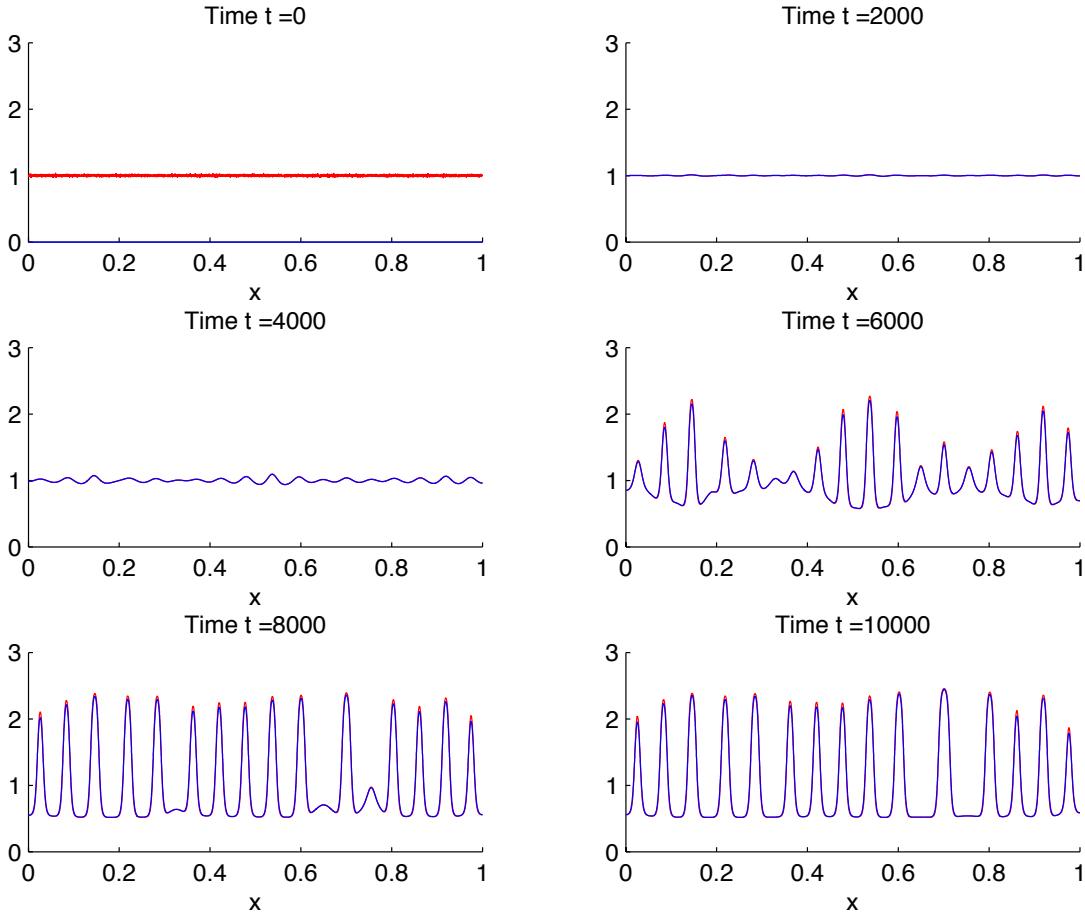


Figure 3.1: Solution of (3.13) in 1-D showing the formation of peaks from a randomly perturbed initial distribution of cells. Cell density, $n$, is shown in red and chemoattractant density, $c$, in blue (indistinguishable for most times). Parameter values are taken from Table 3.1. Solutions were computed for $t = 0..10^4$. In dimensional terms, the total simulation time is approximately three days.

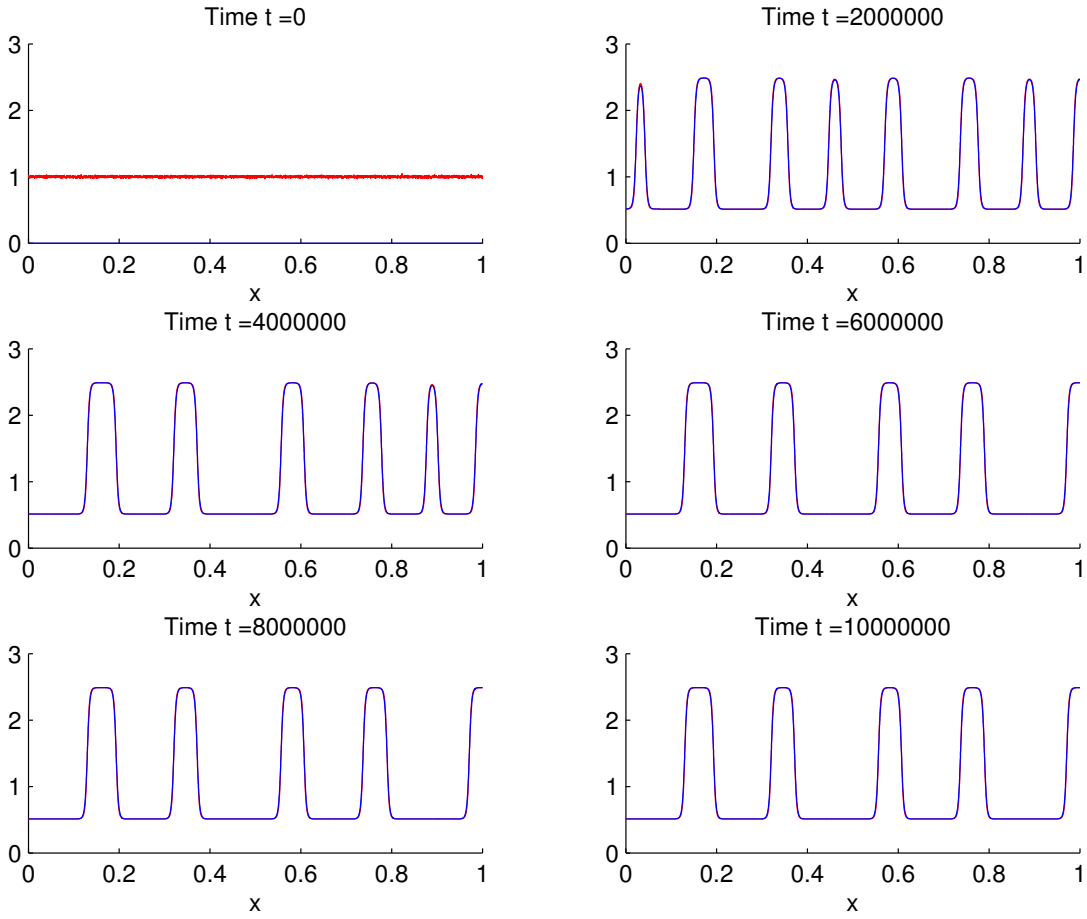


Figure 3.2: Solution of (3.13) in 1-D showing the coarsening of peaks after long times. Cell density, $n$, is shown in red and chemoattractant density, $c$, in blue (indistinguishable for most times). Parameter values used are as in Table 3.1. Equations were solved for $t = 0..10^7$ (approximately eight years in dimensional time).

The value of $\chi$ used in these simulations was chosen in order to produce a similar number of initial peaks as seen in experiments. In our experiments, we found with an initial zoospore concentration of approximately $10^6$ ml$^{-1}$, between ten and twenty peaks would form across the 9cm diameter of the dish. While the number of peaks appear to have been captured by the model, clearly the time scales predicted in these simulations are not realistic. For instance, images in Figure 3.1 show more or less fully

formed peaks in cell density (shown in red) after $10^4$ time units, which is equivalent to three days. Our experiments show that initial formation of peaks can occur after one to fifteen minutes, depending on the starting density. However, these times refer to visible aggregation. After longer times, the pattern evolution slows down considerably as it does in zoospore experiments. In Figure 3.2, cell peaks are seen to drift toward one another. Again, the time scales involved do not agree with our experimental observations. Simulations show that over $\approx 6 \times 10^4$ hours there is barely any change in the distribution of aggregates. This is clearly unrealistic.

The discrepancy between the numerical simulations and the experiments could simply be due to poor estimation of parameter values and hence some sensitivity analysis is required. The scaling factor, $\Gamma$, and the chemotaxis coefficient, $\chi$, are the two parameters that we have the most freedom to vary. That is, properties of the chemoattractant such as its degradation rate as well as the chemotactic sensitivity of zoospores are largely unknown. The non-dimensionalisation (3.12) ensures that $\Gamma$ and $\chi$ can be varied independently of one another and we now discuss the results.

Varying $\chi$ is equivalent to varying the chemotactic sensitivity, $\chi_N$, which does not affect the value of $\Gamma$. Figure 3.3 shows the initial formation of peaks with a fixed value of $\Gamma$ and with different $\chi$ values. Decreasing $\chi$ by a small amount results in fewer peaks in comparison with the default value. Moreover, these peaks take much longer to form. No patterns are formed for $\chi \lessapprox 1.5$. Calculations outlined in Chapter 4 can be used to show that the homogeneous steady state becomes stable, providing an explanation for the lack of patterns in this case. The opposite effect can be induced by increasing $\chi$. For large values of $\chi$, so many peaks are formed that the solutions cannot be confidently separated from numerical error. In Figure 3.4, similar simulations are shown but for varying values of $\Gamma$. These variations are equivalent to varying $\beta$ while keeping the parameter grouping, $\chi$, constant. A decrease in $\Gamma$ causes an increase in the number of peaks, which take longer to form. Increasing $\Gamma$ has the opposite effect. Note

that in Figure 3.4, dimensional times are given since the time scales vary in each plot. Changing other model parameters have similar effects on solutions (not shown) and, based on these observations, it seems that realistic parameter values cannot be selected that produce solutions that agree with our experimental observations. That is, either the correct number of peaks can be obtained over an incorrect time scale or an incorrect number of peaks can be produced over the correct time scale. Despite this discrepancy, we will persevere with the default parameter set given in Table 3.1 as these values are in the main gathered from existing literature or our experimental observations.

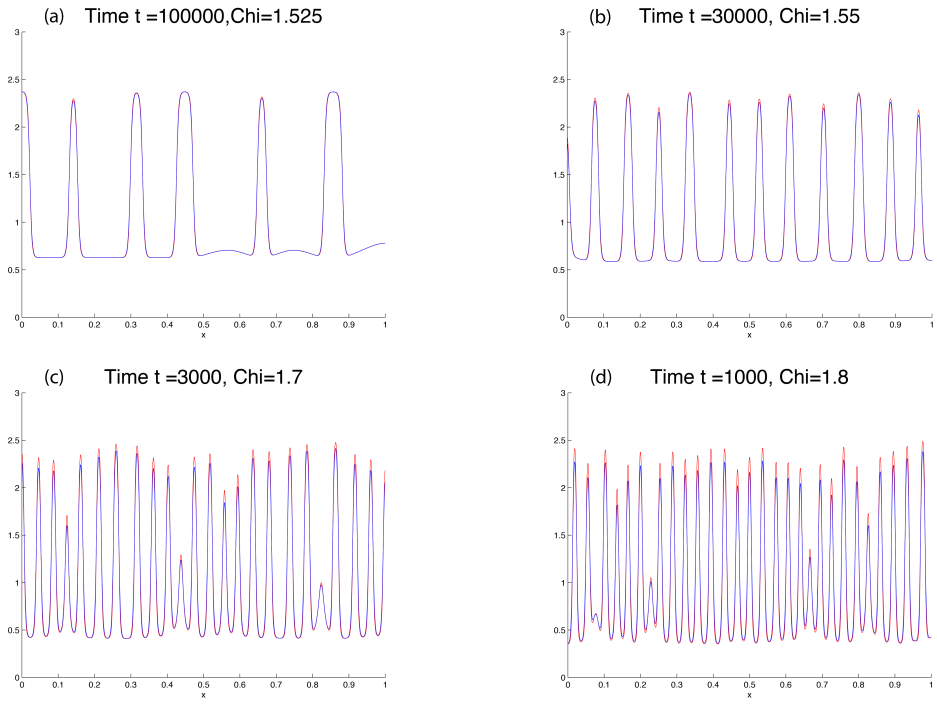


Figure 3.3: Solutions of (3.13) showing cell density and chemoattractant concentration peaks ($n$ and $c$) in 1-D. Values of $\chi$ are small perturbations about the default value: 1.525 (a); 1.55 (b); 1.7 (c) and; 1.8 (d). All other parameters are fixed at the default values given in Table 3.1. The dimensional times taken for each pattern to form can be found by dividing the given time by $\beta = 2.5\text{min}^{-1}$.

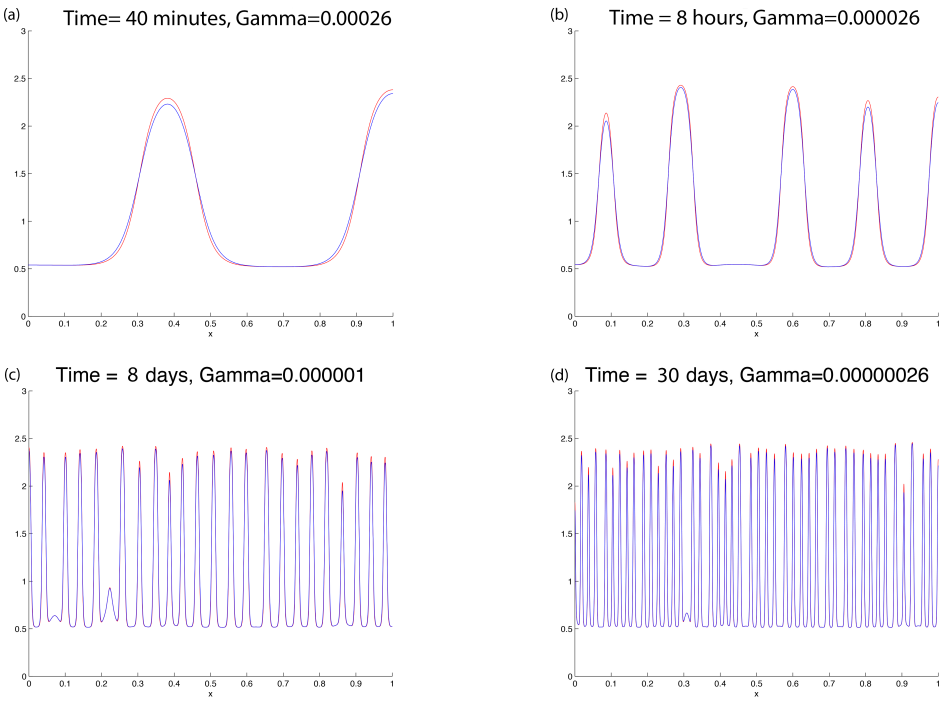


Figure 3.4: Solutions of (3.13) in 1-D showing cell density and chemoattractant concentration patterns ($n$ and $c$) for varying $\Gamma$. Values or $\Gamma$ are $2.6 \times 10^{-4}$ (a); $2.6 \times 10^{-5}$ (b); $1 \times 10^{-6}$ (c) and; $2.6 \times 10^{-7}$ (d). All other parameter values are taken from Table 3.1. Since the time scale differs in each simulation, the approximate dimensional times are shown for clarity.

### 3.4.2 Varying the Domain Shape: 2-D Solutions

To numerically integrate (3.13) in two and three space dimensions we used the COMSOL multiphysics software [4]. This is a finite element analysis package that is widely used for solving problems involving partial differential equations in engineering, physics and biology. COMSOL is ideally suited to solve the chemotaxis equations and we make use of it here to solve system (3.13) with, again, a randomly perturbed uniform cell density and an initial chemoattractant density of zero. In all of the simulations that follow, between $2.5 \times 10^5$-$3.5 \times 10^5$ elements were used in the spatial discretisation depending on the domain area. After checks were made this was found to give

sufficient numerical accuracy. For other settings, see Appendix 7.2. There is a clear advantage to solving the 2-D system as opposed to the 3-D system as this requires far less computing power but, in fact, a 2-D approximation of zoospore auto-aggregation may not be too unrealistic and worthy of interest in its own right. That is, it could be reasonable to assume that the fluid layer in the auto-aggregation experiments can be sufficiently shallow to be considered as two dimensional. We discuss this case next.

As seen in Figure 3.5, early patterns are a complex arrangement of "bands" that subsequently break-up and form distinct spots. These simulations were run for the same computational time as the 1-D case above and the time taken for aggregates to form distinctly is very similar, as are the magnitudes of the peaks. The initial labyrinthine patterns seen in numerical solutions appear to correspond *qualitatively* with the early pattern formation in zoospore auto-aggregation. Figure 3.6 shows the same coarsening behaviour of cell density peaks as observed in the 1-D case occurs over the same (long) time scale. Also, it is worth noting that aggregates are found exclusively on the domain edge after sufficiently long times.

The experimental results presented in Chapter 2 showed that domain shape had a profound effect on aggregation patterns. By solving system (3.13) on a square domain, the effect of the domain shape on solutions to the chemotaxis model can be tested. As shown in Figure 3.7, the patterns are identical to those in the circular domain case. Numerical simulations using other domain shapes did not produce any significantly different spot arrangements (see Figure 3.8 for an example).

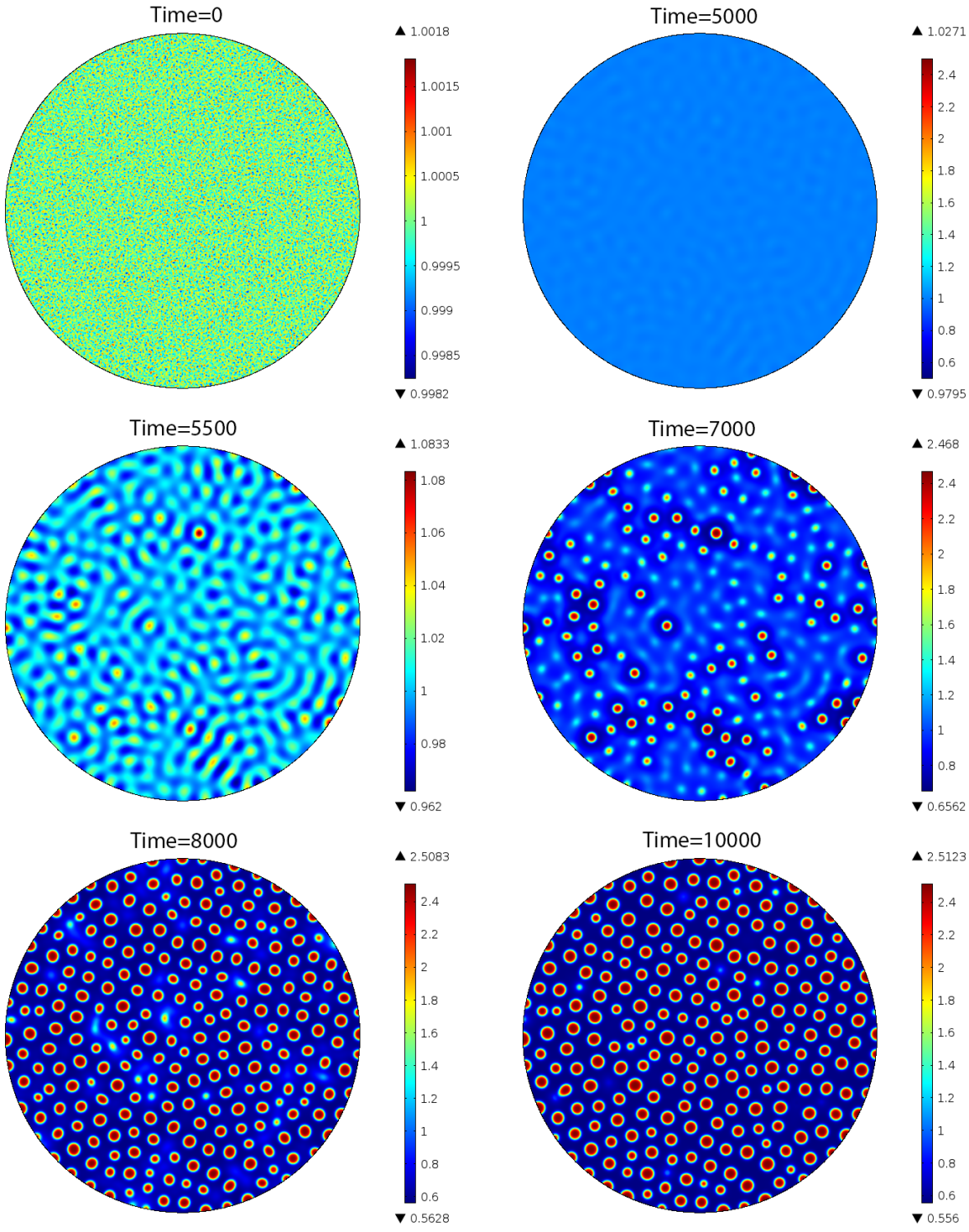


Figure 3.5: Cell density solution, $n$, of system (3.13) in a circular domain for $t = 0..10000$ showing peak formation in 2-D. Dimensional times can be found by dividing the given times by $\beta = 2.5\text{min}^{-1}$. Colours for each plot correspond to the values shown in the given colour bars. Parameter values used are taken from Table 3.1.

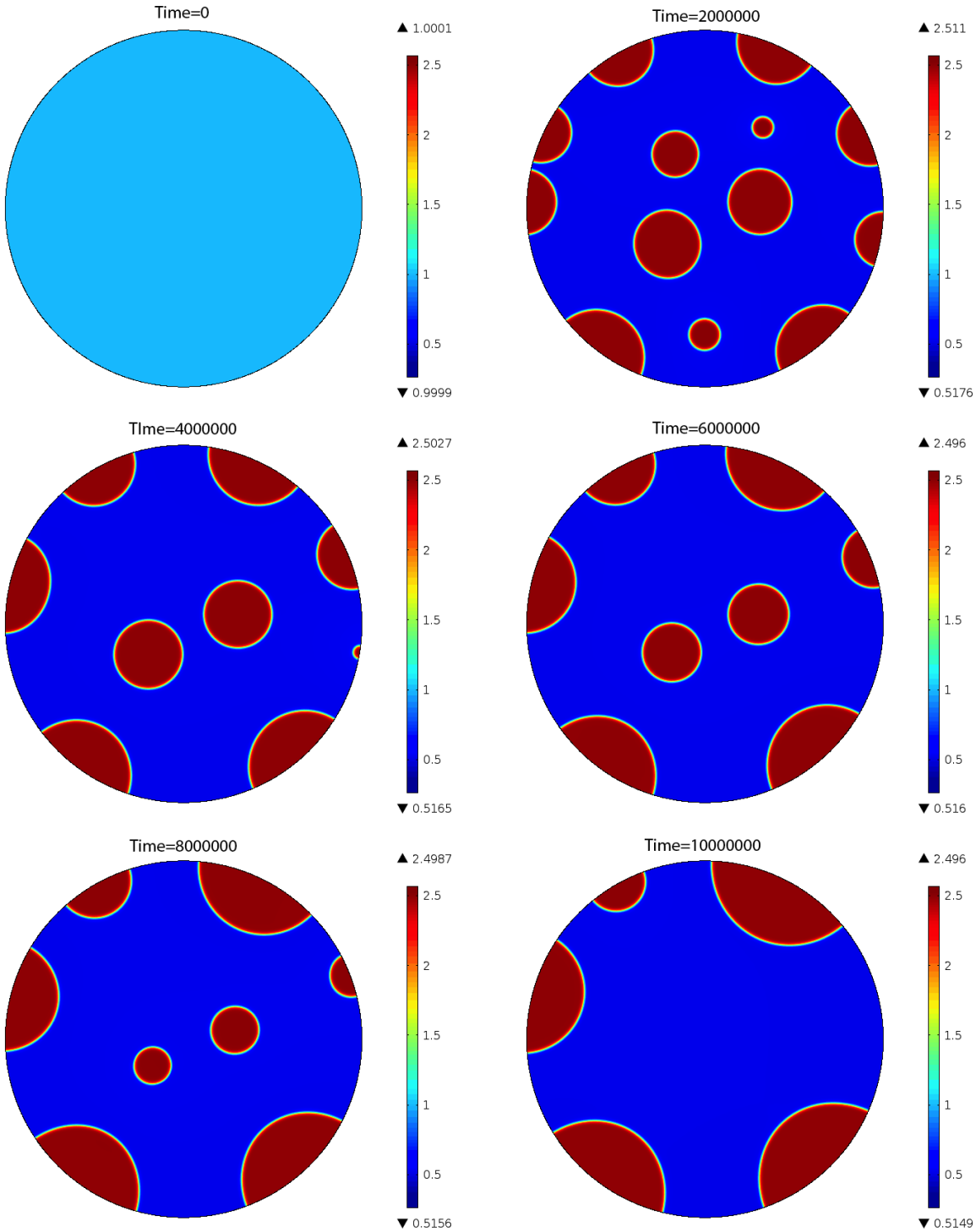


Figure 3.6: Cell density solution, $n$, of system (3.13) in a circular domain for $t = 0..10^7$ showing peak coarsening in 2-D. Dimensional times can be obtained by dividing the given times by $\beta = 2.5\text{min}^{-1}$. Colours for each plot correspond to the values shown in the given colour bars. Parameter values used are taken from Table 3.1.

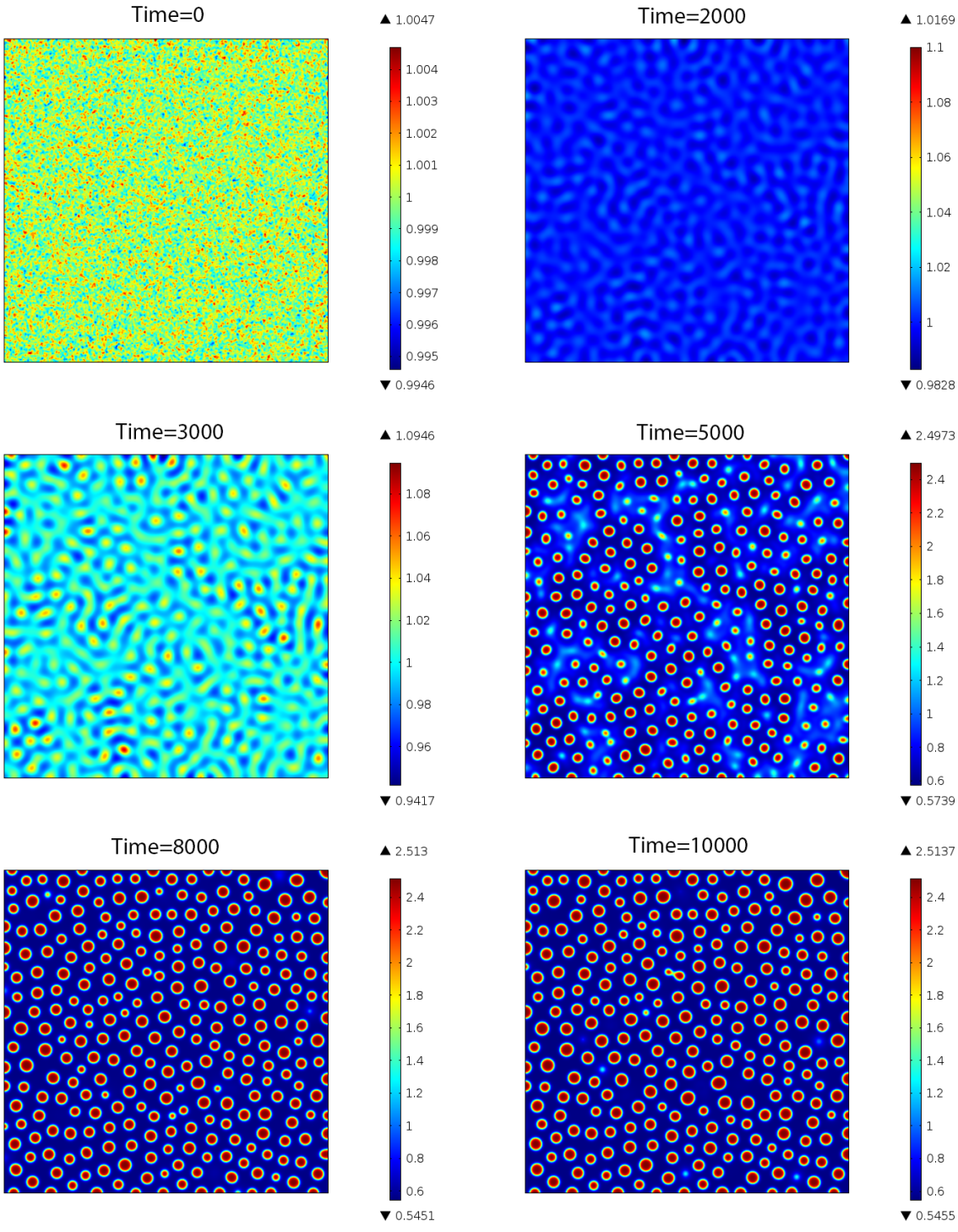


Figure 3.7: Cell density solution, $n$, of system (3.13) in a square domain for $t = 0..10000$ showing the formation of peaks in 2-D. Dimensional times can be obtained by dividing the given times by $\beta = 2.5\text{min}^{-1}$. Colours for each plot correspond to the values shown in the given colour bars. All parameter values used are taken from Table 3.1.

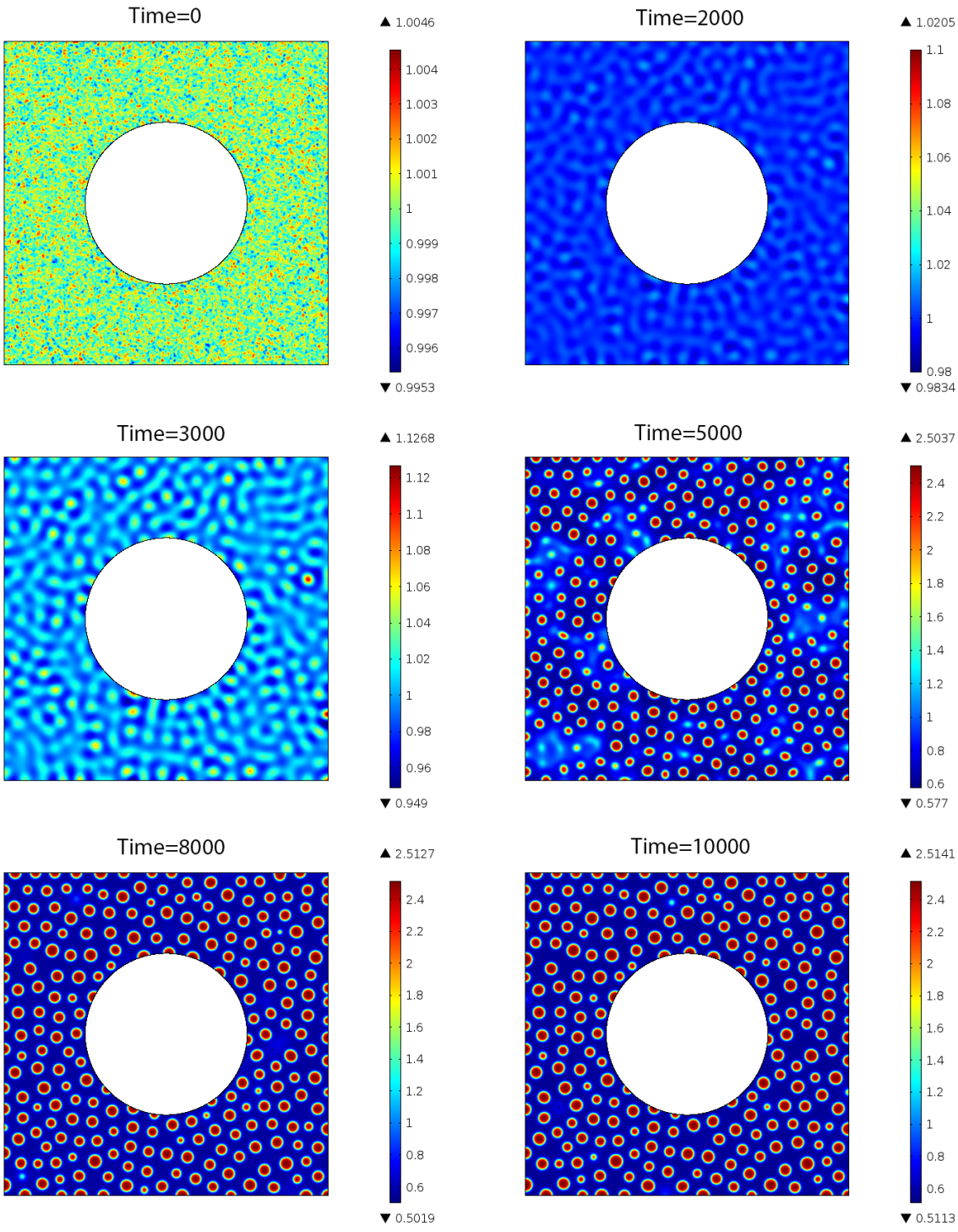


Figure 3.8: Cell density solution, $n$, of system (3.13) in a domain with an outer, square boundary and an inner, circular boundary for $t = 0..10000$ showing the formation of peaks in 2-D. Dimensional times can be obtained by dividing the given times by $\beta = 2.5\text{min}^{-1}$. Colours for each plot correspond to the values shown in the given colour bars. Parameter values used are taken from Table 3.1.

### 3.4.3 The Effect of Depth: 3-D Solutions

Although a 2-D approximation of the system can be considered reasonable, solving system (3.13) in three dimensions will clearly provide the most accurate and realistic results. This can be done by again using the COMSOL multiphysics package, but such 3-D simulations can become very computationally expensive (approximately $8 \times 10^5 - 1 \times 10^6$ elements were needed). First, we simulated a suspension depth commonly used in experiments of 3mm meaning a 30:1 ratio of diameter to depth. Figure 3.9 show the results of these simulations.

Distinct spots are again seen to form within the same time frame as for the one and two dimensional cases. Peaks have local maxima of similar magnitude to those in the 1 and 2-D case and the chemoattractant density, $c$ (not shown) is distributed as $n$. The position of aggregates appears to be random: some are at the surface, some at the bottom and some span the entire depth of the domain. As in the 2-D case, there are also aggregates with irregular shapes that have yet to break up into spots.

The same temporal discrepencies still exist between experiments and simulations. In the aggregation experiments using varying depths as discussed in Chapter 2, the initial patterns were seen to change from spots to high-density bands as the solution depth was increased from 3mm to 7mm (see Figure 2.3). By altering the depth of the domain, $\Omega$, in 3-D simulations, we can test whether or not chemotaxis could be responsible for this pattern variation. Numerical simulations show that the chemotaxis model fails to reproduce this effect: patterns are identical for depths of 3mm and 7mm (See Figures 3.9 and 3.10 respectively).

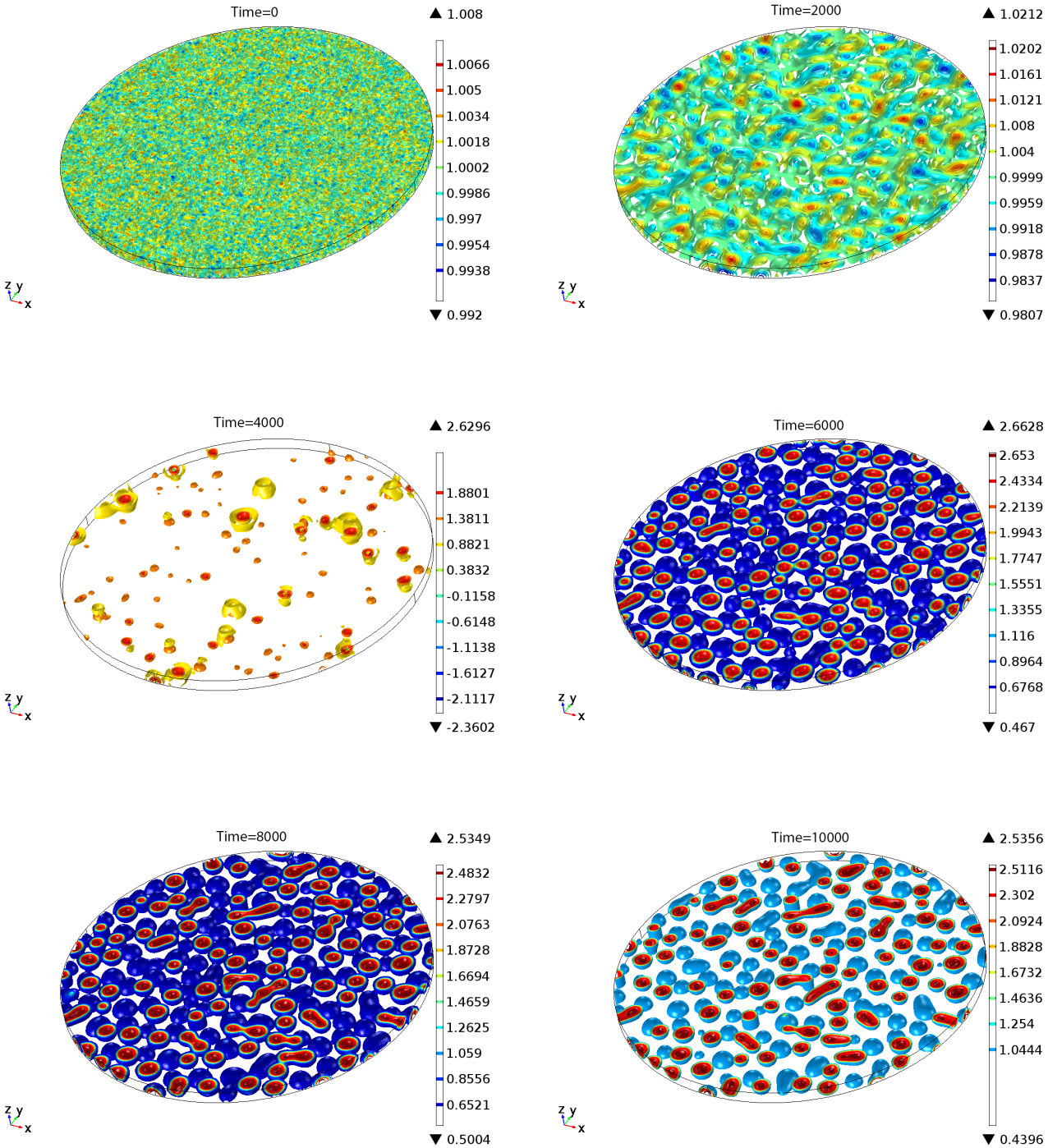


Figure 3.9: Cell density solution, $n$, of (3.13) in a shallow cylindrical domain showing peak formation for $t = 0..10000$ in 3-D. Dimensional times can be obtained by multiplying the given times by $\beta = 2.5\text{min}^{-1}$. Density is represented in an isosurface plot with the colours of solution contours corresponding to the densities in given colour bars. Parameters are taken from Table 3.1.

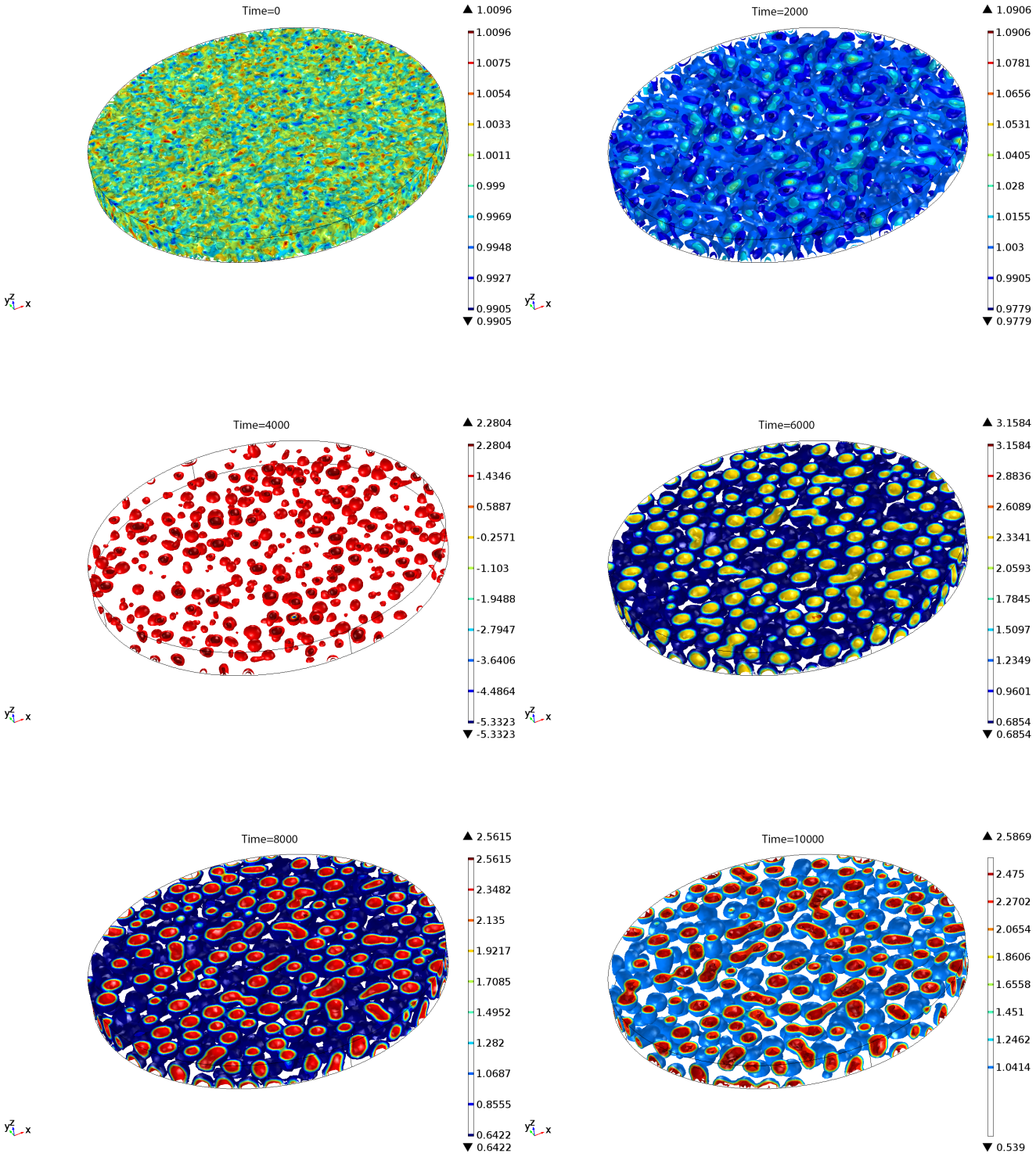


Figure 3.10: Cell density solution, $n$, of (3.13) in a deep cylindrical domain showing peak formation for $t = 0..10000$. Dimensional times can be obtained by multiplying the given times by $\beta = 2.5\text{min}^{-1}$. Density is represented in an isosurface plot with the colours of solution contours corresponding to the densities in given colour bars. Parameters are taken from Table 3.1.

## 3.5 Conclusions

In this chapter we have calibrated and studied a minimal model for chemotactic zoospore aggregation. This model was of Keller-Segel type with an added volume-filling term as first introduced by Painter and Hillen. Model parameters were determined from our experimental observations of individual zoospore swimming reported in Chapter 2 as well as estimates from existing literature. Our aim was to ascertain whether the auto-aggregation patterns presented in Chapter 2 could result from the self-chemotaxis of zoospores to each other.

Solutions of the model in one space dimension were used primarily for parameter sensitivity tests, as these are the least computationally expensive and hence quicker to run. By varying key parameters about their default values derived from our experiments and existing literature, we concluded that a quantitative agreement between numerical solutions and experimental data is not possible with realistic parameter values. In particular, a realistic number of cell density peaks could be obtained but the time scales involved were far from realistic, with initial pattern formation taking many days as opposed to the few minutes required in experiments. However, the 1-D simulations did reveal a qualitative agreement with experiments, in the sense that the subsequent drifting and coarsening of peaks took place over much longer time scales than initial, rapid spot formation.

In higher space dimensions, specifically 2-D and 3-D, the solutions behave in much the same way. In the 2-D case, qualitative predictions look extremely promising: the complex, band structures that precede the formation of spots in the simulations appear to correspond to experimental observations. However, it also appears that this is where the similarities end. In experiments, the initial aggregation patterns were shown to depend on the domain shape, at least to some degree (see Figure 2.1). The spot formation obtained numerically is identical, regardless of the shape of the domain, which

suggests that this effect is independent of chemotaxis (see Figures 3.5 and 3.7). Figure 2.5 and results in the existing literature show that aggregates do not have a uniform density but rather a high density region at the centre of the spot with a lower density cloud of cells surrounding it. While this is true of initial patterns in simulations, this is certainly not the case for solutions over long times as spots have an even density across their surface. Moreover, as illustrated in Figure 3.6, the size of aggregates increases considerably with time. Aggregates are predicted to be circular in shape with the exception of those at the domain edge and a uniform density is maintained within each aggregate. Since the cell density is always limited by the volume-filling term, it is no surprise that the aggregate areas would increase as spots drift together and combine. This seems to contradict what is seen in experiments. Although spots do vary in size to some degree (see Figure 2.5), there are none that even vaguely correspond to the aggregate sizes predicted by the model. It is possible that the sizes of real aggregates are kept below a certain threshold due to other mechanisms not studied here e.g. swimmers being lost through encystment. However, we view that this loss would not have a significant effect. The fact that the chemotaxis model predicts that aggregates after long times are located along the boundary is certainly not in agreement with our experimental observations, as no such aggregates were seen in reality.

In three dimensions, the time taken for peaks to form was similar to that in one and two dimensional simulations. Simulated aggregates were spherical in size and increased in average size over time much as in the 2-D case. Crucially, studying solutions in three space dimensions meant that the effect of suspension depth variation on patterns could be considered and tested. Numerical simulations show that this variation has, in fact, no effect on chemotactic patterns: the positioning of aggregates was random in the $z$-direction, with no preferential depth at which aggregates would form. Altering the domain shape in 3-D (results not shown) also had no effect on patterns.

The evidence we have presented in this chapter leads us to the conclusion that chemotaxis almost certainly cannot be the sole mechanism behind zoospore auto-aggregation. That is not to say that we should disregard it completely, as there are many features of the numerical simulations that seem to confirm our initial characterisation of chemotaxis as a partial contributor. For instance, although not quantitatively accurate, the fast formation of initial patterns followed by slow drifting is a property that is shared by all simulations and is a feature of the experimental system. The details that the chemotaxis model fails to capture, such as the effect of suspension depth, domain shape and the non-uniform density seen across aggregate surfaces, strongly indicate that other processes are in play. To this end we will study the process of bioconvection in Chapter 5 and consider how this process interacts with chemotaxis. Before that, in the following chapter we examine in more detail the fast-slow pattern formation process that was a common feature of the simulations presented in this chapter.

# Chapter 4

# Steady States of the Volume-Filling Chemotaxis Model

## 4.1 Introduction

We consider in more detail the pattern formation observed in the numerical simulations reported in Chapter 3. For ease of reference, we state again the model used to describe chemotactic zoospore movement. The model used is the standard Keller-Segel model with the addition of the volume-filling term proposed by Painter and Hillen. In its non-dimensional form the model is

$$\begin{aligned}
&\frac{\partial n}{\partial t} = \Gamma\nabla\cdot\left[D\nabla n - \chi n\left(1-\frac{n}{\gamma}\right)\nabla c\right], \qquad \mathbf{x}\in\Omega\subset\mathbb{R}^k\ (k=1,2,3),\ t>0\\
&\frac{\partial c}{\partial t} = \Gamma\Delta c + n - c,\\
&\frac{\partial n}{\partial \nu} = \frac{\partial c}{\partial \nu} = 0 \quad \text{on } \partial\Omega, t>0
\end{aligned} \tag{4.1}$$

where $n$ and $c$ represent cell (zoospore) and chemoattractant density, respectively. The parameters $\Gamma, D, \chi$ and $\gamma$ are positive constants that represent a scaling of the domain size, relative diffusion ratio of the cells to chemoattractant, chemotactic sensitivity and maximum cell density (volume-filling), respectively. The spatial domain $\Omega \subset \mathbb{R}^k$, $k = 1,2,3$ with sufficiently smooth boundary $\partial\Omega$. The boundary conditions are of Neumann type with $\frac{\partial}{\partial \nu}$ representing the outward pointing normal derivative as is standard.

The numerical simulations discussed in Chapter 3 concerned the solution of system (4.1) augmented with initial data of the form

$$n(x,0) = n_0(x), \quad c(x,0) = c_0(x), \quad x \in \Omega \tag{4.2}$$

for given positive functions $n_0$ and $c_0$. As stated there, by integrating the first equation in system (4.1), it is straightforward to show that the total cell population is conserved, i.e.

$$\int_\Omega n(x,t)dx = \int_\Omega n_0(x)dx, \quad \forall t > 0. \tag{4.3}$$

Moreover, and again by integration, it immediately follows that when the system is in steady state,

$$\int_\Omega n(x)dx = \int_\Omega c(x)dx. \tag{4.4}$$

Hence, when considering steady states relevant to the initial-boundary value problem studied in Chapter 3, we are restricted to those that satisfy the condition

$$\int_\Omega n(x)dx = \int_\Omega c(x)dx = \int_\Omega n_0(x)dx = |\Omega| \tag{4.5}$$

without loss of generality (this arises from the non-dimensionalisation). We will return to this important point later.

Chemotaxis models like (4.1), have been extensively studied by various researchers (see e.g. [49, 53, 106, 110, 127] and references therein for further details). The review paper [53] by Hillen and Painter presents a comprehensive overview. Steady state solutions of these models have been the focus of many of these papers. For example, in [53], the linear stability of constant steady states for various versions of the above model is discussed. Dispersion relations are presented there for $\Omega \subset \mathbb{R}$ as well as necessary conditions on system parameters for linear instability - suggesting regions in parameter space that could support pattern formation. Numerical simulations are presented in one, two and three space dimensions and comment is made on the coarsening of peaks over time. The subject of peak merging and coarsening was tackled by Potapov and Hillen in [106] for the Keller-Segel model with volume-filling (system (4.1)). Using asymptotic techniques, bifurcation from spatially uniform solutions is studied and it is shown that non-uniform solutions with two or more maxima are marginally unstable - numerical calculations reveal that the eigenvalues of the associated linearisation are positive, but very close to zero.

First, using the approach in [110], we discuss bifurcation from uniform steady states of (4.1). The system is reduced to a single equation, (4.8), which includes a positive constant, $\lambda$. We show that there exist a finite number of bifurcation points along the set of constant solutions to (4.8). We prove the existence of continuous branches of non-trivial steady states that form loops, along which the nodal properties of solutions are conserved. An interesting special case arises for $\gamma = 2m$, where all relevant steady states of (4.1) (i.e. solutions with $\int_\Omega c dx = |\Omega|$) can be obtained with a single value of $\lambda$. We investigate the mathematical reason for this by using an extension of the phase plane analysis given in [49] and [106]. Finally we discuss the stability of all steady states of (4.1) using linear analysis.

## 4.2 Steady States

Steady states of system (4.1) satisfy

$$\begin{aligned} 0 &= \Gamma\nabla\cdot\left[D\nabla n-\chi n\left(1-\frac{n}{\gamma}\right)\nabla c\right], \quad x\in\Omega,\\ 0 &= \Gamma\Delta c+n-c,\\ \frac{\partial n}{\partial \nu} &= \frac{\partial c}{\partial \nu}=0 \quad \text{on } \partial\Omega, \end{aligned} \tag{4.6}$$

To begin with we will consider all possible solutions of system (4.6) before reconsidering those that are relevant as asymptotic states of system (4.1) -(4.2).

It is straight forward to show that any constant with $n = c$ is a solution of (4.6). To study non-constant steady states, we follow [110] and rewrite (4.6) as a single equation. This can be done as follows. [We note that in [110], the standard Keller-Segel model is considered, i.e. without the volume filling term. This led the authors of [106] to comment that the system contraction method presented in [110] could not be used for the volume-filling model. We show here that this can in fact be done and the analysis of the resultant scalar equation provides useful insight into the structure of the solution set of (4.6).]

### 4.2.1 Reduction to a single equation

Let $r:\mathbb{R}^+\to\mathbb{R}^+$ be the (unique) solution of the ordinary differential equation

$$\frac{dr}{ds}=\frac{\chi}{D}r\left(1-\frac{r}{\gamma}\right), \quad r(s_0)=r_0, \tag{4.7}$$

with $0 < r_0 < \gamma$ and $s_0 > 0$.

Define $\phi : \mathbb{R} \times \mathbb{R} \to \mathbb{R}$ by $\phi(s,\lambda) = r(s,\{0,\lambda\})$, where $r(s,\{1,\lambda\})$ denotes the solution of (4.7) with $r(1) = \frac{\gamma}{1+\lambda\exp(-\chi/D)}$. Finally, define the Banach spaces $X, Y, Z$ and $B$ as follows:

$$Y := \{u \in C^{0,\alpha}(\Omega)\}, \quad Z := \{u \in C^{2,\alpha}(\Omega)\}$$

$$X = \{u \in Z \,|\, \partial_\nu u|_{\partial\Omega} = 0\}, \quad B := \{u \in X \,|\, u(\bar{\Omega}) \subset \mathbb{R}^+\},$$

where $\alpha = 0$ for $k = 1$ and $0 < \alpha < 1$ for $k = 2,3$.

Then we have the following result.

**Lemma 4.2.1.** *The pair $(n,c) \in B \times B$ is a solution of* (4.6) *iff, for some $\lambda \in \mathbb{R}^+$,*

$$n(x) = \phi(c(x),\lambda), \quad \textit{for all } x \in \bar{\Omega}$$

*and*

$$\Gamma\Delta c + \phi(c,\lambda) - c = 0.$$

*Proof.* The method of proof is identical to that used to prove Theorem 2.1 in [110]. We note that in our case it is easy to verify that

$$\phi(c,\lambda) = \frac{\gamma}{1+\lambda\exp\left(-\frac{\chi}{D}c\right)}$$

and hence seeking a solution $(n,c)$ to (4.6) is equivalent to seeking a pair $(c,\lambda) \in B \times \mathbb{R}^+$ that satisfies

$$\Gamma\Delta c + f(c,\lambda) = 0, \tag{4.8}$$

where

$$f(c,\lambda) = \phi(c,\lambda) - c.$$

Once $(c,\lambda)$ is found, a solution for (4.6) can be constructed thus: $(n,c) = (\phi(c,\lambda),c)$.

□

An additional constant, $\lambda$, appears in (4.8). This constant arises through integration and serves as a link between the initial data of the time-dependent problem (4.1) and solutions of the steady state problem (4.6). That is, since the integral of $n$ is conserved, the integral of $\phi(c,\lambda)$ must equal that of $n_0(x)$. We use $\lambda$ as the main bifurcation parameter and discuss its significance further later.

To proceed we require to relate the linearisations of system (4.6) and the scalar equation (4.8). This does not follow immediately. However, Theorem 2.2 in [110] does follow without significant alteration and thus the linearisations can be shown to be equivalent. Hence we have an existence result that mirrors Theorem 3.1 in [110], which we now detail. First, some further definitions are required. Let the set of constant solutions to (4.8) be denoted by

$$M := \{(m,\lambda) \in \mathbb{R}^+ \times \mathbb{R}^+ \,|\, f(m,\lambda) = 0\}.$$

The set $M$ is identified with the subset of constant functions in $B \times \mathbb{R}^+$ with the given value. Now let the non-trivial solution set of (4.8) be denoted by

$$S := \{(c,\lambda) \in B \times \mathbb{R}^+ \,|\, (c,\lambda) \text{ solves (4.8)}, c \notin M\}$$

Finally, denote by $(\omega_j,\mu_j)$ the eigenvector - eigenvalue pair associated with $\Gamma\Delta : X \to Y$.

**Lemma 4.2.2.** *Suppose for some* $(m_0,\lambda_0) \in M$,

$$\partial_1 f(m_0,\lambda_0) = \mu_j,\ j \geq 1$$

*with $\mu_j$ a simple eigenvalue of $\Gamma\Delta$ and let $\lambda \to m(\lambda)$ be a parameterisation of $M$ near $(m_0, \lambda_0)$. If in addition*

$$\frac{d}{d\lambda}(\partial_1 f(m(\lambda), \lambda))|_{\lambda=\lambda_0} \neq 0,$$

*then*

1. *$(m_0, \lambda_0)$ is a bifurcation point i.e. $(m_0, \lambda_0) \in \bar{S}$.*

2. *Let $\mathscr{C}(m_0, \lambda_0)$ be a connected component of $\bar{S}$ with $(m_0, \lambda_0) \in \mathscr{C}(m_0, \lambda_0)$. Then $\mathscr{C}(m_0, \lambda_0)$ either joins a bifurcation point in $M$ different from $(m_0, \lambda_0)$ or $\mathscr{C}(m_0, \lambda_0)$ joins $\infty$ in $B \times \mathbb{R}^+$.*

3. *In a neighbourhood $U = U(m_0, \lambda_0) \subset B \times \mathbb{R}^+$, the component $\mathscr{C}(m_0, \lambda_0)$ is a curve, i.e. for some $\varepsilon_0 \in \mathbb{R}^+$ sufficiently small, $\mathscr{C}(m_0, \lambda_0)$ can be represented by*

$$\varepsilon \in (-\varepsilon_0, \varepsilon_0) \to (C(\varepsilon), \Lambda(\varepsilon)), \quad V'(0) = \omega_j,$$

   *for twice continuously differentiable functions $C$ and $\Lambda$.*

4. *For $k = 1$ the nodal properties of $c$ are preserved in $\mathscr{C}(m_0, \lambda_0)$*

The proof of the lemma is standard, and follows from the local and global theorems of Crandall and Rabinowitz and Rabinowitz, respectively (see e.g. [132]). Note that (i) $\partial_1 f(m_0, \lambda_0) = \mu_j > 0$ for $j \geq 1$ and hence the required parameterisation exists (sufficiently close to the bifurcation points in any case, but see below); (ii) the requirement that $\mu_j$ are simple is weak - e.g. for $k = 1$, $\mu_j$ are simple; (iii) in the case $k = 1$, the nodal properties are of $c''(x)$. So solutions on the continuum that bifurcates from the point where $\partial_1 f(m_0, \lambda_0) = \mu_p$ will have exactly $p$ simple zeros of $c''(x)$, i.e. $p$ points of inflection. Below, such solutions will be referred to as $p-$step solutions.

Lemma 4.2.2 ensures the existence of non-trivial solutions to (4.8) and hence to (4.6).

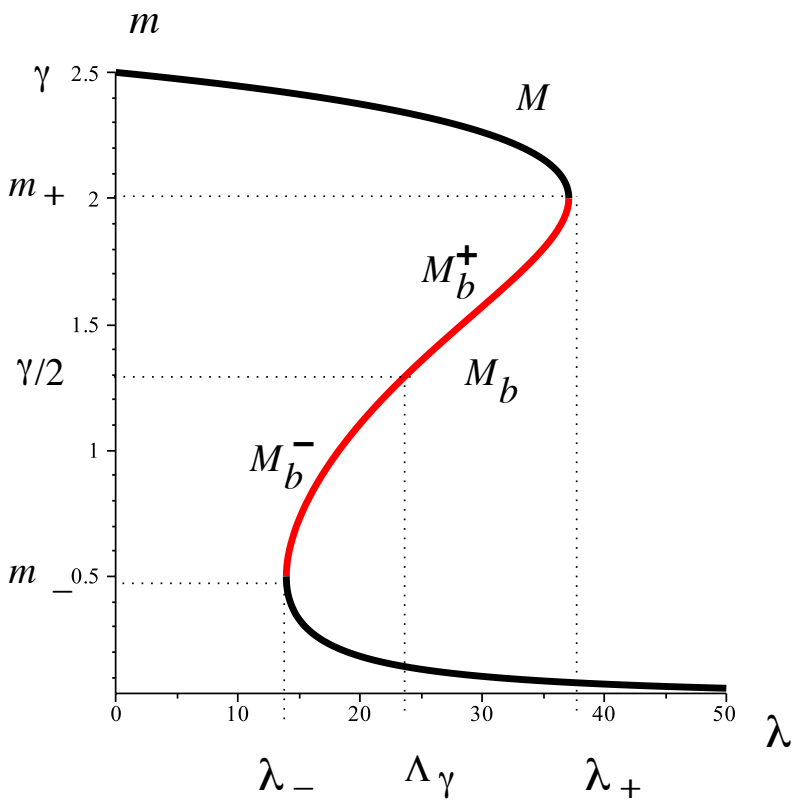


Figure 4.1: Plot of the set $M$ of uniform solutions to (4.8). The points $(\lambda_-, m_-)$ and $(\lambda_-, m_-)$ mark folds in $M$. Bifurcation occurs from the subset $M_b$ shown in red. See text for a description symmetry point $(\Lambda_\gamma, \gamma/2)$. Parameter values used: $\gamma = 2.5, \chi = 25, D = 10$.

The set of trivial solutions, $M$, for the volume filling model considered here is illustrated in Figure 4.1, for a typical choice of parameters. An examination of the function $f$ immediately reveals that the component marked in red corresponds to the portion of the set $M$ for which $\partial_1 f|_M > 0$. If the points $P_\pm$ mark the two folds, then $M \setminus \{P_\pm\}$, can be parameterised by $\lambda \to (m(\lambda), \lambda)$. An alternative and more useful parameterisation that holds for all $M$ is $m \to (m, \lambda(m))$ where

$$\lambda(m) = \frac{\gamma - m}{m} \exp\left(\frac{\chi}{D} m\right). \tag{4.9}$$

The location of the folds is given by $\lambda'(m) = 0$ i.e.

$$-\frac{\exp\left(\frac{\chi}{D}m\right)}{m^2}\left(\frac{\chi}{D}m^2 - \frac{\chi}{D}m\gamma + \gamma\right) = 0 \iff m = m_\pm \text{ with}$$

$$m_\pm := \frac{\gamma}{2}\left(1 \pm \sqrt{1 - \frac{4}{\gamma}\frac{D}{\chi}}\right).$$

Using (4.9), the corresponding values of $\lambda$ are

$$\lambda_\pm := \frac{\gamma - m_\pm}{m_\pm}\exp\left(\frac{\chi}{D}m_\pm\right).$$

Clearly, these folds exist if and only if

$$\gamma\frac{\chi}{D} > 4. \tag{4.10}$$

In this case, $0 < m_\pm < \gamma$ and hence $\lambda_\pm > 0$.

Given that $\mu_j > 0$ for all $j \geq 1$, it follows from Lemma 4.2.2 that (4.10) is a necessary condition for bifurcation from $M$. We will refer to the component of $M$ for which $\partial_1 f|_M > 0$ as $M_b$. It will become apparent that an important point in $M_b$ is where $\partial_1^2 f|_{M_b} = 0$. This marks a symmetry point for bifurcation from $M_b$ separating this set into upper and lower parts, denoted by $M_b^\pm$. By direct calculation, $\partial_1^2 f = 0$ iff

$$\lambda\exp\left(-\frac{\chi}{D}m\right) - 1 = 0$$

and using the expression for $\lambda(m)$ given above, it is straightforward to show that this is satisfied when $(m,\lambda) = (\gamma/2, \Lambda_\gamma)$, with

$$\Lambda_\gamma = \exp\left(\frac{\gamma\chi}{2D}\right).$$

At this point on $M_b$,

$$\partial_1 f(\gamma/2, \Lambda_\gamma) = \frac{1}{4}\gamma\frac{\chi}{D} - 1, \tag{4.11}$$

which is the maximum value of $\partial_1 f|_{M_b}$.

Combining all of these facts leads to the following result.

**Theorem 4.2.1.** *Connected continua $\mathscr{C}(m_j, \lambda_j)$ of non-trivial solutions to* (4.8) *bifurcate from the trivial solution set $M_b$ at the points $(m_j, \lambda_j) \in M_b$ where $\partial_1 f(m_j, \lambda_j) = \mu_j$ for each $0 < \mu_j < \frac{1}{4}\gamma\frac{\chi}{D} - 1$. These continua remain bounded in $B \times \mathbb{R}^+$ and hence rejoin $M_b$ at some $(\hat{m}, \hat{\lambda})$ where $\partial_1 f(\hat{m}, \hat{\lambda}) = \mu_i$ where $i$ may equal $j$, but $(\hat{m}, \hat{\lambda}) \neq (m_j, \lambda_j)$. For the case $k = 1$, $i = j$.*

**Remark 4.2.1.** *The symmetry of the range of values of $\partial_1 f|_{M_b}$ implies that if a bifurcation point $(m_j^+, \lambda_j^+) \in M_b^+$ exists, then so does its mirror $(m_j^-, \lambda_j^-) \in M_b^-$. Therefore, in the above theorem in the case $k = 1$, $(\hat{m}, \hat{\lambda}) = (m_j^-, \lambda_j^-)$, that is the continua form loops connecting the points $(m_j^+, \lambda_j^+)$ with $(m_j^-, \lambda_j^-)$. We conjecture that these loops represent the generic structure of the solution set and that this structure persists for $k > 1$.*

*Proof.* The existence of the bifurcation points $(m_j, \lambda_j)$ and associated continua $\mathscr{C}(m_j, \lambda_j)$ follows directly from Lemmas 4.2.1 and 4.2.2 above. What remains to be proved is the global behaviour of these continua.

First, assume the $\lambda \geq 0$. Multiplying (4.8) by $c$, integrating over $\Omega$ and applying the boundary conditions yields

$$\begin{aligned} \Gamma \int_\Omega |\nabla c|^2 dx &= \int_\Omega c\phi(c, \lambda) dx - \int_\Omega c^2 dx \\ \implies \int_\Omega c^2 dx &\leq \int_\Omega c\phi(c, \lambda) dx. \end{aligned}$$

By Schwartz' inequality,

$$\int_\Omega c\phi(c,\lambda)dx \leq \left(\int_\Omega c^2\phi(c,\lambda)^2dx\right)^{1/2}|\Omega|^{1/2}$$

and since $\phi < \gamma$, it follows that

$$\int_\Omega c^2dx \leq \gamma|\Omega|^{1/2}\left(\int_\Omega c^2dx\right)^{1/2},$$

i.e.

$$\left(\int_\Omega c^2dx\right)^{1/2} \leq \gamma|\Omega|^{1/2}.$$

Hence,

$$\int_\Omega |\nabla c|^2dx \leq \frac{\gamma^2}{\Gamma}|\Omega|.$$

In conclusion we have that $\|c\|_{1,2} \leq K$ for some constant $K$ independent of $\lambda$. Now, for $\Omega \subset \mathbb{R}^3$, the Sobolev embedding theorems ensure that $W^{1,2}(\Omega) \hookrightarrow L^6(\Omega)$ (see e.g. [8]). If $c \in L^6(\Omega)$, then $f(c,\lambda) \in L^6(\Omega)$ so it follows directly from (4.8) that $c \in W^{2,2}(\Omega)$ and that $\|c\|_{2,2} \leq K$. That solutions are bounded in $Y$ follows from the embedding $W^{2,2}(\Omega) \hookrightarrow C^m(\bar{\Omega})$, $0 \leq m \leq 2-k/2$, $k = 1,2,3$.

Finally, the boundedness of solutions in $B$ follows from the smoothness of $f(c,\lambda)$ and standard bootstrapping arguments. Hence we have established that the continua $\mathscr{C}$ must remain bounded in $B$, provided $\lambda$ remains positive.

Next we establish that all continua remain within $\lambda > 0$. Suppose otherwise. Then we can construct a sequence of solutions $(c_i,\lambda_i) \in \mathscr{C}$ with $\lambda_i > 0$ and $\lim_{i\to\infty}\lambda_i = 0$. The bounds obtained above ensure that the limit of this sequence exists and satisfies

$$\Gamma\Delta c + \gamma - c = 0$$

Integrating and applying the boundary conditions yields

$$\int_\Omega c dx = \int_\Omega \gamma dx = |\Omega|\gamma.$$

Hence on setting $y = \gamma - c$, it follows that $\int_\Omega y dx = 0$ and

$$-\Gamma\Delta y + y = 0.$$

But the spectrum $\sigma(-\Gamma\Delta) \geq 0$ and so this equation has the unique solution $y = 0$ i.e. $c \equiv \gamma$. But then the continuum joins the set $M$ at the point $(c,\lambda) = (\gamma, 0)$. We now show that this cannot be the case by invoking the Implicit Function Theorem.

Setting $F(c,\lambda) := \Gamma\Delta c + f(c,\lambda)$, the operator $D_c F(c,\lambda) : B \to Z$ is defined by

$$D_c F(c,\lambda) z = \Gamma\Delta z + \left(\phi_c(c,\lambda) - 1\right) z = \Gamma\Delta z - 2z, \quad z \in B.$$

It follows from standard arguments that $D_c F$ is a Fredholm operator of index zero and as the spectrum $\sigma(-\Gamma\Delta) \geq 0$, $D_c F z = 0 \implies z = 0$. Thus, $D_c F z = 0$ is an isomorphism and we may apply the Implicit Function Theorem to ensure that a unique branch of solutions exists passing through the point $(\gamma, 0)$. But the set $M$ also passes through this point and hence we have reached a contradiction.

Finally, to show that all continua $\mathscr{C}$ remain bounded in $B \times \mathbb{R}^+$, we again assume the contrary. First, it follows directly from the strong elliptic maximum principle that solutions on the continua, $\mathscr{C}$, remain positive. Suppose then there exists a sequence of solutions $(c_i, \lambda_i) \in \mathscr{C}$ with $c_i, \lambda_k \geq 0$ and $\lim_{k\to\infty} \lambda_i = \infty$. Then, as $\phi(c_i, \lambda_i) \to 0$ (uniformly in $\Omega$), the limit $(c_0, 0)$ of this sequence exists and satisfies

$$\Gamma\Delta c_0 - c_0 = 0.$$

Arguing as above, this equation has only the trivial solution $c_0 \equiv 0$ and we have reached a contradiction.

That the continua $\mathscr{C}(m_j, \lambda_j)$ must rejoin the set $M_b$ now follows directly from the alternatives presented in Lemma 4.2.2.

□

Using the numerical continuation package AUTO 07p [2], we can construct a bifurcation diagram in the case $\Omega = [0,1]$. Two examples are shown in Figures 4.2-4.3, where it is seen that the continua $\mathscr{C}$ form loops illustrating the results of Theorem 4.2.1. Note that the value $\Lambda_\gamma$ seems to mark a line of symmetry for the loops of non-trivial solutions. Solutions $(c_j, \Lambda_\gamma) \in \mathscr{C}_j$ have the largest value at the left hand boundary.

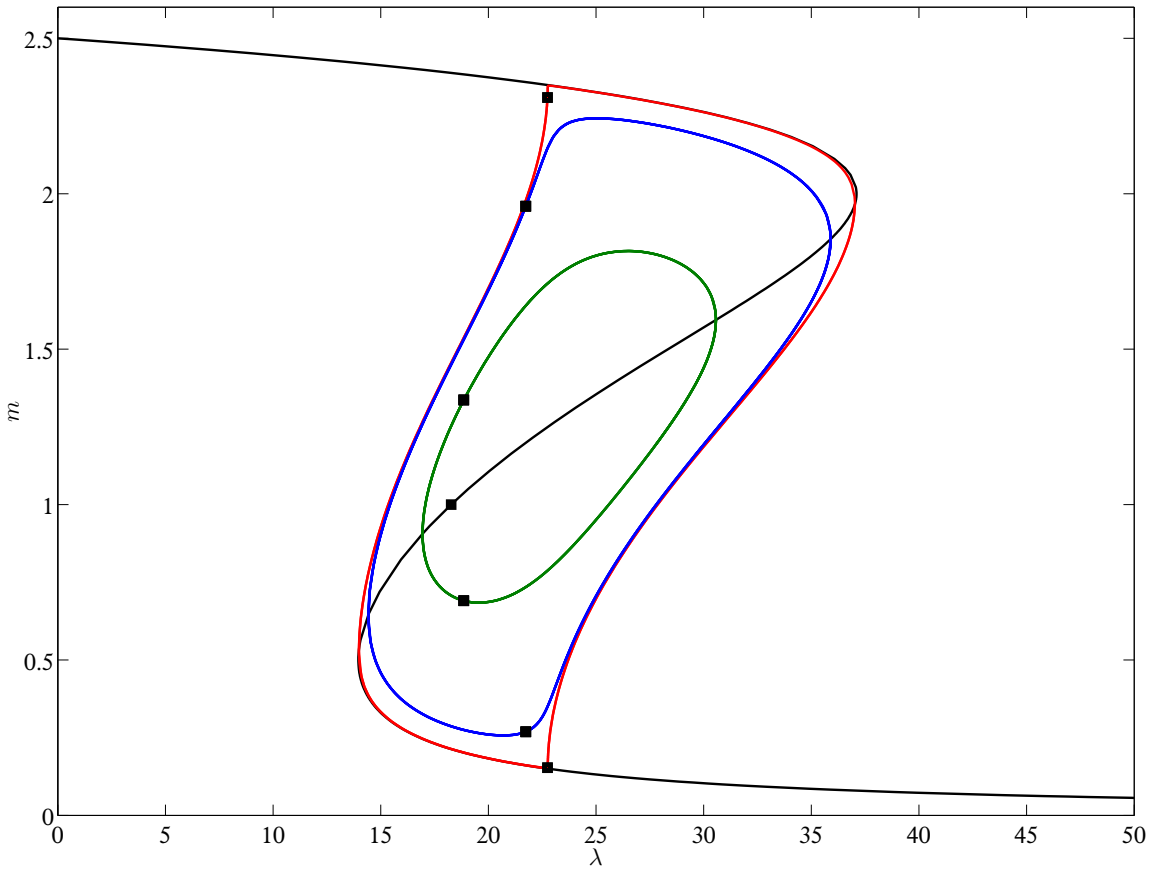


Figure 4.2: Bifurcation diagram for (4.6) computed using AUTO 07p. Steady state solutions of (4.1) as functions of $\lambda$. The solution measure is its value at the left boundary $x = 0$. Shown are uniform solutions (black curve); $1-$step solutions (red curve); $2-$step solutions (blue curve); $3-$step solutions (green curve). Black squares mark the points where the integral of the solution equals one. Parameter values used: $\gamma = 2.5, \chi = 25, D = 10, \Gamma = 0.005$.

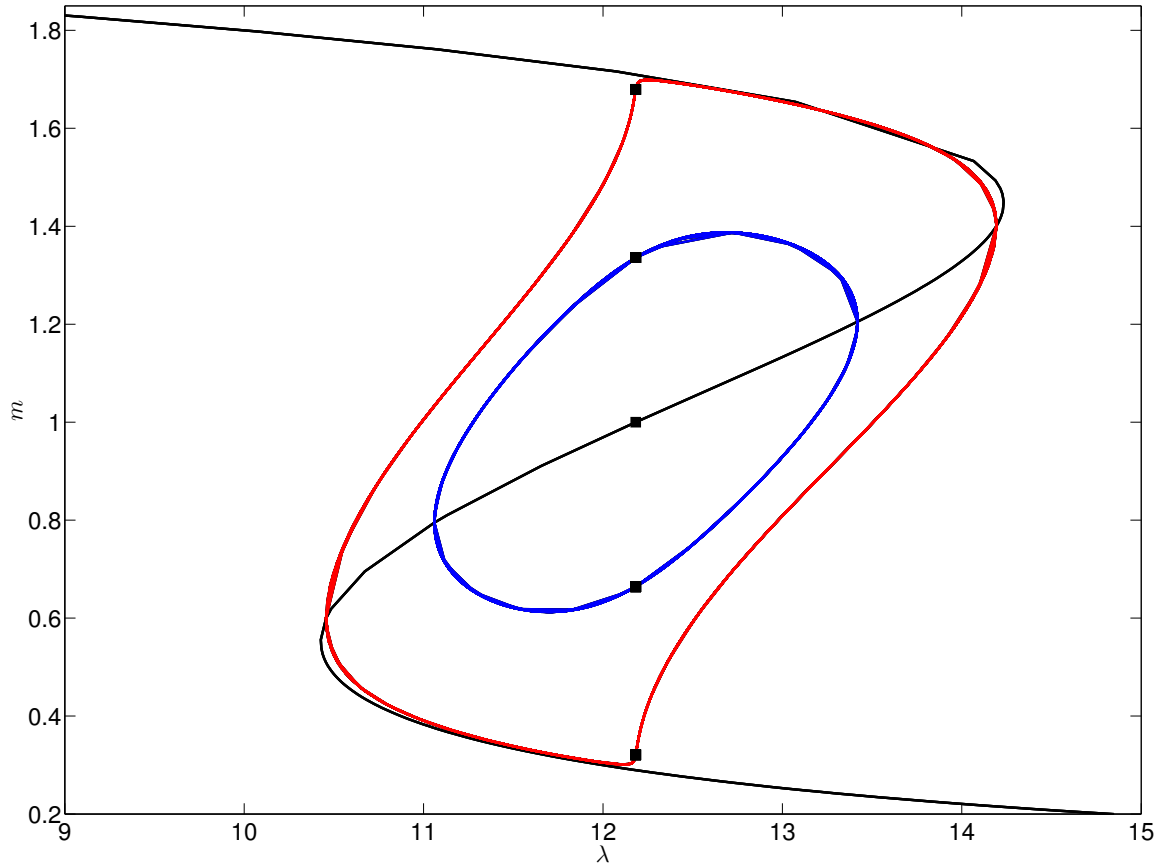


Figure 4.3: Bifurcation diagram for (4.6) computed using `AUTO 07p`. Steady state solutions of (4.1) as functions of $\lambda$. The solution measure is its value at the left boundary $x = 0$. Shown are uniform solutions (black curve); $1-$step solutions (red curve); $2-$step solutions (blue curve). Note that $3-$step solutions do not exist for this set of parameter values. Black squares mark the points where the integral of the solution equals one and are obtained for the single value $\lambda = \lambda(1) = \exp(2.5)$ (see text). Parameter values used: $\gamma = 2, \chi = 25, D = 10, \Gamma = 0.005$.

### 4.2.2 Asymptotic States of the Initial-Boundary Value Problem

Recall that we are interested in steady states of system (4.1). The scaling used in defining this system combined with the conservation of mass property discussed above,

ensures that relevant (asymptotic) steady states must satisfy

$$\int_\Omega n(x)dx = \int_\Omega c(x)dx = |\Omega|. \tag{4.12}$$

Figure 4.2 shows the solution set for a typical set of system parameters and $\Omega = (0,1)$. Here, solutions that satisfy (4.12) are marked. It is seen that in general, we cannot expect that a fixed value of $\lambda$ ensures that all solutions satisfy this integral condition. [Indeed, it is not even guaranteed that any non-trivial solution exists for a given value of $\lambda$.] However, in the special case $\gamma = 2$, the symmetry point of the set $M_b$ is given by $(m,\lambda) = (1,\Lambda_2)$ with $\Lambda_2 = \exp\left(\frac{\chi}{D}\right)$. In this case, the uniform steady state $(c,\lambda) = (1,\Lambda_2)$ satisfies (4.12). Moreover, as can be seen from Figure 4.3, all non-trivial solutions $(c(x),\Lambda_2)$ also satisfy (4.12). This special case was mentioned in [106] but without further discussion. Here, we see that this special case arises from a symmetry of the set $M$ and this single value of $\lambda$, provides all possible heterogeneous steady states for system (4.1) satisfying (4.12). We will discuss this case below in more detail. [Note, there is nothing special about the value $m = 1$ here. What is important is that the homogeneous solution has value $m = \gamma/2$. Thus, if the scaling was such that in the right hand side of the integral condition (4.12), $|\Omega|$ was replaced with $K|\Omega|$ for some positive constant $K$, then the critical value of $\gamma = 2K$. ]

### 4.2.3 Existence of $p$-Step Steady State Solutions for Fixed $\lambda$

In the case $\Omega \subset \mathbb{R}$, system (4.6) reduces to a system of ordinary differential equations. This structure can be exploited to give a fuller description of the solution set. Following Grindrod et al., [49], we now present an analysis of the phase portrait of the steady state system. For $\Omega \subset \mathbb{R}$, the rescaling discussed above (see (3.12)) allows us to consider $\Omega = (0,1)$ without loss of generality. In this case, all solutions of (4.6) must satisfy the following system:

$$
\begin{aligned}
D\frac{d^2n}{dx^2} - \frac{d}{dx}\left(\chi n(1-n/\gamma)\frac{dc}{dx}\right) &= 0, && (4.13)\\
\Gamma\frac{d^2c}{dx^2} + n - c &= 0, && (4.14)\\
\frac{d}{dx}n(x) = \frac{d}{dx}c(x) = 0 \quad \text{at} \quad x &= 0,1. && (4.15)
\end{aligned}
$$

Following the general arguments detailed above, on integrating with respect to $x$ and using the boundary conditions (4.15) yields the single equation

$$
\Gamma\frac{d^2c}{dx^2} + \frac{\gamma}{1+\lambda\exp(\frac{-\chi c(x)}{D})} - c = 0 \tag{4.16}
$$

with $n(x)$ determined by

$$
n(x) = \frac{\gamma}{1+\lambda\exp(\frac{-\chi c(x)}{D})}. \tag{4.17}
$$

The scaling requires that we are only interested in solutions $(n,c)$ that satisfy (4.12) with $|\Omega| = 1$. In this case, the eigenvalue-eignenfunction pairs are $(\mu_j, \omega_j) = (j^2\pi^2\Gamma, \cos(\sqrt{\mu_j}x))$.

By setting $\frac{dc}{dx} = w$ we can re-write (4.16) as the first order system:

$$
\begin{aligned}
\frac{dc}{dx} &= w,\\
\Gamma\frac{dw}{dx} &= c - \frac{\gamma}{1+\lambda\exp(-\frac{\chi c}{D})} = -f_\lambda(c), && (4.18)
\end{aligned}
$$

where $f_\lambda(\cdot) \equiv f(\cdot,\lambda)$ as defined above. Non-trivial (heterogeneous) solutions of (4.13)-(4.15) are therefore represented by trajectories in the phase plane of system (4.18)

(along with (4.17)). Relevant trajectories must intersect with the $c-$axis at points for which $c > 0$. Moreover, the scaling demands that the "total transit time" for these trajectories must be one. In order to ascertain whether such trajectories exist, we consider the phase plane in more detail.

Fixed points of system (4.18) occur when $c \equiv m$ for constants $m$ where $f(m,\lambda) = 0$. The structure of the set $f = 0$ was discussed above. Hence, provided (4.10) holds then for each fixed value of $\lambda$ such that $\lambda_- < \lambda < \lambda_+$, $f(\cdot,\lambda) = 0$ has three solutions $\underline{m} < m_0 < \overline{m}$. For $\lambda = \lambda_{-,+}$ there are two solutions and for $\lambda \notin [\lambda_-,\lambda_+]$ there is only one solution. For $\lambda \in (\lambda_-,\lambda_+)$, $\partial_1 f(m_0,\lambda) > 0$ and hence a standard linear stability analysis reveals that $(c,w) = (m_0,0)$ is a centre for system (4.18) (and similarly that $(c,w) = (\overline{m},0),(\underline{m},0)$ are saddles). Hence, the phase plane of (4.18) contains an infinity of closed orbits centred on $(m_0,0)$. The stable and unstable manifolds of the saddle points at $(\underline{m},0)$ and $(\overline{m},0)$ enclose these closed orbits (see Figure 4.4). Each of these closed orbits, or part of them, potentially generates a non-trivial solution of (4.13)-(4.15). However, two points must be verified: (i) the centre $(m_0,0)$ represents a constant solution of (4.13)-(4.15) and with the adopted scaling this centre must therefore be $(1,0)$; (ii) as detailed above, all relevant non-trivial trajectories must have a total transit time of one. For (i) to hold, from (4.9) we must set $\lambda = \lambda(1) = (\gamma-1)\exp\left(\frac{\chi}{D}\right)$. That $(1,0)$ is a centre is equivalent to $\partial_1 f(1,\lambda(1)) > 0$. After a little algebra, it can be shown that this condition holds provided

$$\frac{\chi}{D} > \frac{1}{1-\frac{1}{\gamma}}. \tag{4.19}$$

As shown in Figure 4.2, (ii) does not hold in general, but as we will now show does hold in the special case $\gamma = 2m_0 = 2$.

### 4.2.4 Symmetry of the Phase Plane

The symmetry of the phase plane and its relation to relevant $p-$step solutions of system (4.13)-(4.15) is best discussed by considering the Hamiltonian associated with (4.18), namely,

$$H(c,w) = \Gamma\frac{w^2}{2} + \frac{D\gamma}{\chi}\ln\left(\lambda + \exp\left(\frac{\chi c}{D}\right)\right) - \frac{c^2}{2} = \text{Constant.} \tag{4.20}$$

The level sets of $H$ form the trajectories in the phase plane as shown in Figure 4.4. It is clear that $H$ is symmetric in $w$. This symmetry ensures that $p-$step solutions to (4.13)-(4.15) are represented by trajectories in the phase plane that connect points $(c,w) = (C_0,0)$ to $(C_1,0)$, where $C_0$ may equal $C_1$. For example, and referring to Figure 4.4, $1-$, $2-$ and $3-$step solutions would be represented by paths of the form $AB$, $ABA$ and $ABAB$, respectively. Note that in the special case $\gamma = 2$, it can be shown that $H$ is also symmetric about $c = 1$. That is solutions of (4.16) satisfy either $c(x) = 2 - c(1-x)$ or $c(x) = c(1-x)$ for odd and even $p$ respectively. From (4.17) symmetry of $c(x)$ implies symmetry of $n(x)$.

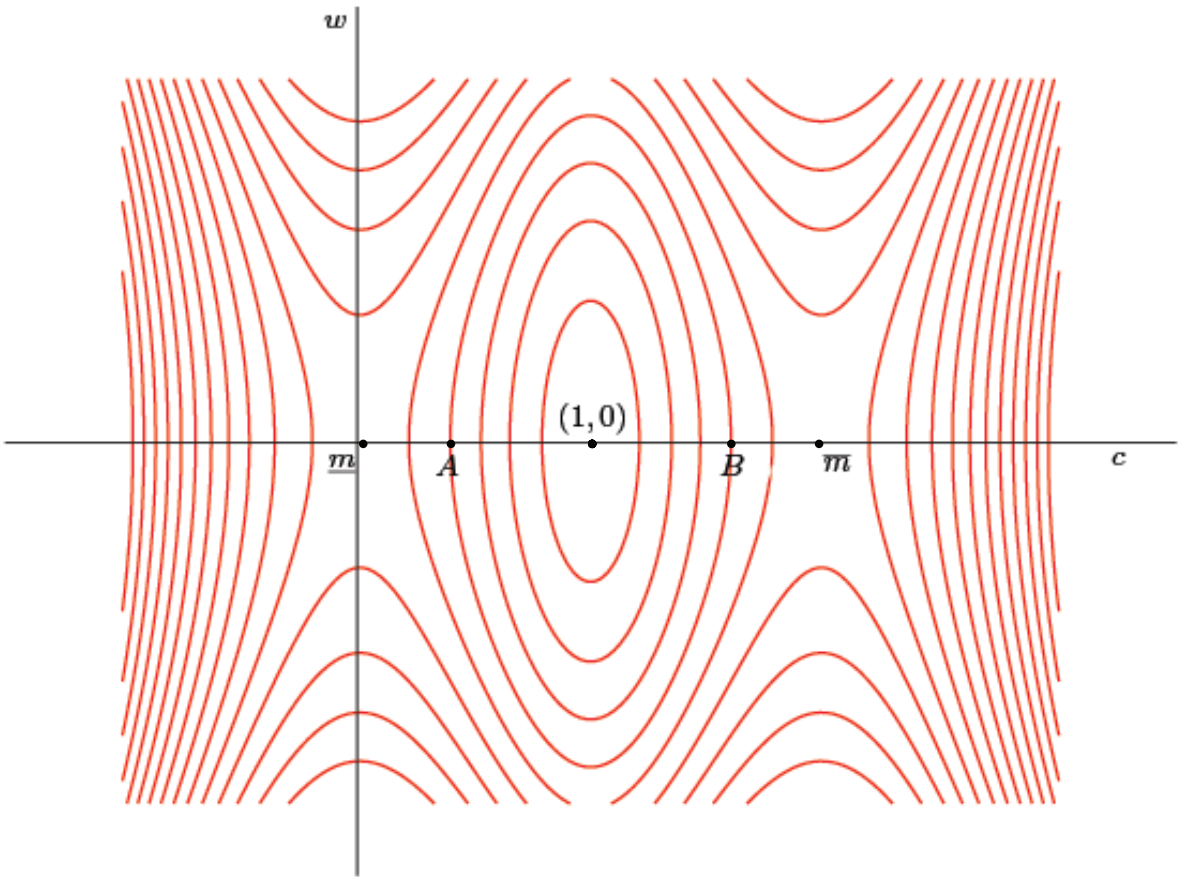


Figure 4.4: Contour plot of $H(c,w)$ given in (4.20). $A$ and $B$ mark the points that a given orbit intersects the $c$-axis. In the case $\gamma = 2$, the phase portrait is symmetric about both the $c$-axis and about $c = 1$. Parameter values : $\chi = 50, D = 10, \gamma = 2, \Gamma = 0.004$.

Following [106], a lower bound for the transit time around the phase plane trajectories can be obtained by an inspection of the system close the centre $(1,0)$. Here, solutions of (4.18) are given approximately by

$$c(x) = A\cos\left(\frac{1}{\sqrt{\Gamma}}\sqrt{\partial_1 f(1,\lambda(1))}\,x\right).$$

Thus the minimum transit time of an orbit $AB$ is

$$T_{\min} := \frac{\pi\sqrt{\Gamma}}{\sqrt{\partial_1 f(1,\lambda(1))}} = \frac{\pi\sqrt{\Gamma}}{\sqrt{\frac{\chi(\gamma-1)}{D\gamma}-1}}.$$

Moreover, it follows directly from the structure of the phase plane that the transit time for orbits of the form $AB$ tends to infinity as $A$ (resp. $B$) approaches the saddle point at $(\underline{m},0)$ (resp. $(\overline{m},0)$). Therefore a phase plane trajectory that corresponds to a $p-$step solution exists if and only if $T_{\min} \leq \frac{1}{p}$ i.e.

$$\frac{\pi\sqrt{\Gamma}}{\sqrt{\frac{\chi(\gamma-1)}{D\gamma}-1}} \leq \frac{1}{p}. \tag{4.21}$$

Now, from (4.11) and Theorem 4.2.1, it follows that $p-$step solutions of (4.13)-(4.15) exist for all $p$ that satisfy $\Gamma p^2\pi^2 < \max \partial_1 f = \frac{\gamma}{4}\frac{\chi}{D} - 1$, i.e.

$$\frac{\pi\sqrt{\Gamma}}{\sqrt{\frac{\gamma}{4}\frac{\chi}{D}-1}} < \frac{1}{p}. \tag{4.22}$$

We can guarantee that both (4.21) and (4.22) are satisfied simultaneously if $\gamma = 2$. Hence, for $\lambda$ fixed, $\lambda = \lambda(1)$, phase plane trajectories can be found that represent all possible $p-$step solutions if $\gamma = 2$. Otherwise, for $\lambda$ fixed, the phase plane trajectories may only represent some or even none of the desired solutions.

## 4.3 Stability

We now consider the stability of the steady state solutions of (4.1) - (4.2). It is simplest to attack the system directly. First, we note some details of the linear stability of homogeneous steady states. As noted previously, the scaling chosen here means that there is only one relevant uniform steady state, $(n,c) = (1,1)$.

### 4.3.1 Stability of the Homogeneous Steady State

By setting $n = 1 + \hat{n}$ and $c = 1 + \hat{c}$, with $\hat{n}$ and $\hat{c}$ assumed to be small ($\ll 1$) and substituting these expressions into (4.1) leads to the following system:

$$\begin{aligned} \frac{\partial \hat{n}}{\partial t} &= \Gamma \nabla \cdot \left[ D \nabla \hat{n} - \chi \left( 1 - \frac{1}{\gamma} \right) \nabla \hat{c} \right], \quad x \in \Omega, t > 0 \\ \frac{\partial \hat{c}}{\partial t} &= \Gamma \Delta \hat{c} + \hat{n} - \hat{c}, \\ \frac{\partial \hat{n}}{\partial \nu} &= \frac{\partial \hat{c}}{\partial \nu} = 0 \quad \text{on} \in \partial\Omega, t > 0. \end{aligned} \tag{4.23}$$

Given the conservation arguments detailed above, and as noted in [110], we only consider zero-mass perturbations. (Otherwise, we would be considering the different problem of adding cells to the system. This would of course result in a different homogeneous steady state.) Thus we seek solutions of the form $\hat{n}, \hat{c} \propto \sum_{j=1}^{\infty} e^{\alpha t} \omega_j(x)$, with $\omega_j$ as defined above. Substituting these expressions into (4.23) yields the following eigenvalue problem and its characteristic equation:

$$\begin{bmatrix} \alpha + D\mu_j & -\mu_j \chi \left( 1 - \frac{1}{\gamma} \right) \\ -1 & \alpha + \mu_j + 1 \end{bmatrix} \begin{bmatrix} \hat{n} \\ \hat{c} \end{bmatrix} = 0;$$

$$\alpha^2 + \alpha \left( \mu_j (1 + D) + 1 \right) + \mu_j \left( D \left( \mu_j + 1 \right) - \chi \left( 1 - \frac{1}{\gamma} \right) \right) = 0.$$

This has solutions:

$$\alpha_{\pm}^{j} = \frac{1}{2}\left[ -\left(\mu_j(1+D)+1\right) \pm \sqrt{\left(\mu_j(1+D)+1\right)^2 - 4\mu_j\left(D\left(\mu_j+1\right) - \chi\left(1-\frac{1}{\gamma}\right)\right)} \right]. \tag{4.24}$$

Hence, the perturbations $(\hat{n},\hat{c})$ grow if $Re(\alpha) > 0$ for any $\alpha$ given by (4.24) and conversely, the steady state $(n,c) = (1,1)$ is stable if $Re(\alpha) < 0$ for all $\alpha$. A necessary and sufficient condition instability is therefore

$$\mu_j\left(D\left(\mu_j+1\right) - \chi\left(1-\frac{1}{\gamma}\right)\right) < 0,$$

i.e.

$$0 < \mu_j < \left(\frac{\chi}{D}\left(1-\frac{1}{\gamma}\right) - 1\right), \tag{4.25}$$

for some $j = 1,2,...$ etc. For (4.25) to hold for any $j$, requires

$$\left(1-\frac{1}{\gamma}\right)\frac{\chi}{D} > 1. \tag{4.26}$$

Note that this is exactly (4.19), i.e. the necessary conditions for instability of the uniform steady state and the existence of non-uniform steady states are identical. If (4.26) is violated, then all the eigenvalues $\alpha_{\pm}^{j}$ have a negative real part and the homogeneous steady state is stable and moreover, no non-uniform steady state solutions exist. If (4.26) is satisfied, then it follows that large eigenvalues, $\mu_j$, will not contribute to growing perturbations and hence any instability will be manifest through low wave

number modes. Note that in general, system parameters could be chosen so that

$$\left(1-\frac{1}{\gamma}\right)\frac{\chi}{D}-1<\mu_j<\frac{\gamma}{4}\frac{\chi}{D}-1, \quad j=1,2,..p$$

in which case, combining the bifurcation results in Lemma 4.2.2 with the above conditions on stability, indicates that bifurcation can occur from the branch of uniform steady states at the point $(n,c)=(1,1)$ but the uniform steady state is stable. This indicates that the bifurcation is subcritical (to an unstable non-trivial solution). Note, that when $\gamma=2$, the left and right hand sides of the above inequalities are equal and hence in this case, if bifurcation does occur, it is associated with a loss of stability of the homogeneous steady state.

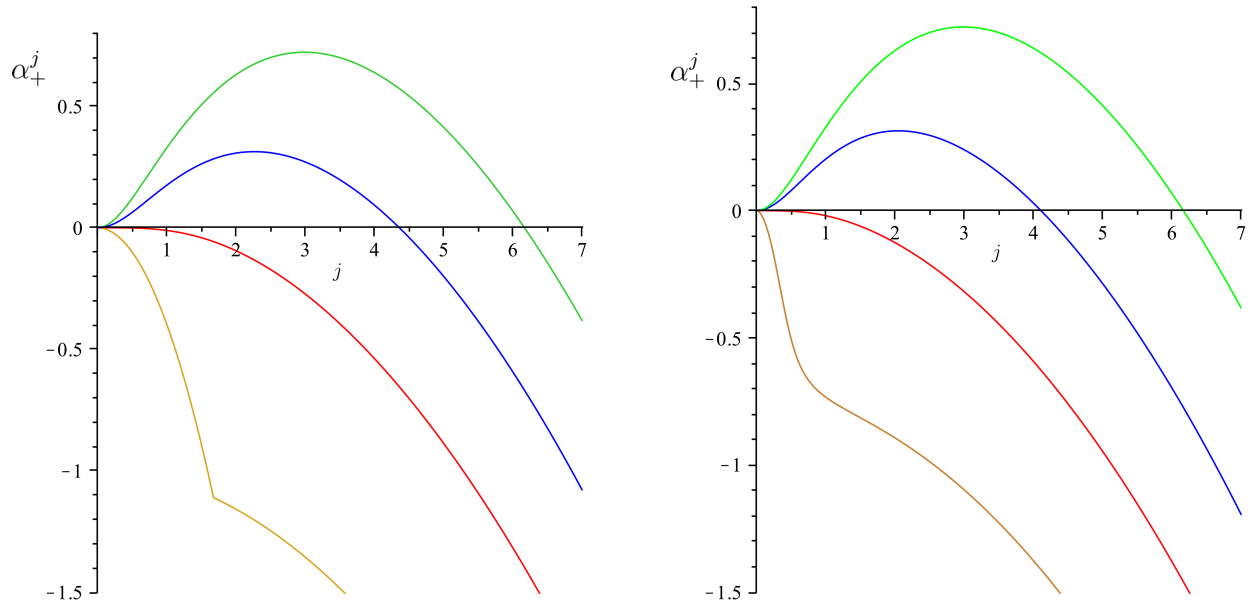


Figure 4.5: Plot of the positive eigenvalue, $\alpha_+^j$, from (4.24) as a function of the wavenumber, $j$. Left: Plot of $\alpha_+^j$ with $\chi=50$ (green), 35 (blue), 20 (red) and 0 (gold). Right: Plot of $\alpha_+^j$ with $D=10$ (green), 15 (blue), 25 (red) and 100 (gold). Other parameter values: $\gamma=2$ and $\Gamma=0.004$.

For $\Omega=(0,1)$, $\mu_j=j^2\pi^2\Gamma$, a plot of $\alpha_+$ as a function of $j$ is shown in Figure 4.5 for range of system parameters. The values of $j$ for which $\alpha_+>0$ are predicted by

the theory to represent growing (unstable) modes. Shown in red are the plots of $\alpha_+$ when $\chi$ and $D$ are on the cusp of violating condition 4.26 and therefore $\mu_+ \leq 0$ for all $j > 0$. An increase in the ratio $\frac{\chi}{D}$ leads to $(1,1)$ becoming unstable to a greater range of wavenumbers. This formalises the intuitive reasoning that the greater the strength of the chemotactic response in relation to diffusion, the faster the autocatalytic cell recruitment takes place and thus more peaks will be formed. The same intuitive reasoning holds on increasing the domain length, represented here by $\Gamma$. Note that $j = 0$ always satisfies (4.25) and has associated eigenvalues -1 and 0. Any uniform perturbation of $(1,1)$ merely translates solutions along the line of constant steady states - this represents a non-zero mass perturbation and as noted above is therefore outwith our interest.

### 4.3.2 Numerical Solutions

In all that follows, we focus on the case $\Omega = (0,1)$ and hence consider the system

$$\left.\begin{aligned} \frac{\partial n}{\partial t} &= \Gamma\left[D\frac{\partial^2 n}{\partial x^2} - \chi\frac{\partial}{\partial x}\left(n\left(1-\frac{n}{\gamma}\right)\frac{\partial c}{\partial x}\right)\right], \\ \frac{\partial c}{\partial t} &= \Gamma\frac{\partial^2 c}{\partial x^2} + n - c, \\ \frac{\partial n}{\partial x} &= \frac{\partial c}{\partial x} = 0 \quad \text{at } x = 0,1, \end{aligned}\right\} \quad x \in (0,1), \tag{4.27}$$

The linear theory outlined above only indicates the fastest growing modes. By solving system (4.27) numerically we can track how these modes develop as solutions of the full system. Figure 4.6 shows numerical simulations of (4.27) generated using the well-known solver `pdepe` in `MATLAB`. The initial data used was a small random perturbation of the homogeneous solution $(1,1)$. As seen in the top figures, the initial number

of peaks corresponds to the fastest growing mode as predicted by the linear analysis ($j = 3$ for the parameters used). This mode-3 solution appears at first sight to be a stable state, but an integration over longer times reveals that that this is not the case. Indeed, as illustrated in the bottom set of figures, this mode-3 solution drifts over a much longer time scale than the initial pattern formation to form after a very long time a mode-1 solution. This "metastable" behaviour will be discussed further in the next section.

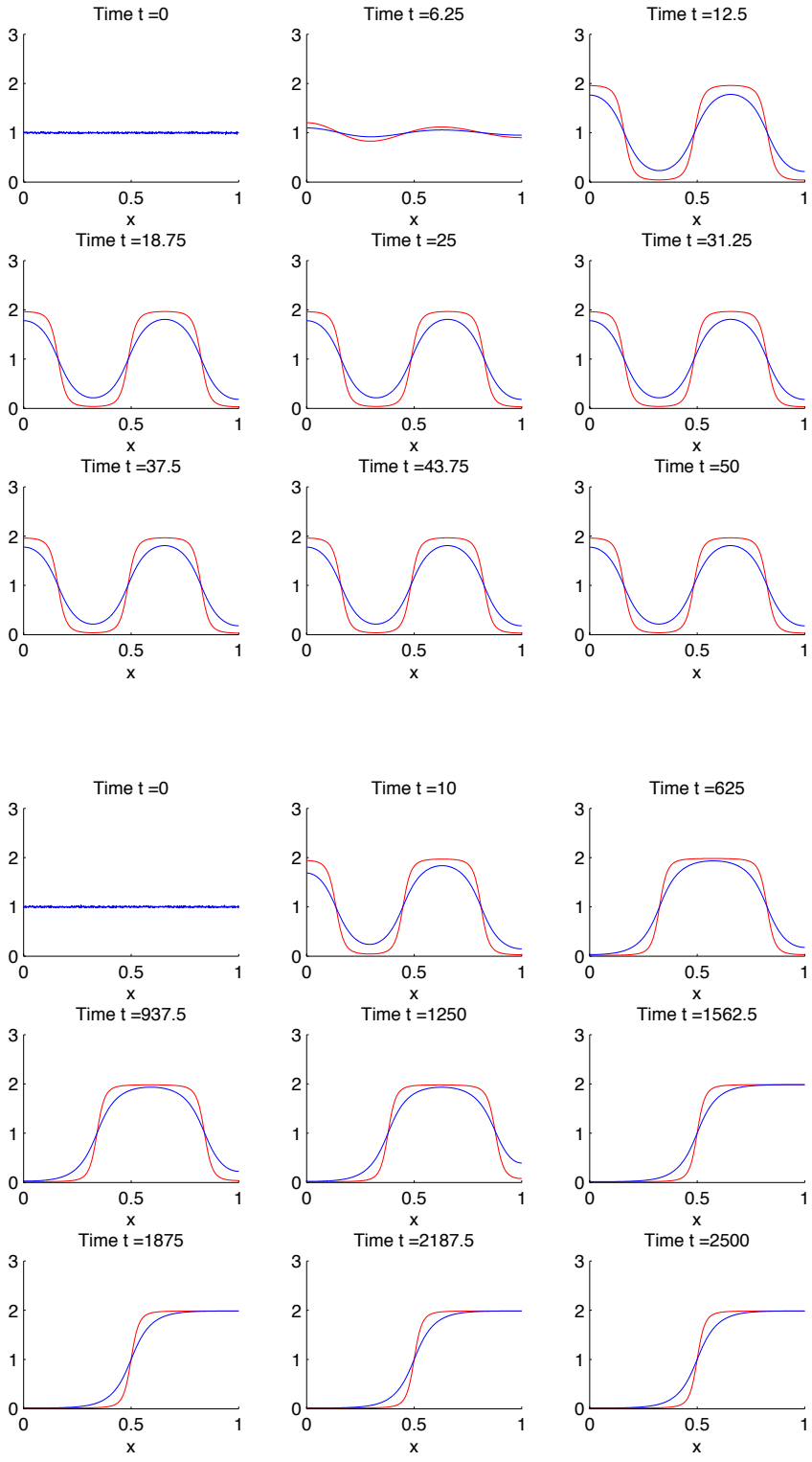


Figure 4.6: Plots of cell density, $n$ (red), and chemoattractant density, $c$ (blue), solutions to (4.1) in 1-D. Top: Initial pattern formation showing the k=3 mode to be the fastest growing. Bottom: Evolution of patterns over longer times. Parameter values: $\chi = 50, D = 10, \gamma = 2$ and $\Gamma = 0.004$.

### 4.3.3 Stability of Non-Homogeneous Steady States

We now investigate the linear stability of $p$-step steady states by formulating an associated eigenvalue problem. Similar calculations were done in [106] using a different scaling. Here, we present an alternative analysis.

To analyse the stability of non-homogeneous steady states we linearise in the usual way: let $(\bar{n}(x), \bar{c}(x))$ represent a nonuniform steady state of (4.27) and set $n(x,t) = \bar{n}(x) + \hat{n}(x,t), c(x,t) = \bar{c}(x) + \hat{c}(x,t)$ with $\hat{n}(x,t) = \hat{n}(x)e^{\nu t}, \hat{c}(x,t) = \hat{c}(x)e^{\nu t}$. Substituting these expressions into (4.27) and equating terms to first order yields the following system:

$$\begin{aligned} \hat{n}_t &= \Gamma\left[D\hat{n}_{xx} - \chi\left(R_x\hat{c}_x + R\hat{c}_{xx} + S_x\hat{n} + S\hat{n}_x\right)\right], \\ \hat{c}_t &= \Gamma\hat{c}_{xx} + \hat{n} - \hat{c}, \end{aligned} \tag{4.28}$$

where $\bar{n}(1-\bar{n}/\gamma) =: R(x)$ and $\bar{c}_x(1-2\bar{n}/\gamma) =: S(x)$. In matrix-vector form, this becomes

$$\begin{bmatrix} \hat{n}_t \\ \hat{c}_t \end{bmatrix} = \begin{bmatrix} \Gamma\left(D\frac{\partial^2}{\partial x^2} - \chi(S_x + S\frac{\partial}{\partial x})\right) & -\chi\Gamma\left(R\frac{\partial^2}{\partial x^2} + R_x\frac{\partial}{\partial x}\right) \\ 1 & \Gamma\frac{\partial^2}{\partial x^2} - 1 \end{bmatrix} \begin{bmatrix} \hat{n} \\ \hat{c} \end{bmatrix}. \tag{4.29}$$

We make a standard assumption that we may write $\hat{n} = e^{\nu t}\sum_{j=1}^{\infty} a_j \cos(j\pi x)$ and $\hat{c} = e^{\nu t}\sum_{j=1}^{\infty} b_j \cos(j\pi x)$. After multiplying equation (4.29) by $\cos(i\pi x)$ and integrating between 0 and 1, we have

$$
\begin{aligned}
\nu \quad & \begin{bmatrix} a_i \\ b_i \end{bmatrix} = \begin{bmatrix} \Gamma(-2N_i - D\mu_i) & \Gamma(2M_i) \\ 1 & -(\Gamma\mu_i + 1) \end{bmatrix} \begin{bmatrix} a_i \\ b_i \end{bmatrix} \\
+ \quad & \Gamma \begin{bmatrix} 2\sum_{j\neq i}^{\infty} \int_0^1 \cos(i\pi x) \left\{ \chi \cos(j\pi x)(-S_x a_j + R\mu_j b_j) + \chi \sin(j\pi x)(Sj\pi a_j + R_x j\pi b_j) \right\} dx \\ 0 \end{bmatrix},
\end{aligned}
\tag{4.30}
$$

where

$$
\begin{aligned}
N_i &:= \chi \int_0^1 S_x \cos^2(i\pi x) - S\frac{i\pi}{2} \sin(2i\pi x) dx, \\
M_i &:= \chi \int_0^1 R\mu_i \cos^2(i\pi x) + R_x \frac{i\pi}{2} \sin(2i\pi x) dx,
\end{aligned}
\tag{4.31}
$$

for $i = 1, 2, 3$ etc. and for ease of notation we reset $\mu_i = i^2\pi^2$. A crucial point to note here is that, as we are linearising around a non-homogeneous steady state, the values of the coefficients $a_i, b_i$ not only depend on $i$ but also on all values of $a_j, b_j$ for $j \neq i$. To deal with this non-locality and make progress, we re-write the non-local terms on the right-hand side of (4.30) as:

$$
\begin{aligned}
2 \quad & \Gamma\chi \sum_{j\neq i}^{\infty} \int_0^1 \cos(i\pi x) \left\{ \cos(j\pi x)(-S_x a_j + R\mu_j b_j) + \sin(j\pi x)(Sj\pi a_j + R_x j\pi b_j) \right\} dx \\
= \quad & 2\Gamma\chi \left[ -a_1 K_{i1} + b_1 H_{i1} - \ldots - a_j K_{ij} + b_j H_{ij} \right] \\
= \quad & 2\Gamma\chi \sum_{j\neq i}^{\infty} -a_j K_{ij} + b_j H_{ij},
\end{aligned}
\tag{4.32}
$$

where

$$
\begin{aligned}
K_{ij} &:= \int_0^1 \cos(i\pi x)\{\cos(j\pi x)S_x - \sin(j\pi x)Sj\pi\}dx, \\
H_{ij} &:= \int_0^1 \cos(i\pi x)\{\cos(j\pi x)R\mu_j + \sin(j\pi x)R_x j\pi\}dx.
\end{aligned} \tag{4.33}
$$

We can therefore formulate (4.30) as an eigenvalue problem in block form:

$$
\nu \begin{bmatrix} \mathbf{a}_1 \\ \mathbf{a}_2 \\ \mathbf{a}_3 \\ \mathbf{a}_4 \\ \mathbf{a}_5 \\ \dots \end{bmatrix} = \begin{bmatrix} A_1 & B_{12} & B_{13} & B_{14} & B_{15} \\ B_{21} & A_2 & B_{13} & B_{14} & B_{15} \\ B_{31} & B_{12} & A_3 & B_{14} & B_{15} \\ B_{41} & B_{12} & B_{13} & A_4 & B_{15} \\ B_{51} & B_{12} & B_{13} & B_{14} & A_5 \end{bmatrix} \begin{bmatrix} \mathbf{a}_1 \\ \mathbf{a}_2 \\ \mathbf{a}_3 \\ \mathbf{a}_4 \\ \mathbf{a}_5 \\ \dots \end{bmatrix}, \tag{4.34}
$$

where

$$
\mathbf{a}_i = \begin{bmatrix} a_i \\ b_i \end{bmatrix}, \quad A_i = \begin{bmatrix} -\Gamma(2N_i + D\mu_i) & 2\Gamma(M_i) \\ 1 & -(\Gamma\mu_i + 1) \end{bmatrix}, \quad B_{ij} = 2\Gamma\chi \begin{bmatrix} -K_{ij} & H_{ij} \\ 0 & 0 \end{bmatrix}. \tag{4.35}
$$

The $A_i$ and $B_{ij}$ blocks represent the local and non-local terms in (4.30), respectively. We will refer to the large block matrix in (4.34) as $Q$ from now on. This is an infinitely large system and so $Q$ should properly be thought of as an operator on an appropriate sequence space. (The formal setup would be $Q : D(Q) \subset l^2(\mathbf{R}) \to l^2(\mathbf{R})$.) However, for computational purposes, we make the reasonable assumption that a finite dimensional approximation will contain all relevant information as will be discussed later. Furthermore, it is possible to simplify the problem and make progress by again considering the

special case $\gamma = 2$ for which the steady states of (4.1) are symmetric. The symmetry of $n$ and $c$ implies that the related functions, $R(x)$ and $S(x)$ are also symmetric.

With $\gamma = 2$, recall that steady states are either odd or even about $x = \frac{1}{2}$, depending on the value of $p$. The consequences of these properties as well as the orthogonality of the sine and cosine functions are summarised in Table 4.1.

| Function | even $j$, odd $i$ | odd $j$, even $i$ |
|---|---|---|
| $K_{ij}$ | $\int_0^1 odd*(even*even-odd*odd)\ dx = 0$ | $\int_0^1 even*(odd*even-even*odd)\ dx = 0$ |
| $H_{ij}$ | $\int_0^1 odd*(even*even-odd*odd)\ dx = 0$ | $\int_0^1 even*(even*odd+even*odd)\ dx = 0$ |

| Function | even $j,i$ | odd $j,i$ |
|---|---|---|
| $K_{ij}$ | $\int_0^1 even*(even*even-even*odd)\ dx \neq 0$ | $\int_0^1 odd*(odd*even-even*odd)\ dx \neq 0$ |
| $H_{ij}$ | $\int_0^1 even*(even*even+odd*odd)\ dx \neq 0$ | $\int_0^1 odd*(even*odd+even*odd)\ dx \neq 0$ |

| Function | even $i$ | odd $i$ |
|---|---|---|
| $N_i$ | $\int_0^1 even*even^2-odd*odd\ dx \neq 0$ | $\int_0^1 even*(odd^2)-odd*odd\ dx \neq 0$ |
| $M_i$ | $\int_0^1 even*(even^2)+odd*odd\ dx \neq 0$ | $\int_0^1 even(odd*odd)+odd*odd\ dx \neq 0$ |

Table 4.1: Orthogonality of $H_{ij}, K_{ij}, N_i$ and $M_i$ functions for $\gamma = 2$. Components of the integrands are in the same order as in the original function definitions given in (4.31) and (4.33).

The results in Table 4.1 allow a simplification of the eigenvalue problem (4.34) as several blocks become zero and thus we have

$$\nu \begin{bmatrix} \mathbf{a_1} \\ \mathbf{a_2} \\ \mathbf{a_3} \\ \mathbf{a_4} \\ \mathbf{a_5} \\ \dots \end{bmatrix} = \begin{bmatrix} A_1 & 0 & B_{13} & 0 & B_{15} & \dots \\ 0 & A_2 & 0 & B_{24} & 0 & \dots \\ B_{31} & 0 & A_3 & 0 & B_{35} & \dots \\ 0 & B_{42} & 0 & A_4 & 0 & \dots \\ B_{51} & 0 & B_{53} & 0 & A_5 & \dots \\ \dots & \dots & \dots & \dots & \dots & \dots \end{bmatrix} \begin{bmatrix} \mathbf{a_1} \\ \mathbf{a_2} \\ \mathbf{a_3} \\ \mathbf{a_4} \\ \mathbf{a_5} \\ \dots \end{bmatrix}. \tag{4.36}$$

Although simpler in structure, (4.36) is still an infinitely large system and so we need to determine whether or not the eigenvalues of a truncated $Q$ are useful in determining stability. To do this we re-examine the functions contained in the blocks $A_i$ and $B_{ij}$.

As suggested by the results in Figure 4.7, it appears that as $i \to \infty$, $N_i \to 0$ in an oscillatory manner and $M_i \to \infty$. Thus the entries on the diagonal of $A_i$, and hence on the diagonal of $Q$, will be dominated by the $\mu_i = O(i^2)$ terms, when $i$ is large. The patterns for $H$ and $K$ are more complicated but it can be seen in Figure 4.8 that both functions generally increase in magnitude with $i$ and $j$.

For a typical set of parameters, using the arguments detailed above, it can be shown that $p_{\max} = 6$. This is illustrated numerically and, for reference, Figure 4.9 shows the symmetry of $n(x)$ and $c(x)$ for $p = 1..6$. These solutions were obtained using the well-known `BVP4C` solver for system (4.6) in `MATLAB`.

We are interested in the conditions that ensure the steady states are unstable and hence seek positive eigenvalues of $Q$. The above results regarding $A_i$ and $B_{ij}$ strongly suggest that if positive eigenvalues exist then they must come from the top-left corner of $Q$, where $i$ and $j$ are both small. Thus we reasonably restrict our attention accordingly to this component of $Q$ for all the subsequent computations. Using `MATLAB`, we can build a finite truncation of the matrix $Q$ and calculate its eigenvalues numerically for various $p$-step solutions (see Appendix 7.1.2-7.1.4 for code). Using the default parameter values, $\chi = 50, D = 10, \gamma = 2$ and $\Gamma = 0.004$, examples of the matrix $Q$ are given for 1,2 and 3-step solutions below. To calculate eigenvalues, a 200 by 200 approximation of $Q$ was used, which we found to be sufficient. That is, increasing this size further did not impact the eigenvalues in any significant way.

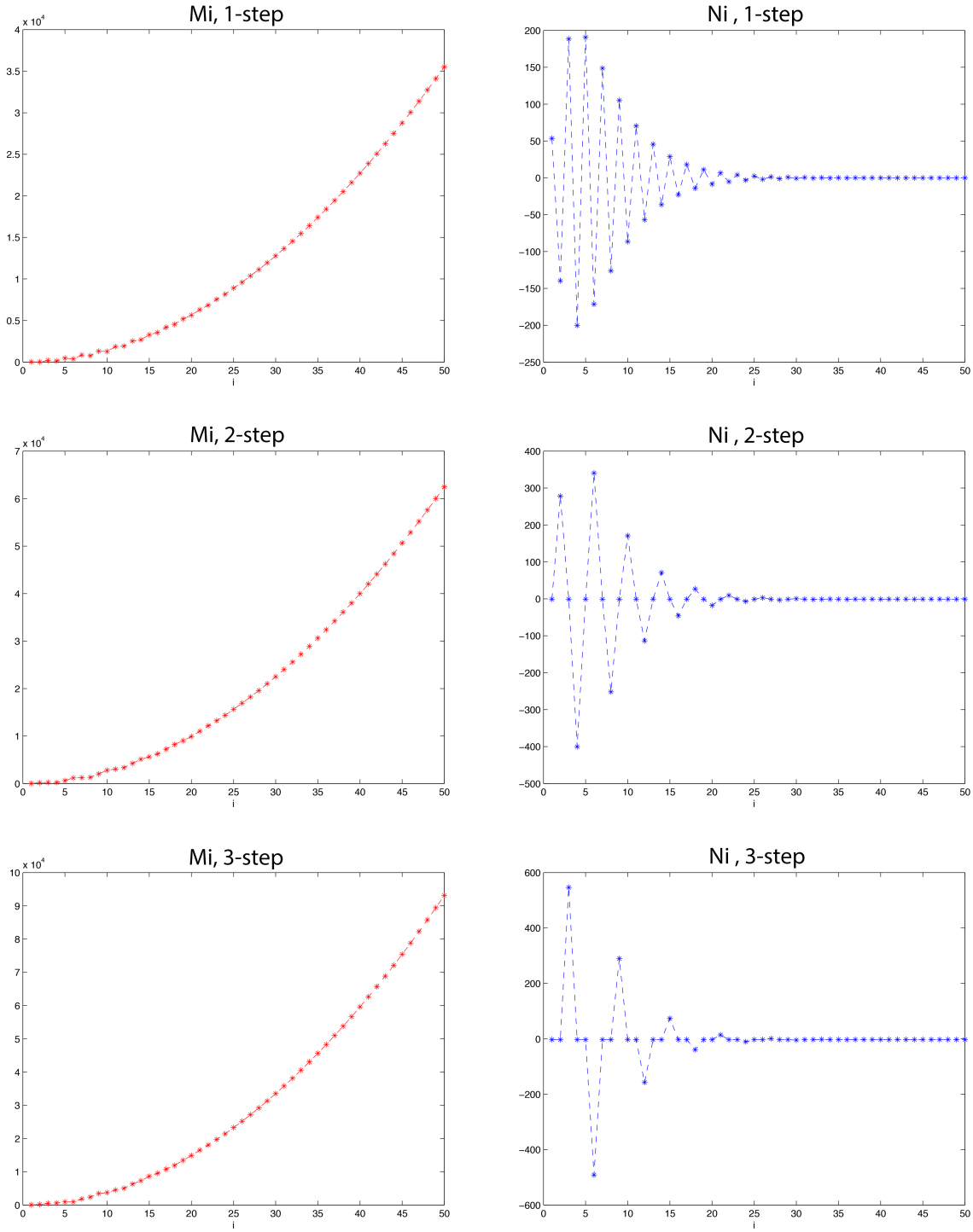


Figure 4.7: Plots of $M_i$ (left column) and $N_i$ (right column) as defined in (4.31) for 1-,2- and 3-step solutions. $i = 1..50$. Parameter values: $\chi = 50, D = 10, \gamma = 2$ and $\Gamma = 0.004$.

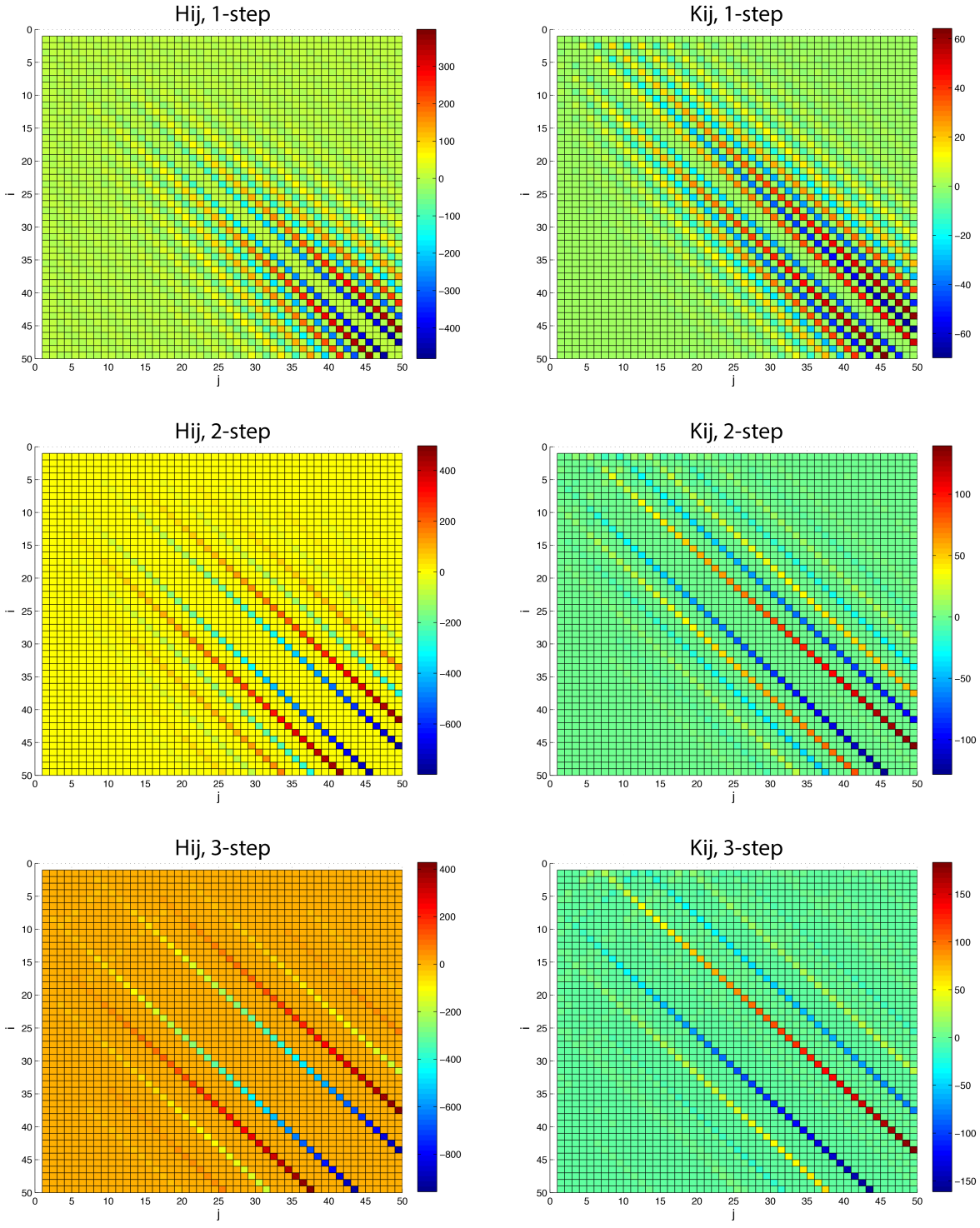


Figure 4.8: Plots of $H_{ij}$ (left column) and $K_{ij}$ (right column) as defined in (4.33) for 1-,2- and 3-step solutions. $i, j = 1..50$. Colours correspond to values in given colour bars. Parameter values: $\chi = 50, D = 10, \gamma = 2$ and $\Gamma = 0.004$.

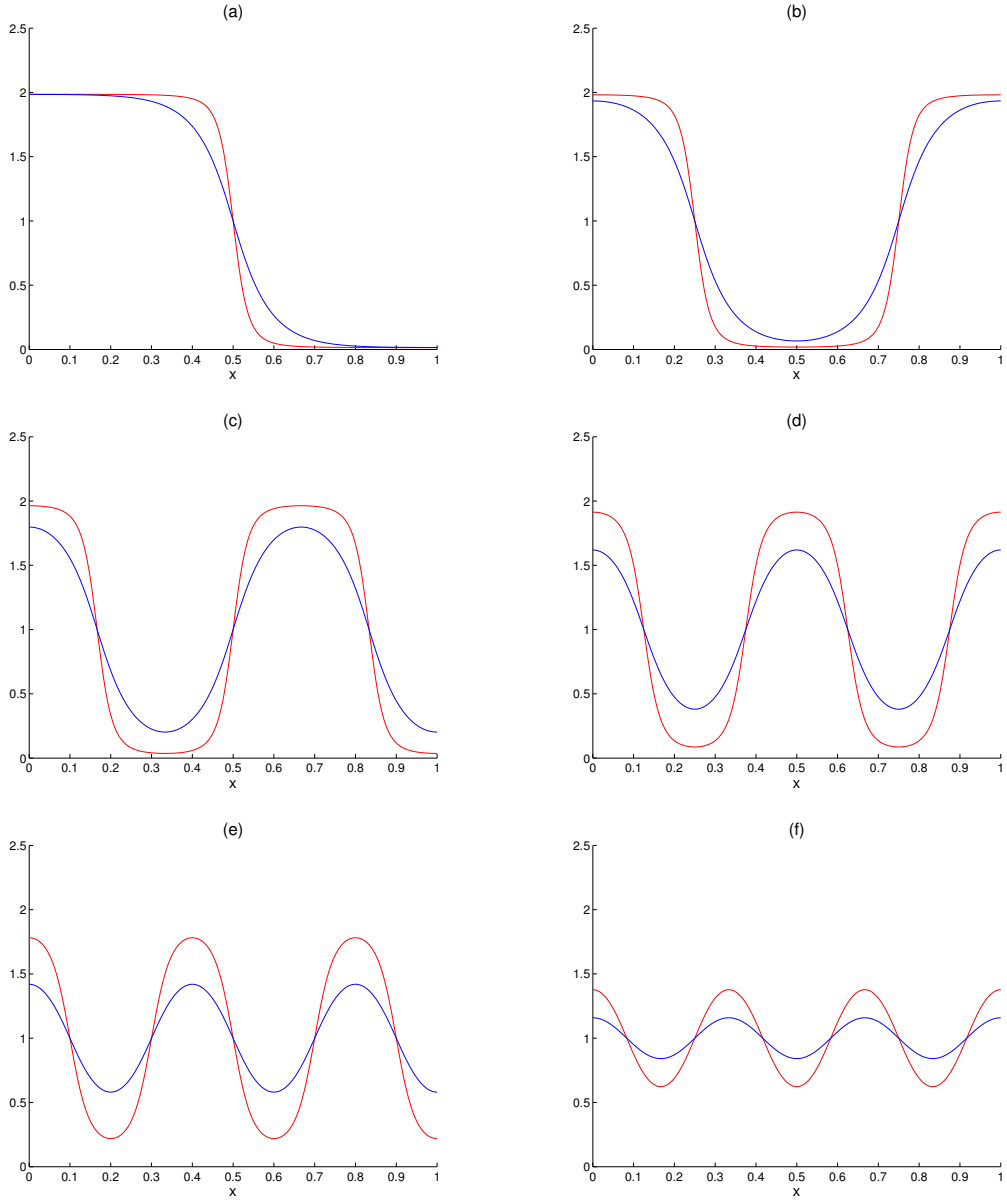


Figure 4.9: Plots of $p$-step solutions to (4.6) obtained using the BVP4C solver in MATLAB. $n(x)$ is shown in red and $c(x)$ in blue. For the parameter values, $\chi = 50, D = 10, \gamma = 2$ and $\Gamma = 0.004$. All steady state solutions that exist are shown in (a)-(f) with $p = 1$ to 6 (see text).

$$Q_{1-step} = \begin{bmatrix} -0.8231 & 0.1940 & 0.0021 & 0.0037 & 0.9870 & -0.4492 & 0.0207 & -0.0115 & \dots \\ 1 & -1.0395 & 0 & 0 & 0 & 0 & 0 & 0 & \dots \\ -0.0232 & 0.0024 & -0.4618 & 0.1770 & 0.0614 & -0.0158 & -0.1481 & -0.1802 & \dots \\ 0 & 0 & 1 & -1.1579 & 0 & 0 & 0 & 0 & \dots \\ 0.3907 & -0.4492 & 0.0082 & -0.0095 & -5.0607 & 1.5433 & -0.0405 & 0.0312 & \dots \\ 0 & 0 & 0 & 0 & 1 & -1.3553 & 0 & 0 & \dots \\ 0.0448 & -0.0071 & -3.7240 & -0.1800 & -0.1138 & 0.0250 & -4.7142 & 1.0605 & \dots \\ 0 & 0 & 0 & 0 & 0 & 0 & 1 & -1.6317 & \dots \\ 0.2797 & 0.6362 & -0.0606 & 0.0119 & -0.1387 & -1.9158 & 0.0482 & -0.0424 & \dots \\ 0 & 0 & 0 & 0 & 0 & 0 & 0 & 0 & \dots \\ \dots & \dots & \dots & \dots & \dots & \dots & \dots & \dots & \dots \end{bmatrix}$$

$$Q_{2-step} = \begin{bmatrix} -0.3878 & 0.2000 & 0.0387 & -0.0067 & -1.1082 & 0.4167 & -0.0211 & 0.0165 & \dots \\ 1 & -1.0395 & 0 & 0 & 0 & 0 & 0 & 0 & \dots \\ -0.0140 & -0.0026 & -3.8027 & 1.3556 & -0.0175 & 0.0202 & 0.0070 & -0.0000 & \dots \\ 0 & 0 & 1 & -1.1579 & 0 & 0 & 0 & 0 & \dots \\ -3.3389 & 0.4168 & -0.0896 & 0.0149 & -3.5460 & 1.7996 & -0.0500 & 0.0444 & \dots \\ 0 & 0 & 0 & 0 & 1 & -1.3553 & 0 & 0 & \dots \\ -0.0588 & 0.0101 & 0.0070 & -0.0000 & -0.1549 & 0.0354 & -3.1140 & 1.6842 & \dots \\ 0 & 0 & 0 & 0 & 0 & 0 & 1 & -1.6317 & \dots \\ -5.5695 & -0.6948 & -0.1212 & 0.0289 & 4.0023 & -1.4207 & 0.0729 & -0.0599 & \dots \\ 0 & 0 & 0 & 0 & 0 & 0 & 0 & 0 & \dots \\ \dots & \dots & \dots & \dots & \dots & \dots & \dots & \dots & \dots \end{bmatrix}$$

$$Q_{3-step} = \begin{bmatrix} -0.3708 & 0.2980 & 0.0643 & -0.0049 & 0.0240 & -0.0000 & 0.1274 & -0.0475 & \dots \\ 1 & -1.0395 & 0 & 0 & 0 & 0 & 0 & 0 & \dots \\ -0.0029 & -0.0015 & -1.5551 & 1.1918 & 0.1477 & -0.0310 & -2.9050 & 1.3923 & \dots \\ 0 & 0 & 1 & -1.1579 & 0 & 0 & 0 & 0 & \dots \\ 0.0240 & -0.0000 & 0.0431 & -0.0188 & -7.9236 & 4.2483 & -0.0562 & 0.0634 & \dots \\ 0 & 0 & 0 & 0 & 1 & -1.3553 & 0 & 0 & \dots \\ 0.0817 & -0.0079 & -5.8362 & 1.3928 & -0.2008 & 0.0504 & -6.2925 & 4.7672 & \dots \\ 0 & 0 & 0 & 0 & 0 & 0 & 1 & -1.6317 & \dots \\ -7.3017 & 0.8706 & -0.1487 & 0.0366 & 0.0240 & 0.0000 & -0.1754 & 0.0456 & \dots \\ 0 & 0 & 0 & 0 & 0 & 0 & 0 & 0 & \dots \\ \dots & \dots & \dots & \dots & \dots & \dots & \dots & \dots & \dots \end{bmatrix}$$

| $p$ | Eigenvalues of $Q$ | | | | | | |
|---|---|---|---|---|---|---|---|
| 1 | -0.5554 | -0.6163 | -1.1025 | -1.2168 | -1.3328 | -1.5779 | ... |
| 2 | -0.0079 | -0.9484 | -1.0036 | -1.2001 | -1.2668 | -1.6316 | ... |
| 3 | 0.0012 | 0.0012 | -0.9851 | -1.0712 | -1.1061 | -1.5453 | ... |
| 4 | 0.0355 | 0.0556 | 0.0556 | -0.9324 | -1.0516 | -1.3007 | ... |
| 5 | 0.0971 | 0.1568 | 0.2285 | 0.2588 | -0.6889 | -0.8808 | ... |
| 6 | 0.2761 | 0.2995 | 0.5165 | 0.5611 | 0.6234 | -0.1665 | ... |

Table 4.2: Small eigenvalues of the matrix $Q$ for different values of $p$ sorted into descending order. Parameter values: $\chi = 50, D = 10, \gamma = 2$ and $\Gamma = 0.004$.

Table 4.3.3 shows the eigenvalues of $Q$ for each $p$-step solution for the default parameter set. Only the smallest six eigenvalues are important as all others are negative. They have been sorted into descending order and all entries of $Q$ as well as the eigenvalues are correct to four decimal places. The results show that the 1-step solution is always

stable and that higher step solutions are increasingly unstable with increasing $p$. The exception here is the 2-step solution, which we have found to have negative eigenvalues. However, the smallest eigenvalue is not only small, but two orders of magnitude smaller than the second smallest. Solutions of the time-dependent problem show the 2-step solution to be unstable. Therefore, we conclude that this result is a numerical artefact and the 2-step solution has a positive eigenvalue that is very close to zero. At the very least we are confident that the number of positive eigenvalues associated with the 2-step solution can be no greater than one.

It appears that, in general, a $p$-step solution has $(p-1)$ positive associated eigenvalues. We note that this was not the case observed in [106]: this interesting point needs further investigation. The appearance of so-called metastable solutions occurs not only in volume-filling chemotaxis models but also in other areas such as microwave heating and Cahn-Hilliard equations (see [61] and [116] for details). As discussed earlier, solutions of (4.1) are spatio-temporal patterns with structures that we can identify by their number of steps. We call these solutions $p$-step solutions as they have exactly $p$ points of infection (see Figure 4.6). Roughly speaking, metastability can be described as follows. By choosing parameter values such that (4.25) is satisfied with $k \geq 1$ we ensure that the uniform steady state is linearly unstable. Analysis of this instability reveals that a $p_m$-step metastable solution is formed where $p_m$ is the number of steps associated with the fastest growing mode. This process is fast compared to what happens next. This solution holds its shape for some time until it destabilises to form a $p < p_m$-step solution. The step reduction process continues until a linearly stable 1-step solution is reached.

Ideally, we would like to be able to prove that for all parameters that permit the existence of a 1-step steady state, this state is also unconditionally stable. A negative upper bound on the eigenvalues of $Q$ would accomplish this. Unfortunately, all methods we have tried have been unsuccessful, including permutation of $Q$ and the Gerschgorin

circle theorem. When applying the latter, lower and upper bounds can be obtained for the smallest eigenvalue and hence a possible range. However, this range does allow for the possibility of a positive eigenvalue and is therefore not helpful. Further exploration of this problem may yield some rigorous mathematical results.

## 4.4 Conclusions

We conclude that spatially uniform and heterogeneous steady states of the volume-filling chemotaxis model are strongly connected. We have found that heterogeneous steady state solutions can only exist provided that the homogeneous steady state is linearly unstable. Moreover, by examining the special case when $\gamma = 2m_0$ we found that, due to the symmetry of solutions, a single value of $\lambda$, $\lambda(1)$ satisfies (4.17) for all heterogeneous steady states of the time-dependent problem. We found that the number of heterogeneous steady states exactly equals the number of unstable modes associated with the constant steady state. Whether or not this is always the case remains open but the fact that we have also shown that heterogeneous steady states can only exist provided the uniform steady state is unstable is certainly consistent with this conjecture.

Solutions of the eigenvalue problem we constructed in Section 4.3.3 provide further support to the conjecture that these $p$-step solutions are metastable and analysis of the matrix, $Q$, reveals that the small non-zero components are largely the cause of the small, positive eigenvalues that are associated with such solutions. Numerical experiments suggest that for all parameters, provided they lie in the range allowing for linear instability of uniform steady states, that metastability is a generic property of the model. Proof of this statement may be the subject of interesting work in the future. Also, we observe that solutions of our eigenvalue problem differ slightly from

previous results: while it was shown that the number of positive eigenvalues certainly increases with $p$, our results differ in the sense that we see a $p$-step steady state has $p-1$ unstable eigenvalues. This hypothesis is in line with the generic situation where the real part of the spectrum of the linearisation slides through zero, one eigenvalue at a time. The reason why our results are different to those given in [106] is unclear at this stage, particularly as no details are given of how eigenvalues are computed, but may be related to differences in the scaling of the problem or the numerical methods used in computation.

# Chapter 5

# Bioconvection

## 5.1 Introduction

The model discussed so far does not fully capture the behaviour seen in zoospore experiments. Solutions of the chemotaxis model discussed in Chapter 3 show that, although the initial formation of spots and the slow drifting of aggregates over longer times were in qualitative agreement with experiments, there are other, perhaps more subtle, details that this model fails to capture. The largest omission up to this point has been the effect of fluid motion on zoospore patterning. As discussed in Chapter 1, the competing hypothesis for zoospore auto-aggregation (besides chemotaxis) is that the patterns are due to bioconvection. Therefore, in this chapter, we study a model for zoospore bioconvection. Moreover, we will present for the first time a combined *bioconvection-chemotaxis* model. In this chapter we begin by giving a general overview of bioconvection in microorganisms and the current evidence for bioconvection in zoospores. We also outline how the mathematical modelling of bioconvection has developed. To construct our mathematical model, we re-derive the continuum model of Pedley *et al.* [98]

and couple this with the chemotaxis model discussed in Chapter 3. Numerical simulations of this model will be examined in the absence of chemotactic effects first, in particular the formation of plumes for varying chamber depths and in wide chambers. The results of these simulations will be compared with experimental evidence. We then examine solutions of the full bioconvection-chemotaxis model and how these compare with those produced by pure bioconvection. Finally, we discuss the implications of our results to zoospore auto-aggregation and how the model could be developed in the future.

### 5.1.1 Bioconvection in Upswimming Microorganisms

Bioconvection patterns are macroscale density distributions observed in suspensions of some swimming microorganisms. The term "bioconvection" was first used by Platt in 1961 [103] in a paper that investigated and aimed to provide an explanation for such patterns, which had been observed as early as 1838 [124]. In order for bioconvection to take place, the organisms in question must have two features: i) they must be slightly more dense than the surrounding fluid and ii) they must have a tendency to swim towards the fluid surface. In a suspension containing large numbers of such organisms, a dense layer of cells forms at the fluid surface and overturning instabilities lead to the formation of concentrated *plumes* of cells (see Figure 2.4). This is analogous to Rayleigh-Bénard convection, which is observed in a shallow, horizontal fluid layer heated from below. The heated fluid rises to the surface and falls back down when it cools, forming a periodic pattern of Bénard convection cells. The upswimming of microbial cells can be caused by many factors. For example, *Bacillus subtilis* cells consume oxygen and in doing so create a gradient as the oxygen is replenished at the water surface. The bacteria can sense this gradient and swim upwards via oxytaxis. *Tetrahymena pyriformis* cells can respond to changes in gravity: cells have been found

to swim upwards in a gravity field without chemical or light gradients present, but swim in random directions in low gravity (0.01 $g$) [87].

### 5.1.2 Gyrotactic Upswimming

Cameron and Carlile reported *Phytophthora* zoospores to exhibit upswimming behaviour [19]. After appropriate tests were conducted, the accumulation of zoospores at the fluid surface was concluded not to be due to phototaxis or oxytaxis (attraction to light or oxygen). In a study of zoospore morphology, Ho *et al.* [57] found that zoospores are slightly larger at the rear than at the front. It is therefore most likely that the mechanism for upswimming in zoospores is *gyrotaxis*, first described by Kessler [68]. Bottom-heavy cells in a fluid experience a gravitational torque that, when balanced with viscous torque, means the cell swims upwards on average. Moreover, gyrotaxis causes cells to swim towards regions of downwelling fluid and away from regions of upwelling fluid. This was confirmed experimentally by Kessler [67]: given a population of gyrotactic cells in a fluid flow in a cylinder, the cells were focussed into a narrow beam in the centre (where the fluid velocity was strongest) when the direction of the flow was in the $-\hat{\mathbf{z}}$-direction. When the direction of the flow was reversed, cells accumulated at the edges of the cylinder (where the fluid velocity was weakest), confirming the role of gyrotaxis in orientation. This mechanism provides a second instability from which bioconvection can develop besides a dense layer of cells at the fluid surface. In a mixed suspension, any small non-uniformities in the cell density distribution will lead these more dense "blobs" of fluid to sink, generating downward fluid motion and thereby concentrating neighbouring cells in their wake [100]. Photographic evidence of this can be seen in [100] for a deep suspension of *C. nivalis* cells: so-called "bottom-standing" plumes can be seen that formed away from the fluid

surface. Whether gyrotactic or overturning instabilities first lead to bioconvection depends on the time scales required for various events: the time for initial fluid motion in a stirred suspension to decay ($t_d$) (stirring is often employed to at the beginning of bioconvection experiments to homogenise suspensions); the time for a dense layer of cells to form at the surface ($t_s$); the time for the growth of overturning instabilities in this layer ($t_{\text{overturning}}$); the growth of gyrotactic instabilities in the suspension below the surface ($t_{\text{gyro}}$). There are three probable cases, as detailed in [100]:

1. Gyrotactic instabilities are observed first if $t_d < t_{\text{gyro}} < t_s + t_{\text{overturning}}$;
2. Overturning instabilities are observed first if $t_d < t_s + t_{\text{overturning}} < t_{\text{gyro}}$;
3. The decaying fluid motions will enable the formation of focussed plumes if $t_d > t_{\text{gyro}}$ and $t_d > t_s + t_{\text{overturning}}$.

Bees and Hill [12] argue that the time for initial fluid motion to decay is short enough to be neglected. That is, for a petri dish and suspension rotating with angular velocity, $\Omega$ ($|\Omega| \backsim 1\ \text{s}^{-1}$), the time taken for the initial fluid motion to decay when the dish is instantaneously brought to rest is $O(E^{1/2}|\Omega|^{-1})$, where $E$ is the Ekman number. It was estimated that this time was approximately ten seconds for a petri dish with diameter of 5cm. Given that auto-aggregation patterns are normally observed in zoospore suspensions at least one or two minutes after initial mixing, we assume that the initial bulk fluid motion does not play a significant role and that bioconvection is likely to arise from case 1 or 2 above. Whether patterns are formed as a result of overturning or gyrotactic instabilities will be discussed further later.

### 5.1.3 Mathematical Modelling Overview

As discussed above, bioconvection can be initiated by a variety of different upswimming mechanisms and this is reflected in the diversity of models that have been developed so far to investigate this phenomenon. The first of these was by Plesset and Winet [104], who considered only the linear stability of a dense layer of cells at the fluid surface, neglecting cell motility. The predictions of pattern wavelengths that would grow from this unstable state were found to be in good agreement with experimental data for *Tetrahymena pyriformis*.

However, it is partial differential equation models that have been favoured by the majority of researchers studying bioconvection patterns in the last few decades. Childress *et al.* presented such a model for upswimming algae in 1974 [28, 76]. This is the most generic model of its kind as it was assumed that the upswimming velocity was a constant of the form $V_N\hat{\mathbf{z}}$, and was not dependent on any specific mechanism such as gyrotaxis or chemotaxis. This basic model was developed further by Pedley *et al.* in 1988, who examined gyrotactic bioconvection in *C. nivalis* cells [98]. The Gyrotaxis mechanism was represented in the model by assuming a constant swimming speed but with a unit direction vector, $\mathbf{p}$, for which an average could be computed. Both of the PDE models discussed so far assumed the diffusion of cells to be isotropic as a first approximation. However, in 1990, Pedley and Kessler re-thought their original approach in [98], reasoning that the assumption of isotropic diffusion with a bias in the average swimming direction was inconsistent. A suitable revision was made in 1990 when the same authors proposed a so-called "new" model, taking a probabalistic approach [99]. That is, the average swimming direction was represented by a probability density function, $f(\mathbf{p})$, that can be determined as a solution of a Fokker-Planck equation. The predictions made by this model were found to be an improvement over the original in a quantitative sense. For bioconvection in *B. subtilis*, a slightly different approach had

to be taken. The model by Hillesdon *et al.* includes a Keller-Segel type chemotaxis flux to account for the cells' attraction towards oxygen [54]. Further complexity arises from the fact that *B. subtilis* cells only swim in the presence of a sufficiently high oxygen concentration and this can lead to an inactive layer of cells where the supply is low. In the model, this was accounted for with the inclusion of a heavyside function multiplying the diffusion and chemotaxis terms, removing their effects for sufficiently low oxygen concentrations. Vincent and Hill investigated the phototactic component of bioconvection in *C. nivalis* cells (they are also gyrotactic) [123]. This was accomplished by assuming that the average swimming velocity was of the form $V_N T(I)\hat{\mathbf{z}}$, where $V_N$ is a constant and $T(I)$ is a taxis function depending on light intensity.

The analysis of PDE models for bioconvection is varied and extensive. Ghorai and Hill studied the original continuum model of Pedley *et al.* and determined conditions for the existence and stability of a 2-D plume in a tall chamber with stress-free sidewalls [43]. Their conclusion was that such a plume is stable in a shallow chamber but becomes unstable as the depth increases. Two specific types of instability were noted: a periodic "varicose" instability where dense blobs moves down the plume (as observed by Kessler in experiments with Poiseuille flow [68]) and a meandering instability where the plume is shifted to one of the side walls. Using linear analysis, the predicted wavelengths of these instabilities were found to be in agreement with numerical solutions of the model. The same authors investigated this model further, specifically considering solutions in a wide chamber and the dependence of horizontal pattern wavelengths on model parameter values and chamber depth [44]. Crucially, solutions in shallow chambers were always found to be steady while those in deep chambers are always unsteady. We discuss this further in this chapter. Bees and Hill analysed the revised model of Pedley and Kessler, using linear analysis to predict the growth rate of patterns via gyrotaxis in a uniform suspension with finite depth [12]. The results compared favourably with quantitative experimental data for *C. nivalis*

[11] and were found to be more accurate than those obtained with the original model. "Perfect" agreement with experiments could be obtained by tuning parameter values within realistic bounds. The same authors carried out non-linear analysis of this model for a deep layer and concluded that bifurcation to instability was supercritical, and hence justifies the use of linear analysis to predict initial pattern wavelengths [13]. The formation of three dimensional plumes has been investigated by Ghorai and Hill [45], and is currently the only such investigation to the best of our knowledge. Using a specially designed numerical scheme, a single plume was seen to form in a shallow chamber, becoming unstable in a sufficiently deep chamber as predicted by 2-D linear analysis. Multiple plumes were not studied, presumably due to computational limitations. The review papers [52, 100] and references therein give an excellent summary of continuum modelling work for bioconvection.

Discrete bioconvection models are less common, with only one having been studied thus far. Hopkins and Fauci [58] employed a discrete-continuum hybrid approach and aimed to apply the model to a range of bioconvection mechanisms, i.e. simple upswimming, gyrotaxis and chemotaxis. The cells are represented as discrete point sources of mass and the fluid velocity is again modelled by the incompressible Navier-Stokes equations. Each cell is assigned a position along with an individual speed and orientation. As in continuum models, the cell microstructure is neglected, allowing the simulation of many cells simultaneously to be computationally feasible. The results show that pattern wavelengths vary with depth and also that the stability of plumes is again dependent on suspension depth. The appeal of using such a model is that an individual cell and its orientation, speed etc. can be accurately tracked as it swims, illustrating how the gyrotactic mechanism orientates individual cells. However, the number of cells that can be tracked (approximately $10^5$ in total) is not enough for proper comparison with experiments in many cases including ours.

Given the fact that the most likely mechanism that would drive bioconvection in zoospores

is gyrotaxis as discussed above, we choose the original continuum model of Pedley *et al.* [98] as a basis for our bioconvection-chemotaxis model.

## 5.2 Combining Bioconvection and Chemotaxis: Model Configuration

In order to construct the model, we make some standard assumptions. Firstly, we assume that all zoospores are idealised as spheres with a fixed volume, $v$, radius $a$, density $\rho_N$ and that their centre of gravity is offset a distance, $h$, from the centre of the cell (see Figure 5.1). We also assume that a zoospore suspension is dilute, i.e. the ratio of total zoospore volume to the total suspension volume is small. We estimate that this value lies between $0.00005 - 0.0005$ ($\ll 1$) for typical concentrations of $10^5 - 10^6$ zoospores ml$^{-1}$ and so this assumption is valid. The microstructure (e.g. the flagella) of zoospores is also neglected since the length scale of auto-aggregation patterns is much larger than cell diameters or average spacing between cells. Finally, we assume that both water and zoospores are incompressible.

We now construct the model following the approach of Pedley *et al.* [98]. It is supposed that a small volume element, $\delta V$, contains $N(\mathbf{X},T)\delta V$ zoospores, where $\mathbf{X}$ is the centre of the element and $T$ is time. The total mass-average velocity of all material in $\delta V$ is defined as $\mathbf{U}(\mathbf{X},T)$ and the average swimming velocity of zoospores is taken to be $V_N\mathbf{p}$, where $V_N$ is a constant and $\mathbf{p}$ is a unit swimming direction vector. The fact that the suspension is dilute means that the Bousinessq approximation can be applied (see e.g. [52, 28]). In this context, this implies that variations in suspension density in the fluid element due to zoospore swimming are assumed to be small. Hence, the zoospores only impact the fluid through negative bouyancy, represented in the momentum equation by $\mathbf{g}(\rho_N - \rho_w)vN(\mathbf{X},T)\delta V$, where $\mathbf{g}$ is the acceleration due to gravity and

$\rho_w$ is the density of water. Following [98], we write the pressure gradient as the sum of hydrostatic and excess components, $\nabla P = \nabla P_h + \nabla P_e$. It is assumed that the fluid density is roughly constant, implying that $-\nabla P_h - \rho_w g\hat{\mathbf{z}} = 0$ and we need only model the excess pressure over hydrostatic. The full momentum equation for the suspension and incompressibility condition are then

$$\rho_w \left( \frac{\partial \mathbf{U}}{\partial T} + (\mathbf{U}\cdot\nabla)\mathbf{U} \right) = -\nabla P_e - (\rho_c - \rho_w) vNg\hat{\mathbf{z}} + \mu\nabla^2\mathbf{U}, \tag{5.1}$$

$$\nabla\cdot\mathbf{U} = 0, \tag{5.2}$$

where $P_e(\mathbf{X}, T)$ is pressure in excess of hydrostatic; $g$ is acceleration due to gravity; and $\mu$ is the dynamic viscosity of the suspension, assumed to be approximately that of water. We now couple equations (5.1) and (5.2) to the chemotaxis model derived in Chapter 3. Since both zoospores and chemoattractant are advected with the fluid, the time derivatives in the evolution equations for zoospores and chemoattractant must be replaced by material derivatives. Using the incompressibility condition (5.2) these can be simplified and written as $\frac{\partial N}{\partial T} + \nabla\cdot(N\mathbf{U})$ and $\frac{\partial C}{\partial T} + \nabla\cdot(C\mathbf{U})$, respectively. The zoospore flux due to upswimming is represented by $V_n\mathbf{p}$. The full bioconvection-chemotaxis model is then given by

$$\left.\begin{aligned}
\rho_w\left(\frac{\partial \mathbf{U}}{\partial T}+(\mathbf{U}\cdot\nabla)\mathbf{U}\right) &= -\nabla P_e-(\rho_c-\rho_w)vNg\hat{\mathbf{z}}+\mu\nabla^2\mathbf{U},\\
\nabla\cdot\mathbf{U} &= 0,\\
\frac{\partial N}{\partial T} &= -\nabla\cdot\left[N\left(\mathbf{U}+V_N\mathbf{p}+\chi_N\nabla C\right)-D_N\nabla N\right],\\
\frac{\partial C}{\partial T} &= -\nabla\cdot\left[C\mathbf{U}-D_C\nabla C\right]+\alpha N-\beta C.
\end{aligned}\right\}\ \mathbf{X}\in\Omega\subset R^k(k=2,3),$$

$$\mathbf{U}(\mathbf{X},0)=\mathbf{U}_0(\mathbf{X}),\quad N(\mathbf{X},0)=N_0(\mathbf{X}),\quad C(\mathbf{X},0)=C_0(\mathbf{X}),\quad P_e(\mathbf{X},T)=P_{e0}, \tag{5.3}$$

where variables and parameters are as defined above. These equations are assumed to hold on a bounded domain $\Omega$ with boundary, $\partial\Omega$. We will consider 2-D domains for now, i.e. a rectangular cross section of a petri dish in the $X-Z$ plane with width $L$ cm and depth $H$cm. The choice of boundary conditions is summarised as follows. For the fluid velocity, we assume no-slip conditions at all solid boundaries as is standard. We take the boundary at $Z=0$, the fluid-air interface, to be free of tangential stress and also that there is zero vertical fluid velocity (fluid cannot leave the domain). For zoospore density and chemoattractant concentration, the boundary conditions are taken to be zero-flux at all boundaries as no material should enter or exit the domain.

$$\begin{aligned}
\mathbf{U}=\mathbf{0} \quad &\text{at} \quad Z=-H \text{ and } X=0,L,\\
\mathbf{U}\cdot\hat{\mathbf{z}}=0 \text{ and } U_z=0 \quad &\text{at} \quad Z=0,\\
\mathbf{J}_N\cdot\hat{\mathbf{x}}=\mathbf{J}_C\cdot\hat{\mathbf{x}}=0 \quad &\text{at} \quad X=0,L,\\
\mathbf{J}_N\cdot\hat{\mathbf{z}}=\mathbf{J}_C\cdot\hat{\mathbf{z}}=0 \quad &\text{at} \quad Z=0,-H,
\end{aligned} \tag{5.4}$$

where $\mathbf{J}_N$ and $\mathbf{J}_C$ represent the flux of zoospores and chemoattractant, respectively.

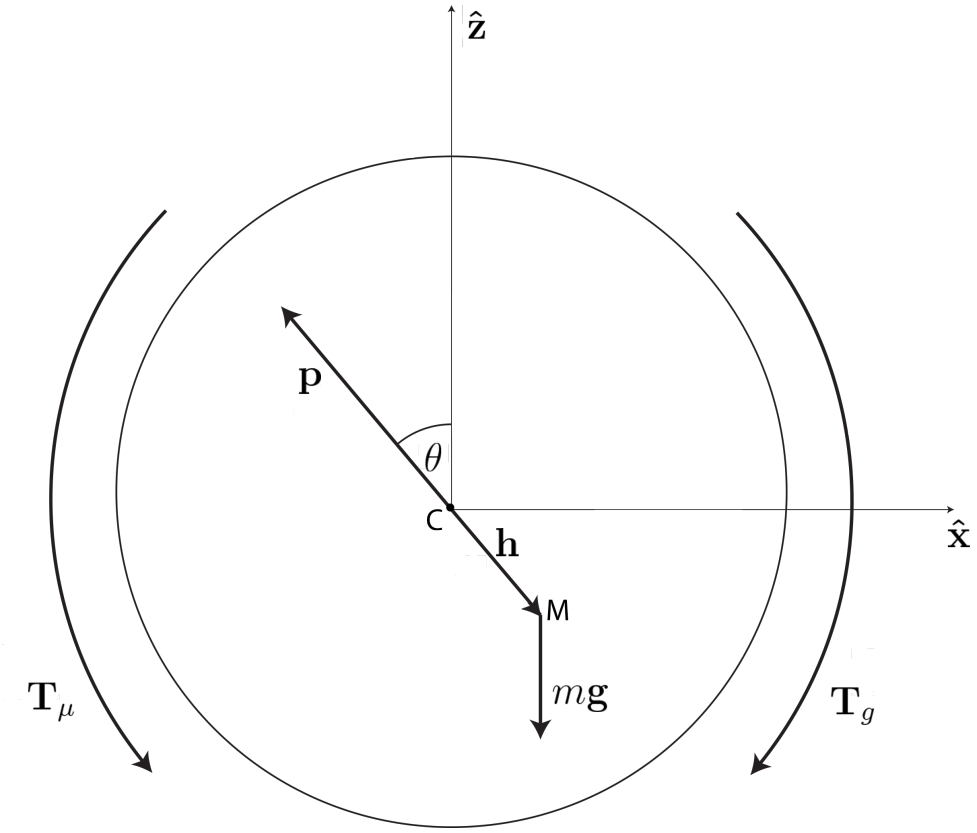


Figure 5.1: An idealised cell with centre, C, and an offset centre of mass at the point M. $\mathbf{h} = -h\mathbf{p}$ is the displacement of the centre of gravity from the centre of the cell and $m\mathbf{g}$ is the force due to gravity. The swimming direction, $\mathbf{p}$, is at an angle, $\theta$ from the vertical axis, which increases in an anti-clockwise manner. $\mathbf{T}_\mu$ and $\mathbf{T}_g$ represent the viscous and gravitational torque, respectively.

The unit vector $\mathbf{p}$ is the unit swimming direction for a cell given by

$$\mathbf{p} = [p_x, p_z] = [-\sin(\theta), 0, \cos(\theta)], \tag{5.5}$$

for which an average, $\bar{\mathbf{p}}$, still needs to be determined. In order to do this, we follow the approach of Ghorai and Hill [43] and idealise cells as being spherical in shape with radius $a$ with an offset centre of gravity, a distance $h$ from the centre of the cell. $\mathbf{p}$ is at an angle $\theta$ from the vertical axis as shown in Figure 5.1. The viscous torque and the gravitational torque act in opposing directions and it is the balance of these forces that

determines the average cell orientation. The gravitational torque is given by $m\mathbf{h} \times \mathbf{g}$, where $m$ is the mass of a cell, $\mathbf{h}$ is the displacement vector of the centre of mass and $\mathbf{g}$ is the acceleration due to gravity. Torque generated through viscosity on a sphere of radius $a$ is given by $4\pi\mu a^3 (\nabla \times \mathbf{U} - 2\Omega)$ [50], where $\Omega$ is the angular velocity of the sphere. The orientation of a cell is determined by the balance of gravitational and viscous torques. This leads to the following time evolution equation for $\theta$ when the total torque is equal to zero:

$$\begin{aligned} \text{Total torque} = \mathbf{T}_{\text{gravity}} + \mathbf{T}_{\text{viscosity}} &= 0 \\ m\mathbf{h} \times \mathbf{g} + 4\pi\mu a^3 (\nabla \times \mathbf{U} - 2\Omega) &= 0 \\ mgh\sin(\theta) + 4\pi\mu a^3 (\omega_y - 2\frac{d\theta}{dT}) &= 0 \\ \frac{B\omega_y + \sin(\theta)}{2B} &= \frac{d\theta}{dT}, \end{aligned} \tag{5.6}$$

where $\omega_y$ is the $y$ component of the fluid vorticity and $B = \frac{4\pi\mu a^3}{mgh}$ is the so-called gyrotactic orientation parameter as defined in [98]. This can be interpreted as the time taken for a cell to re-orientate through gravitational torque against the torque generated by fluid viscosity. Equation (5.6) has an equilibrium solution when $\sin(\theta) = -B\omega_y$ provided that $|B\omega_y| \leq 1$. For the case where $|B\omega_y| > 1$, we again follow the approach used by Ghorai and Hill [43] and compute an average in the following way. Consider $B\omega_y > 1$: Time is re-scaled such that $\tau = \frac{T}{2B}$ and hence (5.6) can be written as

$$\frac{d\theta}{d\tau} = \kappa + \sin(\theta), \tag{5.7}$$

where $\kappa = B\omega_y$. Equation (5.7) has an explicit solution given by

$$\frac{1}{2}\theta(\tau) = \arctan\left(\frac{\eta\tan\left(\frac{\eta(\tau+A)}{2}\right)-1}{\kappa}\right), \tag{5.8}$$

where $\eta = \sqrt{\kappa^2-1}$ and $A$ is a constant of integration. This allows the period of rotation of a cell to be calculated: as $\frac{\theta}{2}$ increases from 0 to $\pi$, $\frac{\eta(\tau+A)}{2}$ must also change by $\pi$. A simple calculation reveals the tumbling period to be $\tau_p = \frac{2\pi}{\eta}$ and hence the average swimming direction is defined by averaging $\mathbf{p}$ over $\tau_p$, i.e.

$$\begin{aligned}\bar{p_x} &= \frac{1}{\tau_p}\int_0^{\tau_p} p_x\, d\tau \\ &= \frac{1}{\tau_p}\int_0^{\tau_p} \kappa - \frac{d\theta}{d\tau}\, d\tau = \kappa - \eta,\end{aligned} \tag{5.9}$$

$$\begin{aligned}\bar{p_z} &= \frac{1}{\tau_p}\int_0^{\tau_p} p_z\, d\tau \\ &= \frac{1}{\tau_p}\int_0^{2\pi} \frac{\cos(\theta)}{d\theta/d\tau}\, d\theta = 0.\end{aligned} \tag{5.10}$$

After a similar calculation for $B\omega_y < -1$, by substituting the above results into (5.5), the average unit swimming direction can be written in general form as

$$\begin{aligned}\bar{\mathbf{p}} &= \left[B\omega_y, (1-B^2\omega_y^2)^{1/2}\right], \quad |B\omega_y| \le 1, \\ \bar{\mathbf{p}} &= \left[\left(B\omega_y - (B^2\omega_y^2-1)^{1/2}\right), 0\right], \quad B\omega_y > 1, \\ \bar{\mathbf{p}} &= \left[\left(B\omega_y + (B^2\omega_y^2-1)^{1/2}\right), 0\right], \quad B\omega_y < -1.\end{aligned} \tag{5.11}$$

We now set $\mathbf{p} = \bar{\mathbf{p}}$ and finally, using standard techniques, system (5.3) can be written in non-dimensional form as

$$\left.\begin{aligned} \frac{1}{S_c}\left(\frac{\partial \mathbf{u}}{\partial t} + (\mathbf{u}\cdot\nabla)\mathbf{u}\right) &= -\nabla p_e - Rn\hat{\mathbf{z}} + \nabla^2\mathbf{u}, \\ \nabla\cdot\mathbf{u} &= 0, \\ \frac{\partial n}{\partial t} &= -\nabla\cdot\left[n\left(\mathbf{u} + v_n\bar{\mathbf{p}} + \chi\nabla c\right) - \nabla n\right], \\ \frac{\partial c}{\partial t} &= -\nabla\cdot\left[c\mathbf{u} - D\nabla c\right] + n - r_d c. \end{aligned}\right\} \mathbf{x}\in\Omega\subset R^k (k=2,3),$$

$$\mathbf{u}(\mathbf{x},0) = \mathbf{u}_0(\mathbf{x}), \quad n(\mathbf{x},0) = n_0(\mathbf{x}), \quad c(\mathbf{x},0) = c_0(\mathbf{x}), \quad p_{e0}(\mathbf{x},0) = p_{e0}(\mathbf{x}), \tag{5.12}$$

with boundary conditions given by

$$\begin{aligned} \mathbf{u} &= \mathbf{0} && \text{at} && z = -1 \text{ and } x = 0, \frac{L}{H} \\ \mathbf{u}\cdot\hat{\mathbf{z}} = 0 \text{ and } u_z &= 0 && \text{at} && z = 0, \\ \mathbf{J}_n\cdot\hat{\mathbf{x}} = \mathbf{J}_c\cdot\hat{\mathbf{x}} &= 0 && \text{at} && x = 0, \frac{L}{H}, \\ \mathbf{J}_n\cdot\hat{\mathbf{z}} = \mathbf{J}_c\cdot\hat{\mathbf{z}} &= 0 && \text{at} && z = 0, -1. \end{aligned} \tag{5.13}$$

Letting $N_{ss}$ represent the background zoospore density in auto-aggregation experiments as in Chapter 3, non-dimensional parameters and re-scaled variables are set as

$$S_c = \frac{\mu}{D_N\rho_w}, \quad R = \frac{(\rho_c - \rho_w)vN_{ss}gH^3}{\mu D_N}, \quad v_n = \frac{V_n H}{D_N}, \quad \chi = \frac{\chi_N \alpha N_{\mathrm{ss}} H^2}{D_N^2},$$

$$D = \frac{D_C}{D_N}, \quad r_d = \frac{\beta_0 H^2}{D_N}, \quad n = \frac{N}{N_{ss}}, \quad G = \frac{BD_N}{H^2},$$

$$c = \frac{AD_{N0}}{\alpha_0 N_{\mathrm{ss}} H^2}, \quad \mathbf{x} = \frac{\mathbf{X}}{H}, \quad p_e = \frac{P_e H^2}{\mu D_N}, \quad t = \frac{D_N T}{H^2}, \quad \mathbf{u} = \frac{H\mathbf{U}}{D_N}. \tag{5.14}$$

$R$ and $S_c$ are known as the Rayleigh and Schmidt numbers respectively and are defined as is standard in bioconvection modelling. The boundary conditions are defined as above on the computational domain now defined by $z \in [-1, 0]$ and $x \in [0, \frac{L}{H}]$. Note that volume-filling has not been included in the chemotaxis equation. Our omission of the volume-filling term is equivalent to setting the maximum zoospore density $N_M$ to be large and hence the chemotactic flux is simply given by $\chi_N N \nabla C$. Our experiments show that this is reasonable.

Estimates for the dimensional and non-dimensional parameter values for the model are given in Table 5.1 along with appropriate references. The physical properties of water such as viscosity and density as well as gravitational acceleration are set as standard. The density of a zoospore is based on a measurement by Kessler for *C. nivalis* [68] and is slightly higher than that of water. The volume of a zoospore was calculated based on the assumption that cells are spherical with a radius of $5\mu$m. Parameters related to chemotaxis are again estimated based on results for *D. discoidium* attraction to cAMP. The values used here have been tuned within reason in order to best match experimental observations and so differ slightly from those in Chapter 3. The gyrotactic orientation parameter, $B$, is assumed to be the same as for *C. nivalis* also. $D_N$ is estimated using values from the upper end of the data set collected and analysed in Chapter 2 (average swimming speed: $150\mu\mathrm{m\ s}^{-1}$, average run length: $200\mu$m) in order to best match experimental data and is in line with previous investigations of bioconvection. The upswimming speed, $V_n$, is difficult to estimate directly and has again been set here to

| Dimensional parameter | Description | Value | Reference |
|---|---|---|---|
| $\rho_w$ | Density of water | 1 g / cm$^3$ | As standard |
| $\rho_n$ | Density of a cell | 1.05 g / cm$^3$ | Value for *C. nivalis* [68] |
| $\frac{\mu}{\rho_w}$ | Viscosity | 0.6 cm$^2$ min$^{-1}$ | As standard |
| $v$ | Volume of a cell | $5 \times 10^{-10}$ cm$^3$ | Established here |
| $V_n$ | Upswimming speed | 33.3 $\mu$m s$^{-1}$ | Set here |
| $B$ | Gyrotactic orientation time | $\approx 0.0566$ min | Estimate for *C. nivalis* [68] |
| $g$ | Gravitational acceleration | $3.528 \times 10^6$ cm min$^{-2}$ | As standard |
| $\alpha$ | Chemo production rate | $1.125 \times 10^{-9}$ $\mu$mol cell$^{-1}$ min$^{-1}$ | Set here |
| $\beta$ | Chemo degradation rate | 0.25 min$^{-1}$ | Estimate based on cAMP [79] |
| $H$ | Suspension depth | 0.1-0.7 cm | Set here |
| $N_{ss}$ | Background cell density | $10^6$ cm$^{-3}$ | Established here |
| $D_N$ | Diffusion rate of zoospores | $6 \times 10^{-3}$ cm$^2$ min$^{-1}$ | Established here |
| $D_C$ | Chemo diffusion rate | $3 \times 10^{-3}$ cm$^2$ min$^{-1}$ | Estimate based on cAMP [15] |
| $\chi_N$ | Chemotactic sensitivity | $1.7 \times 10^{-3}$ cm$^2$ $\mu$M$^{-1}$ min$^{-1}$ | Set here |
| Non-dimensional parameter | | | |
| $R$ | Rayleigh number | 24500 $H^3$ | - |
| $S_c$ | Schmidt number | 100 | - |
| $v_n$ | Scaled upswimming speed | $\approx 33.3$ $H$ | - |
| $G$ | Scaled gyrotaxis number | $3.4 \times 10^{-3}$ / $H^2$ | - |
| $D$ | Diffusion ratio | 0.5 | - |
| $\chi$ | Chemotaxis coefficient | 54 $H^2$ | - |
| $r_d$ | Chemo degradation | 40 $H^2$ | - |

Table 5.1: Estimates for parameter values of the bioconvection-chemotaxis model including units of measurement and references where appropriate.

best match experimental observations. Since we study a range of suspension depths, $H$ is left free in non-dimensional definitions.

## 5.3 Gyrotactic Instability of the Uniform Steady State

As discussed above, bioconvection in populations of gyrotactic microorganisms can result from two different instability mechanisms: i) the overturning instability of a dense layer of cells at the fluid surface and ii) the gyrotactic focusing of cells in the wake of sinking dense "blobs" of fluid below the surface. The latter can be illustrated mathematically by considering the linear stability of a uniform suspension of cells in an infinitely deep suspension as in [98]. We now outline this result.

Neglecting chemotaxis, system (5.12) admits a steady state solution with uniform zoospore density and zero fluid velocity. We linearise around this steady state in the usual way by setting $n = 1 + \hat{n}$, $\mathbf{u} = \hat{\mathbf{u}} = [\hat{u}, 0, \hat{w}]$, $p_e = -Rz + \hat{p}_e$ and $\hat{\mathbf{p}} = \hat{\mathbf{z}} + \bar{\mathbf{p}}'$ ($\bar{\mathbf{p}}' \cdot \hat{\mathbf{z}} = 0$), where the magnitude of the perturbations is assumed to be small. Substituting these into (5.12) gives the linear equations,

$$\begin{aligned} \frac{1}{S_c}\frac{\partial \hat{\mathbf{u}}}{\partial t} &= -\nabla \hat{p}_e - R\hat{n}\hat{\mathbf{z}} + \nabla^2 \hat{\mathbf{u}} \\ \nabla \cdot \hat{\mathbf{u}} &= 0 \\ \frac{\partial \hat{n}}{\partial t} &= \nabla^2 \hat{n} - v_n \frac{\partial \hat{n}}{\partial z} - v_n \nabla \cdot \bar{\mathbf{p}}'. \end{aligned} \tag{5.15}$$

Given that $\theta = \hat{\theta}$ and $\omega_y = \hat{\omega}_y$, it follows from (5.5) and (5.6) that $\bar{\mathbf{p}}' = G\hat{\omega}_y \hat{\mathbf{x}} \Rightarrow$

$\nabla \cdot \bar{\mathbf{p}}' = -G\nabla^2 \hat{w}$, where $\hat{w}$ is the perturbed vertical fluid velocity and the incompressibility condition has been used. Assuming that all perturbation functions are proportional to $\exp(\sigma t)\exp(i(kx+mz))$, (5.15) leads to the following eigenvalue problem and dispersion relation:

$$\begin{bmatrix} -ik & -im & 0 & 0 \\ \frac{1}{S_c}\sigma + K^2 & 0 & 0 & ik \\ 0 & \frac{1}{S_c}\sigma + K^2 & R & im \\ 0 & K^2 G v_n & (\sigma + K^2 + v_n im) & 0 \end{bmatrix} \begin{bmatrix} \hat{u} \\ \hat{w} \\ \hat{n} \\ \hat{p}_e \end{bmatrix} = 0;$$

$$\left(\frac{1}{S_c}\sigma + K^2\right)\left(\sigma + v_n im + K^2\right) - k^2 v_n RG = 0, \tag{5.16}$$

where $K^2 = k^2 + m^2$. The uniform steady state is unstable if $Re(\sigma) > 0$. It is worth noting two special cases at this stage. Firstly, suppose $G = 0$ and there are no gyrotactic effects present, then cells swim vertically upwards only and it follows from (5.16) that

$$\sigma_{+,-} = -S_c K^2, -(K^2 + i v_n m). \tag{5.17}$$

Clearly, both eigenvalues have a negative real part and so in the absence of gyrotaxis the uniform steady state is linearly stable. Secondly, if only horizontal perturbations are considered, i.e. $m = 0$, equation (5.16) has solutions

$$\sigma_{+,-} = \frac{1}{2}\left[-k^2(1+S_c) \pm \sqrt{k^4(1+S_c)^2 - 4S_c(k^4 - k^2 RG v_n)}\right]. \tag{5.18}$$

Given that the model parameters are positive, there is one positive eigenvalue, $\sigma_+$, for wavenumbers satisfying

$$k < k_c = \sqrt{v_n RG}, \tag{5.19}$$

and so disturbances with sufficiently large wavelengths will grow in time.

Now, returning to the general case, the solution of (5.16) with the largest real part is given by

$$\sigma_+ = \frac{S_c}{2}\left[-\left(K^2 + \frac{1}{S_c}(K^2 + v_n im)\right) + \sqrt{\left(K^2 + \frac{1}{S_c}(K^2 + v_n im)\right)^2 - \frac{4}{S_c}\left(K^2(K^2 + v_n im) - k^2 v_n RG\right)}\right], \tag{5.20}$$

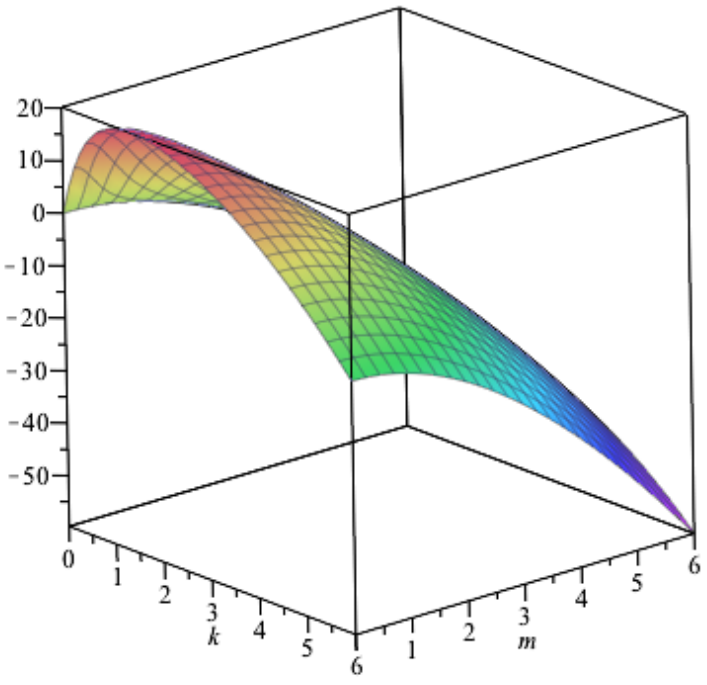


Figure 5.2: Plot of the real part of $\sigma_+$ from (5.20) using parameter values from Table 5.1 with depth $H = 0.3$cm. Instability is only possible for $k < k_c \approx 5$ for all $m$.

Figure 5.2 shows an example range of horizontal and vertical wavenumbers for which

the real part of $\sigma_+$ is positive. We see that, with the inclusion of vertical wavenumbers, instability occurs for $k < k_c$ only. Instabilities are possible with $m \neq 0$ and $k > k_c$ for sufficiently elongated cells such as rod shaped bacteria (see Pedley *et al.* [98] for details), but this is not relevant in the zoospore case. If the imaginary terms are assumed to be negligible (as in [98]), an explicit condition for instability can be obtained. The case of a chamber with finite depth is of particular interest and it is reasonable to assume that the linear theory is valid sufficiently far away from the boundaries if only small vertical wavelengths are considered. That is, for $m > m_0 = 2\pi$, it follows from equation (5.20) that the uniform state is unstable if

$$k_c^2 k^2 > (k^2 + m^2)^2,$$

and therefore the critical values of the horizontal wavenumber, $k_1$ say, satisfy

$$k_1^2 - k_c k_1 + m_0^2 = 0. \tag{5.21}$$

Using this result, it is straightforward to show that a real, horizontal perturbation can only exist when $m_0^2 < \frac{1}{4}k_c^2$. Or, after re-arrangement, instability is only possible if

$$v_n RG > 16\pi^2. \tag{5.22}$$

For the default parameters in Table 5.1 and the depths in which we are interested, this inequality certainly does not hold. In conclusion, we should expect bioconvection patterns to be initiated via an overturning, not a gyrotactic, instability. However, since the uniform steady state under consideration does not satisfy the zero-flux boundary conditions at the horizontal boundaries, these results are only of qualitative relevance

but our numerical simulations agree with this prediction.

## 5.4 Numerical Simulations

### 5.4.1 Plume Formation in Shallow and Deep Chambers, $\chi = 0$

We use the COMSOL multiphysics package (discussed in Chapter 3) to solve this system in a 2-D, rectangular domain representing the cross-section of a petri dish, i.e. the chamber width used in simulations is equal to the diameter of the dish. We assume that a two dimensional approximation is valid as plumes are generally symmetric about their centre. The vast majority of numerical investigations of bioconvection in the existing literature have been in 2-D, due in part to the computational challenges of simulating in 3-D. The number of elements used ranged from approximately $8 \times 10^3$-$1 \times 10^5$ depending on the size of domain under consideration. We found this to be sufficient to rule out numerical error in solutions. For other settings used, see Appendix 7.2.

Firstly, we investigate the formation of single plumes and the effect of depth on their shape and features in the absence of chemotaxis and so set $\chi = 0$. The initial data is given by $n_0(x,z) = 1 + \varepsilon(x,z)$, $\mathbf{u}_0(x,z) = 0$ and $p_{e0}(x,z) = 0$, where $\varepsilon(x,z)$ is a small, sinusoidal perturbation that ensures that plumes form in the centre of the domain, purely for computational convenience and without loss of generality. To minimise the effect of the vertical boundaries, we use periodic boundary conditions for both zoospore density and fluid velocity. All other boundary conditions are as described above in (5.13).

We examine plume formation for four different depths, $H = 0.1, 0.3, 0.5$ and 0.7cm. For a sufficiently shallow suspension, no bioconvection takes place at all (see Figure 5.3). In this case, the zoospore density, $n$, forms a stratified state with a dense layer at

the fluid surface. In fact, this profile can be computed directly by considering a steady state of (5.12) with $\mathbf{u} = 0$ and $n(x,z) = \bar{n}(z)$:

$$\bar{n}(z) = \frac{v_n \exp(v_n z)}{1 - \exp(-v_n)}, \quad \bar{p}_e = -R\bar{n}z, \tag{5.23}$$

where the fact that the total zoospore number is conserved in time has been used to determine the constant of integration. This exactly describes the pattern seen in Figure 5.3. Figure 5.4 shows the formation of a single plume in a shallow suspension with depth, $H = 0.3$cm. Initially, the formation of a dense layer of cells can be seen before instability develops, which closely resembles an exponential profile in the $\hat{\mathbf{z}}$-direction. After a few minutes, instability develops at the fluid surface (t=0.22). This confirms our earlier assumption that bioconvection would most likely result from overturning as opposed to gyrotactic instability. The final snapshot (t=0.5) shows a fully formed and steady plume, i.e. the structure, shape and position of the plume remain constant after long times. Figure 5.5 shows the formation of a plume with $H$=0.5cm. The process is much the same as for $H = 0.3$cm case, however the plume features, such as the widening at the bottom and narrowing nearer the top, appear more pronounced and exaggerated. For instance, the plume shown for $H = 0.5$cm has a maximum width of approximately 0.7cm compared with 0.2cm for the plume shown in Figure 5.4. Upon increasing the suspension depth to $H = 0.7$cm, the plume formed is far less stable as Figure 5.6 shows. In fact, the plume splits into two: once the dense blob of cells has sunk to the bottom, a secondary plume is formed. This plume exhibits a varicose instability as described above for some time before rejoining the main, anchor-shaped plume on the right. The motion of zoospores in each of these cases can be better understood by examining the fluid velocity. The horizontal and vertical fluid velocities for the cases where $H = 0.3$cm and $H = 0.5$cm are shown in Figure 5.7 and a clear convection pattern can be seen. [Note that images in Figure 5.7 show

the fluid velocity profiles after the system has reached a steady state. We omit the fluid velocity plots for $H = 0.7$cm as the solutions continuously evolve and no such steady state is attained.] At the surface, zoospores are focused towards the centre of the plume, where the density is highest, and pulled downwards into the region of most rapid downward flow. At the bottom, the plume widens as the cells spread out and then move back towards the surface. Subtle features of plumes can be altered by the choice of parameter values. Increasing/decreasing $v_n$ has the effect of stretching/compressing plumes (in the z-direction) respectively. Plumes become wider/narrower at the bottom upon increasing/decreasing $G$.

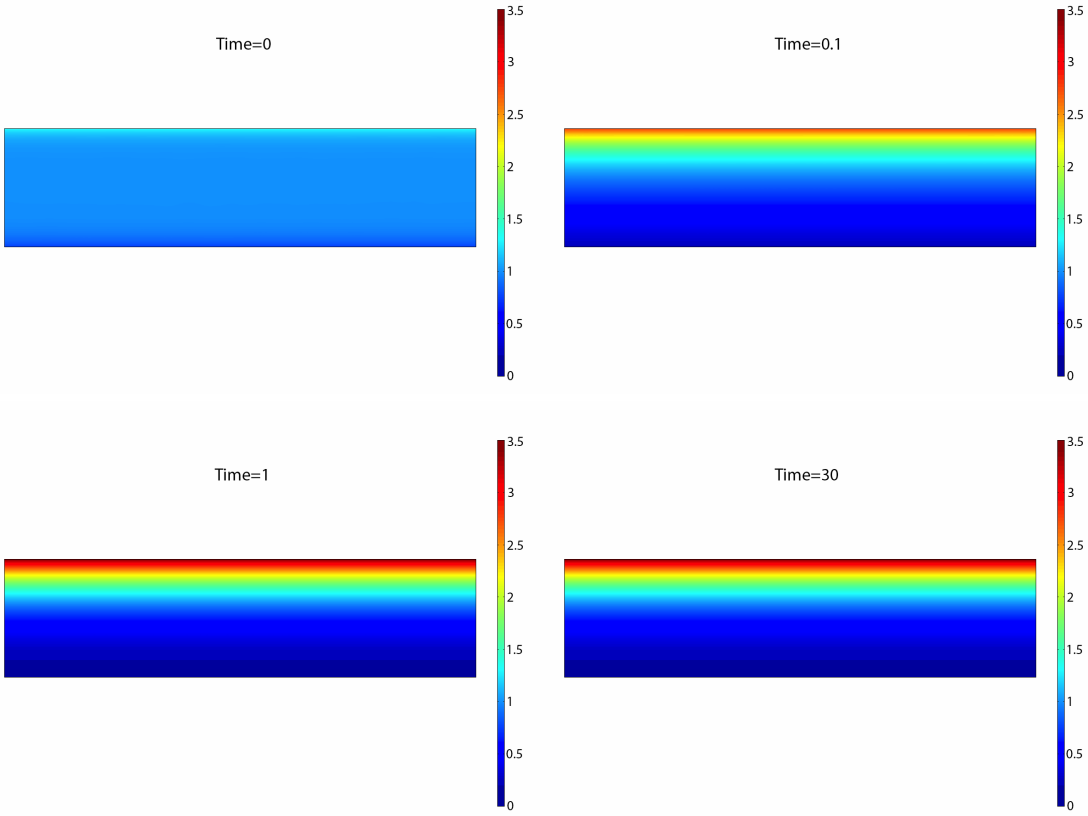


Figure 5.3: Shallow chamber ($H = 0.1$cm) showing the formation of a dense layer of cells at the fluid surface but no bioconvection patterns. Solution of system (5.12) in 2-D showing cell density, $n$, for $t = 0..10$. The chamber is approximately 0.2cm wide. Dimensional times can be found by multiplying the given times by $\frac{H^2}{D_N} \approx 1.6$ min. Colours for each plot correspond to the values shown in the given colour bars. Parameter values used are taken from Table 5.1.

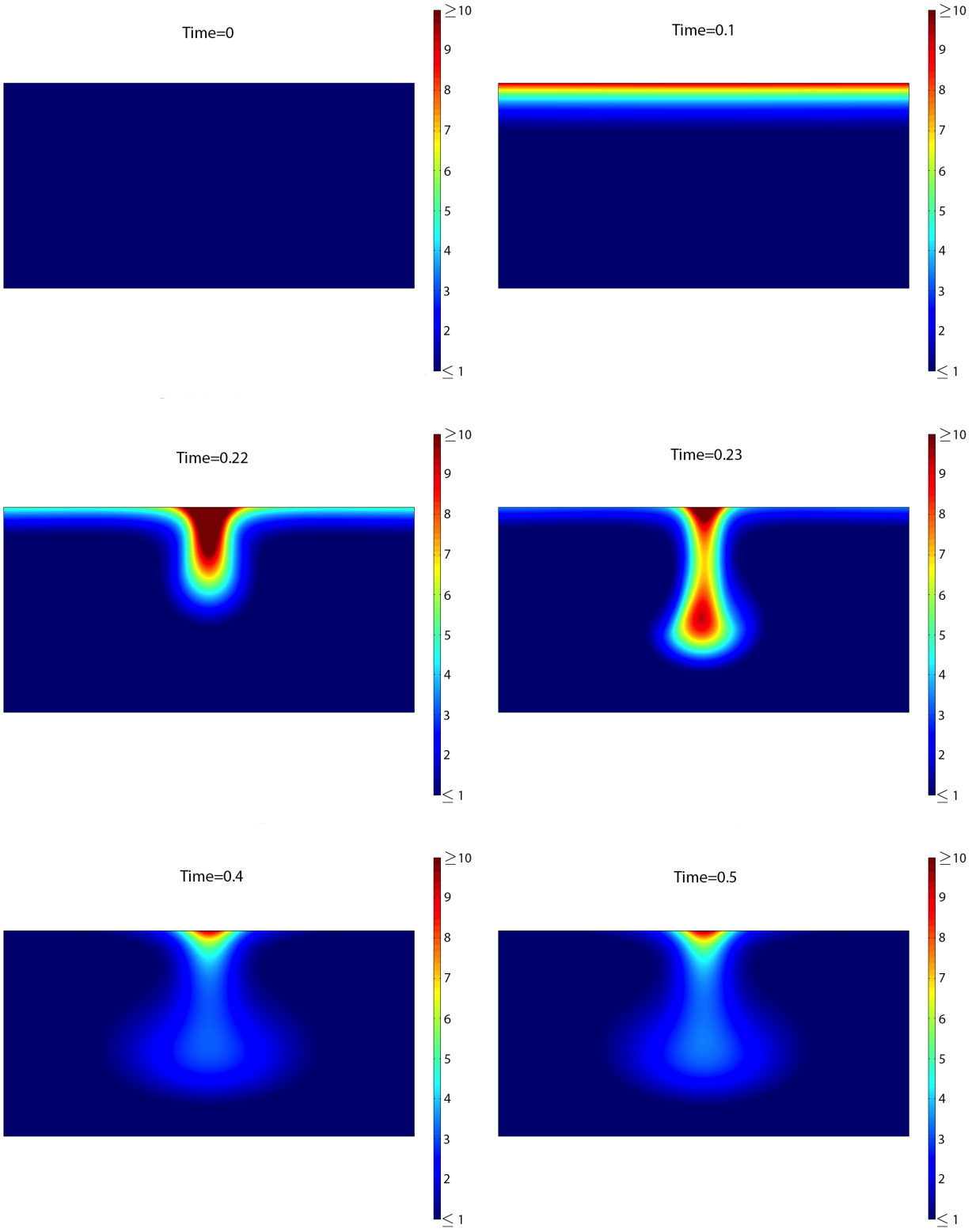


Figure 5.4: Formation of a single bioconvection plume for $H = 0.3$cm. Plots show cell density solutions, $n$, of system (5.12) in 2-D for $t = 0..0.5$. The chamber is 0.6cm wide. Dimensional times can be found by multiplying the given times by $\frac{H^2}{D_N} = 15$ min. Colours for each plot correspond to the values shown in the given colour bars. Parameter values used are taken from Table 5.1.

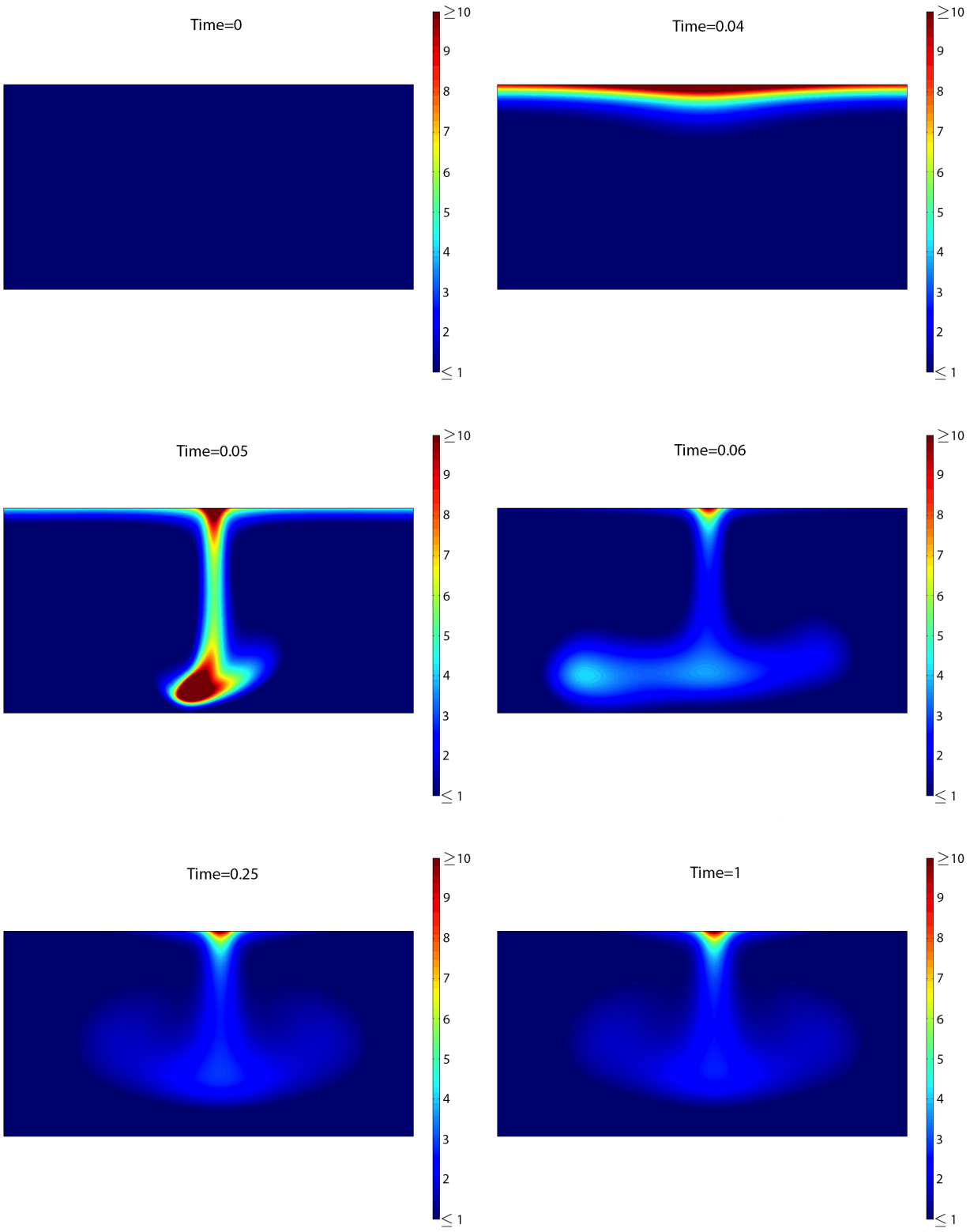


Figure 5.5: Formation of a single bioconvection plume for $H = 0.5$cm. Plots show cell density solutions, $n$, of system (5.12) in 2-D for $t = 0..1$. The chamber is 1cm wide. Dimensional times can be found by multiplying the given times by $\frac{H^2}{D_N} \approx 40$ min. Colours for each plot correspond to the values shown in the given colour bars. Parameter values used are taken from Table 5.1.

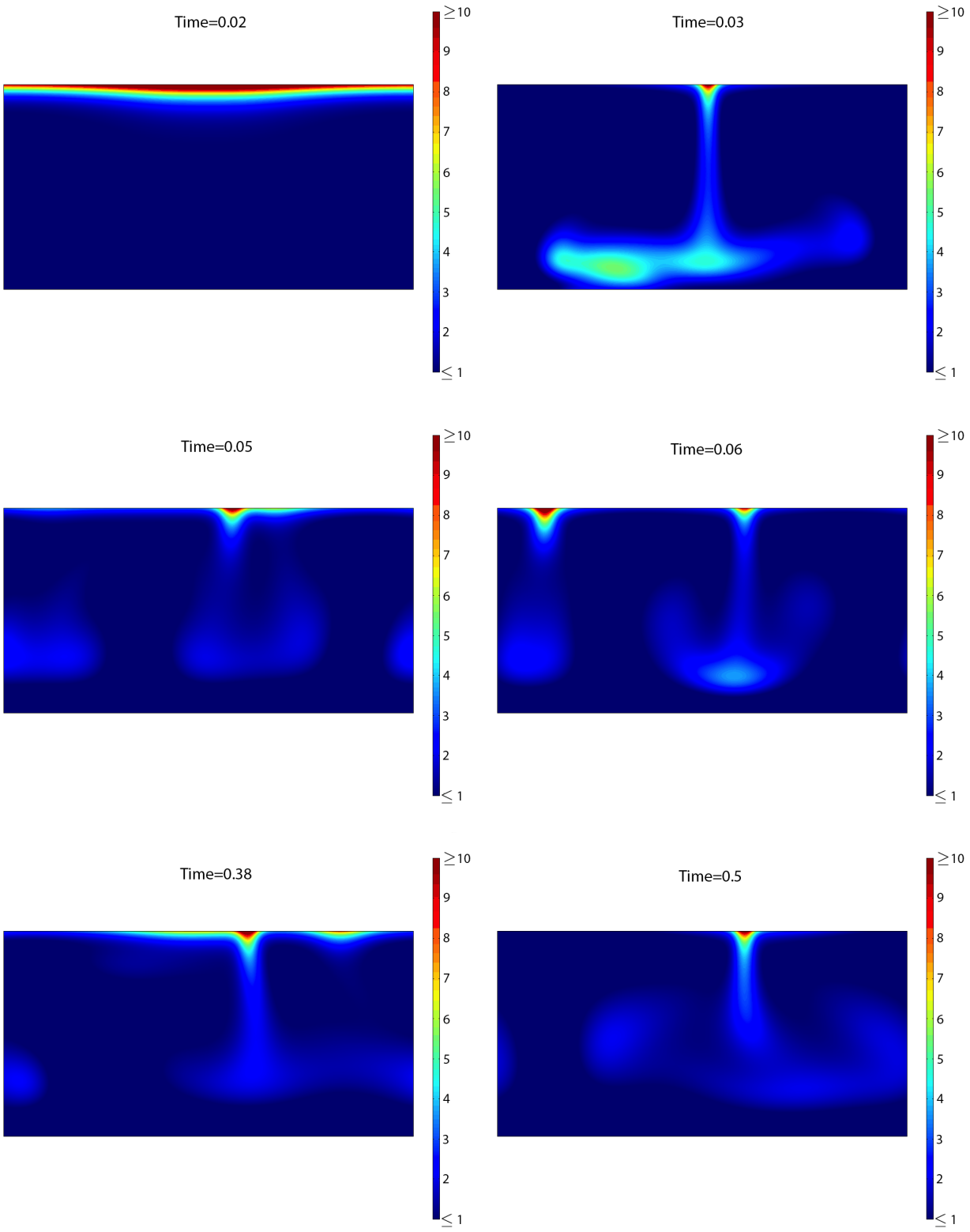


Figure 5.6: Unstable bioconvection for $H = 0.7$cm. A single plume forms and splits into two, which subsequently re-merge. Plots show cell density solutions, $n$, of system (5.12) in 2-D for $t = 0..0.5$. The chamber is 1.4cm wide. Dimensional times can be found by multiplying the given times by $\frac{H^2}{D_N} \approx 80$ min. Colours for each plot correspond to the values shown in the given colour bars. Parameter values used are taken from Table 5.1.

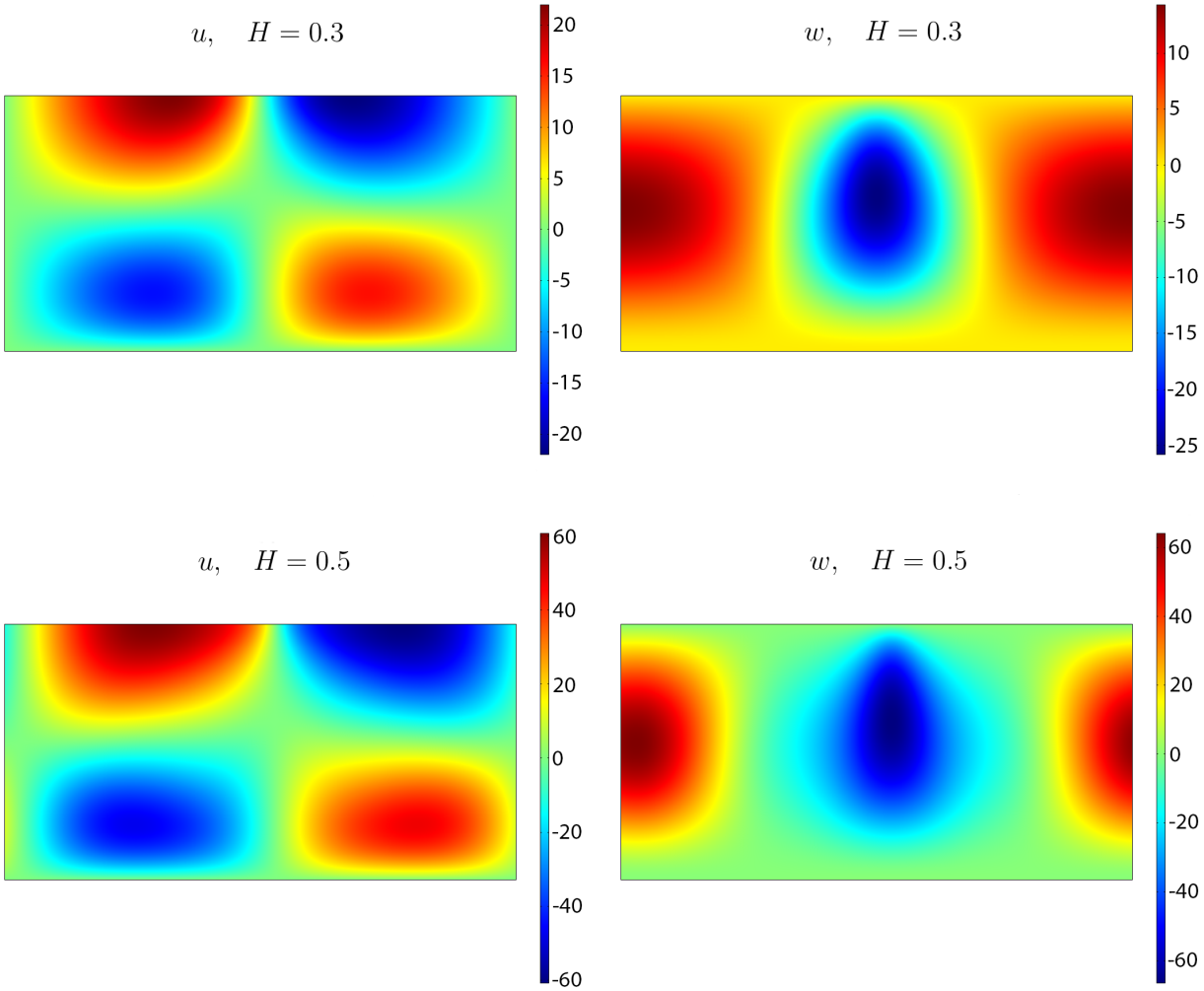


Figure 5.7: Fluid convection for $H = 0.3$cm and $H = 0.5$cm. Plots show fluid horizontal and vertical fluid velocity solutions, $u$ and $w$, of system (5.12) in 2-D after a plume has fully formed. Velocities are shown for $H = 0.3$cm at $t = 0.5$ (top) and $H = 0.5$cm at $t = 1$ (bottom). The convection pattern is approximately symmetric about $x = L/2$, where $L$ is the width of the chamber. Colours for each plot correspond to the values shown in the given colour bars. The region of greatest downward velocity is in the centre of the plume and the greatest horizontal velocity is at the fluid surface. Parameter values used are taken from Table 5.1.

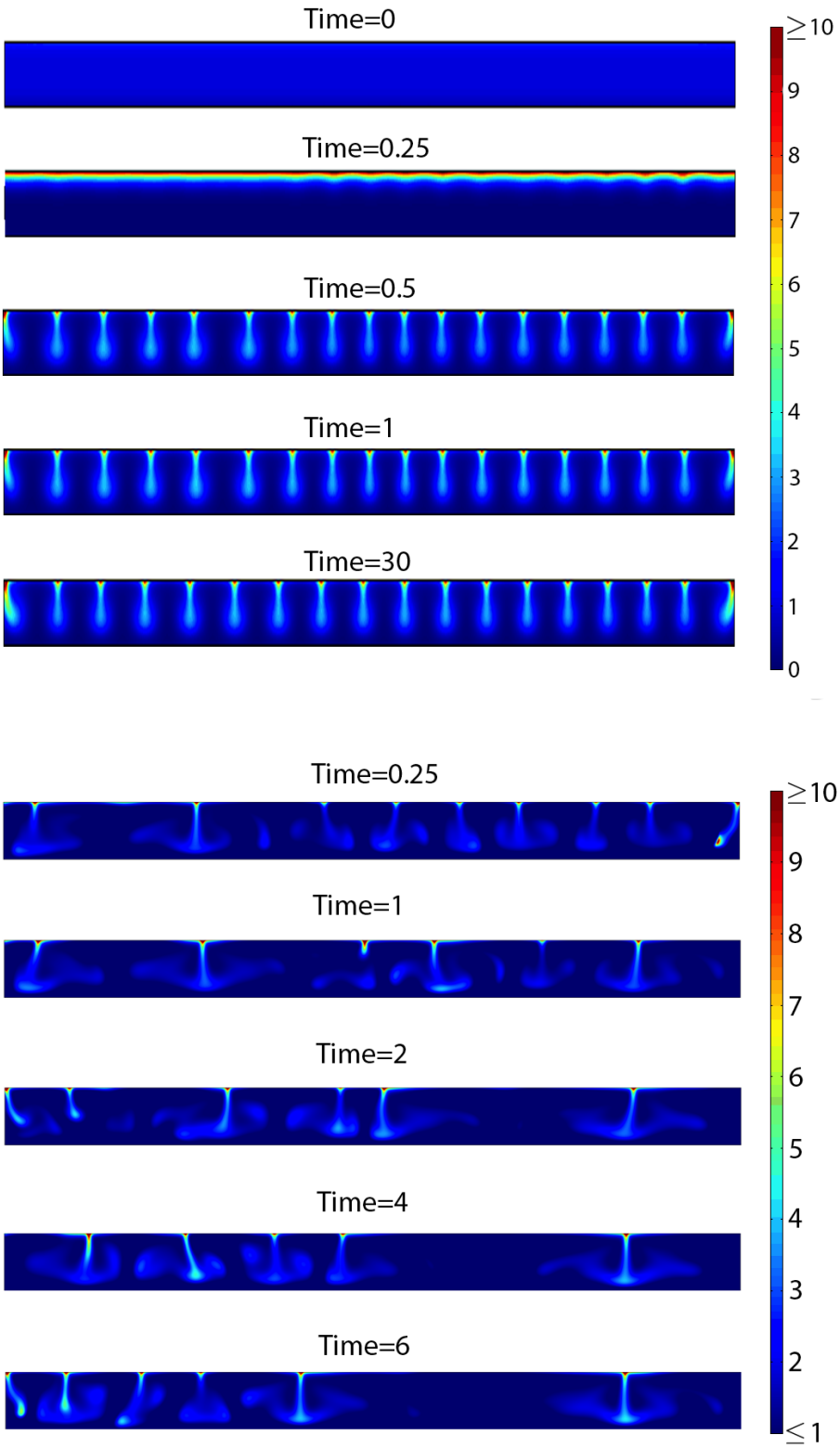


Figure 5.8: Bioconvection in shallow and deep chambers with width 9cm. Plots show cell density solutions, $n$, of system (5.12) in 2-D in a wide chamber for $H = 0.3$cm (top) and $H = 0.7$cm (bottom). A shallow chamber produces a steady array of plumes and a deep chamber produces continually evolving, unstable plumes. Both simulations are run for approximately eight hours in dimensional time and all parameter values are taken from Table 5.1. Images with $H = 0.3$cm have been stretched in height to make patterns more clear.

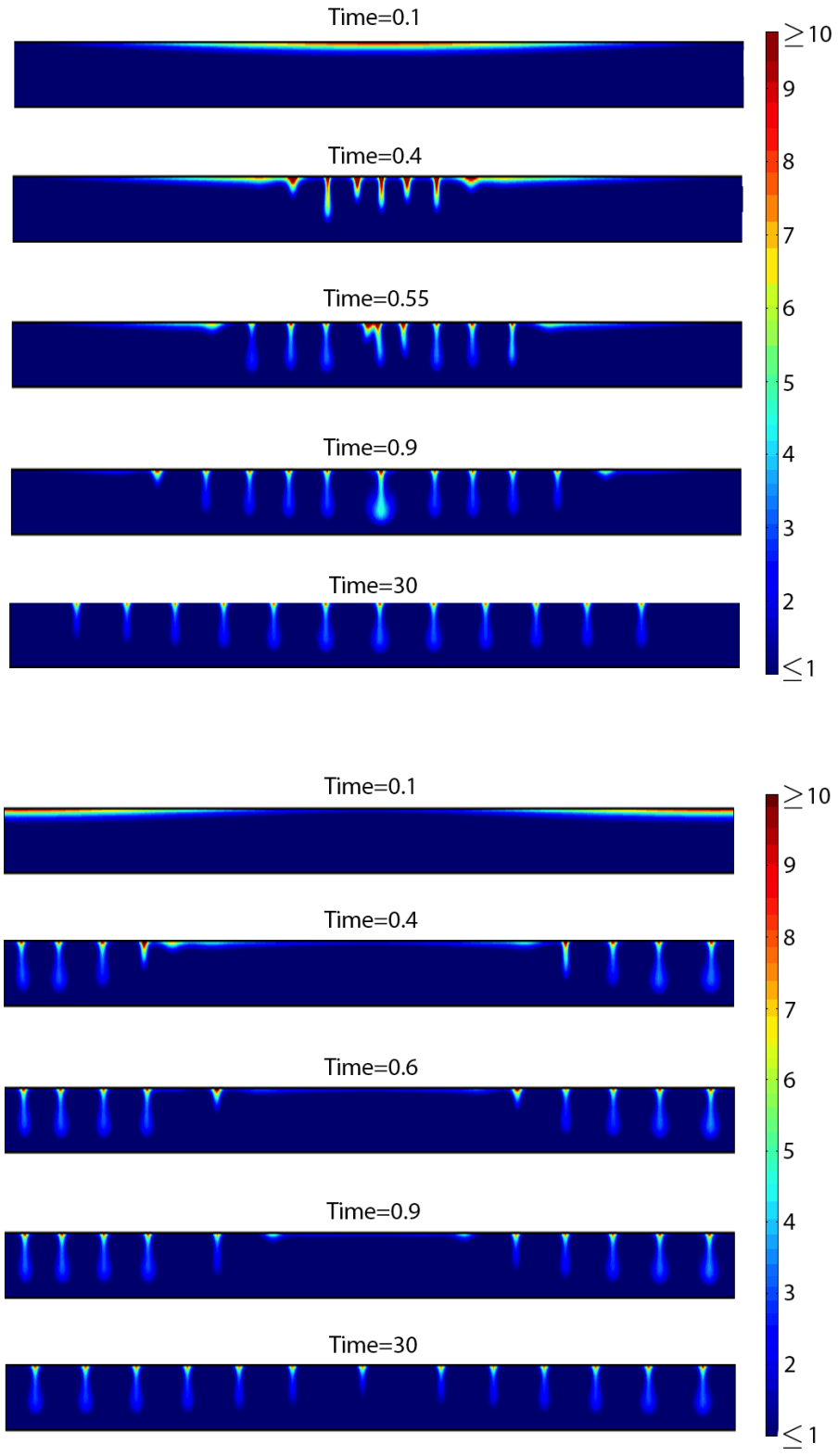


Figure 5.9: Bioconvection in a wide chamber for non-uniform initial data. Solution of system (5.12) in 2-D showing zoospore density, $n$, with zoospores initially concentrated in the centre of the domain (top) and at the sides of the domain (bottom). Initial data was set as $n_0 = e^{-0.01(x-15)^2}$ (top) and $n_0 = e^{-0.01x^2} + e^{-0.01(x-30)^2}$ (bottom). In both cases plumes form fastest in the areas of highest zoospore concentration and drift outwards until a stable pattern is reached. Both simulations are run for approximately eight hours in dimensional time and all parameter values are taken from Table 5.1 with $H = 0.3$cm. All images have been stretched in height to make patterns more clear.

Figure 5.8 shows the formation of multiple plumes in a wide chamber, representing a cross section (9 cm) of a petri dish commonly used in experiments. Boundary conditions are as in (5.13), i.e. the sidewalls are set as solid boundaries. We show the zoospore density solution for a shallow and deep chamber, with $H = 0.3$cm and $H = 0.7$cm. The dimensional time scale for both of these is approximately eight hours. In the shallow chamber, eighteen discrete plumes are formed and the total number of plumes remains constant, with only slight shifting of plume positions after long times. Two of these plumes lie at the boundary and appear distorted in comparison with those away from the edge. This distortion is simply a numerical artefact due to the no-slip boundary conditions and we do not observe this behaviour in experiments. The final state of the system appears to be steady with evenly spaced plumes. In the deep chamber ($H = 0.7$), the plumes formed are unstable as is expected. The pattern wavelength is generally larger than in the shallow case, but crucially the solution is constantly evolving and no steady plume arrangement is reached. Moreover, the plume number fluctuates as plumes can merge or occasionally dense blobs break off and form separate plumes. The observation of steady plumes in a shallow chamber and unsteady plumes in a deep chamber is consistent with the previous investigations of gyrotactic bioconvection discussed above. Figure 5.9 shows the evolution of bioconvection patterns for non-uniform initial data for a shallow chamber ($H = 0.3$). By prescribing a high concentration of zoospores at the centre (top) and at the sides (bottom) of the domain, plumes form first in these regions and the pattern spreads out over time. The final plume arrangement in each case is steady.

Both the size and structure of individual plumes are in good agreement with experimental observations of auto-aggregation patterns. Although, the predicted zoospore densities within the centre and periphery of the plume are slightly higher than experimental measurements made by Ko and Chase in [71]. However, these quantities are not easily measured experimentally and there are many model parameters that have

been estimated and so these discrepancies are not a cause of concern. In Chapter 2, the suspension depth was found to have an effect on auto-aggregation patterns, i.e. the overall pattern wavelength increases as depth increases and high-density bands are seen in deeper suspensions (see Figure 2.3). In simulations, the increase in pattern wavelength is captured and there are band-like regions in the deep chamber simulation in Figure 5.8. Whether or not these correspond directly to bands in experiments is not clear but comparison is not unreasonable. Ochiai *et al.* reported that zoospores of the *Phytophthora citricola* species swim towards the centre of these bands [89]. Assuming this is also the case for *P. infestans* zoospores, this means that bands are intrinsically three dimensional structures and cannot properly be captured or represented in a 2-D simulation.

One critical element of auto-aggregation we are interested in, the drifting of plumes observed in experiments with shallow suspensions (see Figures 2.5 and 2.6), is certainly not captured here: plume arrangements are consistently steady after long times. In Chapter 2, we discussed that the arrangement of spots could be altered through initial fluid mixing (see Figure 2.2). The simulations shown in Figure 5.9 confirm that the initial distribution of aggregates is not important to the evolution of bioconvection patterns, as plumes are seen to spread out over time, and do not drift together. We now investigate the solutions of the full bioconvection-chemotaxis model in the next section.

### 5.4.2 Bioconvection and Chemotaxis

Simulations without any chemotactic effects present and in a wide chamber show that multiple plumes form that appear to be steady. Since plumes in deeper chambers have been shown to be unstable anyway, we are only interested in shallow chambers in this section. Specifically, we would like to determine whether chemotaxis can destabilise

such a state, with chemotactic effects taking place over much longer time scales than bioconvection. To start, we consider a small section of the full domain in order to observe plumes in detail. Initial conditions are as above with $c_0(x,z) = 0$. Boundary conditions are as given in (5.13) but with periodic conditions at the vertical sidewalls to minimise their effect on the solution.

Figure 5.10 shows the formation of three plumes with $\chi = 0$ from random initial data. These plumes appear to be steady as they do not move over long times. The same setup but with $\chi = 4.86$ (see Table 5.1) is shown in Figure 5.11. Here, three plumes are again formed initially but those at the left and in the middle merge into one. Just before merging takes place, the smaller of the two plumes appears to be distorted as it gets closer to the larger, middle plume ($t = 2.2$). Otherwise, the overall structure of the plumes is kept roughly intact as they move. Subsequently, the two remaining plumes start to drift together and finally only one remains near the centre of the domain ($t = 5$). This final plume is steady and the zoospore density within it as well as its overall size is slightly greater than that in comparison to that of the three that formed initially.

Next we examine effect of chemotaxis in the full-sized chamber with width, $L = 9$ cm. The boundary conditions used are as given in (5.13) and we assume again that $c_0(x,z) = 0, \mathbf{u}_0(x,z) = 0, p_{e0}(x,z) = 0$ and $n_0 = 1 + \varepsilon(x,z)$, where $\varepsilon$ is a small, random perturbation applied at each mesh point. The plume formation in the absence of chemotaxis can be seen in Figure 5.8 and has been discussed above. A simulation with $\chi > 0$ for the default parameter set in Table 5.1 is shown in Figure 5.12. It can be seen that this change has a dramatic effect on the solution. Initially, over twenty plumes form, which is again a greater number than in the $\chi = 0$ case. [Note: it is very probable that this change could be quantified through linear analysis of the model, i.e. we expect that the predicted initial pattern wavelength would vary with $\chi$]. Plumes then begin to drift together and seem to split into three groups on the left, middle and right of the domain. Eventually, the final image shows three, dense plumes after approximately

two and a half hours. The second plot shown in Figure 5.12 illustrates that the choice of parameter values also seems to be important. That is, for a slightly reduced value of $\chi$, plumes drift towards one another but do not merge even after very long times ($\approx 25$ hours), with the exception of those closest to the left boundary. Therefore, it seems that the chemotactic effect has to be sufficiently strong in order to break through the opposing fluid motion that acts to keep plumes separate. Decreasing the diffusion ratio, $D$ or increasing the chemoattractant degradation rate has a similar effect on solutions.

In comparison with experimental data, the simulations have many encouraging features. For instance, when two or more plumes merge, the composite plume that results is slightly larger and more dense than the individuals. This can be seen in experiments, e.g. in Figures 2.5 and 2.6 where plumes at later times appear brighter (more dense) and larger than those formed initially. The predicted speed of plume drifting and merging also seems to lie within a realistic range. In the simulation shown in Figure 5.11, plumes formed at the left and at the centre that were a distance of 0.6cm apart initially and subsequently drifted and merged over a period of thirty minutes. We reported a similar situation in Chapter 2 where two plumes drift and merge over a distance of 0.78cm in twenty five minutes (see Figure 2.6).

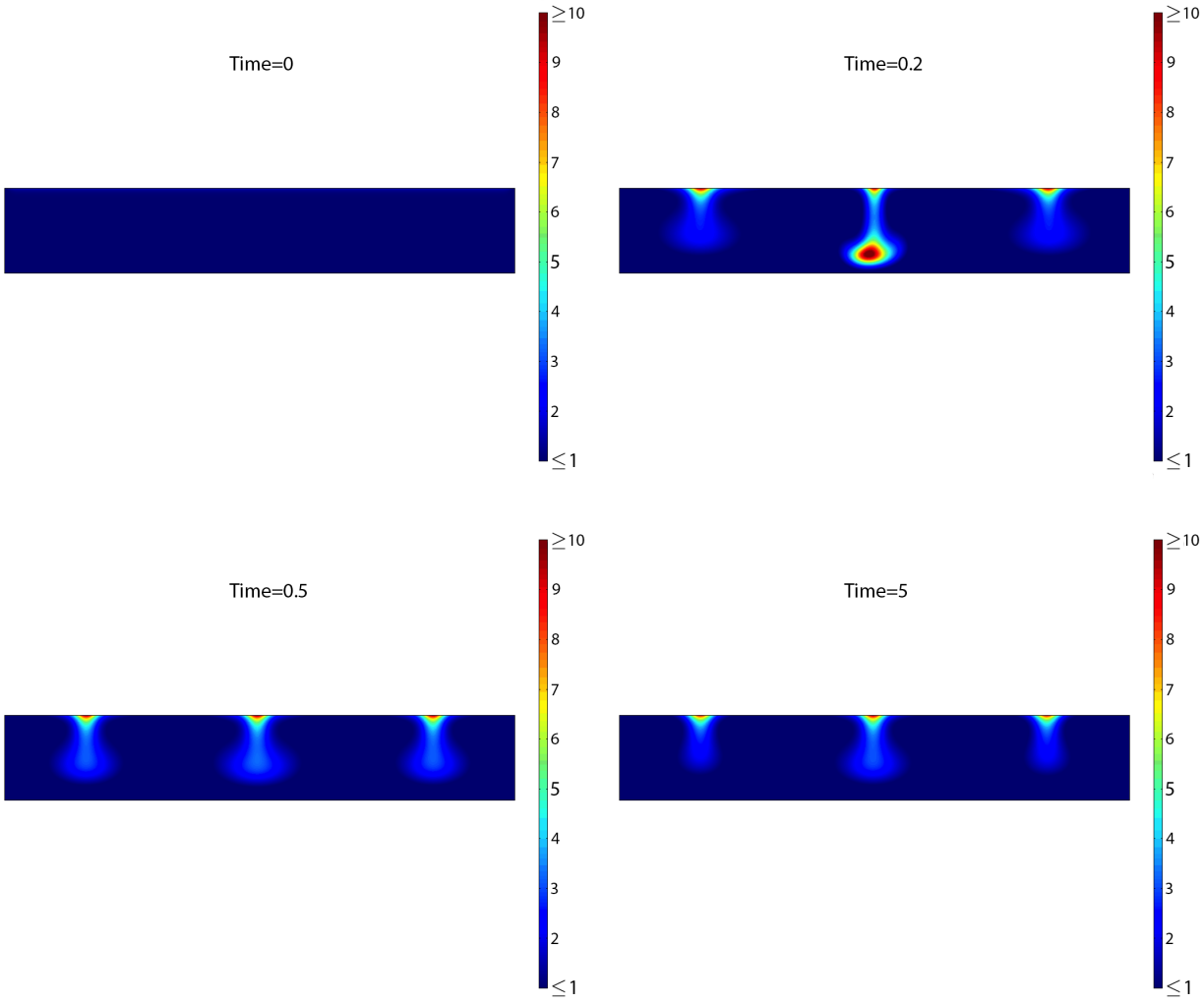


Figure 5.10: Bioconvection with no chemotaxis showing the formation of steady plumes. $H$=0.3cm and the chamber is approximately 1.8cm wide with periodic boundary conditions at the vertical walls. Plots show cell density solutions, $n$, of system (5.12) in 2-D for $t = 0..5$. Three plumes form and remain stationary after long times. Dimensional times can be found by multiplying the given values by $\frac{H^2}{D_N} = 15$ min. Colours for each plot correspond to the values shown in the given colour bars. $\chi = 0$ and all other parameter values are as in Table 5.1.

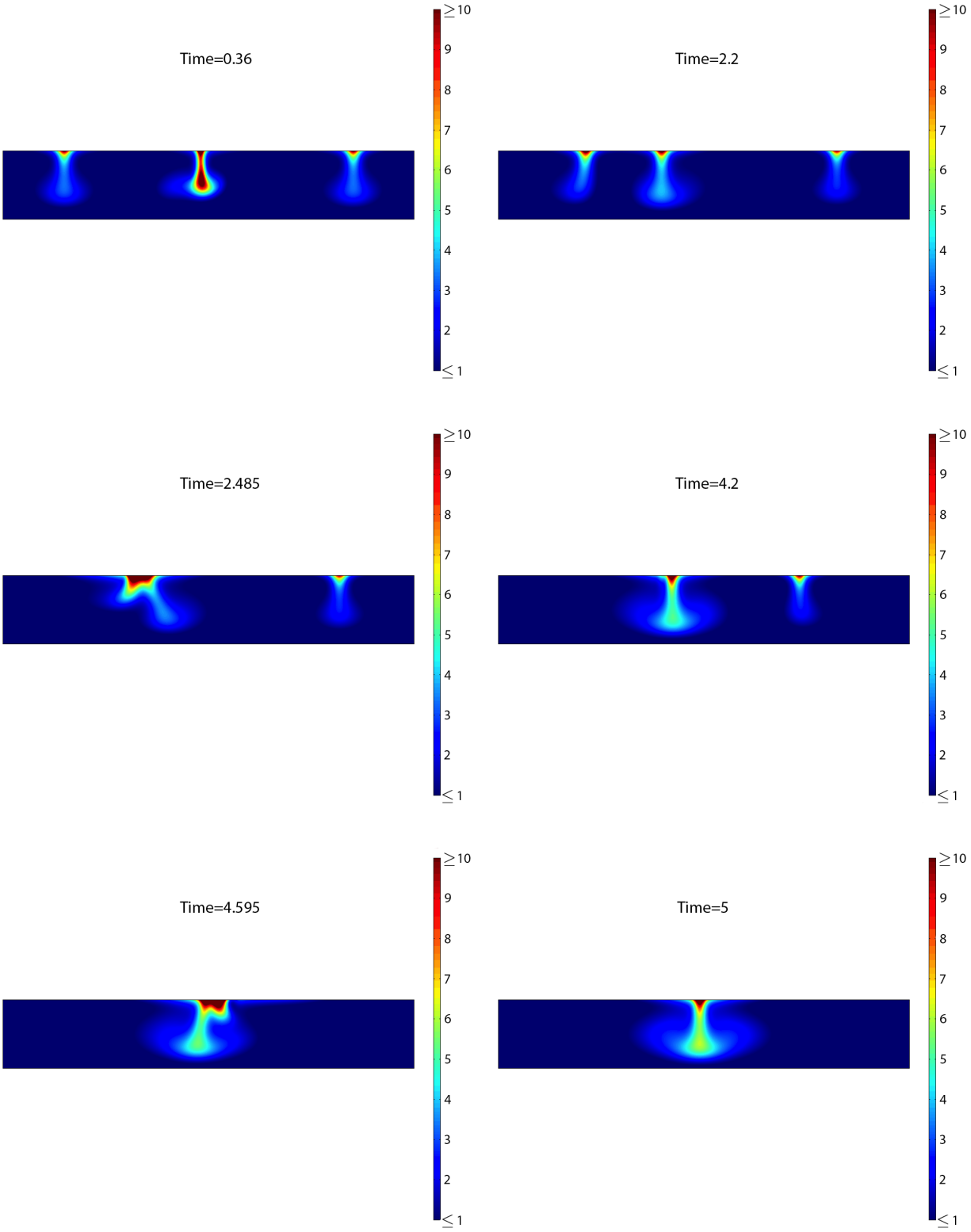


Figure 5.11: Bioconvection with chemotaxis showing plume formation and merging. $H$=0.3cm and the domain is approximately 1.8cm wide with periodic boundary conditions at the vertical walls. Plots show cell density solutions, $n$, of system (5.12) for $t = 0..5$. Dimensional times can be found by multiplying the given values by $\frac{H^2}{D_N} = 15$ min. Colours for each plot correspond to the values shown in the given colour bars. Parameter values used are taken from Table 5.1.

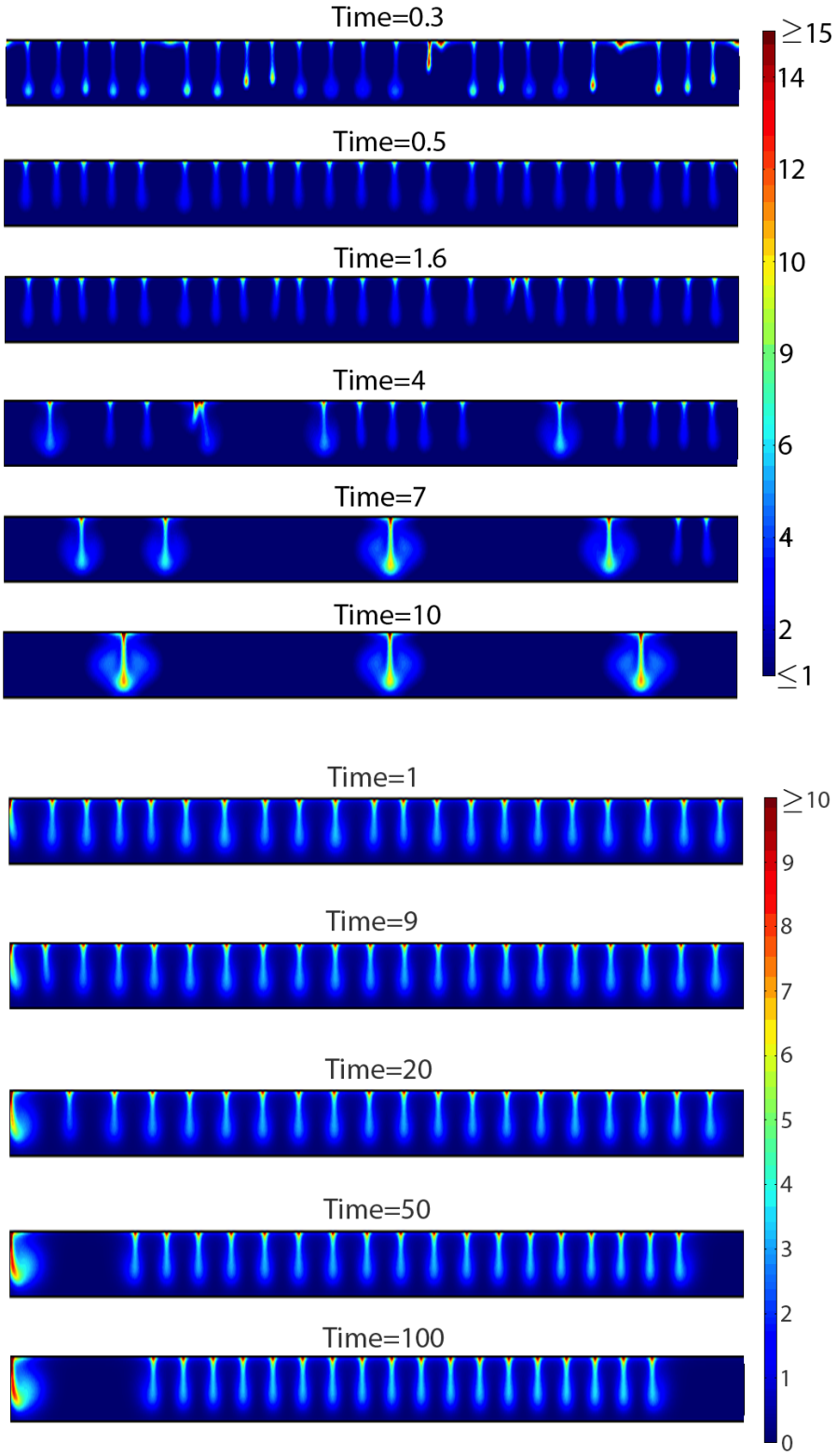


Figure 5.12: Bioconvection and chemotaxis in a wide chamber. $H = 0.3$cm and the chamber is 9cm wide. Plots show cell density soluitons, $n$, of system (5.12) in 2-D. Plumes drift and merge for $\chi = 4.86$ (top) and do not merge for $\chi = 3$ (bottom). All other parameter values are taken from Table 5.1. Dimensional times can be found by multiplying the given times by $\frac{H^2}{D_N} = 15$ min. All images have been stretched in height to make patterns more clear.

### 5.4.3 Plume Formation in 3-D

Obtaining numerical simulations of bioconvection in 3-D is very computationally expensive since a high number of mesh points are required in spatial dicretisation. Nonetheless, the study of such solutions is of interest given that bioconvection patterns are, of course, three dimensional. There has been just one such study that we are aware of by Ghorai and Hill [45], where the formation and stability of single plumes in deep chambers was considered.

We use COMSOL to solve system (5.12) in a 3-D domain with square cross section defined by $x, y \in [0, \frac{L}{H}]$ and $z \in [-1, 0]$. We impose periodic boundary conditions at the sidewalls and all other boundary conditions are given by

$$\begin{aligned} \mathbf{u} &= 0 \qquad \text{at} \qquad z = -1, \\ \mathbf{u}\cdot\hat{\mathbf{z}} = 0 \quad \text{and} \quad u_z = v_z &= 0 \qquad \text{at} \qquad z = 0, \\ \mathbf{J}_n\cdot\hat{\mathbf{z}} = \mathbf{J}_c\cdot\hat{\mathbf{z}} &= 0 \qquad \text{at} \qquad z = 0, -1, \end{aligned} \tag{5.24}$$

where $\mathbf{u} = [u, v, w]$ and other variables are as defined above. $\mathbf{u}_0 = 0, p_{e0} = 0, c_0 = 0$ and $n_0 = 1 + \varepsilon$, where $\varepsilon$ is a small, random perturbation.

Figure 5.13 shows the formation of a single plume with $\chi = 0$, $H = 0.3$cm and $L = 0.6$cm. As in the 2-D simulations above, a dense layer of cells forms at the fluid surface and becomes unstable. A steady plume then forms with shape and features similar to those in 2-D results above. The pointed shape seen for $n = 2$ once the plume has formed, we believe, is an artefact due to the boundary conditions and the fact that the pattern wavelength is slightly too large compared with domain size. This aside, the simulated plume features agree with experimental observation.

Study of the formation of single plumes is not particularly useful for our investigations. Of much greater interest is the study of the formation of multiple plumes and their interaction. Unfortunately, this is non-trivial and a large amount of computing power is required. The formation, drifting and merging of multiple plumes in 3-D with non-zero $\chi$ will be the subject of our upcoming work.

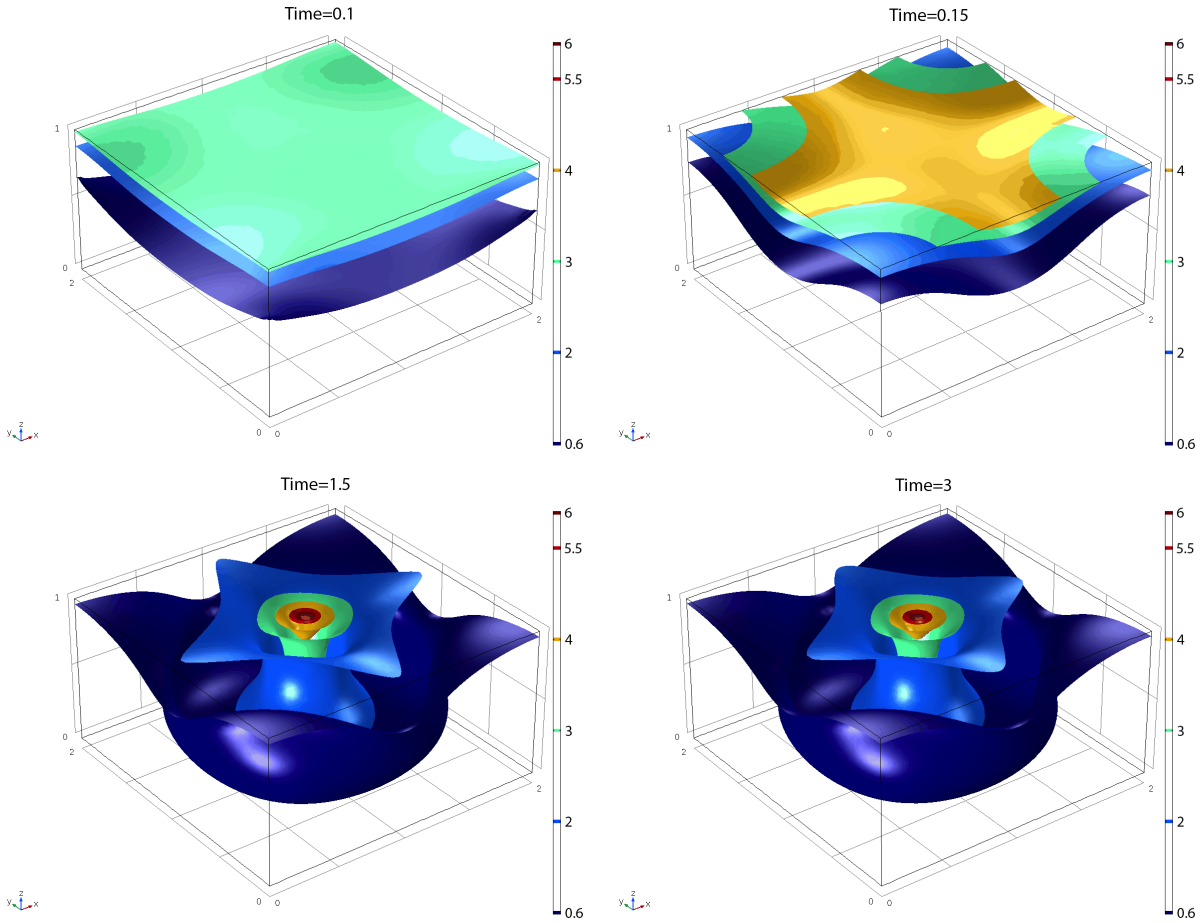


Figure 5.13: Formation of a single plume in 3-D. Isosurface plots show cell density solutions, $n$, of (5.12) for $t = 0..3$. $H$=0.3cm and the sides are 0.6cm in length. Dimensional times can be found by multiplying the given values by $\frac{H^2}{D_N} = 15$ min. Colours for each plot correspond to the values shown in the given colour bars. $\chi = 0$ and all other parameter values are as in Table 5.1.

## 5.5 Conclusions

In this chapter we have studied a mathematical model for zoospore auto-aggregation based on a combination of two distinct mechanisms: bioconvection and chemotaxis. The model was based on the bioconvection model of Pedley *et al.* [98] and coupled with the Keller-Segel type chemotaxis model discussed in Chapter 3.

The bioconvection process was studied in isolation first with $\chi = 0$. Based on results shown here and other reports in the literature, there can be little doubt that the spot formation in auto-aggregation experiments with *P. infestans* zoospores is the result of bioconvection. Single plumes could be formed in small chambers and the features of these plumes agreed well with experimental observations for varying values of $H$. Plumes viewed from above would show a high density spot in the centre surrounded by a lower density "cloud" of cells, exactly as observed in the experiments discussed in Chapter 2. Side-on photographs of aggregates shown in Chapter 2 also show the same structure as predicted here. We have shown that plume stability decreases with depth as reported in previous studies by various researchers. This is in line with our experimental observations as well. Plume formation was also studied in wide chambers, representing a cross section of a petri dish. The predicted number of plumes and the pattern wavelength is representative of the initial patterns observed in experiments. As depth increases, the pattern wavelength increases (see Figure 2.3).

The crucial difference between the simulations and experiments is that simulated plumes appear to be steady. That is, the number of plumes in the chamber remains roughly constant over approximately eight hours, which is the approximate time scale of auto-aggregation experiments. This is clearly different from our experimental observations, where it is seen that the plumes drift and merge. Therefore, it seems very unlikely that the large scale auto-aggregation phenomenon can arise from bioconvection alone.

We have found that by introducing chemotactic attraction between zoospores into the gyrotactic bioconvection model, arrangements of plumes that were previously steady are de-stabilised. The overall effect is that plumes slowly drift towards one another and hence the number of plumes is reduced over time, as seen in Figure 5.12. Moreover, the shape and increased density of plumes after merging is in agreement with our experimental observations (see Figure 2.5).

A logical way of testing our hypothesis, based on model predictions, would be to try and separate bioconvection from chemotaxis in experiments. For example, if chemotaxis could be removed from the system, we would expect to see the formation of bioconvective plumes that remain stationary after long times. One such method that we attempted was to use a calcium chelator, EGTA, to remove calcium from a zoospore suspension and observe any pattern formation. Given the importance of calcium in zoospore-cyst attraction, the assumption that calcium could be attracting swimming zoospores toward each other was reasonable. Unfortunately, calcium is also important for other cellular processes, including swimming. Therefore, we were unable to obtain conclusive results from the experiment as no auto-aggregation patterns were observed. The model also predicts that no bioconvection or chemotactic pattern formation occurs in sufficiently shallow chambers (see Figure 5.3). Our laboratory experiments with shallow zoospore suspensions ($H = 0.1$cm) also failed to produce patterns and so separating bioconvection from chemotaxis in this way does not seem possible. In the future, this may be achievable using genetic mutation, e.g. to alter zoospore geometry and suppress upswimming, or by varying gravity in the system using a centrifuge. Crucially, normal swimming behaviour would need to be preserved in such experiments for results to be meaningful.

In general, exact quantitative results are difficult to obtain from the model because of the dependance of its solutions on many, largely unknown, parameter values. The

importance of encystment is also unclear at this stage. In Chapter 2, we make comment that, over longer times, a sub-pattern of encysted cells can be seen. Given the scale of this sub-pattern, this would suggest that our assumption that the total number of zoospores is conserved may break down after long times. This may provide an explanation for the fact that we have been unable to obtain complete aggregation (reduction to one plume) within a realistic time scale thus far: reduced plume density after long times due to encystment may reduce the strength of the fluid convection sufficiently to allow chemotaxis to draw plumes together. The interaction of plumes with encysted cells due to zoospore-cyst attraction may also require investigation. Although the model is a good first approximation, we cannot expect to fully capture all aspects of auto-aggregation at this stage.

However, the fact remains that neither the model for gyrotactic bioconvection alone or other, more detailed bioconvection models for that matter, predict the slow drifting and reduction to a single plume seen in zoospore auto-aggregation experiments. The evidence presented here strongly suggests that chemotaxis between individual cells is capable of destabilising a steady arrangement of plumes in a shallow suspension and pulls them toward one another. Therefore, we believe that cell-cell chemotaxis in *P. infestans* zoospores is worthy of further experimental study and could well be an important factor in the overall infection process.

# Chapter 6

# Conclusions and Future Work

## 6.1 Conclusions and Discussion

In this thesis we have presented mathematical modelling and experimental evidence that the zoospore auto-aggregation phenomenon results from a combination of both chemotaxis and bioconvection. In order to do this we have taken a continuum modelling approach and studied two types of model in particular. The first was of Keller-Segel type, for which it was assumed that zoospores exhibit chemotactic attraction towards one another. The second was a model for bioconvection in microorganisms, for which we assumed zoospores swim upwards, on average, as a result of an offset centre of mass (gyrotaxis). Finally, we considered a combination of both these effects in what we believe to be the first bioconvection-chemotaxis model for zoospore auto-aggregation.

To motivate and inform the mathematical modelling in this thesis, we conducted a series of laboratory experiments, the results of which are reported in Chapter 2. We collected data on the behaviour of individual zoospores of *P. infestans* in a variety of

controlled conditions. Using video analysis, we observed that, much like many bacterial cells e.g. *E. coli*, zoospores swim in straight lines that are punctuated by tumbles that occur at random times. By using statistical analysis, we classified zoospore swimming as a simple random walk, i.e. the length of straight runs were found to follow an exponential probability distribution. The orientation angle after tumbling also appeared to be random.

In addition to the behaviour of individuals, we studied the evolution of large-scale auto-aggregation patterns as well. We found that *P. infestans* zoospores exhibit aggregation patterns in a very similar manner to those described for *P. palmivora* zoospores by Ko and Chase [71]. The form of patterning observed varied with suspension depth, with the wavelength of patterns seen to increase with depth. On close inspection, the shape and structure of individual aggregates strongly indicated that they had been produced by bioconvection. We also concluded that the initial distribution of aggregates was explicitly dependent on the shape of experimental chamber used and implicitly dependent on the initial fluid motion. When a suspension was poured into a circular petri dish, a circular pattern was observed. Similarly, when a suspension was poured into a square dish, bands would form with a square outer ridge. By gently shaking a suspension in a circular dish from side to side, aggregates were clearly seen to form on the left and right side of this dish, which is presumably a consequence of greater zoospore concentration there. We therefore concluded that the initial distribution of aggregates could be affected by bulk fluid motion, but this was not an influence on subsequent pattern evolution.

A particular focus of our experimental work was on the evolution of zoospore auto-aggregation patterns over long time scales, which is a subject that has not been previously discussed. Our experiments consistently showed that after bioconvective plumes had formed, they drifted slowly toward one another. This drifting could continue over many hours, the end result being a reduction in the number of plumes by merging.

In light of the data that we obtained from our experiments, we hypothesised that a likely explanation for the drifting of aggregates over long times was chemotactic attraction between zoospores. For this to be true, chemotaxis must work at a much slower rate than bioconvection, as the drifting plumes are kept more or less intact. Given that the fluid motion within bioconvection plumes has been reported to be faster than cell swimming speed, this is reasonable. We therefore predicted that zoospore auto-aggregation is likely to be a two stage process. First, the zoospores swim to the surface of the fluid (most likely due to gyrotaxis) and form bioconvective plumes due to gravitational instabilities. If indeed the zoospores are releasing a chemical attractant, the second stage would be that the plumes will be drawn together over time due to the chemical gradients that will form between aggregates.

In Chapter 3, we calibrated and studied a minimal model for chemotactic zoospore aggregation. This model was of Keller-Segel type with an added volume-filling term. Our aim was to ascertain whether the density patterns presented in Chapter 2 could result from the self-chemotaxis of zoospores to each other, without the influence of external effects.

Results of numerical simulations showed that it was indeed possible to obtain a realistic number of zoospore density peaks (aggregates) by tuning model parameters. Qualitatively, these results had several features in common with observed auto-aggregation in experiments. Aggregates in two and three dimensional simulations were circular (or spherical) in shape and did drift towards one another after long times (far longer than the time required for initial patterns to form). However, the patterns generated by the model were independent of the domain shape and 3-D simulations in particular revealed that aggregation occurred uniformly in the vertical direction, unlike the patterns observed in experiments. Certainly, aggregates of similar structure to those discussed in Chapter 2 could not be obtained. Moreover, the predicted time scale for the evolution of these patterns was vastly unrealistic, with drifting of aggregates taking place

over time scales equivalent to several days as opposed to the observed time scale of hours. We deduced that a quantitative agreement between solutions of the chemotaxis model and experiments was not possible with realistic parameter values. Therefore, we concluded that chemotaxis could only reasonably be considered a partial contributor to zoospore auto-aggregation patterns at most.

In Chapter 4, we digressed to explore the mathematics of the volume-filling chemotaxis model in greater detail. Using bifurcation analysis and phase plane arguments, we were able to derive conditions on model parameters for the existence of $p$-step steady-state solutions. In fact, the number of steady states that exist for given parameters exactly equals the number of unstable modes predicted by linear analysis. Whether or not this holds in general remains open. We also found that there is a strong connection between the stability of spatially uniform solutions and the existence of non-uniform solutions. Specifically, the necessary condition for a linearly unstable uniform state and the necessary condition for non-uniform solution existence were shown to be identical, meaning the latter cannot exist without the former. The stability of spatially non-uniform solutions was investigated through linear analysis. This revealed that $p$-step solutions are "metastable", i.e. all steady states are unstable for $p \geq 2$ with the number and magnitude of associated positive eigenvalues decreasing with $p$. Hence, the general evolution of the system is towards a 1-step steady state, which is linearly stable.

Returning to the study of auto-aggregation, we studied a combined bioconvection-chemotaxis model in Chapter 5. The model was based on the bioconvection model of Pedley *et al.* [98] and coupled with the Keller-Segel type chemotaxis model discussed in Chapter 3. Having studied 2-D solutions of the bioconvection-chemotaxis model without chemotactic effects ($\chi = 0$), we concluded that the spot and band pattern formation seen in auto-aggregation and reported in Chapter 2 are indeed the result of zoospore bioconvection. The shape and structure of simulated plumes agreed well with

experimental observations for shallow and deep suspensions. Plume stability was also correctly predicted to decrease with depth. However, a critical difference between the simulations and experimental observations was seen when solutions in a wide chamber were considered, i.e. a chamber with width equal to the diameter of a petri dish used in experiments. Multiple plumes would form that remained steady after long times. This is certainly not what we observed in experiments as plumes were seen to drift together and merge until a single plume remained. By varying initial data, we investigated the effect of a non-uniform initial distribution of zoospores that could be induced by mixing (as reported in Chapter 2). By prescribing a high initial zoospore density at the centre and sides of the domain, plumes form preferentially in these regions and were then seen to spread out to form a regular pattern, and certainly did not merge. We do not believe, therefore, that the initial distribution of aggregates is important to the auto-aggregation process. We concluded that it was very unlikely that bioconvection alone was sufficient to describe zoospore auto-aggregation.

By studying solutions of the full bioconvection-chemotaxis model ($\chi > 0$), we were able to test our hypothesis that auto-aggregation arises as the result of both of these processes. Again considering 2-D solutions in a wide chamber, we found that by introducing chemotactic attraction, arrangements of plumes that were previously steady are de-stabilised. The overall effect was that plumes slowly drifted towards one another and hence the number of plumes was reduced over time. Moreover, the shape and increased density of plumes after they had merged was found to be in qualitative agreement with our experimental observations. Our main conclusion from these results was that zoospore auto-aggregation is far more likely to be the result of a combination of bioconvection and chemotaxis than either of these processes in isolation.

Bioconvection and chemotaxis are both concentrative phenomena. Therefore it is intuitive to imagine that both of these processes would lead to zoospore populations in a

natural environment becoming more dense and hence promote a higher rate of infection at suitable sites. For *P. infestans* zoospores in the context of infection, a common and important situation to consider is a population of zoospores confined to a water droplet on a plant leaf. If this droplet were suspended underneath a leaf, for example, then the upswimming of and accumulation of zoospores at the water-solid interface would have an obvious advantage. For a water droplet on the top of a leaf, the implications are less clear however some interesting results have been reported that may be of particular relevance. A study by Dombrowski *et al.* of the bioconvection of *Bacillus subtilis* cells in water droplets (1cm across) have shown that plumes formed at the surface in the centre of the drop move down the slanted meniscus [32]. This in turn leads to a high accumulation of cells at the narrow region at the edge of the water, air, solid boundary. If this were also the case for zoospores, accumulation of this type would presumably be advantageous as many zoospores would be brought into contact with the plant leaf. Perhaps also, given the high density in these regions, zoospore-zoospore chemotaxis would amplify this effect. Further experimental work and modelling in this area may yield useful results.

## 6.2 Future Work

### 6.2.1 General Comments

The work discussed in this thesis has raised a number of important questions that could form a rich area for further research. First and foremost, we have presented evidence that chemotaxis between zoospores is a factor in auto-aggregation and so experiments to investigate this further, such as chemotaxis assays for *P. infestans* zoospores, would be illuminating. Furthermore, experimental studies of bioconvection in ecologically relevant domains would also be of interest, e.g. in water droplets or a porous medium to

represent soil. Results from experiments such as these may help to determine the ecological impact of bioconvection and chemotaxis in zoospores' natural environments.

Mathematically, there are also many unanswered questions. The bioconvection-chemotaxis model could be developed further. Perhaps most importantly, the effect of zoospore encystment during zoospore auto-aggregation could be considered. In the model, this could be accomplished by introducing an evolution equation for cysts that assumes zero diffusion, the production of a (possibly new) chemoattractant and that cysts are produced at some rate proportional to the concentration of swimming zoospores. The flux of cysts would include advection with the fluid and since cysts are non-motile and relatively dense, they would sink. Suitable evolution equations could be of the form:

$$\frac{\partial A}{\partial T} = -\nabla \cdot \left[A\left(\mathbf{u} - gv(\rho_c - \rho_w)\hat{\mathbf{z}}\right)\right] + E(N,T)N, \tag{6.1}$$

where $A(\mathbf{X},T)$ is the concentration of encysted cells and $E(N,T)$ is a production term describing the rate of encystment, assumed to depend on the zoospore density and on time. All other variables are as described in previous chapters. Encystment is thought to be triggered by collisions and also when a zoospore's internal nutrient reserves are depleted. Hence the rate of encystment should be non-linear and would presumably increase with time and with zoospore density. Loss of zoospores due to encystment would need to be included in the cell evolution equation as $-E(N,T)N(\mathbf{X},T)$ as well as modification of the chemotactic flux to include attraction to the chemical, $C_1$. To complete the model, a final equation governing the evolution of $C_1$ is needed, for which it would be reasonable to assume linear production, degradation and diffusion.

Solutions of the bioconvection-chemotaxis model appear to have some interesting properties. Setting $\chi > 0$ was seen to increase the initial number of bioconvective plumes formed. Linear analysis of the model would perhaps provide a mathematical

explanation for this. The merging of peaks seems to occur for a range of parameter values related to chemotaxis ($\chi, D, r_d$) and through analysis it may be possible to determine conditions on parameters that guarantee the merging of plumes, and also how these conditions could depend on parameter values in the bioconvection model.

### 6.2.2 Modelling Individual Zoospores

In this thesis we have considered only continuous, deterministic models of zoospore movement. Whilst these are very helpful for studying large scale pattern formation, in the future it may be useful to examine the behaviour of individual cells using agent based modelling. This could be of particular use when studying auto-aggregation in the context of infection, where the effect of complex domains are of interest and more detail on zoospore movement could be included, e.g. flagella. Here, we outline some preliminary work for zoospore chemotaxis toward plant root exudates with this goal in mind.

NetLogo [85] is a multi-agent modelling package, which uses its own variant of the Logo programming language, simply called the NetLogo language. Originally developed for educational purposes, this language allows a great deal of flexibility and is well-suited for preliminary investigations. NetLogo is agent based, the two main types being: “patches” - square sections of the domain; and “turtles” - mobile agents that move within the grid of patches. Simulations can be carried out in 2-D, square domains.

We assume each cell moves a constant distance after each time step according to the direction it is facing. Also, we assume that each cell has some default probability of tumbling at the end of each time step that is mediated by the chemoattractant concentration. Each time step can be thought of as a Bernoulli trial, with probability

of success (tumbling) given by $p$. The probability of a run of a given length is then described by a geometric probability distribution (the discrete analogue of the exponential distribution discussed in Chapter 2). The orientation after a tumble is chosen at random from 1 to 360 degrees. Each cell has a memory of the chemical concentration at the previous patch it was in. If the concentration was greater in the previous patch, the tumbling probability is reduced and *vice versa*. Note this would perhaps be too simplistic when considering zoospore-zoospore chemotaxis as no account of the magnitude of chemical concentration is taken. Cell-cell collisions are taken into account by forcing a random tumble if two or more cells are found in the same patch. The chemical diffuses in space by equally distributing a fraction of the concentration value at a given patch to all neighbouring patches after each time step. Boundary conditions are taken to be periodic at all boundaries.

Figure 6.1 shows the chemotactic response of cells toward a point source of chemoattractant at the centre of the domain. As expected, cells aggregate in the centre where the chemical concentration is highest. In Figure 6.2 a more complicated situation is considered where the source of chemoattractant is a wound site on the right-hand side of a plant root. This root is shown in green and is impenetrable by cells: if a collision occurs, the cell tumbles. We see that after some time, cells have aggregated around the wound site. These early results provide a glimpse into possible future applications of an individual-based model for zoospore infection.

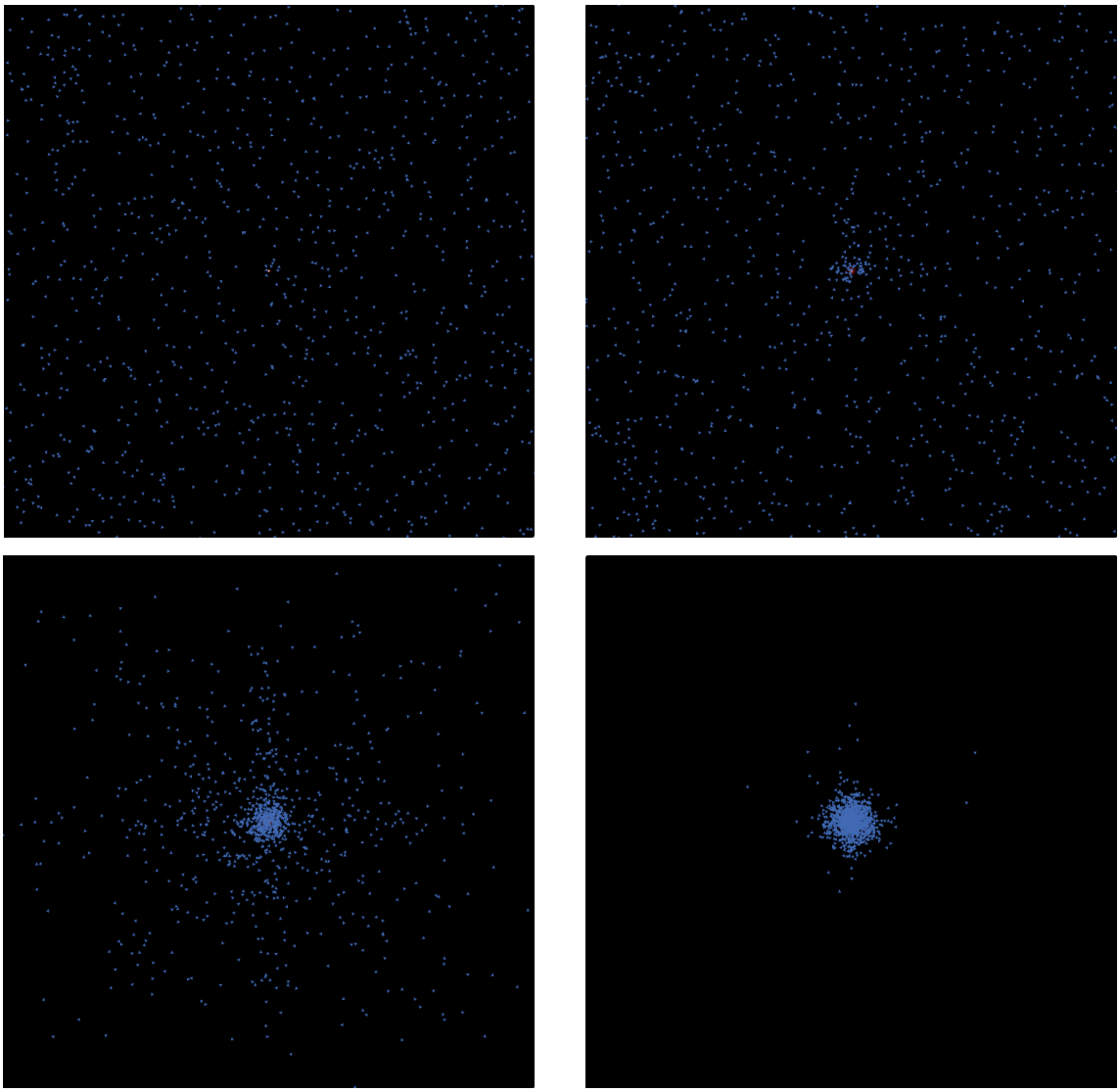

Figure 6.1: NetLogo output after 0, 100, 300 and 1000 steps from left to right. Initial setup is 1000 cells randomly positioned in space and with random orientation. Cells are shown in blue and chemical concentration in red. Cells aggregate at the point of greatest chemical concentration.

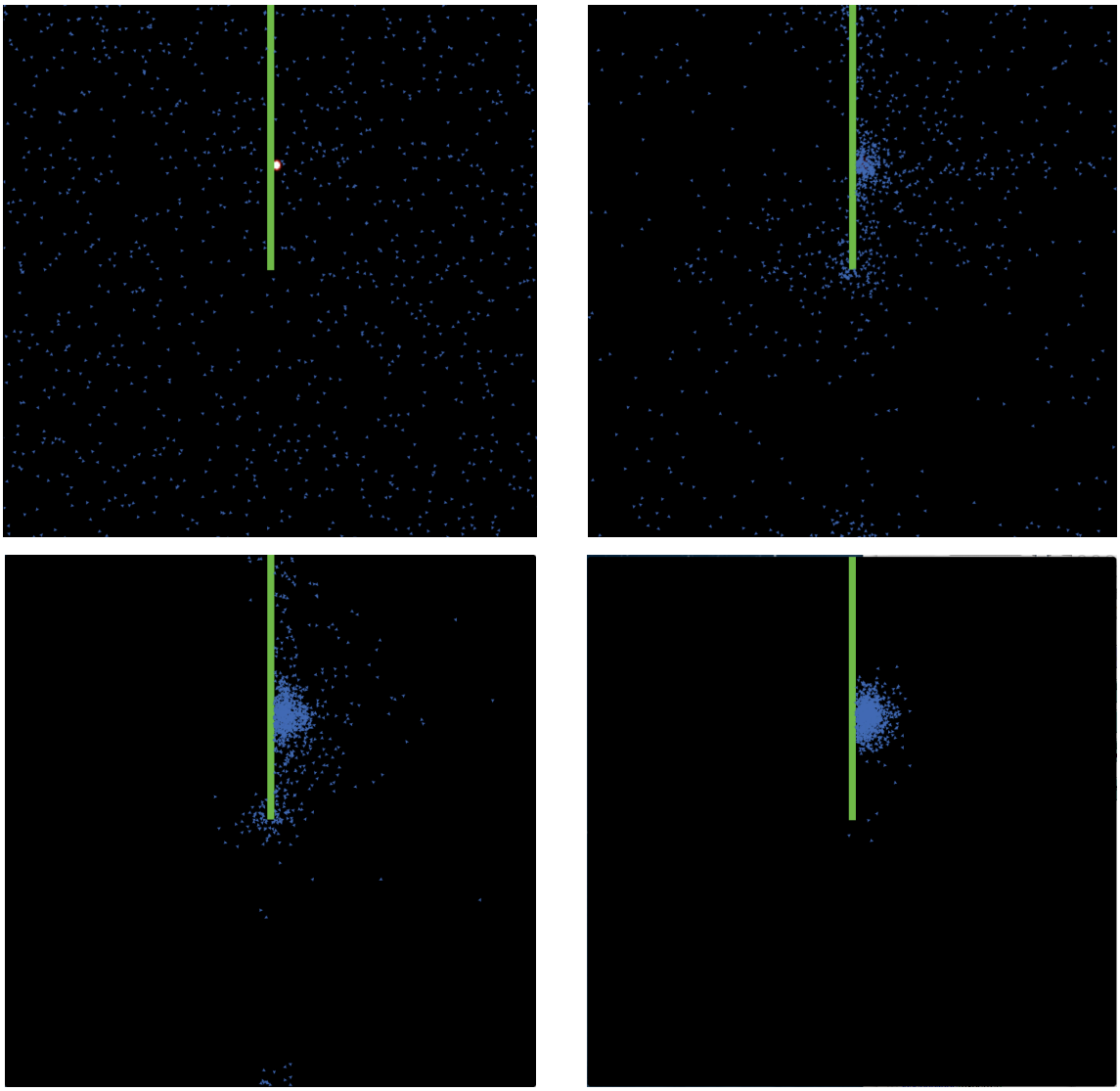

Figure 6.2: NetLogo output after 0, 450, 900 and 1500 steps from left to right. Initial setup is 1000 cells randomly positioned in space and with random orientation. Cells are shown in blue, chemical concentration in red and the plant root in green. Cells accumulate at a wound site on the right-hand side of the root.

# Chapter 7

# Appendix

## 7.1 MATLAB files

### 7.1.1 'Vfillsolve' Program

Program that uses the PDEPE solver to solve system (3.13) in 1-D and plot the results.

```
%%%%%%%%%%%%%%%%%%%%%%%%%%%%%%%%%%%%%%%%%%%%%%%%%%%%%%%%%%%%%%%%%%%%%%%%%%%%%%%%
function Vfillsolve
clc
clear all
close all

global D chi G gamma  %( Here G is the scaling factor Dv/beta*L^2)

% Set parameter values
D=10; gamma=3; G=0.004; chi=50;
```

```
deltax=5001;                % Number of grid points
tmax=500;                   % Maximum time
deltat=501;                 % Number of time points

% m is required by PDEPE and is set to zero in our case
% (see MATLAB documentation)
m=0;

% Define space and time vectors using spacings defined above
x=linspace(0,1,deltax);
t=linspace(0,tmax,deltat);

%-----------------------------------------------------------------------
% Set error tolerances
options=odeset('RelTol',1e-6,'AbsTol',1e-6);

% Call PDEPE
sol=pdepe(m,@vfill_pde,@vfill_ic,@vfill_bc,x,t,options);

% Extract Solutions from PDEPE output
n=sol(:,:,1);
c=sol(:,:,2);
%-----------------------------------------------------------------------
% Still Plots

figure(1);
```

```
subplot(3,2,1);
hold on
title('Time t =0');
xlabel('x');
plot(x,n(1,:),'r');
plot(x,c(1,:),'b');
hold off

subplot(3,2,2);
hold on
title(['Time t =',num2str(tmax/5)]);
xlabel('x');
plot(x,n((deltat-1)/5,:),'r');
plot(x,c((deltat-1)/5,:),'b');
hold off

subplot(3,2,3);
hold on
title(['Time t =',num2str(2*tmax/5)]);
xlabel('x');
plot(x,n(2*(deltat-1)/5,:),'r');
plot(x,c(2*(deltat-1)/5,:),'b');
hold off

subplot(3,2,4);
hold on
title(['Time t =',num2str(3*tmax/5)]);
```

```
xlabel('x');
plot(x,n(3*(deltat-1)/5,:),'r');
plot(x,c(3*(deltat-1)/5,:),'b');
hold off

subplot(3,2,5);
hold on
title(['Time t =',num2str(4*tmax/5)]);
xlabel('x');
plot(x,n(4*(deltat-1)/5,:),'r');
plot(x,c(4*(deltat-1)/5,:),'b');
hold off

subplot(3,2,6);
hold on
title(['Time t =',num2str(5*tmax/5)]);
xlabel('x');
plot(x,n(5*(deltat-1)/5,:),'r');
plot(x,c(5*(deltat-1)/5,:),'b');
hold off
%-----------------------------------------------------------------------
function [c,f,s]=vfill_pde(x,t,u,DuDx)
global chi gamma D G

% Define the system of equations
n=u(1);
c=u(2);
```

```
s=[0;n-c];
f=[G*(D*DuDx(1)-chi*n*(1-n/gamma)*DuDx(2));G*DuDx(2)];
c=[1;1];
%--------------------------------------------------------------------
function n0=vfill_ic(x)

% Initial Conditions with random perturbation
n0=[1+0.01*rand;0];

%--------------------------------------------------------------------
function [pl,ql,pr,qr]=vfill_bc(xl,nl,xr,nr,t)

% Set zero-flux boundary conditions
pl=[0;0];
pr=[0;0];
qr=[1;1];
ql=[1;1];

%%%%%%%%%%%%%%%%%%%%%%%%%%%%%%%%%%%%%%%%%%%%%%%%%%%%%%%%%%%%%%%%%%%%%%%
```

### 7.1.2 'Vfillbvp' program

Boundary value problem solver to find solutions to (4.18) and store these solutions along with related functions, $R(x)$ and $S(x)$.

```
%%%%%%%%%%%%%%%%%%%%%%%%%%%%%%%%%%%%%%%%%%%%%%%%%%%%%%%%%%%%%%%%%%%%%%%%%%%%
function Vfillbvp

clc
clf
clear all
close all

global chi D gamma G lambda %( Here G is the rescaling factor,
                            %   Gamma = Dv/beta*L^2)
% Set parameter values
D=10;
chi=50;
gamma=2;
G=0.004;
lambda=exp(5);

% Set number of grid points
deltax=501;

% m is required by BVP4C and is set to zero in our case
% (see MATLAB documentation)
m=0;
```

```
% Set the domain size using the number of grid points defined above
x=linspace(0,1,deltax);

% Call BVP4C to solve the ODE system
solinit=bvpinit(x,@vfill_init);
sol=bvp4c(@vfill_ode,@vfill_odebc,solinit);

% Extract solution for c and build n
S=deval(sol,x);
cstat=S(1,:);
nstat= gamma./(1+lambda*exp(-chi.*cstat./D));

% Define R(x) and S(x) functions
cdash=diff(cstat)./diff(x);
cdash(deltax)=0;

ndash=diff(nstat)./diff(x);
ndash(deltax)=0;

R=nstat.*(1-nstat./gamma);
S=cdash.*(1-2.*nstat./gamma);

% Calculate R_x and S_x
Rdash=diff(R)./diff(x);
Rdash(501)=0;
```

```
Sdash=diff(S)./diff(x);
Sdash(501)=Sdash(500);

% Save the results for future calculations
save nandc2step

% Plot the solutions
figure(2)
axis([0 1 0 2.5])
hold on
plot(x,nstat,'r')
plot(x,cstat,'b')
title('Plot of n(x) (red) and c(x) (blue)')
xlabel('x')
hold off

% Check that the integrals of the c and n solutions equal 1
% and display the results.
intc=trapz(x,cstat)
intlam=trapz(x,gamma./(1+(gamma-1)*exp(chi/D)*exp(-chi.*cstat./D)))
%-----------------------------------------------------------------------
function dudx=vfill_ode(x,u)

global D gamma chi G lambda

% Define the ODE system. u(1)=c, u(2)=w.
dudx=[u(2)
```

```
      (1/G).*(u(1)-gamma./(1+lambda.*exp(-chi.*u(1)./D)))];

%-----------------------------------------------------------------------
function res=vfill_odebc(ua,ub)

% Set the boundary conditions. In this case, we set w
% equal to zero at the boundaries.
res=[ua(2)
     ub(2)];

%-----------------------------------------------------------------------
function guess=vfill_init(x)

% Initial guess function. This can be chosen to find p-step solutions
% by selecting an appropriate wavenumber.
guess=[1+cos(2*pi*x)
          0];

%%%%%%%%%%%%%%%%%%%%%%%%%%%%%%%%%%%%%%%%%%%%%%%%%%%%%%%%%%%%%%%%%%%%%%%
```

### 7.1.3 'AsandBs' program

Program to build all block matrices, $A_i$ and $B_{ij}$ (see (4.35), and store them so as they can be used to construct $Q$ (see (4.34)).

```
%%%%%%%%%%%%%%%%%%%%%%%%%%%%%%%%%%%%%%%%%%%%%%%%%%%%%%%%%%%%%%%%%%%%%%%%%%%%
function AsandBs
clc
clear all
clf

% Load the desired p-step solution and related functions computed
% using vfillbvp.
load nandc2step

% Set the size of the Q approximation (2*jmax by 2*jmax).
jmax=100;

for i=1:jmax
%-------------------------------------------------------------------------
% Define M_i and N_i
Mi=chi*trapz(x, R.*(i^2*pi^2).*(cos(i*pi*x)).^2
      +Rdash.*(i*pi/2).*sin(2*i*pi*x) );
eval(['M_' num2str(i) '=Mi;'])

Ni= chi*trapz(x, Sdash.*(cos(i*pi*x)).^2-S.*(i*pi/2).*sin(2*i*pi*x) );
eval(['N_' num2str(i) '=Ni;'])
```

```
% Build A_i
Ai=[ -G*(2*Ni+D*(i^2*pi^2)) 2*G*Mi ; 1 -(G*(i^2*pi^2)+1)];
eval(['A_' num2str(i) '=Ai;'])
%-----------------------------------------------------------------------
for j=1:jmax

% Define and label the K_i_j and H_i_j matrices
Hij = trapz(x, cos(i*pi*x).*cos(j*pi*x).*R.*j^2*pi^2
        +cos(i*pi*x).*sin(j*pi*x).*Rdash*j*pi );
eval(['H_', num2str(i) '_' num2str(j) '=Hij;'])

Kij = trapz(x, cos(i*pi*x).*cos(j*pi*x).*Sdash
        -cos(i*pi*x).*sin(j*pi*x).*S*j*pi );
eval(['K_', num2str(i) '_' num2str(j) '=Kij;'])
%-----------------------------------------------------------------------
% Build the Bij matrices

Bij=[-2*G*chi*Kij 2*G*chi*Hij ; 0 0];
eval(['B_',num2str(i) '_' num2str(j) '=Bij;'])

end
end

% Create matrix of K_ijs, KMatrix
for i=1:jmax;
for j=1:jmax;
Kmatrix(i,j)= eval(['K_' num2str(i) '_' num2str(j)]);
```

```
end
end

% Create matrix of H_ijs, HMatrix
for i=1:jmax;
for j=1:jmax;
Hmatrix(i,j)= eval(['H_' num2str(i) '_' num2str(j)]);
end
end

% Plot values of H and K matrices using surface plots
figure(1)
surf(Kmatrix-diag(diag(Kmatrix)))
% Note that the main diagonal is omitted as j cannot equal i.

title('Values of K_i_j for a 2-step n,c','fontsize',14)
xlabel('i','fontsize',13)
ylabel('j','fontsize',13)
colorbar

figure(2)
surf(Hmatrix-diag(diag(Hmatrix)))
title('Values of H_i_j for a 2-step n,c','fontsize',14)
xlabel('i','fontsize',13)
ylabel('j','fontsize',13)
colorbar
```

```
for i=1:jmax
    Nivec(i)=eval(['N_' num2str(i)]);
end

for i=1:jmax
    Mivec(i)=eval(['M_' num2str(i)]);
end

% Plot the N_j and M_j functions
figure(3)
plot(Nivec,'--*b')
xlabel('i')
title('Values of N_i for 2-step n,c')

figure(4)
plot(Mivec,'--*r')
xlabel('i')
title('Values of M_i for 2-step n,c')

% Save the results for further calculations.
save AsandBs2stepjmax100
```

%%%%%%%%%%%%%%%%%%%%%%%%%%%%%%%%%%%%%%%%%%%%%%%%%%%%%%%%%%%%%%%%%%%%%%%%%%%%%%%

### 7.1.4 'Qbuilder' Program

Program to construct a finite approximation of the matrix, Q (see (4.34)), and calculate its eigenvalues.

```
%%%%%%%%%%%%%%%%%%%%%%%%%%%%%%%%%%%%%%%%%%%%%%%%%%%%%%%%%%%%%%%%%%%%%%%%%%%%
function Qbuilder

% Load A_i and B_ij matrices computed using 'AsandBs'.
load AsandBs2stepjmax100

% Build the matrix, Q:
%-------------------------------------------------------------------

% Build each row separately and label them. IF statements determine
% which As and Bs go where.
for i=1:jmax;
for j=1:jmax;

    if j==i && i==1
        qtemp=eval(['A_' num2str(j)]);
        eval(['Q_row' num2str(i) '=qtemp;']);
    elseif j==i
        qtemp=[qtemp eval(['A_' num2str(j)])];
        eval(['Q_row' num2str(i) '=qtemp;']);
    elseif j==1
        qtemp=[eval(['B_' num2str(i) '_' num2str(j)])];
        eval(['Q_row' num2str(i) '=qtemp;']);
```

```
    else
        qtemp=[qtemp eval(['B_' num2str(i) '_' num2str(j)])];
        eval(['Q_row' num2str(i) '=qtemp;']);
    end
end
end

% Take each row and join one under the other to build Q.
Qfull= Q_row1;
for i=2:jmax
   Qfull= [Qfull ; eval(['Q_row' num2str(i);])];
end

%-----------------------------------------------------------------------

% Calculate eigenvalues of Q.
[V,nu]=eig(Qfull);

% Display eigenvalues correct to 15 decimal places in descending order.
format long
QEigenvalues=sort(eig(Qfull))

%%%%%%%%%%%%%%%%%%%%%%%%%%%%%%%%%%%%%%%%%%%%%%%%%%%%%%%%%%%%%%%%%%%%%%%%%%%
```

## 7.2 COMSOL Multiphysics Settings

Given below are general mesh and solver settings used in COMSOL setup when solving (3.13) and (5.12). Settings were the same for all simulations with the obvious exception of domain geometry and model equations, both of which can be set up by following COMSOL documentation.

1. Modules Used
    - Navier-Stokes equations: 'Laminar flow (ns)' (incompressible)
    - Chemotaxis equations: 'PDE (g)'
2. Boundary Condition Types Used
    - No-slip: 'Wall'
    - Fluid-air interface: 'Symmetry'
    - All boundaries for $n$ and $c$: 'Zero Flux'
    - Pressure at surface: 'Pressure Point Constraint'
    - 'Periodic Flow Condition' and 'Periodic Condition' were used where indicated (see text)
3. Mesh Settings
    - Sequence Type: 'Physics-controlled mesh'
    - Maximum element size: '0.028' (example. see text for number of elements used)
    - Minimum element size: '4.0E-4'
    - Resolution of curvature: '0.25'
4. Shape Functions

- $n$: 'LaGrange (Quadratic)'
- $c$: 'LaGrange (Quadratic)'
- $u, v, w$: 'LaGrange (Quadratic)'
- $p_e$: 'LaGrange (Linear)'

5. Time-Dependent Solver
   - Absolute Tolerance
     - Global method: 'Unscaled'
     - Update scaled absolute tolerance: 'Off'
   - Time Stepping
     - Method: 'Generalized alpha'
   - Output
     - Store time-derivatives: 'Off'
     - Store solution out-of-core: 'Off'
   - Advanced
     - Error estimation: 'Exclude algebraic'
     - Matrix Symmetry: 'Nonsymmetric'
   - Linear Solver
     - Solver: 'PARDISO'
     - Preordering algorithm: 'Nested dissection'
     - Check error estimate: 'Yes'
     - Factor in error estimate: '4000000'

# Bibliography


[1] The American Phytopathological Society webpage. www.apsnet.org.

[2] AUTO 07p webpage. http://cmvl.cs.concordia.ca/auto/.

[3] Center for Biofilm Engineering webpage. http://www.biofilm.montana.edu.

[4] COMSOL webpage. http://www.uk.comsol.com/.

[5] EasyFit webpage. http://www.mathwave.com/.

[6] Kinovea webpage. http://www.kinovea.org.

[7] Minitab 16 Statistical Software. www.minitab.com, 2010.

[8] R A Adams and J J F Fournier. *Sobelov Spaces*. Elsevier, second edition, 2003.

[9] J Adler. Chemoreceptors in bacteria. *Science*, 166(3913):1588–1597, 1969.

[10] M D Baker, P M Wolanin, and J B Stock. Signal transduction in bacterial chemotaxis. *BioEssays*, 28(1):9–22, 2006.

[11] M A Bees and N A Hill. Wavelengths of Bioconvection Patterns. *The Journal of Experimental Biology*, 200(10):1515–1526, 1997.

[12] M A Bees and N A Hill. Linear bioconvection in a suspension of randomly swimming, gyrotactic micro-organisms. *Physics of Fluids*, 10(8):1864–1881, 1998.

[13] M A Bees and N A Hill. Non-linear bioconvection in a deep suspension of gyrotactic swimming micro-organisms. *Journal of Mathematical Biology*, 38(2):135–168, 1999.

[14] H M Behrens, M H Weisenseel, and A Sievers. Rapid Changes in the Pattern of Electric Current around the Root Tip of *Lepidium sativum* L. following Gravistimulation. *Plant Physiology*, 70(4):1079–1083, 1982.

[15] H C Berg. *Random Walks in Biology*. Princeton University Press, revised edition, 1993.

[16] H C Berg. The Rotary Motor of Bacterial Flagella. *Annual Review of Biochemistry*, 72:19–54, 2003.

[17] H C Berg. *E. Coli in Motion*. Springer-Verlag, New York, 2004.

[18] C Brasier. *Phytophthora* Biodiversity: How Many *Phytophthora* Species Are There? *Proceedings of the Fourth Meeting of IUFRO Working Party S07.02.09*, pages 101–116, 2009.

[19] J N Cameron and M J Carlile. Negative Geotaxis of Zoospores of the Fungus *Phytophthora*. *Journal of General Microbiology*, 98:599–602, 1977.

[20] J N Cameron and M J Carlile. Negative chemotaxis of zoospores of the fungus *Phytophthora palmivora*. *Journal of General Microbiology*, 120:347–353, 1980.

[21] M J Carlile. *Motility, taxis and tropism in Phytophthora*. American Phytopathological Society, 1983.

[22] M J Carlile. The zoospore and its problems. *Symposium series - British Mycological Society. Symp Ser Mycol Soc*, 11:105–118, 1986.

[23] C E Caten and J L Kinks. Spontaneous variability of single isolates of *Phytophthora infestans*. I. cultural variation. *Canadian Journal of Botany*, 46(4):329–348, 1968.

[24] S Chandrasekhar. Stochastic Problems in Physics and Astronomy. *Reviews of Modern Physics*, 15(1):1–89, 1943.

[25] M Chaplain. Mathematical modelling of angiogenesis. *Journal of Neuro-oncology*, 50(1-2):37–51, 2000.

[26] M Chaplain and A Stuart. A model mechanism for the chemotactic response of endothelial cells to tumour angiogenesis factor. *IMA journal of mathematics applied in medicine and biology*, 10(3):149–68, 1993.

[27] P Chavanis. A stochastic Keller-Segel model of chemotaxis. *Communications in Nonlinear Science and Numerical Simulation*, 15(1):60–70, 2010.

[28] S Childress, M Levandowsky, and E A Spiegel. Pattern formation in a suspension of swimming microorganisms: equations and stability theory. *Journal of Fluid Mechanics*, 69(3):591–613, 1975.

[29] J C Dallon and H G Othmer. A discrete cell model with adaptive signalling for aggregation of *Dictyostelium discoidium*. *Philisophical Transactions of the Royal Society of London. Series B: Biological Sciences*, 352(1351):391–417, 1997.

[30] A de Bary. Researches into the nature of the potato fungus, *Phytophthora infestans*. *Journal of the Royal Agricultural Society of England, Series 2*, 2:239–269, 1876.

[31] J W Deacon and S P Donaldson. Molecular recognition in the homing responses of zoosporic fungi, with special reference to *Phythium* and *Phytophthora*. *Mycological Research*, 97(10):1153–1171, 1993.

[32] C Dombrowski, L Cisneros, S Chatkaew, R Goldstein, and J O Kessler. Self-Concentration and Large-Scale Coherence in Bacterial Dynamics. *Physical Review Letters*, 93(9):098103, 2004.

[33] A Drenth, E M Janssen, and F Govers. Formation and survival of oospores of *Phytophthora infestans* under natural conditions. *Plant Pathology*, 44(1):86–94, 1995.

[34] D Dufour, V Leung, and C M Lévesque. Bacterial biofilm: structure, function, and antimicrobial resistance. *Endodontic Topics*, 22(1):2–16, 2010.

[35] J M Duncan. *Phytophthora* - an abiding threat to our crops. *Microbiology Today*, 26:114–116, 1999.

[36] L Edelstein-Keshet. *Mathematical Models in Biology*. Classics in Applied Mathematics 46. Siam, 2005.

[37] T Engelmann. Neue Methode zur Untersuchung der Sauerstoffaussheidung pflanzlicher und thierischer Organsismen. *Pflügers Archiv: European Journal of Physiology*, 25(1):285–292, 1881.

[38] T Engelmann. Zur Biologie der Schizomyceten. *Pflügers Archiv: European Journal of Physiology*, 26(1):537–545, 1881.

[39] E F Foxman, E J Kunkel, and E C Butcher. Integrating Conflicting Chemotactic Signals: The Role of Memory in Leukocyte Navigation. *Journal of Cell Biology*, 147(3):577–588, 1999.

[40] W Fry. *Phytophthora infestans* : the plant (and R gene) destroyer. *Molecular Plant Pathology*, 9(3):385 – 402, 2008.

[41] E Galiana, S Fourré, and G Engler. *Phytophthora parasitica* biofilm formation: Installation and organisation of microcolonies on the surface of a host plant. *Environmental Microbiology*, 10(8):2164–2171, 2008.

[42] J Galindo and M E Gallegly. The Nature of Sexuality of *Phytophthora infestans*. *Phytopathology*, 50:123–128, 1960.

[43] S Ghorai and N A Hill. Development and stability of gyrotactic plumes in bioconvection. *Journal of Fluid Mechanics*, 400:1–31, 1999.

[44] S Ghorai and N A Hill. Wavelengths of gyrotactic plumes in bioconvection. *Bulletin of Mathematical Biology*, 62(3):429–450, 2000.

[45] S Ghorai and N A Hill. Gyrotactic bioconvection in three dimensions. *Physics of Fluids*, 19:054107, 2007.

[46] S B Goodwin and A Drenth. Origin of the A2 Mating Type of *Phytophthora infestans* Outside Mexico. *Phytopathology*, 87(10):992–999, 1997.

[47] L J Grenville-Briggs, V L Anderson, J Fugelstad, A O Avrova, J Bouzenzana, A Williams, S Wawra, S C Whisson, P R J Birch, V Bulone, and P van West. Cellulose Synthesis in *Phytophthora infestans* Is Required for Normal Appressorium Formation and Successful Infection of Potato. *The Plant Cell*, 20:720–738, 2008.

[48] J M Griffith, J R Iser, and B R Grant. Calcium control of differential of *Phytophthora palmivora*. *Archives of Microbiology*, 149(6):565–571, 1988.

[49] P Grindrod, J D Murray, and S Sinha. Steady-State Spatial Patterns in a Cell-Chemotaxis Model. *IMA Journal of Mathematics Applied in Medicine and Biology*, 6(2):69–79, 1989.

[50] J Happel and H Brenner. *Low Reynolds Number Hydrodynamics*. Springer, 1983.

[51] C J Hickman. Biology of *Phytophthora* Zoospores. *Phytopathology*, 60(7):1128–1135, 1970.

[52] N A Hill and T J Pedley. Bioconvection. *Fluid Dynamics Research*, 37(1-2):1–20, 2005.

[53] T Hillen and K Painter. A user's guide to PDE models for chemotaxis. *Journal of Mathematical Biology*, 58(1-2):183–217, 2009.

[54] A J Hillesdon, T J Pedley, and J O Kessler. The Development of Concentration Gradients in a Suspension of Chemotactic Bacteria. *Bulletin of Mathematical Biology*, 57(2):299–344, 1995.

[55] H H Ho and C J Hickman. Asexual Reproduction and Behaviour of Zoospores of *Phytophthora megasperma* var. sojae. *Canadian Journal of Botany*, 45(11):1963–1981, 1967.

[56] H H Ho and C J Hickman. Factors Governing Zoospore Responses of *Phytophthora megasperma* var. sojae to Plant Roots. *Canadian Journal of Botany*, 45(11):1983–1994, 1967.

[57] H H Ho, C J Hickman, and R W Telford. The Morphology of Zoospores of *Phytophthora megasperma* var. sojae and Other Phycomycetes. *Canadian Journal of Botany*, 46(1):88–89, 1968.

[58] M M Hopkins and L J Fauci. A computational model of the collective fluid dynamics of motile micro-organisms. *Journal of Fluid Mechanics*, 455:149–174, 2002.

[59] D Horstmann. From 1970 until present: The Keller-Segel model in chemotaxis and its consequences i. *Jahresberichte DMV*, 105(3):103–165, 2003.

[60] P A Iglesias and P N Devreotes. Navigating through models of chemotaxis. *Current Opinion in Cell Biology*, 20(1):35–40, 2008.

[61] D Iron and M J Ward. The Stability and Dynamics of Hot-Spot Solutions for Two One-Dimensional Microwave Heating Models. *Analysis and Applications*, 2(1):21–70, 2004.

[62] I M Jánosi, A Czirók, D Silhavy, and A Holczinger. Is bioconvection enhancing bacterial growth in quiescent environments? *Environmental Microbiology*, 4(9):525–531, 2002.

[63] I M Jánosi, J O Kessler, and V K Horváth. Onset of bioconvection in suspensions of *Bacillus subtilis*. *Physical Review E*, 58(4):4793–4800, 1998.

[64] H S Judelson and F A Blanco. The spores of *Phytophthora*: weapons of the plant destroyer. *Nature Reviews Microbiology*, 3(1):47–58, 2005.

[65] E F Keller and L A Segel. Initiation of slime mold aggregation viewed as an instability. *Journal of Theoretical Biology*, 26(3):399–415, 1970.

[66] E F Keller and L A Segel. Model for chemotaxis. *Journal of Theoretical Biology*, 30(2):225–234, 1971.

[67] J O Kessler. Hydrodynamic focusing of motile algal cells. *Nature*, 313:218–220, 1985.

[68] J O Kessler. Individual and collective fluid dynamics of swimming cells. *Journal of Fluid Mechanics*, 173:191–205, 1986.

[69] K L Khew and G A Zentmyer. Chemotactic Response of Zoospores of Five Species of *Phytophthora*. *Phytopathology*, 63:1511–1517, 1973.

[70] W H Ko and M J Chan. Aggregation of *Phytophthora capsici* Zoospores and their Interaction with Zoospores of *P. Palmivora*. *Journal of General Microbiology*, 80(2):549–551, 1974.

[71] W H Ko and L L Chase. Aggregation of Zoospores of *Phytophthora palmivora*. *Journal of General Microbiology*, 78(1):79–82, 1973.

[72] R Kolter and E P Greenberg. Microbial sciences: the superficial life of microbes. *Nature*, 441:300–302, 2006.

[73] M Latijnhouwers, W Ligterink, V G Vleeshouwers, P van West, and F Govers. A G$\alpha$ subunit controls zoospore motility and virulence in the potato late blight pathogen *Phytophthora infestans*. *Molecular Microbiology*, 51(4):925–936, 2003.

[74] S S Leach. Effects of copper and copper fungicide soil residues on *Phytophthora infestans*. *American Potato Journal*, 43(12):431–438, 1966.

[75] C Leifert. Development of a systems approach for the management of late blight in EU organic potato production. Project Report: `http://ec.europa.eu/research/agriculture/projects/qlrt_1999_31065_en.htm`, 2001.

[76] M Levandowsky, W S Childress, E A Spiegel, and S H Hutner. A mathematical model of pattern formation by swimming microorganisms. *Journal of Protozoology*, 22(2):296–306, 1975.

[77] P S Lovely and F W Dahlquist. Statistical measures of bacterial motility and chemotaxis. *Journal of Theoretical Biology*, 50(2):477–496, 1975.

[78] M Madigan, J Martinko, D Stahl, and D Clark. *Brock Biology of Microorganisms*. Pearson Education, thirteenth edition, 2011.

[79] J Martiel and A Goldbeter. A Model Based on Receptor Desensitization for Cyclic AMP Signalling in *Dictyostelium* Cells. *Biophysical Journal*, 52(5):807–828, 1987.

[80] B M Morris and N A R Gow. Mechanism of Electrotaxis of Zoospores of Phytopathogenic Fungi. *Phytopathology*, 83:877–882, 1993.

[81] B M Morris, B Reid, and N A R Gow. Tactic response of zoospores of the fungus *Phytophthora palmivora* to solutions of different pH in relation to plant infection. *Microbiology*, 141(5):1231–1237, 1995.

[82] J D Murray. *Mathematical Biology, I: An Introduction*, volume 1. Berlin: Springer-Verlag, 2002.

[83] J D Murray. *Mathematical Biology II: Spatial Models and Biochemical Applications*, volume 2. Berlin: Springer-Verlag, 2003.

[84] M R Myerscough, P K Maini, and K J Painter. Pattern Formation in a Generalised Chemotactic Model. *Bulletin of Mathematical Biology*, 60(1):1–26, 1998.

[85] NetLogo. Wilensky, U. Center for Connected Learning and Computer-Based Modeling, Northwestern University. Evanston, IL. `http://ccl.northwestern.edu/netlogo/`, 1999.

[86] E G Ninfa, A Stock, S Mowbray, and J Stock. Reconstitution of the bacterial

chemotaxis signal transduction system from purified components. *Journal of Biological Chemistry*, 266:9764–9770, 1991.

[87] D A Noever, R Cronise, and H C Matsos. Preferred Negative Geotactic Orientation in Mobile Cells: *Tetrahymena* Results. *Biophysical Journal*, 67(5):2090–2095, 1994.

[88] M Nowicki, M R Foolad, M Nowakowska, and E U Kozik. Potato and Tomato Late Blight Caused by *Phytophthora infestans*: An Overview of Pathology and Resistance Breeding. *Plant Disease*, 96(1):4–17, 2012.

[89] N Ochiai, M I Dragiila, and J L Parke. Pattern swimming of *Phytophthora citricola* zoospores: An example of microbial bioconvection. *Fungal Biology*, 115(3):228–235, 2011.

[90] A Okubo and S A Levin. *Diffusion and Ecological Problems: Modern Perspectives*. Springer, 2nd edition, 2001.

[91] G W Ordal. Bacterial Chemotaxis: Biochemistry of Behaviour in a Single Cell. *Critical Reviews of Microbiology*, 12(2):95–130, 1985.

[92] H G Othmer, S R Dunbar, and W Alt. Models of Dispersal in Biological Systems. *Journal of Mathematical Biology*, 26:263 – 298, 1988.

[93] H G Othmer and A Stevens. Aggregation, Blowup and Collapse: The ABC's of Taxis in Reinforced Random Walks. *Journal of Applied Mathematics*, 57(4):1044 – 1081, 1997.

[94] K J Painter. Continuous Models for Cell Migration in Tissues and Applications to Cell Sorting via Differential Chemotaxis. *Bulletin of Mathematical Biology*, 71:1117–1147, 2009.

[95] K J Painter and T Hillen. Volume-Filling and Quorum-Sensing in Models for Chemosensitive Movement. *Canadian Applied Mathematics Quarterly*, 10(4):501–543, 2002.

[96] J S Parkinson. Signal transduction schemes of bacteria. *Cell*, 73(5):857–871, 1993.

[97] C S Patlak. Random Walk with Persistence and External Bias. *Bulletin of Mathematical Biophysics*, 15(3):311–338, 1953.

[98] T J Pedley, N A Hill, and J O Kessler. The growth of bioconvection patterns in a uniform suspension of gyrotactic micro-organisms. *Journal of Fluid Mechanics*, 195:223–237, 1988.

[99] T J Pedley and J O Kessler. A new continuum model for suspensions of gyrotactic micro-organisms. *Journal of Fluid Mechanics*, 212:155–182, 1990.

[100] T J Pedley and J O Kessler. Hydrodynamic Phenomena in Suspensions of Swimming Microorganisms. *Annual Review of Fluid Mechanics*, 24:313–358, 1992.

[101] B Perthame. *Transport Equations in Biology*. Frontiers in Mathematics. Birkhäuser, 2007.

[102] W Pfeffer. Uber chemotaktische bewegungen von bacterien, flagellaten and volvocineen. *Untersuchungen aus dem Botanischen Institut zu Tübingen*, 2:582, 1888.

[103] J R Platt. "Bioconvection Patterns" in Cultures of Free-Swimming Organisms. *Science*, 133(3466):1766–1767, 1961.

[104] M S Plesset and H Winet. Bioconvection patterns in swimming micro-organism cultures as an example of Rayleigh-Taylor instability. *Nature*, 248:441–443, 1974.

[105] J R Porter and D S Shaw. Aggregation of *Phytophthora drechsleri* zoospores; pattern analysis suggests a taxis. *Transactions of the British Mycological Society*, 71(3):515–518, 1978.

[106] A B Potapov and T Hillen. Metastability in Chemotaxis Models. *Journal of Dynamics and Differential Equations*, 17(2):293–330, 2005.

[107] K B Raper. *Dictyostelium discoidium*, A New Species of Slime Mold from Decaying Forest Leaves. *Journal of Agricultural Research*, 50(2):135–147, 1935.

[108] B Reid, B M Morris, and N A R Gow. Calcium-Dependent, Genus-Specific, Autoaggregation of Zoospores of Phytopathic Fungi. *Environmental Mycology*, 19(3):202–213, 1995.

[109] A Y Rossman and M E Palm. Why are *Phytophthora* and other Oomycota not true Fungi? *Outlooks on Pest Management*, 17:217–219, 2006.

[110] R Schaaf. Stationary Solutions of Chemotaxis Systems. *Transactions of the American Mathematical Society*, 292(2):531–556, 1985.

[111] G L Schumann and C J D'Arcy. Late blight of potato and tomato, 2000.

[112] D Shaw, Z Nagy, and D Thomas. Variation in *Phytophthora infestans*: determination of mating types and pathogenicity. Technical report, British Potato Council, March 2006.

[113] M Silverman and M Simon. Chemotaxis in *Escherichia coli*: Methylation of *che* gene products. *Proceedings of the National Academy of Sciences USA*, 74(8):3317–3321, 1977.

[114] J Stelling. Mathematical models in microbial systems biology. *Current Opinion in Microbiology*, 7(5):513–518, 2004.

[115] F Suffert, E Latxauge, and I Sache. Plant pathogens as agroterrorist weapons: assessment of the threat for European agriculture and forestry. *Food Security*, 1(2):221–232, 2009.

[116] X Sun and M J Ward. The Dynamics and Coarsening of Interfaces for the Viscous Cahn-Hilliard Equation in One Spatial Dimension. In *Studies in Applied Mathematics 105*, pages 203–234, 1999.

[117] T Suzuki. *Free Energy and Self-Interacting Particles*. Birkhäuser, 2005.

[118] D D Thomas and A P Peterson. Chemotactic auto-aggregation in the water mould *Achlya*. *Journal of General Microbiology*, 136(5):847–853, 1990.

[119] K J Tomchik and P N Devreotes. Adenosine 3',5'-monophosphate waves in *Dictyostelium discoideum*: a demonstration by isotope dilution–fluorography. *Science*, 212(4493):443–446.

[120] R Tyson, S R Lubkin, and J D Murray. Model and analysis of chemotactic bacterial patterns in a liquid medium. *Journal of Mathematical Biology*, 38(4):359–375, 1999.

[121] P van West, A A Appiah, and N A R Gow. Advances in research on oomycete root pathogens. *Physiological and Molecular Plant Pathology*, 62(2):99–113, 2003.

[122] P van West, B M Morris, B Reid, A A Appiah, M C Osborne, T A Campbell, S J Shepherd, and N A R Gow. Oomycete Plant Pathogens Use Electric Fields to Target Roots. *Molecular Plant-Microbe Interactions*, 15(8):790–798, 2002.

[123] R V Vincent and N A Hill. Bioconvection in a suspension of phototactic algae. *Journal of Fluid Mechanics*, 327:343–371, 1996.

[124] H Wager. On the Effect of Gravity upon the Movements and Aggregation of *Euglena viridis*, Ehrb., and other Micro-organisms. *Philisophical Transactions of the Royal Society of London B*, 201:333–390, 1911.

[125] C A Walker, M Koppe, L J Grenville-Briggs, A O Avrova, N R Horner, A D McKinnon, S C Whisson, P R J Birch, and P van West. A putative DEAD-box RNA-helicase is required for normal zoospore development in the late blight pathogen *Phytophthora infestans*. *Fungal Genetics and Biology*, 45:954–962, 2008.

[126] C A Walker and P van West. Zoospore development in the oomycetes. *Fungal Biology Reviews*, 21(1):10–18, 2007.

[127] G Wang and J Wei. Steady State solutions of a Reaction-Diffusion System Modelling Chemotaxis. *Mathematische Nacrichten*, 233-234(1):221–236, 2002.

[128] Z Wang and T Hillen. Classical solutions and pattern formation for a volume filling chemotaxis model. *Chaos*, 17(3):037108, 2007.

[129] G M Waterhouse. *Key to the species of Phytophthora de Bary*. Issue 92 of Mycological papers. Commonwealth Mycological Institute, 1963.

[130] S A West, S P Diggle, A Buckling, A Gardner, and A S Griffin. The Social Lives of Microbes. *Annual Review of Ecology, Evolution, and Systematics*, 38:53–77, 2007.

[131] D E Woodward, R Tyson, M R Myerscough, J D Murray, E O Budrene, and H C Berg. Spatio-temporal patterns generated by *Salmonella typhimurium*. *Biophysical Journal*, 68(5):2181–2189, 1995.

[132] E Zeidler. *Nonlinear Functional Analysis and its Applications I: Fixed-Point Theorems*. Springer-Verlag, New York, 1986.

[133] G A Zentmyer. Chemotaxis of Zoospores for Root Exudates. *Science*, 133(3464):1595–1596, 1961.

[134] M Zhang, Y Meng, Q Wang, D Liu, J Quan, A R Hardham, and W Shan. PnPMA1, an atypical plasma membrane $H^+$-ATPase, is required for zoopsore development in *Phytophthora parasitica*. *Fungal Biology*, 116(9):1013–1023, 2012.